UNIVERSITY OF SOUTHAMPTON
FACULTY OF PHYSICS AND APPLIED SCIENCE
PHYSICS AND ASTRONOMY

Radio/X-ray variability and structure investigation of Seyfert galaxy NGC 4051

by

Sadie Jones

Thesis for the degree of Doctor of Philosophy
27th April 2012

UNIVERSITY OF SOUTHAMPTON

ABSTRACT

FACULTY OF PHYSICS AND APPLIED SCIENCE

PHYSICS AND ASTRONOMY

Doctor of Philosophy

Radio/X-ray variability and structure investigation of Seyfert galaxy NGC 4051

by Sadie Jones

This thesis is an investigation into the emission from an individual Narrow Line Seyfert 1 (NLS1) Active Galactic Nuclei (AGN) NGC 4051. NLS1s have all the properties of Seyfert galaxies but show peculiar characteristics, including the narrowest Balmer lines, strongest Fe II emission and extreme properties in the X-rays. NGC 4051, is one of the most X-ray bright Seyferts and it has been studied extensively by a number of X-ray observatories. Recent studies have also revealed that Seyfert cores are variable at radio wavelengths, however, there are very few Seyfert radio variability investigations, and this is one of the first that also investigates the radio/X-ray (jet/disc) coupling. It has been known for some time that both the X-ray and continuum radio observations provide an optimal tool to access the innermost regions of the AGN. A combination of X-ray, radio and optical data is used here to give an in depth analysis of both the core and extended emission regions of NLS1 NGC 4051.

This work reveals that there is no clear evidence for radio variability in the core emission of NGC 4051 at 8.4 GHz with the possible exception of very low amplitude ~ 0.12 mJy variations detected in VLA A configuration. Deep VLA observations reveal a mean spectral index value of $\alpha \sim -0.3$ for the core, suggesting a self absorbed jet. The surrounding radio emission has steeper spectral index values in the range of $-0.5 < \alpha < -1.6$ which suggests the extended radio emission is optically thin synchrotron emission. During the A configuration observations both VLA radio data sets (2000-2001 and 2008-2009) reveal a very weak positive correlation between the radio and much larger amplitude X-ray variations but there is no evidence for a β value much greater than ~ 0.1 for the $L_R \propto L_X^{\beta}$ relationship, which is consistent with a constant radio luminosity for the core. Collimated VLBI structure is detected which hints at the presence of an unseen jet. The proposed jet is of non-negligible power and estimates of the buoyancy speed of the lobes, and the break timescales from the radio spectral index provide evidence for radio activity in NGC 4051 occurring on timescales greater than $> 10^6$ years. Also, a change in the relative distance of the SW hotspot with respect to the core (seen in VLBI images) gives an apparent jet velocity 0.012 pc yr^{-1}, equivalent to a speed of $11,700$ kms^{-1} (~ 0.04 c). Deep VLA radio imaging of NGC 4051 shows double lobed radio emission, which lies along the same PA as optical [OIII] emission. The nucleus of the [OIII] emission is coincident with the core radio emission. This structure suggests the presence of a double sided ionisation cone, where both radio and optical emission are collimated by the same disc or tori.

CONTENTS

LIST OF TABLES

LIST OF FIGURES

DECLARATION

I, Sadie Jones, declare that the thesis entitled *Radio/X-ray variability and structure investigation of Seyfert galaxy NGC 4051* and the work presented in the thesis are both my own, and have been generated by me as a result of my own original research. I confirm that:

- this work was done wholly or mainly while in candidature for a research degree at this University;
- where any part of this thesis has previously been submitted for a degree or any other qualification at this University or any other institution, this has been clearly stated;
- where I have consulted the published work of others, this is always clearly attributed;
- where I have quoted from the work of others, the source is always given. With the exception of such quotations, this thesis is entirely my own work;
- I have acknowledged all main sources of help;
- where the thesis is based on work done by myself jointly with others, I have made clear exactly what was done by others and what I have contributed myself;
- Chapter 2 of this work have been published as:
  - Jones, S., McHardy, I., Moss, D., Seymour, N., Breedt, E., Uttley, P., Körding, E., & Tudose, V. 2011, Mon. Not. R. Astron. Soc., 412, 2641. 2011, MNRAS, 397, pp. 666-676.
- Papers based upon the work in Chapters 3 and 4, are in preparation.
- The published paper has been reformatted to comply with the University's thesis requirements.
- This thesis contains approximately 52 000 words.

Sadie Jones, 27th April 2012

ACKNOWLEDGEMENTS

Without the following people this thesis would never have got completed, and I almost certainly would have given up without their support. For this I cannot thank them enough, or buy them enough tea/pints/cocktails.

Thank you for believing in me, far more than I believe in myself.

Firstly to my parents who are my greatest inspiration. Always laughing and always crazy. You have given me so much support especially during my many PhD woes. You are both immensly awesome and hilarious and I love you big. Thank you also for all the financial support, walks, and lots of tea. Ta for letting me watch Button Moon, which apparently provided very early astronomy inspiration.

My Mam especially for sending me crazy inspiring text messages, sometimes up to twice a day, they really did keep me going, and for that reason many of the quotes feature in this thesis.

My Dad for being so wise, kind and athletic, and doing crazy things like Ironman Triathlons, which show me that you can really do anything when you put your mind to it.

Lovelly Nanny, thank you for being lovelly, for keeping me fed with the bestest Sunday dinners in the Universe and all the Parallel Universes. You were the bestest Nanny ever, thanks for being so kind, caring and nutty. I miss you every day.

My dearest 'special' Jimmy for getting me through this final year. You deserve a medal, one day when I am rich I will buy you a really awesome bike which is worth more than a car to say thanks. Thanks for all the stress relieving bike rides in the New Forest and other very muddy locations, oh and thanks for putting up with my emotions! I am so glad we found each other. Ta for keeping me well fed and cared for with a roof over ma' head, also thanks for teaching me how to use a dish washer. I massively appreciate your tough love attitude and all the banter. Big Cwtches.

Bestest friends: The Valley girls for much partying, dancing, laughing, take-away eating and gossiping. You guys keep me grounded and make sure I don't loose my Welsh accent. Cariad Mawr. Hollie and Jo, love you long time, we will always have Australia, thanks for driving the jeep, we will have to go back when we are much older now that I can drive us! Jack, Ta for all the moral support, letting me moan at you, being a great friend even when I am being self centered, unappreciative, and really dramatic. Thanks also for all the stress relieving running training, and helping me to learn to drive. Also, thanks for attempting to help with my English grammar, and allowing me to be in your quiz team, despite my lack of general knowledge. Jo, Sharon and Lee whom I very much enjoyed living with in halls/houses in Southamp-

ton, thanks for me making me feel welcome and helping me adjust to living in this scary land that they call England.
Southampton Astro people: Grace for being the most awesome office mate and inspiring much tea drinking and gossiping. Thanks for putting up with my general strangeness and singing/outbursts in the office. Elme for being all knowing and generally lovely. Martin for much radio astronomy help and much alcohol fueled fun. Derek for much late night radio astronomy/GMRT fun? and sending me a very nice email about not giving up when the GMRT data drove me to distraction. Liz for being dramatic with, running with, astrodome-ing with and drinking cocktails with, Tana for all the dancing, wine drinking, watching 'awesome' TV with. Lee and Seb for circuit training with, feel the burn! - you are indeed two of the most manly men. Thanks to Ian for the enthusiastic supervision which has made me a much stronger person, and hopefully more astronomically intelligent?, thankyou for all the useful discussions. Especially not forgetting Simon for helping with all my AIPS/computer/laptop/hard drive/linux/x-server problems, of which there were many, with immense enthusiasm.
Thank you big style to all the people who helped me with the horrid thesis writing up bit: Mam, Dad, Grace, Jack, Jim, Phil, Ian, Elme, Valeriu, and Tony W.
Welshies: Fraser, for small number statistics and bringing me creme eggs. Paul for letting me do two projects with the FT and letting me go to Alicante with Fraser and Vanessa to see what PhD life could be like. AIPS, because of you I will never eat bananas. I consider you Welsh also because you too do not like vowels.
I thank Facebook & my Twitter followers for providing councelling/procrastinational therapy. NGC 4051 I thank for being so 'complex' and 'interesting'. I must also give big final thanks to Doctor Who (specifically the David Tennant Doctor, whose poster has been on my office wall since the PhD journey began). Thank you to the Doctor for being such an inspirational Timelord. I aspire to be like you. Maybe one day the Astrodome will morph into the TARDIS ? Finally I thank Pearl for telling all the students that we have done outreach work with over the last 4 years that some day I (Sadie) will be a Dr, just like Doctor Who...here's hoping!

Sadie Jones, 27th April 2012

To Mam, Dad and Lovelly Nanny

May the astrobiological forces muster the strength of the Universe to help you fulfil your task. Onward and upward to the stars!

MAM

Mam I think my paper has started a war.

ME

Well leave them to get on with the warmongering, who knows what them black holes are doing....?
On a more serious note, do NOT miss Corrie tonight, people are gonna get killed by a tram!

MAM

PREFACE

The original aim of the PhD project was to make high quality 610 MHz GMRT maps of the 13^H deep survey field so that, in combination with 1.4 GHz observations from Seymour *et al.* (2004) I could measure spectral indices of all sources. The spectral indices would then be one of the main diagnostics, in combination with morphological structure from VLA and MERLIN observations (McHardy, 2007) and IR colours e.g. Seymour *et al.* (2009), as a discriminant of AGN from starburst emission. However, it is known that GMRT analysis is difficult, so to obtain experience with aperture synthesis interferometry, I began by analysing VLA observations of NGC 4051 to study the relationship between X-ray and radio variability in this Seyfert galaxy. However, due to the difficulties of removing the contribution from extended emission in the different VLA configurations, this work itself turned out to be very extensive and, in the end, forms the majority of the work presented here.

If we knew what it was we were doing, it would not be called research, would it?

ALBERT EINSTEIN

1 Introduction

This chapter gives an introduction to radio galaxies, with a focus on Active Galactic Nuclei (AGN) and their radio emission. Also explained is the motivation for investigating both the radio and X-ray variability of Seyfert type AGN specifically and their radio and optical [OIII] structure.

1.1 Radio Galaxies

The major focus of this thesis is the investigation of the radio emission from an individual active galaxy. Galaxies can be detected in all parts of the electromagnetic (EM) spectrum. Most galaxies are detected by their optical emission resulting from thermal radiation from stars within the galaxy. Stellar populations in galaxies also have a spectral component that peaks in the near infrared (NIR) and the dust of the interstellar medium (ISM) emits in the mid infrared (MIR) and the far infrared (FIR). The optical spectra of the nuclei of the host galaxies (which are coincident with the point-like radio nuclei) are used to define the two different types of radio galaxies, these being broad line radio galaxies (BLRGs) and narrow line radio galaxies (NLRGs). Galaxies also emit in the radio, ultraviolet and X-ray parts of the spectrum, and it is the radio emission which is the main concern of this thesis,

which in some places is compared with the X-ray emission.

Radio emission from galaxies comes in two forms, thermal and non-thermal. The thermal radio emission which is dependent on the temperature of the emitting object includes black body, free-free and spectral line emission. The non-thermal emission results from synchrotron radiation from electrons spiralling in magnetic fields, usually along jets that protrude from the centre of the optical galaxy. Non-thermal radiation processes are discussed later in Section 1.3.3 as these are the main emission process investigated in this work. Another source of non-thermal radio emission from galaxies is due to supernovae in star formation regions. For more information on this process see Section A.2. It is widely accepted that the radio emission from the galaxy is an extinction free tracer of the star formation rate. This relationship is discussed further in Appendix A.

1.2 Active Galaxies

Active Galaxies have a high output of radiation, higher than 'normal' galaxies where radiation is mainly from stars, dust and binary systems. Their active compact cores, known as Active Galactic Nuclei (AGN) are found in $\sim\ 20-50\%$ of galaxies (Ho *et al.*, 1997; Miller *et al.*, 2003). It is widely accepted by the astronomical community that supermassive black holes (SMBH) exist at the centres of all large galaxies, typically with masses between 10^6 and $10^9\ M_\odot$. The energy emitted by 'active' galaxies is as a result of the accretion onto a SMBH with much of the galaxy activity localised to a region $<$1pc in size (Wiita, 2006). AGN emit right across the EM spectrum from radio to gamma rays. Although there is no direct proof of SMBHs, both energetic and dynamical arguments provide strong evidence for their existence. There is much evidence for highly dense concentrations of mass at the centre of galaxies deduced from dynamical measurements of the stars and gas in the disc. Also, no known source, other than a black hole can produce such a large amount of energy from such a small volume. It is widely accepted that the only process which will generate energy with such a high efficiency is accretion onto a compact object. The Eddington limit gives a description of the maximum luminosity of a source fueled by spherical accretion onto a central compact object. The limit is calculated by assuming that the inward gravitational force on the gas and the outward radiation pressure force on the gas must balance for the source to remain intact. The equation for calculating the Eddington Luminosity is shown in Equation 1.1 where σ_e is the Thompson scattering cross-section for an electron with

a photon, m_p is the mass of a proton and M is the mass of the central object.

$$L_E = \frac{4\pi}{\sigma_e} M = 1.26 \times 10^{38} \frac{M}{M\odot} \text{ erg s}^{-1} \tag{1.1}$$

For a typical quasar with luminosity $L_{quasar} \sim 10^{46}$erg s^{-1} $\sim 2.6 \times 10^{12} L_\odot$ the Eddington luminosity equation gives a central mass $M \sim 10^8 M_\odot$. The only known physical object with such a large mass is a SMBH. One of the other key arguments for nuclei in AGN is the observed rapid variability of X-ray emission. The Narrow Line Seyfert 1 (NLS1) galaxy NGC 4051 (Seyfert AGN are discussed in Section 1.2.1) which is the focus of this thesis, is an example of an AGN which displays rapid variability on timescales of few hours to several years. An upper limit on the size of the emission region is based on the size scale (R) of the emitting region. Variations are smoothed out by the difference in the travel time between the furthest and nearest parts of the emitting regions, by $\Delta t = \frac{R}{c}$. Therefore, if variability is observed on timescales of Δt the emission regions must be of order $R = c\Delta\, t$, or even smaller. The fast variations observed in AGN imply that the observed X-ray emission originates in a region no more than a few light-hours across.

There are several different types of AGN, and their names derive from the methods in which they were discovered. The key science that allowed the unification of the various AGN types came from the discovery that AGN are not spherically symmetric (Antonucci and Miller, 1985; Urry and Padovani, 1995). Early radio detections showed the presence of geometrically opposing extended lobes which confirmed this. The different AGN types and the 'unification of AGN' are discussed in the following sections, starting with Seyfert AGN which were discovered first.

1.2.1 Seyferts

In the 1940's Carl Seyfert carried out an intensive study of the spectra of spiral galaxies which had particularly bright optical emission in their nuclei (Seyfert, 1943). He noticed that the cores of the galaxies investigated showed high excitation emission lines which were very broad. It was not until the 1970's that Khachikian and Weedman (1974) noticed that the spectra of these Seyfert galaxies could be classified into two types. Seyfert 1 galaxies contain both 'narrow' and 'broad' lines, and Seyfert 2's have 'narrow' lines only.

For AGN these different emission line regions are split into a Narrow Line Region (NLR) and a Broad Line Region (BLR). Narrow lines are defined as those with widths of $100 - 1000$ km s^{-1}, which are characteristic of low density ionised gas. The NLR has both permitted and forbidden lines. Broad line features have widths of $1000 - 10000$ km s^{-1} and are seen in permitted lines only. The absence of forbidden lines suggested the gas in the BLR was at a higher density than the NLR ($n_e \sim 10^9$ cm^{-3}). Further gradations can be made i.e. as the strength of the narrow component increases relative to the broad components, the AGN are assigned as Types 1.5, 1.8 and 1.9. Also, generally speaking, the Type 1's exhibit strong keV X-ray emission while the Type 2's do not. This is likely a result of the obscuring which absorbs the X-ray emission and reprocesses it in the infra-red.

In Figure 1.1 the optical spectra of the Seyfert 1 galaxy NGC 5548 from Peterson (1997) is presented where the prominent broad lines and the strong absorption features of the host galaxy are labeled. This galaxy is the same type of Seyfert as the AGN discussed in this work. The discovery of a broad-line region (BLR) which results from fast moving clouds of gas inside the torus, on a scale of $\approx$1pc around the BH and non-stellar continuum by Antonucci and Miller (1985) in the polarised flux spectrum of a Seyfert 2 galaxy, NGC 1068 led to the unification of AGN. Details are given on the 'unification of AGN' and the AGN model currently used by astronomers in Section 1.2.6.

1.2.2 Quasars

Quasar type AGN were discovered in the 1960's from work on the first radio surveys. In these surveys most of the radio sources were coincident with star-like optical emission, with optical spectra dominated by emission lines. This puzzled the astronomers who expected normal galaxies to have absorption as opposed to emission line spectra. These star-like objects were dubbed as 'quasi-stellar radio sources' or 'quasars'. Studies of the optical spectra of these quasars showed very broad emission lines, which at the time could not be identified. The mystery was only unravelled when Maarten Schmidt discovered that these spectra could be explained if he corrected for an extraordinarily large redshift for the galaxies e.g. z=0.158 for 3C 273 (Schmidt, 1963). In a later work by Schmidt (1969) it was suggested that a quasar should have the following properties: It should be a star-like object, have a time-variable continuum flux, a large UV flux, broad emission lines and have a large redshift. These properties were used later when searching through fields containing radio sources. Use of this method has revealed that over 90% of the known quasar

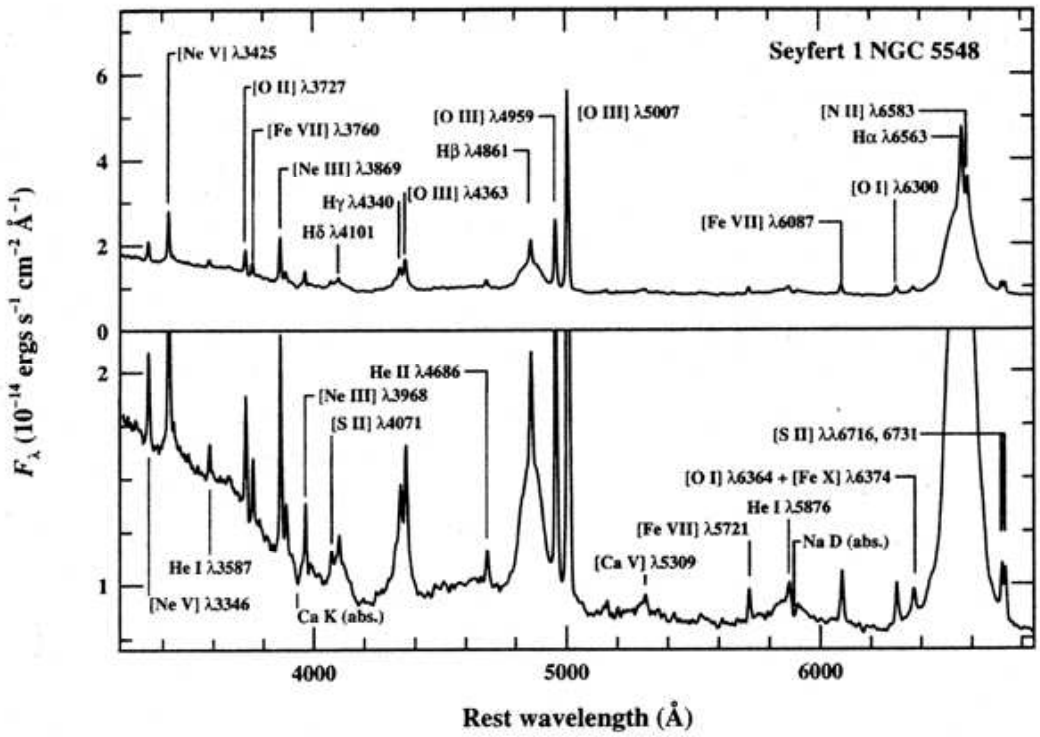

Figure 1.1: Optical spectra of the Seyfert 1 galaxy NGC 5548 from Peterson (1997) prominent broad lines and the strong absorption features of the host galaxy are labelled. The lower panel is a zoomed in version of the weaker features.

population consists of 'radio-quiet' quasars.

1.2.3 LINERs

Low-ionisation nuclear emission line regions (LINERs) are another type of narrow line AGN, much like Seyfert 2 galaxies. They are very common in spiral galaxies and might be detectable in nearly half of all spiral galaxy environments (Ho *et al.*, 1994). However, in LINERs the relative strength of the low-ionisation emission lines, for example, [OI] $\lambda 6300$ and [NII] $\lambda 6548, 6583$, are greater than in Seyfert galaxies. In order to distinguish LINERs from HII regions the intensity of at least two, closely spaced pairs of emission lines are used to determine if the original ionising spectra is a power-law (with AGN origin) or blackbody (of HII origin).

1.2.4 BL Lac Objects & Optically Violent Variables

Both BL Lacs and Optically Violent Variable (OVV) type AGN are particularly variable sources. The first 'BL Lac' object was actually identified as a highly vari-

able star, and named after the prototype of the class, BL Lacertae. However, after detailed spectra were acquired it was shown that the source was extragalactic and, by applying simple energetic arguments, it was clear that the object must be an AGN due to its large mass and comparatively small power source. BL Lacs are distinguished by an absence of strong absorption or emission lines in their spectra. This makes estimating BL Lac distances very difficult, but, the galaxies in which the AGN are embedded can be used to acquire the cosmological redshifts required to estimate distance (Wiita, 2006).

Optically Violent Variables (OVVs) have abnormally large, short time scale variations, sometimes as short as a day at visible wavelengths, with $\Delta m \gtrsim 0.1$ mag. The OVV sources are always radio loud and show much higher polarisation than standard AGN (usually $\sim 1\%$). Both OVVs and BL Lacs are thought to be AGN with a strong relativistically beamed component close to the line of sight. Both classes of AGN are known as 'blazars', a term introduced by Edward Spiegel in 1978 to combine the two classes. All known blazars are examples of radio sources.

1.2.5 XBONGs

These X-ray Bright, Optically Normal Galaxies (XBONGs) were discovered in the first deep *Chandra* surveys. They are luminous X-ray sources with X-ray spectra not dissimilar to quasars, but their optical spectra show no sign of AGN activity (e.g. no emission lines). However, the X-ray luminosity values ,$\gtrsim 10^{42}$erg s^{-1}, are hard to reconcile without invoking the presence of an AGN (Browne and Marcha, 1993; McHardy *et al.*, 2003; Hornschemeier *et al.*, 2003).

1.2.6 Unification of Active Galactic Nuclei

The Unification Paradigm devised by Antonucci (1993) and Urry and Padovani (1995) suggests that the different types of AGN observed, particularly Seyferts 1 and 2, are intrinsically identical sources with the apparent differences a result of the observer's viewing angle. The reason for the differences in appearance is a torus of material of very thick optical obscuration (Krolik, 1998). The main components of the unified model are a supermassive black hole and an accretion disc which emits at optical/UV wavelengths. The optically thick clouds which orbit the black hole are known as the broad line region (BLR) and the low density, low velocity clouds, much further from the centre are known as the narrow line region (NLR). There is also a dusty torus which restricts our view of the BLR when viewed from high in-

clination angles. A cartoon representation of the AGN Unification Paradigm which illustrates the relative geometry of these components is shown in Figure 1.2.

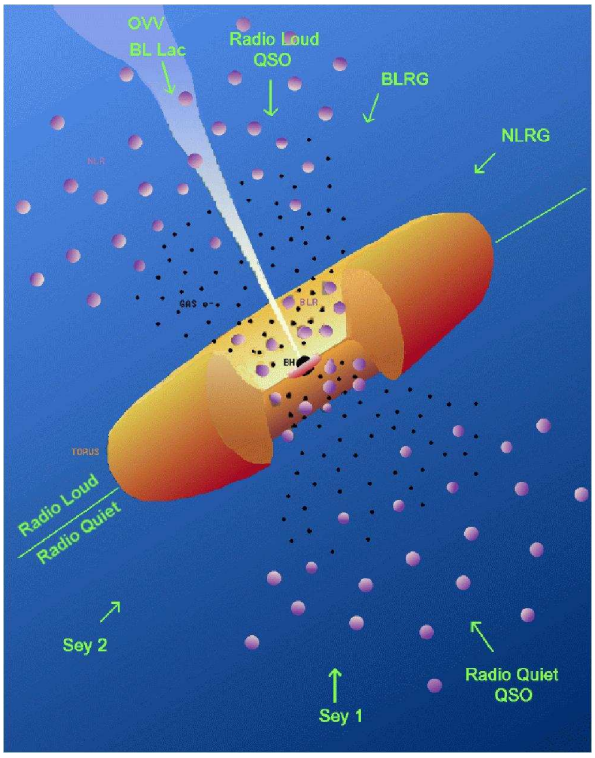

Figure 1.2: Cartoon representation of the AGN Unification Paradigm devised by Antonucci (1993) and Urry and Padovani (1995) which shows that the observed differences in the AGN are likely the accident of the viewing angle of the observer. For a radio quiet AGN which is viewed edge-on it is thought that the torus obscures the BLR and the accretion disk and the object is defined as Seyfert 2. When both the disk and BLR are visible the AGN is defined as a Seyfert 1 (like AGN NGC 4051). Note that Seyfert galaxies are generally radio quiet and therefore have a weak or non-existent jet. Radio Loud objects meanwhile have a prominent jet, when the observer views the jet along the line of sight this object is defined as a BL Lac. *Image credit: NASA HEASARC.*

The torus provides obscuration of the inner components and causes the observed difference between Type 1 and Type 2 Seyferts. The reported discovery of a hidden BLR in the Seyfert 2 galaxy NGC 1068 was evidence for the unified scheme of AGN. Antonucci and Miller (1985) suggested that the nuclei in Type 2 Seyferts are obscured from direct view by a geometrically thin and optically thick disc or torus. Dust in the torus absorbs radiation from the central, high energy source and re-radiates it as thermal energy. Evidence for this absorption is shown in the X-ray spectra of Seyfert 2 galaxies, below energies of 2-3 keV (e.g. Moran *et al.*, 2001). The levels of absorption observed are consistent with an obscuring, high column

density, cold material i.e. the molecular torus. It is therefore suggested that Seyfert 2's have a BLR, but this is hidden from view by the torus. However, the BLR can be seen when nuclear radiation is scattered by electrons above and below the poles of the torus into the observers line of sight. This suggests that Seyfert 2's are indeed the same intrinsic source as Seyfert 1's (where both the BLR and NLR are detected). **?** argued that viewing angle alone does not explain the differences between Seyferts. They find evidence that Seyfert 2's have intrinsically different radio properties, implying that they are not just Seyfert 1 galaxies seen at a different angle. They suggest the absence of the BLR makes the real difference between the two. The differences in radio emission can then be explained if it is assumed that the BLR inhibits the escape of the radio-emitting plasma into the NLR (Osterbrock, 1984).

Radio-loud AGN are thought to host a powerful radio jet, and when observed directly along the jet, the source is known as a 'blazar'; this AGN type is discussed further in Section 1.2.4; however, I give a brief description here. Blazars are the most powerful sources of X-ray and radio emission and demonstrate rapid variability and high polarisation. They have a flat radio spectrum due to observing down the jet axis. The violent variability which is observed in blazars is thought to result from viewing the source along the jet axis, which causes emission to be enhanced by relativistic beaming. The flat spectral shape is due to regions of plasma at different densities which are observed at the same time. The radio spectra of each density region has a specific turn-over frequency and the superposition of many spectra, each with different turn-over frequencies combine to give a flat radio spectrum. For further discussion of radio spectra in AGN see Section 1.3.3.

It is worth mentioning that the reason why some AGN are radio loud and others radio quiet is not understood. It is possible that another parameter, such as black hole spin, might be required to explain all the properties of AGN. The relatively narrow broad lines and very rapid variability seen in Narrow Line Seyfert 1 (NLS1) galaxies requires another parameter beyond the AGN Unification, possibly linked to accretion rate. If the narrowing of the lines in NLS1s is due to a lower mass central black hole, then the accretion rate must be high given that the luminosities detected are comparable to other Seyfert 1's. Finally, it is also unclear as to how the jets in AGN are created. Nevertheless, the unification scheme is a good starting point from which to try to understand AGN and the geometry discussed in this section is assumed throughout this work.

1.2.7 Radio properties of AGN

At radio wavelengths the brightest AGN, quasars, are generally described by two components: a compact component coincident with the central position of the optical galaxy and an extended component which is usually symmetric about the compact centre. The extended component is attributed to the synchrotron radiation from jets.

Fanaroff and Riley (1974) investigated the radio luminosity and morphology of many radio galaxies and deduced that there were two distinct types of extended emission. Fanaroff-Riley (FR) I sources have weaker radio emission and have bright emission close to the centre of the optical galaxy. In FR II sources the radio emission is dominated by edge brightened lobes or 'hot spots' at the end of the jets. The FR II jets are often one sided: either no counter jet is seen or it is much fainter than the brighter feature identified as the jet. Work by Fanaroff and Riley (1974) revealed a method to separate between FR I and FR II sources using their radio luminosity at 178 MHz ($L_{178\mathrm{MHz}}$). They discovered that all sources with $L_{178\mathrm{MHz}} < 2.11 \times 10^{43}$ erg s^{-1} are FR I sources. This limit is used later in this thesis (Section 4.4.2) to estimate the FR morphology class of AGN NGC 4051.

The asymmetry between FR I and FR II sources in generally attributed to relativistic beaming of jet emission since the large scale lobe morphology is usually symmetric, however; the real picture is likely to be more complex. The compact cores are generally unresolved, which means one cannot resolve the central compact object from the base of the jet. Assuming a power law, the compact core has a flat radio spectrum whereas the extended components tend to have steep radio spectra. Several times in this work the spectral index is used as a diagnostic tool for an individual Seyfert galaxy. See Section 1.3.3 for a more thorough introduction to radio spectra.

The degree of 'radio loudness' is another way to investigate the radio properties of galaxies, and can be used in conjunction with the morphology method of Fanaroff and Riley (1974) to determine galaxy type. Members of the radio loud category include BL Lac objects, radio galaxies and radio-loud quasars. Radio quiet objects include Seyfert galaxies and radio-quiet quasars. In order to determine if a source is radio loud (RL) or radio quiet (RQ) one must first calculate the relative amounts of radio emission associated with the central engine and accretion disk. The $\mathfrak{R}$ parameter is defined as the ratio of radio flux density at 6 cm (5 GHz) to the 4400 Å optical flux density. For RL AGN $\mathfrak{R} > 10$ and for RQ AGN $\mathfrak{R} < 10$ (Kellermann *et al.*, 1989). In Rafter *et al.* (2011) they suggest a higher value for the bimodal

distribution at $\Re < 10^{1.75}$. This higher division ensures that RL AGN are those with different and extreme conditions in their central engines compared with the more numerous radio-quiet AGNs. Overall the radio loud objects have large-scale radio lobes associated with compact and luminous cores which often exhibit superluminal motion. Radio quiet objects on the other hand have most of their emission confined to sub-kpc scales.

1.2.8 AGN SEDs

Generally, AGN show continuum variability at all the wavelengths of the EM spectrum. It is possible to construct Spectral Energy Distributions (SEDs) from the standard AGN model discussed previously, see Section 1.2.6. We expect a broadband spectrum of emission from stars due to the superposition of their thermal spectra, which peaks in the near infrared. In fact, the thermal emission from the accretion disc itself is the superposition of many black body thermal spectra, since T varies continuously across the disc. The accretion disc spectrum for an AGN is usually centred in the ultra-violet (UV) part of the spectrum. X-ray emission from AGN is hypothesised to result from a corona of hot electrons which surround the inner regions of the disc. The hot electrons Compton scatter thermal photons from the accretion disc up to X-ray energies giving off a power-law spectrum. The X-ray and UV/optical photons that are absorbed by obscuring material are re-emitted in the infrared.

AGN with jets (FRIs, FRIIs, blazars, radio loud quasars and radio galaxies) emit synchrotron emission which is seen at radio wavelengths. This emission is given off by electrons spiralling in the magnetic fields which are thought to collimate the jet. This emission can emit at all EM wavelengths; however, the power-law shape of its spectrum means that components emitted from the host galaxy outshine the synchrotron emission, except at radio wavelengths. The blazar is an exception to this case because of the Doppler boosting of velocities of emitting material along the line of sight. This 'boosting' allows the synchrotron component to dominate the entire SED. The high energy synchrotron electrons can 'up-scatter' jet photons to hard γ-ray energies. The physics of synchrotron spectra is discussed further in Section 1.3.3. The luminosity of an individual AGN is therefore dependent on the relative contributions from the stars, accretion disc and jet. These contributions change arbitrarily from galaxy to galaxy, and are also dependent on the viewing angle of the observer.

1.3 Radio Astronomy

Most of the science data reduced by the author and discussed in this thesis is radio data. In this section the history and science of radio interferometry is discussed. In addition, the radio emission processes relevant to this thesis are presented.

1.3.1 Radio Interferometry

The science of radio astronomy began in 1932 when Karl Jansky detected radio waves from space while carrying out interference experiments for Bell laboratories. Jansky (1933) measured three possible sources of interference for communication systems: local thunderstorms, distant thunderstorms and a mysterious signal that occurred 4 minutes later every day. The fact that the mysterious signal was coming from a certain direction in space which was fixed relative to the stars, but not fixed with respect to the Earth or Sun allowed him to identify its position as the centre of our Galaxy, the Milky Way.

Further developments in radio astronomy were hindered by the Second World War. However, amateur radio astronomer Grote Reber, inspired by Jansky's work, took on the challenge of building his own steerable parabolic reflector dish which was 30 feet in diameter. With this device he was able to map the sky at radio wavelengths and for the first time the startling differences between the optical sky and the radio sky were observed (Smith, 1974). By the 1940's the need for high resolution radio images was recognised, and several radio interferometers were built.

The diffraction limited angular resolution of a telescope is given by the relationship $\theta \sim \frac{\lambda}{D}$ radians. Therefore, in order to image radio emission, which is the longest wavelength emission in the EM spectrum, we need large diameter telescopes. The largest single aperture radio telescope in Arecibo has a diameter $\sim$ 300 m. When Arecibo is observing at $\lambda = 3$ cm it can only achieve a resolution (θ) of the order of $20''$. Optical telescopes, such as the Faulkes Telescope in Hawaii can achieve a resolution limited by atmospheric seeing at $\theta = 0.5''$. In order to get comparable resolutions at radio wavelengths an aperture of $\sim$ 100 km is needed, which is neither physically or financially viable. In the 1940's the resolution problem at radio wavelengths was solved by Martin Ryle's pioneering work in aperture synthesis (Ryle and Vonberg, 1948). Aperture synthesis works by combining two signals from two separate antenna. It is then possible to synthesise a beam with the resolving power of a single aperture with an equivalent diameter which was equal to the distance between the antenna (Ryle and Hewish, 1960). The resulting inter-

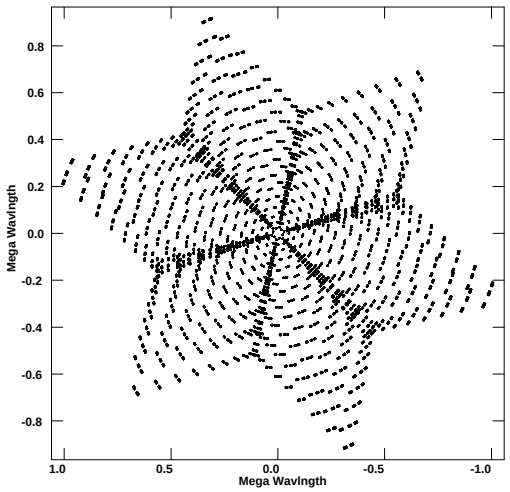

Figure 1.3: The *uv*plane coverage for a VLA *uv* dataset at 8.4 GHz (in A configuration) with an integration time on source of $\sim$ 18 minutes. Showing the projection of the antenna as seen by the source on a plane perpendicular to the source. Where the East-West direction is *(u)* (x-axis) and the North-South direction is *(v)* (y-axis).

ferometer used a correlator to combined the signals from each antenna. It amplified one of the signals, then multiplies the signal by the complex conjugate of the other. As a result of this correlation the real signal is amplified and the noise signal is averaged out, this gives a representation of the coherence of the electromagnetic field in area of the source. The coherence function or 'fringe' produced is a sinusoidal representation of the sensitivity to real sources on the sky.

Each pair of antennae within an interferometer is known as a 'baseline'. Different baseline lengths sample different spatial scales i.e. long baselines give the highest resolution and short baselines give the best sensitivity to extended structure. As the Earth rotates, the antennae are carried across the *uv* plane. This plane represents the projection of the baseline in the East-West *(u)* and North-South *(v)* directions measured in wavelengths as seen from the source and because of the rotation of the Earth, the projection (the *uv* plane) varies with hour angle. Delays are therefore added to the signal of one antenna to move it into a perpendicular plane. Modern interferometers aim to fill the *uv* plane to give the best coverage possible. Figure 1.3 shows the *uv* coverage for an integration of $\sim$ 18 minutes using the VLA. Several interferometers relevant to this work are discussed in the next section.

1.3.2 Interferometers

Details are given on a selection of interferometers and observatories that are relevant to this study and future work on variability and structure of AGN.

1.3.2.1 Very Large Array (VLA)

Data from the VLA taken at 4.8 GHz and 8.4 GHz comprises the majority of radio data which is discussed in this work. The VLA is operated by the National Radio Astronomy Observatory (NRAO) and is situated in New Mexico, USA. The interferometer was opened in 1980 and consists of 27 antennae, each 25 m in diameter, placed in a 'Y' shape configuration. The array operates from 74 MHz to 48 GHz. Individual antenna are moved along tracks to increase the baseline length. The most compact configuration (D) has the lowest resolution ($7.83''$ at 8.4 GHz) but has the highest sensitivity to extended emission. The configurations cycle through C configuration and then B configuration increasing in baseline length and resolution before reaching the A configuration. A configuration has the highest resolution ($0.24''$ at 8.4 GHz) and a maximum baseline of 36 km.

In 2012 the Expanded Very Large Array (EVLA) is expected to be completed. This expansion on the VLA includes upgrading of the receivers, electronics and the installation of a more powerful and versatile correlator. The EVLA, when complete, will be an order of magnitude more sensitive than the VLA. Some of the radio data presented in this thesis (from 2008-2009) contain a combination of VLA *uv* data and *uv* EVLA data, as only some of the antennae had been upgraded in 2008-2009. Corrections are made for reducing the data from mixed VLA and EVLA data to ensure the calibration is performed accurately. The reduction of both VLA and EVLA data is discussed in Sections 2.2.2 and 3.2.2 respectively.

1.3.2.2 Very Long Baseline Interferometry (VLBI)

The AGN discussed in this thesis was observed with the VLBI to probe the inner regions of the galaxy at high resolutions. The VLBI interferometer links telescopes across the surface of the Earth to attain high resolution with the longest possible baseline lengths. It combines two main networks: The European VLBI Network (EVN) and The Very Long Baseline Array (VLBA). The EVN includes antennae in the UK, Germany, Netherlands, Italy and Spain. Antennae outside Europe, in South Africa and China can also be included in EVN observations. The VLBA links 10 antennae across the United States and achieves a maximum baseline of ~ 8600 km. The highest resolutions possible from Earth are achieved by these arrays, however, observations using VLBI have low sensitivity due to the lack of short baselines.

1.3.2.3 Giant Metrewave Radio Telescope (GMRT)

In Appendix A I discuss the deep survey radio data from the GMRT telescope taken at 610 MHz. In the future this survey will be used to investigate the radio emission from faint radio sources, particularly AGN and starburst galaxies. The goal of this work is to combine the 610 MHz and 1.4 GHz data to obtain spectral index values.

The GMRT is situated near Pune, India and consists of 30 wire mesh antennae, each 45 m in diameter. Fourteen of the antennae are contained in a compact central array within an area of 1km^2 and the remaining sixteen are positioned in a 'Y' shaped array, with the maximum baselines reaching 25 km. The array operates between 50 and 1420 MHz. The GMRT has been operational since 2002 and was therefore one of the first devices to look at the low frequency sky at high resolution. Faint sources which can be detected at these low frequencies in deep surveys allow the measurement of the spectra of the sources. The spectral index values will be used in combination with other diagnostics to distinguish between AGN and starburst galaxies in the survey field.

1.3.3 Radio emission

This work is a study of radio emission from an individual Seyfert AGN; therefore, it is important to explain the different radio emission mechanisms. Radio emission from AGN comes in two forms: Synchrotron and Bremsstrahlung (free-free) radiation (Blandford and Konigl, 1979; Longair, 2010). Bremsstrahlung radiation results from electrons which are deflected by ions, and consequently become accelerated or decelerated. Considering a single electron which is accelerated by a nearby charged atom, the kinetic energy the electron gains is released as a photon. In AGN, thermal Bremsstrahlung radio emission is thought to originate in the hot and dense plasma within the central regions of the AGN. Also, non-thermal relativistic Bremsstrahlung can occur where relativistic particles interact with ionised gas in these central regions. The energy distribution of the relativistic electrons has a power law form in most cases.

The synchrotron emission from AGN results from electrons spiralling in the magnetic fields, where these fields are thought to be launched from the nucleus of the AGN. When an individual charged electron enters a magnetic field it begins to spiral and will experience a centripetal acceleration, giving off cyclotron radiation. For highly relativistic electrons, the radiation becomes channelled into a tight cone of emission with an opening angle for the cone proportional to the energy of

the electrons (Longair, 2010). In the observer's frame there are two relativistic effects which account for the strong radio emission from synchrotron electrons: The total power of the emission is multiplied by the Lorentz factor squared (γ^2) and the beaming of the radiation turns the slow sinusoidal variations into a series of sharp pulses. These pulses contain power at much higher frequencies resulting in the observed frequency ν being proportional to the gyro frequency ν_g according to the relationship $\nu \sim \gamma^2 \nu_g$.

The spectrum of an ensemble of electrons emitting synchrotron radiation is obtained by integrating over the energy distribution of the emitting electrons. For compact sources, such as AGN, the spectral shape tends to be flat, getting steeper at higher frequencies. The compact source has a flat spectrum because the separate regions of the complex source become optically thin at different frequencies, each single electron has a spectrum which peaks at some critical frequency. The superposition of many electrons which have different critical frequencies causes the flattening of the electron energy distribution.

The steepening at higher frequencies is due to the fact that the higher energy electrons will radiate their energy faster. The power ($P = \frac{dE}{dt}$) emitted by electrons spiralling in magnetic fields is proportional to the energy of the electrons squared (E^2). Therefore, the electron population which emits at the highest energies will become depleted causing the spectrum to become steeper at high frequencies.

A typical spectral energy distribution (SED) for an AGN has a very small fraction of the total power from the the radio part of the spectrum. Even the radio part of the spectrum of a RL AGN contributes very little to the bolometric luminosity. However, studies of the radio emission from these sources are important as a probe of the central regions of the AGN where physical processes accelerate particles emitting non-thermal synchrotron radiation. Evidence for non-thermal radio emission from AGN comes from the steep spectral shape, the polarisation and the brightness temperatures detected. The brightness temperature (T_B) for a source can be calculated from the specific intensity at a given frequency, I_ν, measuring the flux S_ν and angular size θ of the source. At radio wavelengths the intensity can be equated to the brightness temperature using the Rayleigh-Jeans approximation to the Planck function:

$$I_\nu = \frac{S_\nu}{\pi\theta^2} \approx B_\nu = \frac{2kT_B}{\lambda^2}, \tag{1.2}$$

The brightness temperature is equivalent to the temperature a source would have if it were radiating as a black body. For an optically thick source the brightness temperature equals the kinetic temperature; for an optically thin source the brightness temperature is less than the kinetic temperature. For extragalactic compact radio sources brightness temperatures are in the range $T_B = 10^{11} - 10^{12}K$ which clearly suggests a non-thermal origin for radio emission, since normal galaxies have a maximum brightness temperatures typically of $T_B = 10^5 K$. The energy density of the magnetic field, $U_{mag} = B^2/8\pi$, explains why brightness temperatures rarely exceed $10^{12}K$ since it controls the rate of synchrotron energy losses. This energy density relates to the radiation energy density U_{rad}, which controls the rate of inverse Compton scattering. If $U_{rad} > U_{mag}$ due to increased synchrotron radiation the electrons which Inverse-Compton scatter the synchrotron-emitted photons to higher energies, will have less energy. This effect is known as Inverse-Compton "cooling" and it increases the energies of the photons by rate $\sim \gamma^4 U_{rad}$. This "cooling" quickly becomes a runaway process up to the onset of the Klein-Nishina cross section, at this point the runaway is terminated limiting the brightness temperature to $10^{12}K$.

For a synchrotron emitting source producing low frequency radiation the brightness temperature, T_B will approach the effective electron temperature, T_e. When $T_e = T_B$ the source is said to be synchrotron self absorbed, i.e the source has become optically thick and optical depth (τ) is much greater than 1. For an opaque but truly thermal source the intensity I_ν varies as ν^2 and $T_e \propto \nu^{\frac{1}{2}}$. Substituting these relations with the relationship $c = \nu\lambda$ (where λ is wavelength and ν is frequency, and c, speed of light) into Equation 1.2, and replacing T_B with $T_e \propto \nu^{\frac{1}{2}}$, gives the following relation:

$$I_\nu = \frac{2kT_B\nu^2}{c^2} \propto \nu^{\frac{1}{2}}\nu^2 B^{-\frac{1}{2}} \propto \nu^{\frac{5}{2}} B^{-\frac{1}{2}} \tag{1.3}$$

Since the flux density at a particular frequency, $S(\nu)$ is proportional to the intensity I_ν of a source for a given solid angle, it follows that for a synchrotron self absorbed source emitting at a frequency ν, the resulting spectrum varies with a power law giving the relation $S(\nu) = \nu^{\frac{5}{2}}$. A turnover in the spectrum occurs at a specific frequency $\frac{\nu}{\nu_1}$, and depends on the energy distribution and density of the electron population responsible for the emission. For optically thin synchrotron emission the spectral index value is $\alpha = -0.7 \pm 0.2$, for relationship of the form $S(\nu) = \nu^\alpha$. As described previously, the flattening of the spectrum is caused by superposition of many optically thick components, each representing different electron populations.

Each population has its own turnover frequency, so the superposition results in a flat spectrum. The compact regions of AGN are often observed with flat spectrum properties where $\alpha \sim 0$ because the radio emission from different populations in the jet cannot be resolved by the interferometer used i.e. the jet appears point like. The extended lobes of AGN are also typically observed with very steep spectra (e.g. $\alpha_{8.4\ \mathrm{GHz}}^{4.8\ \mathrm{GHz}} \approx\sim -1.6$. In this thesis I calculate the spectral index in the form of $S(\nu) = \nu^{\alpha}$ for several components of the individual AGN observed to predict the physical properties of each component.

For work described in the Appendix it was the intention to use the spectral index values to discriminate between star forming galaxies (SFGs) and AGN. Star formation is expected to produce α measurements in the range of -0.7 to -0.8. Jet emission also produces similar spectra index values (-0.7) which means other diagnostics, in combination with the radio flux density are required to make the discrimination between SFGs and AGN.

1.4 X-ray Astronomy

In this section I give details of X-ray observatories and X-ray emission mechanisms relevant to this thesis.

1.4.0.1 Rossi X-ray Timing Explorer (RXTE)

The majority of X-ray data presented in this thesis was taken by the RXTE. The individual AGN discussed in this work has been observed by RXTE since 1996 to look for both short and long timescale variability. RXTE was launched on 30th December 1995 and was designed specifically to investigate the variability of X-ray sources. It covers timescales from microseconds to months within a spectral energy range of 2-250 keV. It features high throughput (up to 150,000 counts s^{-1}) and $\approx$ 1 μs time resolution. For AGN sources a time resolution of 16 s is typically used. The Explorer has two pointed large area instruments on board, the Proportional Counter Array (PCA) which covers the lower energy range, the High Energy X-ray Timing Experiment (HEXTE) which covers the upper energy range. These instruments work together and observe the sky through a 1° field of view. The third instrument, the All-Sky Monitor (ASM) surveys about 80% of the sky in each orbit. The PCA, which was the only instrument from which data were obtained for this thesis, has five Proportional Counter Units (PCUs) with an effective area of 6250 cm^2 and sensitive to photons in the range of 2-60 keV. Each of the PCUs

has a top layer of propane followed by three layers of Xenon. PCA data which are presented in this thesis was extracted from the top layer only, since I am most concerned with the faint variability information which is detected in this top layer, as opposed to background information detected in the bottom layers.

1.4.0.2 Chandra

A small sample of the X-ray data which is presented in this work, which I compare with quasi-simultaneous RXTE data, was taken using NASA's *Chandra* X-ray observatory. This observatory was launched on 23rd July 1999, and is the most sophisticated X-ray observatory to date. For faint sources it has a sensitivity twenty times that of previous X-ray observatories. Chandra has four instruments on board, the ACIS, the HRC, the LETG and the HETG. The Advanced CCD Imaging Spectrometer (ACIS) and the High Resolution Camera (HRC) are focal plane imaging instruments which provide information about the incoming X-rays such as their number, position, energy and time of arrival. The Low Energy Transmission Grating (LETG) and High Energy Transmission Grating (HETG) are spectrometers which measure the amount of energy in the X-ray photons. The ACIS instrument was used for the X-ray data presented in this thesis.

1.4.1 X-ray emission

For AGN, the X-ray continuum emission mechanism comes primarily from two mechanisms Bremsstrahlung (free-free) radiation and Compton scattering (also Inverse Compton scattering) or X-ray synchrotron (in Blazars). Like Bremsstrahlung radiation at radio wavelengths, discussed in Section 1.3.3, X-ray Bremsstrahlung results from electrons deflected by ions within a charged plasma. X-ray radiation can also result from blackbody emission, nuclear line emission (resulting in hard X-rays) and bound-bound atomic transitions (resulting in soft X-rays). In Compton scattering a high energy photon collides with an electron, the electron gains energy and the photon loses energy. For the case of Inverse Compton, the collision of a high energy electron with a photon causes the photon to gain energy. This process is particularly important for our understanding of the inner workings of AGN. In current AGN models it is assumed that the low energy thermal photons (the UV/optical seed photons) in the accretion disc are upscattered (Inverse Compton scattered) to higher energies by relativistic electrons in the corona of material which surrounds the disc. Therefore, the high energy X-ray emission is thought to arise from the innermost regions; from the vicinity of the black hole.

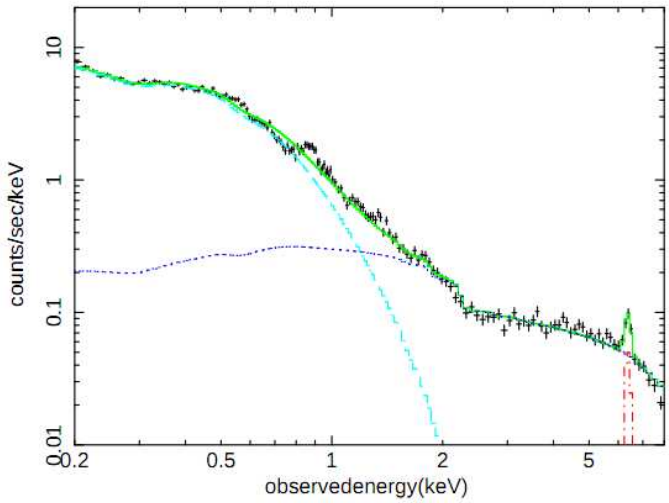

Figure 1.4: Spectral Energy Distribution (SED) of the 'soft state' Seyfert AGN NGC 4051 at X-ray wavelengths fitted with two components. The hard power law and soft Comptonised continuum components are shown as dotted and dashed lines respectively and the Fe Kα emission line is shown in red. *Figure from Pounds and Vaughan (2011).*

X-ray emission contributes a large amount to the bolometric luminosity of AGN; however, the origin of X-ray emission is not well understood. The favoured emission model involves an optically thin corona above the inner accretion disc (Sunyaev and Titarchuk, 1980). The corona above the disc is envisaged to behave similarly to the solar corona i.e. heated by magnetic reconnection events in the disc (Di Matteo, 1998). The power law spectra in AGN SEDs can be successfully explained by Comptonisation models. The SED as a whole is modified by several components (see Figure 1.4). At the low energy end the spectrum is thought to be absorbed by cold gas in the vicinity of the nucleus. At high energies a cut off exists due to electron-positron pair production in the compact corona. At energies $\lesssim 2$ keV there are absorption features due to heavy elements. Generally at $\sim$ 10-50 keV a 'Compton reflection hump' is observed which results from the accretion disc. At 6.4 keV there exists a Fe Kα emission line (shown in red in Figure 1.4). This line is thought to originate from X-rays reflected by cold material, probably in the accretion disc, within a few gravitational radii of the black hole; however, some of the the line emission may result from reflection from very far out in the disc. The fact that the line at 6.4 keV suffers from heavy broadening and a redshifted profile suggests it originates from close to the black hole (Tanaka *et al.*, 1995). Narrower Fe lines also exist in the spectrum and are likely the result of X-rays reflected by cold material

much further from the black hole.

1.5 Radio and X-ray Variability of Seyferts

The powerful radio emission from radio galaxies and blazars is well established to be synchrotron emission from powerful jets. However, much weaker radio emission is sometimes detected from Seyfert galaxies and its origin is unknown. Attempting to understand the origin of this radio emission and its possible links to X-ray emission forms a large part of the work in this thesis.

The variability of the flux density across all wavelengths of the EM spectrum is recognised as a strong characteristic of AGN. Short term variability time scales are known to exist at X-ray, Optical and UV wavelengths (e.g. Breedt (2009); M^{c}Hardy *et al.* (2004)) with the largest variations at radio wavelengths seen in BL Lacs and core dominated quasars (e.g. Lister (2001)). Several models exist which describe the radio and X-ray variability of compact sources (e.g. Marscher and Gear (1985)). The rapid variability observed from AGN constrains the X-ray emitting region to the vicinity of the SMBH; therefore, it follows that X-ray emission acts as a tracer for the accretion onto the SMBH.

The region which emits X-rays is known as the 'corona'; however, its exact geometry is unknown. The variations in the X-ray emission are thought to result from fluctuations in the accretion flow, which is inferred from the non-linear properties of the light curves (Uttley *et al.*, 2005) and the spectral timing properties (Arévalo *et al.*, 2006).

There are two explanations for the radio emission from Seyferts. The first is the starburst model, in which radio emission is explained by the cosmic rays accelerated along magnetic fields in supernovae explosions (e.g. Condon *et al.* (1982)). Using energy equipartition between the magnetic fields and particles for both the variable compact core and the extended emission (where equipartition is explained further in Section 1.6.2) one can calculate that the energy content in these regions is much larger than the energy content of supernova. The second and more favoured explanation for radio emission from the core and extended parts of Seyferts is therefore based on the model of a directed outflow from the central core (either by jets or winds). Flux variations detected in the core are linked to variations explained primarily by Doppler boosting of nuclear emission by the jets (Mundell *et al.*, 2009).

The variations seen at radio and X-ray wavelengths from the central regions of Seyferts provide constraints on the physical processes that occur in the central

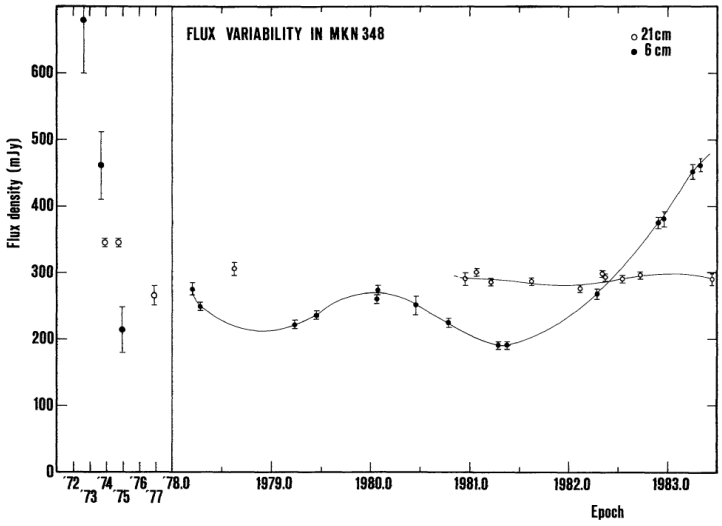

Figure 1.5: Flux variability at 6 and 21 cm for Mkn 348 over 11 years. Timescale in earlier years is compressed. Filled circles and open circles are 6 cm and 21 cm measurements respectively. The source is variable on timescales of months, with a quiescent level at about 200-300 mJy at both frequencies. The rise in the 6 cm flux in 1982 is the beginning of an outburst. *Figure from Neff and de Bruyn (1983).*

engine and the surrounding area. Observations of (quasi-) simultaneous X-ray and radio can reveal if there is any coupling between the accretion disc (emitting X-rays) and the jet (emitting radio) powers.

Radio variability has been detected previously in Seyfert galaxies but observations are not extensive. Very few investigations of radio variability in individual radio quiet Seyferts exist, with no previous investigations into the quasi-simultaneous X-ray and radio emission. In the first investigation of Seyfert radio variability by Neff and de Bruyn (1983) of Seyfert 2 galaxy Mkn 348, the source was monitored at radio wavelengths for 4 years and found to be highly variable at 5 GHz (6 cm) where the flux varied by $> 20\%$ on $\sim$yearly timescales, but was only modestly variable at 1.5 GHz (21 cm), see Figure 1.5 . These findings, combined with evidence of at least two radio components with different spectral indexes, one optically thin ($\alpha \sim -0.8$) and the other optically thick ($\alpha \sim 0.9$), are consistent with the galaxy having jets and a compact core respectively.

Another investigation into the radio variability of Seyfert 1 NGC 5548 by Wrobel (2000) found variability at 8.4 GHz by $33 \pm 5\%$ and $52 \pm 5\%$ between VLA observations separated by 41 days and 4 days respectively. The 41 day changes are milder at 4.8 GHz at $19 \pm 5\%$ and the spectral index is inverted with $\alpha = 0.3 \pm 0.1$. The radio continuum variability of NGC 5548 is shown in Figure 1.6. This figure

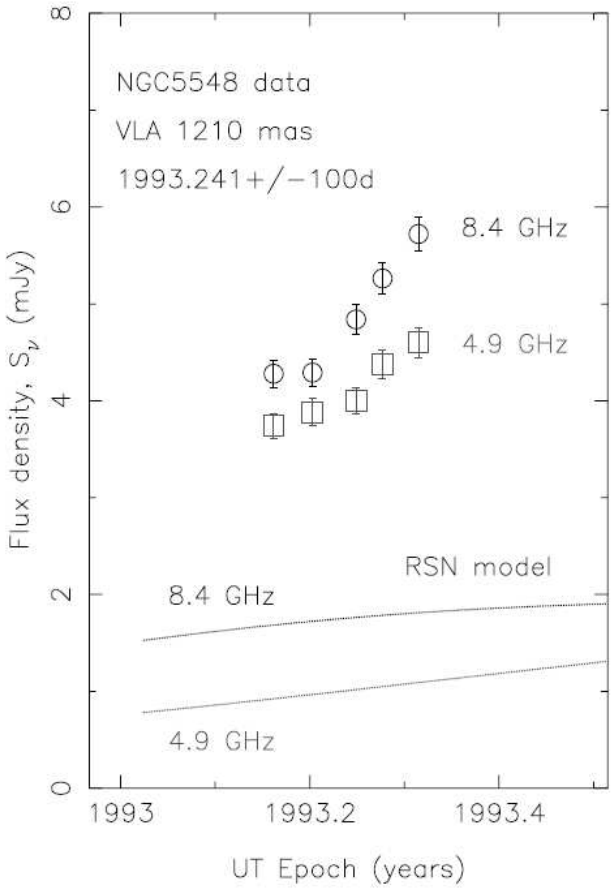

Figure 1.6: Photometric monitoring of the nucleus of Seyfert 1 NGC 5548 during the 41 day flare event, compared with models of the photometric evolution of the radio supernova (RSN) SN 1998Z. *Figure from Wrobel (2000).*

reveals that the variability in the radio flux which is observed on timescales of tens of days cannot be accounted for by radio supernova models (labelled RSN in the figure). Wrobel (2000) found that the combined photometric variability and astrometric stability detected from this Seyfert 1 galaxy is consistent with jets on the scales of $\lesssim$ 500 pc.

Falcke *et al.* (2001a) conducted a survey of 8.4 GHz emission from 30 radio quiet and radio intermediate quasars and found that 80% of sources have at least marginal evidence for variability over a two year period, with some showing a significant variation on a month-to-month basis. A survey by Mundell *et al.* (2009) found that five out of the eleven Seyferts they investigated showed nuclear flux variation over 7 years. These results support the existence of relativistic parsec-scale radio jets in Seyferts. The study by Mundell *et al.* (2009) specifically suggests that all Seyferts might exhibit variation in their nucleur flux density at 8.4 GHz, but this

variation is more easily recognised in compact sources where the variable nucleus is not contaminated with constant flux density from the jet (usually within the inner $\lesssim$ 50pc). The removal of contaminating flux forms a large part of the discussion set out in Chapter 2 of this thesis.

A lot of the most recent work on radio and X-ray variability has been carried out on the smaller black hole systems, black hole X-ray binaries (BHXRBs) with masses $\sim 10M_{\odot}$. These Galactic Black Hole Binary (BHB) systems are often classified as being in one of a small number of 'states'. The most common states are the 'hard' and the 'soft' states. The hard state was originally defined as the state where the 2-10 keV X-ray flux is low and the X-ray spectrum is hard, and the 'soft' state, where the 2-10 keV X-ray flux is high and the X-ray spectrum is soft (McClintock and Remillard, 2006). The hard state is dominated by a power-law component, and the 'soft' state is characterised by a component which results from the superposition of many black body components. The main physical parameter driving the states is the accretion rate with that rate being higher in the soft than in the hard state (Fender *et al.*, 2004; Fender, 2010; Belloni, 2010). Another major observational distinction between the hard and the soft states is that compact, powerful radio-emitting jets are usually present in the hard states (Fender, 2001a; Stirling *et al.*, 2001) but have not yet been detected in the soft state (Fender *et al.*, 1999). There have been detections of weak radio emission in soft state systems (Brocksopp *et al.*, 2002; Corbel *et al.*, 2004; Russell *et al.*, 2010) but this emission is usually thought to represent emission from relic plasma left over from a previous hard-state jet i.e. the central black hole is not powering an active jet.

In order to investigate the radio variability and black hole (BH) states of Seyferts, astronomers compare their observations with the smaller Black Hole X-ray Binaries (BHXRBs) which show variability on timescales of days to decades. Because the timescale of the physical processes in these systems are much shorter in these objects it means they can be used to probe the time variable jet to accretion coupling. For the supermassive black holes in AGNs with $10^5 M_{\odot} \leqslant M \leqslant 10^{10} M_{\odot}$ this coupling takes place on timescales of thousands to millions of years. Therefore, based on the proviso that the central accretion process is relatively straightforward to scale with mass the BHXRBs are used to investigate timescales of BH states. For example, in 'hard state' black holes the emission is dominated by high frequency X-ray emission with flat spectrum radio emission from a synchrotron self-absorbed steady state jet. Above a critical X-ray luminosity the disc contribution dominates and the X-ray emission softens. In this thermal dominant 'soft state' the amount of radio emission drops significantly and the jet is thought to be quenched (Fender

et al., 1999; Gallo *et al.*, 2003; Corbel *et al.*, 2004; Russell *et al.*, 2010). In the BHXRB Cygnus X-1 the state transition from the hard to soft has been observed, with the 'soft' state power spectral density (PSD) very closely resembling the PSD of the AGN NGC 4051 discussed in this thesis.

Recently Bell *et al.* (2011) have studied the X-ray and radio variability of the LINER AGN NGC 7213 and found a weakly significant correlation between the radio and X-ray bands. LINERs have much lower accretion rates than Seyfert galaxies, being similar in accretion rate to the hard state BHBs. LINERs are also much more radio loud than Seyfert galaxies, which is in agreement with the hard state scenario, and so an X-ray/radio correlation is expected. In 'soft-state' Galactic Black Holes (GBHs), as the radio emission has been scarcely detected, one does not know what the exact relationship to the X-ray emission might be. Correlated radio and X-ray observations of Seyfert galaxies may therefore provide us with important hints on the radio properties of the soft state systems.

The scaling of accretion processes with mass is supported by a relation between X-ray luminosity (L_X), radio luminosity (L_R) and black hole mass (M_{BH}) (Gültekin *et al.*, 2009; Merloni *et al.*, 2003; Falcke *et al.*, 2004) know as the 'fundamental plane of black hole activity'. The relationship between radio and X-ray luminosities is $L_R \propto L_X^{0.6}$, first devised by Corbel *et al.* (2003); Gallo *et al.* (2003) for individual BHs holds across several orders of magnitude in black hole mass and luminosity for all versions of the plane e.g. Gültekin *et al.* (2009); Merloni *et al.* (2003); Falcke *et al.* (2004). However, the measurements of X-ray and radio luminosities for individual BHs used in both studies by Merloni *et al.* (2003) and Falcke *et al.* (2004) are average (or single) measurements. Extensive X-ray and radio data does not exist for individual objects and therefore radio and X-ray emission is not measured simultaneously. The non-simultaneity of these measurements, relativistic beaming and source peculiarities are thought to introduce scatter into the fundamental plane, making the fit less accurate. In work by Körding *et al.* (2006a) where the unknown intrinsic scatter is parametrised it is shown that when only 'hard state' objects are used the plane agrees with predictions of a synchrotron/jet model. When the 'soft state' objects are included, the scatter about the plane increases and the correlation moves closer to a disc/jet model. Therefore, investigations where the X-ray luminosity and radio luminosity are measured simultaneously over extended periods of time for both hard and soft state objects are required to provide a more accurate 'fundamental plane of black hole activity'. As a result of simultaneous observations the scatter in the plane might reduce. An investigation of this kind was carried out by the author on the Seyfert NGC 4051 and is presented in Chapter 2.

Correlations between the radio and X-ray luminosities for BHs can also be investigated by studying time delays between the two regimes. These measured delays reveal information about the physical scales that exist for individual objects detailing how the signals propagate, for example, from the accretion flow to the jet. Variability studies between X-ray and optical report small lags between the regimes which are consistent with optical variations due to X-ray heating of the accretion disc (Breedt *et al.*, 2009, 2010). In the recent study by Bell *et al.* (2011) of LLAGN NGC 7213 cross-correlation functions revealed time lags between events in the radio and X-ray bands to be 24 ± 12 days (with the 8.4 GHz emission lagging X-ray emission). Cross correlation analysis of the Seyfert AGN discussed in this thesis is carried out in Section 3.5 to determine the possible time lag between X-ray and radio emissions, if any, which exists for AGN.

1.6 Structure & Energetics of Seyfert AGN

Information on the structure and spectral index of AGN from radio observations are integral to unravelling the mysteries surrounding the SMBH at the centre of active galaxies. In this section I discuss how both radio morphology and spectral index values are used later in this thesis to determine information about 'jet' energetics.

1.6.1 Radio structure

Radio structures found in the compact nucleus of Seyfert galaxies are complex, comprising of multiple aligned components, S-shaped or linear features, loops and lobes (Gallimore *et al.*, 2006). High-resolution radio observations of Seyferts have revealed double and triple sources which suggests a collimated ejection of material. AGN are traditionally divided into radio quiet (RQ) and radio loud (RL) with the latter being particularly powerful having large scale jets and bright cores. Even though Seyferts are 'radio quiet', they are not radio silent and many exhibit high brightness temperature emission and anisotropy in the form of low power collimated jets or outflows. These are analogous to the large jets in radio galaxies, but possibly stunted by the interaction with the interstellar medium (ISM) of the host galaxy (Ulvestad *et al.*, 1981; Booler *et al.*, 1982; Wilson and Ulvestad, 1982; Neff and de Bruyn, 1983; Gallimore *et al.*, 2006). It is well established that in RL AGN synchrotron radiation from particles accelerated in the jets is responsible for the radio emission. The origin of the radio emission from RQ AGN is less clear.

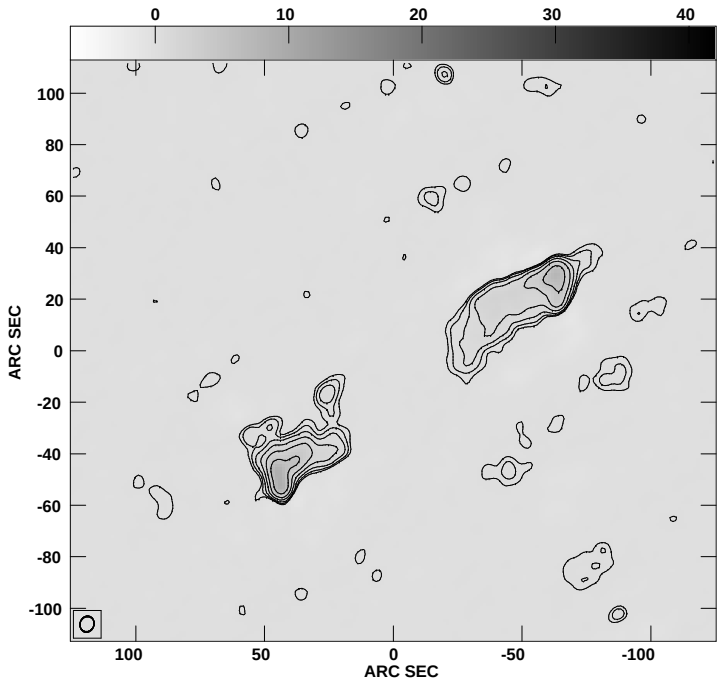

Figure 1.7: Image showing the radio morphology of a bright FRII source imaged by the author from the 13^H field at 0.6 GHz. The radio morphology of the two symmetrical lobes is strong evidence for a source powered by nuclear activity. Contours are at $5.4 \times\ 10^{-05}$ Jy $\times\ 2.8, 5.6, 11, 23, 45, 90, 180$.

Investigation of the structure and morphology of radio components is used in this work to determine if the individual AGN discussed in this work has an active jet. Generally, the radio morphology of AGN is described in terms of two components: the 'extended' component which is spatially resolved and the 'compact' component which is usually unresolved at $\sim 1''$ resolution. The two components have different spectral index values, despite synchrotron processes existing in both cases, as discussed in Section 1.3.3. The extended component is generally in the form of two symmetric lobes of radio emission either side of centre of the galaxy, with the largest lobes having radii > 100 kpc. An example of an FR II source featuring two lobes of emission imaged by the author, using GMRT deep field data is shown in Figure 1.7. This FR II source has extended bright lobes with hot spots which dominate the emission. These features provide evidence for an active jet existing in this galaxy. Investigating the radio morphology of black holes is an important for determining the presence of an active jet. Radio morphology is also relevant to future work on the GMRT deep field because the morphology of the radio emission from galaxies can be used to discriminate between AGN and star forming galaxies (SFGs). The GMRT data is discussed in Appendix A and the radio morphology of

Seyfert AGN NGC 4051 is discussed in Section 4.4.2.

Through studying both the non-thermal radio emission and the optical narrow-line emission from Seyfert nuclei it has become apparent that these two types of emission are related (de Bruyn and Wilson, 1978; Wilson and Heckman, 1985). Both types of emission can be used to reveal the geometry of the active nucleus on extremely small scales. Several Seyferts show a wedge-shaped area of optical emission lines resulting from ionised gas, which is roughly aligned with the radio structure (Wilson and Tsvetanov, 1994). It is thought that the optical line emission is due to cones of ionising radiation from the AGN, centred on the radio axis. The position of centre of the optical nucleus is coincident with the compact radio component. In the dusty spiral arms of the galaxy seen in the optical we also detect radio emission from magnetic fields which accelerate particles producing synchrotron radiation, where the strong magnetic fields are coincident with the dust lanes. Also, the structure imaged from forbidden lines, which are emitted isotropically from the NLR, have been shown to coincide with the extended diffuse radio emission from Seyferts. The first suggestion of a physical relationship between the NLR and the radio structure came from the discovery of a correlation between the radio power and the luminosity and line width of [OIII]λ5007 Å. The Oxygen forbidden line, [OIII]λ5007 Å, is the most easily measured of all the forbidden lines found in Seyfert galaxy spectra. [OIII]λ5007 Åemission is relevant to this work because it is used to study the structure of the individual AGN described in this thesis. The forbidden line region (FLR) for AGN is found to exist on scales of 1 kpc, which is in agreement with the scale of radio emission from Seyferts. This agreement in the physical size of the two regions can explain the correlation found between the optical and radio luminosities because both types of radiation are emitted from the same volume of space (de Bruyn and Wilson, 1978). The relation between the [OIII]λ5007 Å line and the radio emission is interpreted as a pressure balance between the enveloping cosmic rays and magnetic fields necessary for the radio emission and the thermal gas in the FLR (de Bruyn and Wilson, 1978). There are good alignments between the NLRs and the radio jet axes in a number of Seyferts suggesting that they are collimated by the same, or coplanar, nuclear discs or tori (Wilson and Colbert, 1995).

1.6.2 Energetics of accretion & jets

As discussed in previous sections, the observable properties of AGN are interpreted as a result of accretion onto a black hole. In these accreting systems the material

moves toward the centre of the system and in doing so a fraction of the material may be ejected in the form of outflows. The exact physical nature of the outflows is still unknown; however, it is known that these outflows have mechanical and radiative effects on the surrounding environment. Outflows are seen not only from SMBHs but also neutron stars and stellar mass black holes [e.g. Cohen *et al.* (1979); Margon (1982); Mundt (1985)]. Despite decades of study into jet outflows from black holes there is no comprehensive theory that can account for the mechanism(s) of jet production, collimation, acceleration and the issue of coupling between the outflow of matter and accretion flow. Strong magnetic fields are required to produce the amount of collimation seen at high resolutions and this is believed to be related to the rate of spin of the central BH. Considering the scaling between BHXRBs and AGN one would expect an AGN with an PSD synonymous with a 'soft state' BHXRB to have quenched core radio emission. The Seyfert galaxy NGC 4051, investigated in this thesis, has an PSD similar to that of the High Mass X-ray Binary (HMXRB) Cygnus X-1 during its 'soft state' (see Figure 1.8 taken from M$^{\rm c}$Hardy *et al.* (2004)). I will show in the following chapters evidence for jet structure in NGC 4051 which somewhat contradictory to the current view of 'soft state' binary BHs where the radio jet is suppressed. In fact, several studies of radio quiet AGN have revealed extended collimated radio emission on scales of the NLR (10-1000 pc) (Nagar *et al.*, 1999; Rosario *et al.*, 2008; Mundell *et al.*, 2009; Foschini *et al.*, 2011).

The first step in quantifying the jet energetics is to assume that the minimum total energy (E_{min}) of both the particles in the jet and the magnetic fields can be approximated to the energy value where the energy densities of the jet particles and magnetic fields are equal. This theorem is known as the equipartition theorem, it assumes that the radio emission observed is the result of a synchrotron process. The relativistic (synchrotron) electrons have an energy density U_e and a magnetic energy density $U_B = \frac{B^2}{8\pi}$. To estimate U_e one assumes a power law distribution of electrons producing synchrotron radiation over a frequency range 10-10,000 MHz, giving the relation $U_e \propto B^{-\frac{3}{2}}$. Therefore the total energy density, $U = (1-\eta)U_e + U_B$ where η is the ion/electron energy ratio. For $U_E = (1-\eta)U_e \propto B^{-\frac{3}{2}}$ and $U_B \propto B^2$, the total energy density (shown by the thick black line in Figure 1.9) has a sharp minimum just above the equipartition point where $U_B = U_E$, as shown in Figure 1.9. Thus, the minimum energy E_{min} corresponds closely to the point of *equipartition* (Burbidge, 1959; Longair, 2010).

In Section 4.5 I use equipartition arguments to determine the the physical properties and energetics for individual AGN components (core and lobes) from mea-

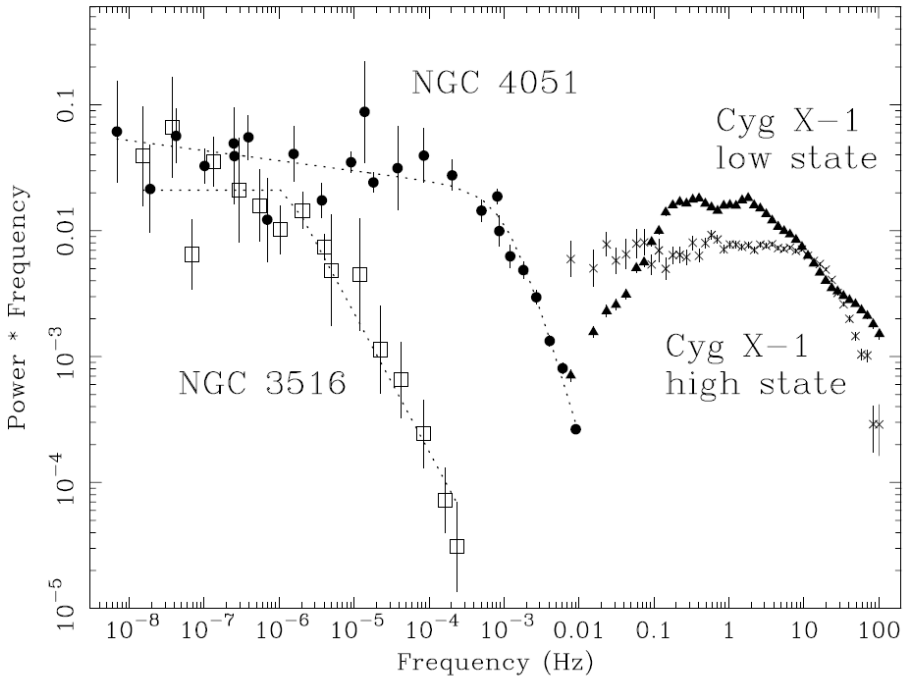

Figure 1.8: Unfolded PSDs of NGC 4051 (filled circles), NGC 3516 (open squares) and Cygnus X-1 in the low (filled triangles) and high (asterisks) state. *Figure 18 from M*^{c}*Hardy* et al. *(2004).*

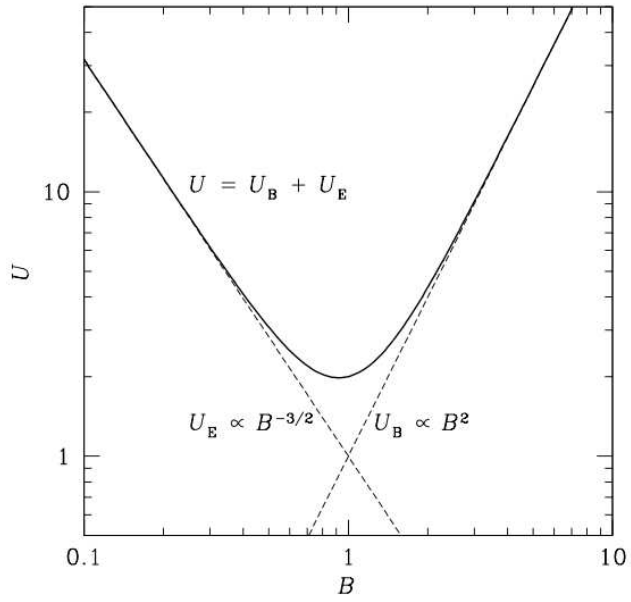

Figure 1.9: For a synchrotron source with a known flux density the minimum energy density E_{min} (or U) can be calculated assuming that equipartition occurs, i.e. $U_B = U_E$. (*Figure from http://www.cv.nrao.edu/course/astr534/SynchrotronSrcs.html.*)

surements of the component size, flux density and spectral index. Recent X-ray imaging studies which use both the *Chandra* and XMM-Newton observatories have shown the interaction of radio sources with the surrounding intracluster medium (ICM). Decrements in observed X-ray emission where coincident radio emission exists are interpreted as 'bubbles' blown in the ICM by a central radio source, and this interpretation is supported by spectral information and imaging using *Chandra* (Fabian *et al.*, 2000). Since the radio emission is embedded in the ICM, the energy content of the lobes can be more accurately measured by assuming a pressure balance between the thermal ICM and the relativistic plasma in the bubbles, and the use of equipartition is not required. The total energy in the lobe is simply $E = 4PV$ where V is the volume of the bubble and P is the pressure of the surrounding gas, which can be calculated from the particle number density value, determined from the high resolution X-ray images of the surrounding medium. If high resolution X-ray imaging does not exist, which is the case for the AGN discussed in this thesis, one can only estimate a pressure value based on the equipartition theory, this pressure measurement can then be used to estimate the power of the lobes. It has recently become apparent that jets carry away significant fractions of the accretion power and might act as a major source of energy and entropy for the interstellar medium. It is interesting scientifically to quantify the energy of the radio lobes and compare with other AGN. In this work I investigate the physical properties of the core and jets of Seyfert 1 NGC 4051 and compare the results to other Seyfert 1's and 'soft state' XRBs in an effort to acquire an understanding of both the radio-jet driven motion and the impact of the jet, if any, on the surrounding medium . I also hoped to determine if the observed outflow is active.

1.7 Summary of this thesis

The main aim of this study was to carry out a comprehensive comparison between the X-ray and radio variability from the core region of an individual Seyfert 1 type AGN, NGC 4051, specifically to determine the origin of the continuum radio emission. The variability of the radio emission was investigated in comparison to the X-ray emission to determine if a coupling exists between the accretion disc and the extended emission (from jets). To this end, I present in this thesis an analysis of the first quasi-simultaneous study of the X-ray and radio emission from a Seyfert 1 galaxy analogous to a 'soft state' BHXRB.

The appendix gives an introduction to the radio reduction of spectral line data of

the 13^H field. The aim of this study was to calculate the spectra of faint sources in the field data.

The remainder of this thesis is arranged as follows:

Chapter 2 details the radio and X-ray variability of the NLS1 AGN NGC 4051,

Chapter 3 discusses the possibility of a distinct disc jet coupling in AGN NGC 4051,

Chapter 4 discusses the structure, morphology and energetics of AGN NGC 4051,

Chapter 5 summarises the conclusions of this work and details their implications for X-ray/radio variability and structure studies of Seyferts. The future of this work is also discussed in this section.

Finally in Appendix A I present a description of the radio reduction of deep field images of 13^H field and their use for discriminating between AGN and star forming galaxies (SFGs).

Note that throughout this thesis I assume a distance to NGC 4051 of 15.2 Mpc, calculated from the Tully-Fisher relationship by Russell (2003) ($1''$ is equivalent to 74 pc). For the mass of the SMBH at the centre of AGN NGC 4051 I assumed a mass $M_{SMBH} = 1.91 \times 10^6\ M_{\odot}$, as determined by Peterson *et al.* (2004) using reverberation mapping.

May the Seyfert galaxies emit brightly to illuminate your path!

MAM

2

Radio and X-ray variability of Seyfert 1 AGN NGC 4051

This chapter has been published in MNRAS: Jones, S., McHardy, I., Moss, D., Seymour, N., Breedt, E., Uttley, P., Körding, E., & Tudose, V. 2011, Mon. Not. R. Astron. Soc., 412, 2641.

All VLA radio reduction and radio/X-ray analysis was performed by myself. The X-ray reduction/lightcurves were provided by Ian McHardy, Phil Uttley and Elme Breedt. The data for the fundamental plane graph shown in Figure 2.14 was provided by Elmar Körding. Derek Moss, Nick Seymour and Valeriu Tudose all collaborated with myself on the best radio reduction techniques to use.

In this chapter I present an investigation of Seyfert 1 galaxy NGC 4051 at radio wavelengths (both 4.8 GHz and 8.4 GHz) and at X-ray wavelengths (at 2-10 keV). Lightcurves of the radio and X-ray emission from the nuclear core of the AGN i.e. from the vicinity of the black hole (BH) is used to access the variability of radio and X-ray emission. The possible correlation between radio/X-ray flux from the core of NGC 4051 is introduced. The radio/X-ray correlation is also discussed in the con-

text of the 'fundamental plane of black hole activity', where the plane indicates that AGN and Galactic Black Hole (GBH) systems have a disc/jet coupling relationship which scales with mass.

2.1 Introduction

NGC 4051 is a relatively nearby [15 Mpc from (Russell, 2002)] Narrow Line Seyfert 1 (NLS1) galaxy with a central black hole mass of $M_{SMBH} = 1.91 \pm 0.78 \times 10^6 M_{\odot}$ (Peterson *et al.*, 2004). It is one of the brightest and most variable Active Galactic Nuclei (AGN) in the X-ray sky and has been extensively observed by a number of X-ray observatories (M$^{\rm c}$Hardy *et al.*, 2004; Ponti *et al.*, 2006; Terashima *et al.*, 2009; Breedt *et al.*, 2010). One of the major results to emerge from these studies is that the X-ray variability characteristics of NGC 4051, as parametrised by the power spectral density (PSD), are very similar to those of the GBH Cygnus X-1 when in the 'soft state' (M$^{\rm c}$Hardy *et al.*, 2004). A classification of NGC 4051 as a soft state system is supported by the relatively high accretion rate ($\sim 10\%\ L_{Edd}$, calculated in Section 4.5.0.1). If it were entirely analogous to a soft state GBH then a bright active radio-emitting jet would not be expected. Although the X-ray observations of other Seyfert galaxies are less extensive, the data are consistent with Seyfert galaxies being soft state systems (e.g. also see M$^{\rm c}$Hardy *et al.* (2005)).

NGC 4051 has been known for some time to host a weak nuclear radio source of unknown origin (e.g. Ulvestad and Wilson, 1984a; Kukula *et al.*, 1995; Christopoulou *et al.*, 1997). In the year 2000 the disappearance of the HeII $\lambda 4686$ line from the rms spectrum at low X-ray flux levels was observed. Peterson *et al.* (2000) suggested that the reason for this disappearance may be that the inner part of accretion disc had changed from being optically thick to being advective at low accretion rates, leading to the expectation of increased radio emission (e.g. Di Matteo *et al.*, 1999). Therefore, over a period of 16 months in 2000 and 2001, a joint radio (with the Very Large Array, VLA) and X-ray (with the Rossi X-ray Timing Explorer, RXTE) monitoring programme to search for this predicted rise in radio emission during the period of low X-ray flux was carried out. It is important to note here that if the accretion disc was found to be advective then the analogy with 'soft state' GBHs would break down, as advective discs are 'hard state' objects.

Preliminary analysis of the resultant data did not, however, reveal a strong radio/X-ray anti-correlation, with high radio flux corresponding to low X-ray flux. Instead the fluxes appeared to be positively correlated (M$^{\rm c}$Hardy, 2005). Correlated

radio/X-ray variability is commonly seen in hard state, jet-dominated GBHs, suggesting that the radio emission in NGC 4051 may also come from a jet. To learn more about the radio structure Very Long Baseline Interferometry (VLBI) observations were carried out both with the European VLBI Network (EVN) in 2003 and the Global VLBI network in 2004. A triple structure consisting of a compact core with a barely resolved ($\sim$ few milliarcsec) component on each side of the core, separated by ~ 0.5 arcsec and almost in a straight line, was detected (M^{c}Hardy, 2005). See Section 4.3.3 for more information on these data. This structure is similar to the core and hot spots of an FRII radio source and strongly suggests an underlying jet with the hot spots being the places where the jet hits some surrounding medium. Similar EVN observations were later performed by Giroletti and Panessa (2009), revealing a broadly similar structure. A definitive analysis of the X-ray and radio variability of the nucleus of NGC 4051 was hindered by the fact that the VLA array configuration changed approximately every 4 months and thus the size of the synthesised beam changed, encompassing greater or lesser amounts of surrounding extended emission (see Figure 2.1). The radio emission of NGC 4051 is therefore carefully modelled on different spatial scales in order to remove the contribution from extended emission to the flux from the nucleus, which is then compared to the X-ray flux.

Investigation of the radio emission from the vicinity of a SMBH gives an insight into the physical processes which occur in that region. By comparing the radio emission with other wavelengths of radiation emitted near the SMBH one can assess if a coupling exists between these regimes. Specifically, the X-ray emission is compared to the radio emission in order to explore how accretion (from X-rays) is coupled to jet production (from radio). A correlation between radio luminosity (L_R) and X-ray luminosity (L_X) has been established for BHXRBs in low/hard and quiescent states, where $L_R \propto L_X^{\beta}$ where $\beta = 0.6 - 0.7$ (**?**Gallo *et al.*, 2003). The relationship has been extended by several studies, e.g. Merloni (2003); **?**, to show that the X-ray and radio luminosities scale with the the mass of the BH. This relationship, known as the 'fundamental plane of black hole activity' shows that $\beta \sim 0.7$ over many orders of magnitude of luminosity and black hole mass. For Seyfert galaxies the relationship has been established 'globally', from single or average measurements of multiple sources, but very few studies exist that define the relationship 'intrinsically' using multiple measurements in X-ray and radio on the same source. One of the first 'intrinsic' investigations of this relationship for a Seyfert galaxy is presented here on the 'soft state' Seyfert 1 AGN NGC 4051. Recently another intrinsic study of a Seyfert 1.5 LINER galaxy NGC 7213 has been carried out by Bell

et al. (2011). For the 'hard state' NGC 7213 Bell *et al.* (2011) found a significant correlation between the two regimes with a factor ~ 2 variability seen in both bands and the averaged X-ray and radio luminosity value sits well on the refined version of the 'fundamental plane of black hole activity' relation using a sample of 'hard state' Low Luminosity Active Galactic Nuclei (LLAGN) (Körding *et al.*, 2006a). For further information on the 'fundamental plane of black hole activity' see Sections 1.5 and 2.6.2. For NGC 7213 a least squares fit to the individual simultaneous X-ray and radio luminosities gives $L_R \propto L_X^{0.2\pm0.056}$, with $L_R \propto L_X^{0.58\pm0.014}$ when the radio data are shifted by -35 days with respect to the X-ray. The Seyfert investigated by Bell *et al.* (2011) is a 'hard state' object, therefore, correlated radio/X-ray variability with values close to the $\beta = 0.7$ relation are expected. For this first investigation of a 'soft state' Seyfert it is interesting to determine the value of β for the system and to determine its position on the 'fundamental plane of black hole activity'.

In Section 2.2 the radio observations are presented with the radio analysis. Section 2.3 considers the radio variability as observed with the A and B array configurations, in which sensitivity to core radio flux variations is greatest, and compare it with quasi-simultaneous X-ray observations. Section 2.4 discusses how to remove the contribution from extended radio emission in the B, C and D array configurations. Section 2.5 shows simulations designed to determine the accuracy with which the extended contribution can be measured. Section 2.6 considers the implications of the results for radio emission models for radio quiet AGN. I also include here discussion of jet models which underlay the so-called 'fundamental plane', relating black hole mass to radio and X-ray luminosity (Falcke *et al.*, 2004; Merloni *et al.*, 2003) and also discuss coronal models (Laor and Behar, 2008). Conclusions are detailed in Section 2.7.

2.2 Observations and Data Reduction

NGC 4051 was observed by the VLA 29 times between 16 June 2000 and 3 September 2001 with a typical interval between observations of 2 weeks. On each occasion the source was observed at both 8.4 GHz and 4.8 GHz with a total time on source, in each band, of approximately 12 minutes. Six of the observations were made with the VLA in A configuration, 2 in BnA, 6 in B, 1 in BnC, 6 in C, 3 in DnC and 5 in D. Observations were carried out in 2IF mode, which means the source was observed at two separate [intermediate frequency (IF)] bands, with 50 MHz bandwidth at both frequencies. The phase calibrator was J1219+484 and the flux calibrator was

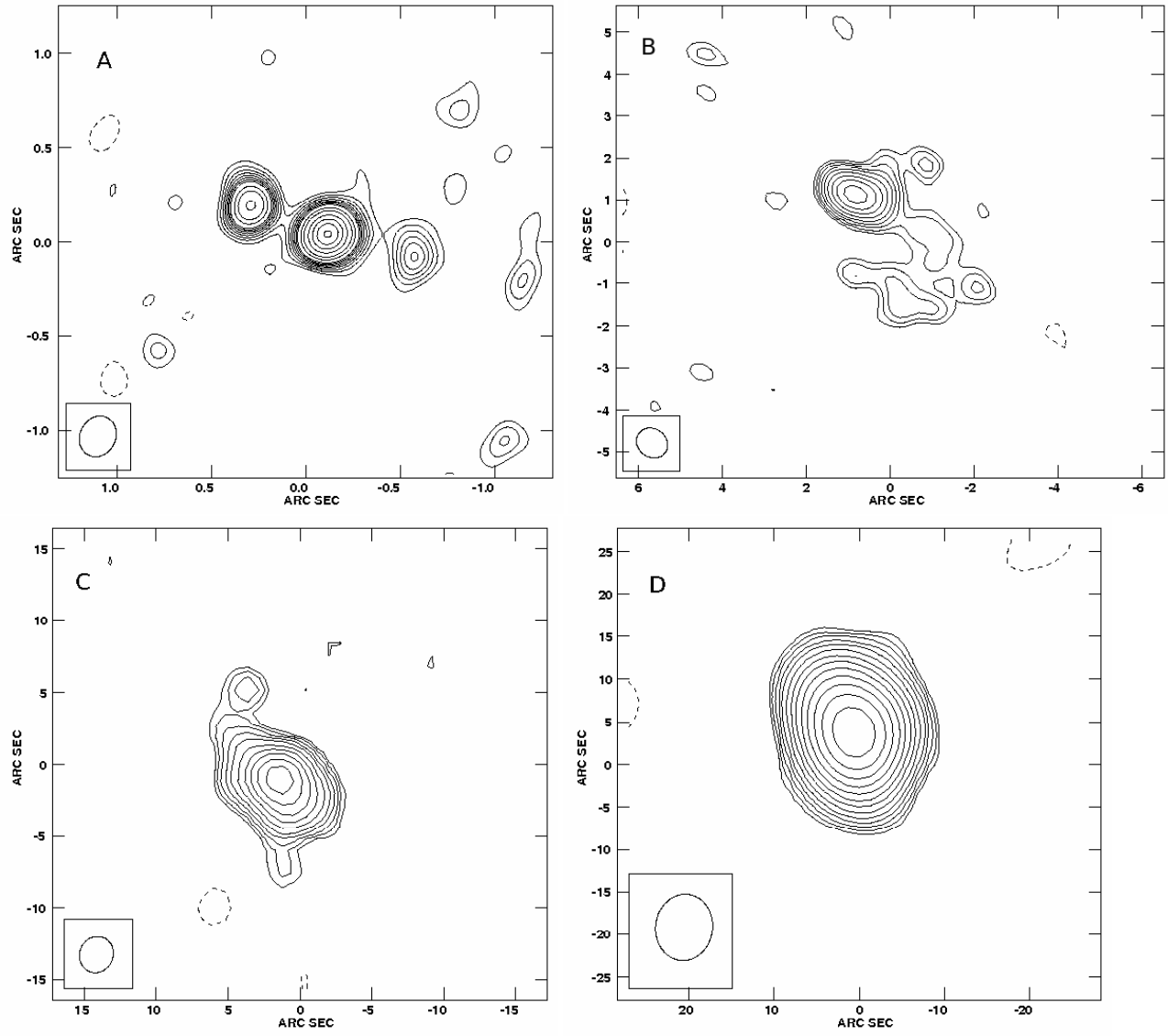

Figure 2.1: Representative maps made from single 8.4 GHz observations in each of the four main VLA array configurations. The configuration (A, B, C or D) is listed in the top left corner of each map. The maps are all centred on the nucleus of NGC 4051. The rms noise level in each A, B, C and D map is $16, 2, 2.2$ and 1.61μJy/beam and the major axis of the restoring beam is 0.22", 0.78", 2.54" and 7.83" respectively . The contours are at $rms \times -2.8, 2.8, 4, 5.6, 8, 11, 16, 23, 32, 45, 64, 90, 127, 180, 254$.

Table 2.1: Observational Details of VLA 2000-2001 data at 4.8 and 8.4 GHz. For both frequencies the phase calibrator is J1219+484 and the flux calibrator 3C286. The phase calibrator was observed for $\approx$ 5 min and the flux calibrator was observed for $\approx$ 4 min per run.

Date JD-2450000	Configuration	Time on Source (seconds)
1701.583	C	1130
1722.514	DnC	1170
1734.542	DnC	1130
1741.505	DnC	1090
1750.467	D	1210
1756.535	D	1210
1771.465	D	1100
1803.335	D	1140
1817.342	D	770
1852.222	A	1150
1865.185	A	1160
1879.148	A	1140
1893.131	A	1080
1909.066	A	1090
1929.926	A	1140
1941.001	BnA	1000
1956.956	BnA	1070
1985.710	B	1130
2005.781	B	1120
2023.773	B	1120
2034.660	B	1150
2046.649	B	1120
2060.660	B	1210
2078.464	BnC	1250
2091.505	C	1140
2101.560	C	1120
2114.444	C	770
2132.351	C	1130
2156.272	C	1230

3C286 (1331+305). For more information on these observations see Table 2.1.

2.2.1 RXTE data

NGC 4051 is part of a long term AGN X-ray monitoring program using the Rossi X-ray Timing Explorer (RXTE), which started on 23 April 1996. Discussion of

the X-ray reduction is presented in McHardy *et al.* (2004). Observations are in the form of 1 ks snapshots using the proportional counter array (PCA) on board RXTE. To obtain the flux measurement Phil Uttley fitted a power-law model to the spectra using XSPEC and integrated the flux in the range of 2-10 keV. The errors on the flux measurements were calculated from the counts in each observed spectrum, weighted by a response function. The normalised 2-10 keV light curve is shown in the top panel of Figure 2.10.

2.2.2 Radio data reduction

All VLA data reduction was carried out by the author using the NRAO Astronomical Image Processing System (AIPS). The first step in the reduction involves flagging erroneous data from the beginning of each scan, using the task QUACK. By utilising the tasks UVPLT and TVFLG further flagging is carried out on radio frequency interference (RFI) and correlator errors in both IF's. Both amplitude and phase are investigated for errors before starting the calibration.

2.2.2.1 Calibration

To calibrate the data one must start by using the task SETJY which enters the flux of the flux calibrator source into the solution table to be used in the calibration. The flux calibrator for NGC 4051 is 3C286 which has a flux at 8.4 GHz of $\sim$ 5.1 Jy in both IF's. The tasks CALIB and CLCAL are then used to calibrate source data using the flux calibrator and the phase calibrator respectively. The calibration was checked using the task UVPLT to plot *uv* coverage, graphs of amplitude versus *uv* distance, phase versus *uv* distance, phase and amplitude versus time and amplitude and phase difference with time. Finally the task TVFLG was used to flag out remaining RFI, correlator errors or antenna errors by displaying amplitude difference and phase difference versus *uv* distance in both IF's for both the source and calibrators. After flagging the calibration was re-run before imaging.

2.2.2.2 Imaging strategy

Images were made using the task IMAGR, with 3 clean fields used for each image. The first field contained the science source NGC 4051 and the remaining 2 fields were set around two fainter neighbouring sources, one approximately 5.5 arcmin to the north-east and another approximately 3.5 arcmin to the south. The extra fields were used during cleaning to remove sidelobe flux from these sources which creates

extra flux and noise features in the image and causes inaccuracies in measurements of flux density of the primary target.

After experimenting with different iterations of cleaning it was decided that 10,000 iterations gave the highest image fidelity. Self calibration was not used on the final images. All early experimentation with self calibration revealed the source to be too faint, and resulting images were not improved by this method.

2.2.2.3 Measuring core flux density

The aim here is to search for a possible relationship between the X-ray and radio fluxes. The X-rays vary very rapidly, and hence come from a very small region, tens or hundreds of light seconds across. If there is any relationship with the radio emission, I must therefore expect that the radio emission comes from a region which, although possibly not as small as that of the X-ray emission region, is unlikely to be light years across. At the distance of NGC 4051 (15.2 Mpc), 1 ” is equivalent to $\sim$ 74 pc and hence we are concerned here with the core radio flux. However, measuring of core flux accurately for a source with any extended structure is far from trivial and, even for a core which is almost resolved from the extended emission it is not easy, as I discuss further in Section 2.3.1.

The standard AIPS task for measuring the peak and integral flux densities is JMFIT. This task fits a Gaussian model to the values within a box drawn around the source and outputs the integral flux density (Jy) values and peak flux density (Jy/beam) values. Although I am interested in intrinsic core flux, measurements of both peak and integral flux densities have value for this study and so both were recorded.

A box was placed around the nuclear core of NGC 4051 in each map using the task COWINDOW. The box size was different for each array configuration and was chosen so it included all the nuclear flux, and the smallest amount of extended emission possible. I kept the box size constant when calculating flux density values within the same array. JMFIT outputs errors depending on the Gaussian fitting to the nucleus of the source. These JMFIT errors were then combined in quadrature with the standard 5% error on the flux density value to calculate the error on each of the 29 flux readings.

2.3 Variability of the Nucleus

2.3.1 During period of A configuration observations

2.3.1.1 8.4 GHz Observations

In Figure 2.1 I present images of NGC 4051 at 8.4 GHz from representative individual observations made in each of the four VLA array configurations. One can see that, within the A configuration, the radio emission from the core is almost separate from the neighbouring eastern and western components. Higher resolution maps made from observations by MERLIN (e.g. Christopoulou *et al.*, 1997)) or the EVN (Giroletti and Panessa, 2009; M^{c}Hardy, 2005) show the same structure (see Chapter 4 for further details on the structure of the NGC 4051 maps). Thus the flux of the central component, as seen in the A configuration observations, can be taken as reasonably representative of the nuclear flux. In all other array configurations measurements of the nuclear flux are contaminated by extended emission, which restricts the conclusions which can be drawn from these data. I consider the problem of contamination in more detail in Sections 2.3.2 and 2.3.3 but here I consider the specific concerns related to the A configuration observations.

The integral flux density is the desired measurement for slightly extended, but otherwise isolated sources, such as one might find in deep surveys. However the peak flux is generally the best measure of the true core flux. If the source is compact and isolated but there are significant phase errors in the calibration which move some of the flux slightly to the side, then the integral flux density would be a better measure. (For a very brief discussion of how one might measure core fluxes see, for example, Mullin *et al.* 2008 and papers referred to therein.) However, if the core is surrounded by extended emission then the integral flux density will be much more affected by small changes in beam shape which may include different amounts of extended emission. The A configuration maps, although showing a core which is close to being resolved consistently, indicate an extension of approximately 0.1", along the line of the 3 main source components and so the problem of extended emission exists even for the A configuration observations.

In the top panel of Figure 2.2 I show the 8.4 GHz peak core flux densities with fixed beam (filled circles) and default beams (open hexagons) as derived using JMFIT. For the non-fixed beam maps the restoring beams were left free, to be determined only by the *uv* coverage and the use of ROBUST 0 in IMAGR. The size of the fitted Gaussian component were also left free. As the observations were made within a relatively short period, at mostly the same hour angles, in practice

the restoring beams, were very similar although not identical. The fitted Gaussians were similar, although there was some scatter in width.

In order to try to standardise the flux measurements further, I remade all the maps with a fixed restoring beam with parameters at the mean of the unconstrained restoring beam (i.e. for A configuration the beamsize 0.24" $\times$ 0.19" and position angle of 137 degrees was used) with ROBUST 0 as this gives a balance between natural weighting at ROBUST 5 and uniform weighting ROBUST -5.

The first point to note from Figure 2.2 is that any variation of the core 8.4 GHz flux, if real, is very small, and certainly of much lower amplitude than the variation seen in the X-ray observations (lower panels of Figure 2.2). The quoted errors are the statistical error given by JMFIT combined in quadrature with the 5% error usually assumed as the maximum likely uncertainty on the flux density calibration. The calibration uncertainty therefore slightly dominates the total resultant error which is typically twice the statistical error, or slightly more. This total error is the correct error to use when comparing the flux density from the same object in different observations. To determine the relative flux densities of different objects within the same observation, however, one would not include the flux calibration uncertainty.

It is noted that minor calibration errors, or sidelobes from distant sources which have not been perfectly removed, can lead to flux measurement errors which are typically twice the statistical error. I can use observations of other structures in the maps to make a crude estimate of the real errors on the flux density of the central source. In this case components are visible on either side of the core in the A configuration maps which one might assume to be constant if they arise from extended components related to NGC 4051. The (brighter) eastern component is definitely more extended than the core, and the (fainter) western component is probably the peak of a low surface brightness extended structure which extends to the south and so flux measurements of both will be a little more sensitive to the exact beamshape than will measurements of the core. While the default beamshape does not change greatly, variations in peak flux by twice the statistical error, and occasionally by more, are seen between observations. I conclude that the error which was used throughout this investigation, (the statistical error from JMFIT combined in quadrature with a 5 percent amplitude calibration error), may be a slight underestimate of the true total error.

I have also examined 8.4 GHz A configuration observations of NGC 4051 made by other observers before 2001-2002 data set. From an observation on 24 June 1999, Kukula *et al.* (1995) list the core peak flux as 0.54 mJy and the integral flux as 0.60 mJy from a map with rms noise level of 73 μ Jy/beam. In an observation on

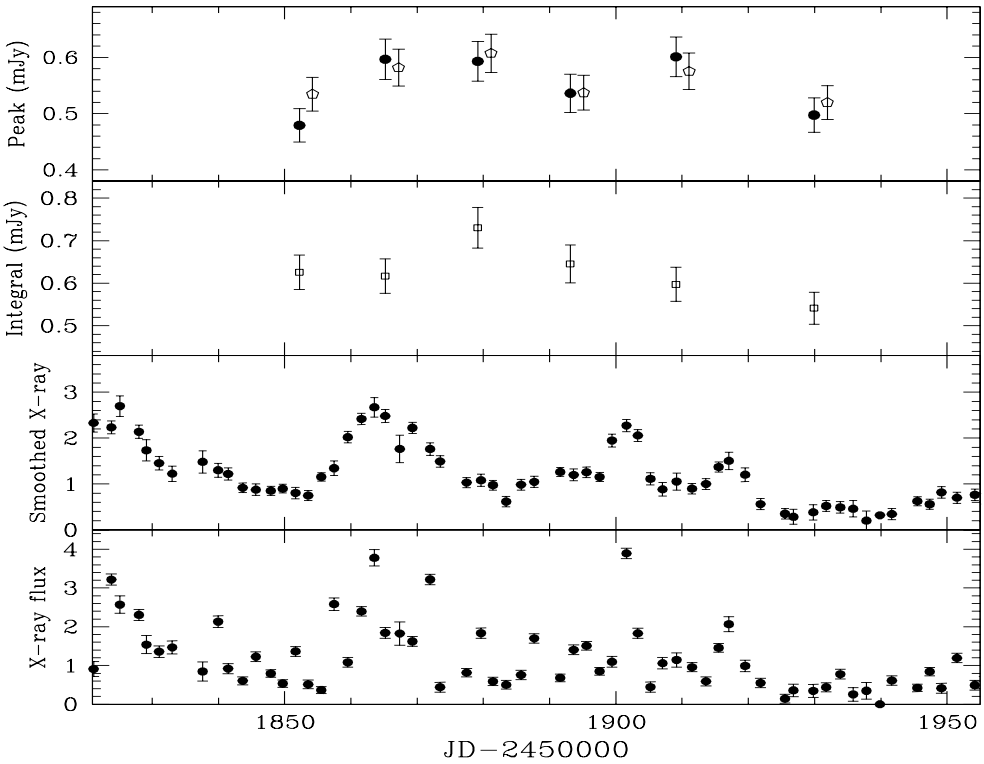

Figure 2.2: 8.4 GHz flux densities during A configuration and RXTE X-ray fluxes. Top panel: A configuration peak 8.4 GHz core flux densities with **fixed beam** (filled circles) and the non fixed **default beam** (open pentagons). Note the default beam points (open hexagons) were moved forwards by 2 days to the make them easier to see. The flux values were derived from JMFIT by fitting to the maps made with both fixed and default beams. See text for more details. 2nd panel: A configuration integral intensity values for 8.4 GHz core derived from maps made with a default restoring beam. 3rd panel: RXTE fluxes slightly smoothed (with a 4 point boxcar moving average) to remove high frequency variability. Bottom panel: 2-10 keV RXTE fluxes ($\times 10^{-11}$ erg cm^{-2} s^{-1}). Observations occur approximately once every 2 days with typical duration 1 ksec.

1 September 1991, which I reduced, a peak flux of 0.50 mJy is measured with rms noise of 40 µJy/beam (I do not quote the integral flux density as the beam is more distorted than that of any other A configuration maps which I consider here). These measurements are very similar to those which were measured from the 2001-2002 observations of NGC 4051.

I conclude that although I formally measure variations of $\sim$ 25% on a timescale of 2 weeks between the first two observations in the maps made with fixed restoring beam, the variation is barely more than 0.1 mJy and, given that the error is likely an underestimate of the true error the observations could be consistent with a constant source.

Table 2.2: A configuration core peak flux density values at 8.4 GHz and 4.8 GHz for maps made with **fixed** restoring beams.

Radio Date JD-2450000	Peak Flux Density at 8.4 GHz $\times 10^{-4}$ Jy	Peak Flux Density at 4.8 GHz $\times 10^{-4}$ Jy
1852.222	4.79 $\pm$0.30	5.91 $\pm$0.36
1865.185	5.97 $\pm$0.36	6.36 $\pm$0.37
1879.148	5.93 $\pm$0.35	6.59 $\pm$0.38
1893.131	5.36 $\pm$0.34	6.41 $\pm$0.39
1909.066	6.01 $\pm$0.35	7.39 $\pm$0.43
1929.926	4.97 $\pm$0.31	5.98 $\pm$0.36

2.3.1.2 8.4 GHz to 4.8 GHz spectral variations

The same map making procedure was carried out on the 4.8 GHz A configuration observations. In this case a fixed beam size at 0.385 " $\times$ 0.328 " was used, with PA -15°, quite similar to the PA of the 8.4 GHz observations. The resulting peak flux densities are listed in Table 2.2 and plotted in Figure 2.3. A broadly similar pattern of variations to that seen at 8.4 GHz is found and the amplitudes of variability are similar to those seen in NGC 5548 by Wrobel (2000).

In Figure 2.3 the 8.4-4.8 GHz two-point spectral index, α, where $S(\nu) \propto \nu^{\alpha}$ is shown. Given the difficulty of measuring core fluxes I do not over-interpret these results; however, it should be noted that all the maps from which the fluxes were derived were constructed in an identical way. With that proviso I note that these observations reveal an average $\alpha = -0.3$, with a slight hardening at the beginning of the observations followed by a gradual softening such as might be explained by an injection of electrons with a relatively flat energy distribution, perhaps as a result of a shock,for example, followed by radiative energy losses.

My main investigation here is centred on core radio variability, therefore, given the fact that the problems of nuclear flux contamination by extended emission are even greater at 4.8 GHz than at 8.4 GHz, I did no further work on the 4.8 GHz data from configurations other than A configuration. In the A configuration the nucleus is still reasonably resolved at 4.8 GHz; this work is presented later. A full discussion of the spectral index values of both the core and extended emission for NGC 4051 is presented in Chapter 4.

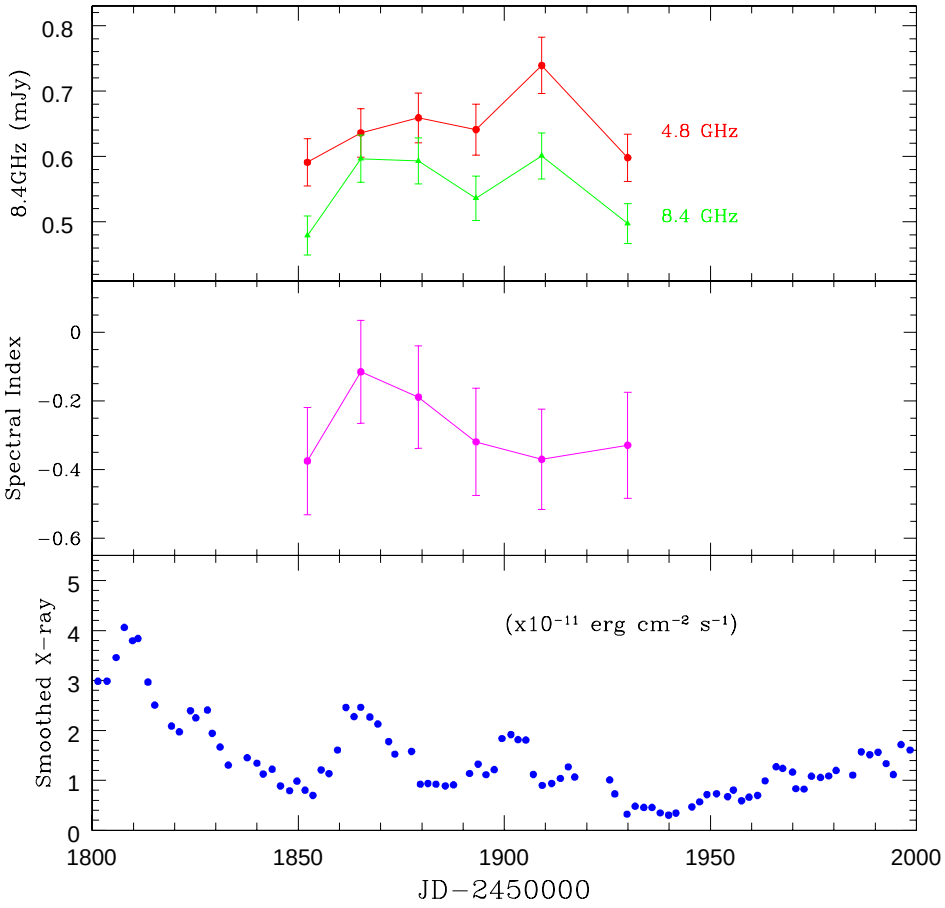

Figure 2.3: The evolution of radio spectral index including X-ray variations during A configuration. Upper panel: The core peak flux density (mJy) at 4.8 GHz and 8.4 GHz during the A configuration derived from maps made with identical restoring beams at each frequency. Middle panel: The 2-point 8.4 GHz to 4.8 GHz spectral index, α where $S(\nu) \propto \nu^{\alpha}$. Bottom panel: Smoothed X-ray flux for the time period of the observations in A configuration.

2.3.1.3 Radio/X-ray correlation

In Figure 2.2 I show (bottom panel) the 2-10 keV X-ray fluxes derived from the RXTE monitoring programme using the Proportional Counter Array (PCA). During the period of the A configuration the RXTE observations typically occurred every 2 days, with a duration of 1 ksec. Description of the X-ray reduction techniques can be found in Section 2.2.1 and M^{c}Hardy *et al.* (2004). It is well known that NGC 4051 varies very rapidly, and this rapid variability can be seen in Figure 2.2. Although there are slow, long term trends in the average flux of the source, observations with higher time resolution by XMM-Newton (e.g M^{c}Hardy *et al.*,

2004) reveal that variations by a factor of 2 occur not uncommonly on timescales of an hour. It is therefore relevant to consider how close in time the X-ray and radio observations should be in order to be useful for any study of correlated variability. The answer depends on what one thinks are the physical mechanisms responsible for the X-ray and radio emission. For example, in blazars where the variable emission in both the X-ray and lower frequency bands is believed to come from shocks in a relativistic jet oriented towards the observer, time separations of a few hours or less are required (e.g. M^{c}Hardy *et al.*, 2007). Although the VLBI radio morphology of three compact co-linear components is most easily explained by the presence of an unseen jet, the radio/X-ray ratio is much lower than in typical blazars and a similar relativistic jet-like origin for both emissions is unlikely. The currently most favoured, and energetically simplest, paradigm for the X-ray emission is Comptonisation of optical-UV disc photons by very hot thermal ($T > 10^9$ K) or non-thermal electrons in a corona above the accretion disc (e.g. Shapiro *et al.*, 1976). One possibility for the radio emission is that it is synchrotron emission from that same corona, although the size of the radio emitting region at the frequencies considered here would be typically 100 times larger than that of the X-ray emitting region (see Laor and Behar, 2008, for an extensive discussion of this model). I do not expect to detect radio variability on the rapid timescales seen in the X-ray band and it would be more appropriate to look for correlations between the radio emission and a longer-term averaged X-ray emission which may represent longer term accretion rate fuelling of the overall emission regions.

In order to avoid pre-judging the issue, I have therefore investigated the relationship between both the smoothed, and unsmoothed, X-ray fluxes. (The X-ray lightcurve is only gently smoothed with a running Gaussian function of half-width 2 days.) The smoothed X-ray lightcurve is shown in the second panel from the bottom in Figure 2.2.

In case the time difference between the radio and X-ray observations is important, I have listed the radio observation dates and the nearest RXTE observation dates in Table 2.3. Listed are both the directly observed, unsmoothed X-ray fluxes and the fluxes interpolated to the time of the radio observations. It is noted that the greatest separation is 0.59 days but that three of the separations are within 3 hours. In fact, there is not a great deal of difference between the nearest observed and interpolated X-ray fluxes.

In Figure 2.4 the 8.4 GHz radio flux from the maps made with the same (fixed) restoring beam is plotted against both the interpolated unsmoothed and interpolated smoothed X-ray fluxes. There is a weak correlation between the radio and X-ray

fluxes detected here (for the unsmoothed X-ray top graph the pearson rank coefficient, r is 0.69). If I were to repeat this investigation with a slightly larger error, the radio fluxes could be consistent with being constant. Smoothing the X-ray flux does not improve the appearance of the relationship. In Figures 2.5 and 2.6 I have plotted the same relationship for the peak, and integral 8.4 GHz flux densities derived from the maps made with the default restoring beams (restoring beam size determined by the *uv* data used to make the image). Similar pearson rank correlation values are determined (using the unsmoothed X-ray data only) for both Figures 2.5 and 2.6 with r values of 0.79 and 0.70 respectively . The simple power law X-ray spectral indices are measured for each of the RXTE observations and, in Figure 2.7 I plot the interpolated photon number indices, from both smoothed and unsmoothed lightcurves as before, against radio flux density for the 8.4 GHz maps made with the same restoring beam. Again, a weak to moderate positive correlation is seen here (Pearson rank coefficient r = 0.83). Although, I state with caution that there is usually a good relationship between X-ray flux and photon number spectral index for Seyfert galaxies such as NGC 4051 (Lamer *et al.*, 2003) so these plots are not completely independent of the previous flux-flux plots.

Hardening of radio spectra with increasing flux followed by softening with decreasing flux can be simply explained in the context of jet models by the injection of particles with a hard spectrum followed by subsequent radiative losses, and so might explain the observations of radio variability. However if the X-ray emission also arose predominantly in the jet I would expect a similar spectral behaviour, which is not seen here. I refrain from speculating too much given the quality of the data but the correlated variability seen here, if real, may simply reflect changes in fuelling rate to both emission regions.

2.3.2 During period of B configuration observations

2.3.2.1 8.4 GHz observations

From Figure 2.1, one can see that in the B configuration observations the core is not resolved from the components on either side. Measurement of the core flux therefore becomes more difficult and flux density measurement errors will be larger than for the A configuration observations. Nonetheless it is still possible to measure the peak, and integrated flux densities.

In Figure 2.8 I show the lightcurves during the period of the B configuration observations. Here the radio flux densities used are both the peak core flux densities

Table 2.3: 8.4 GHz observation dates with the nearest RXTE X-ray observation dates. X-ray fluxes are given both as observed and interpolated to the time of the radio observation. Dates are JD-2450000. X-ray fluxes are in units of 10^{-11} erg cm^{-2} s^{-1}.

Radio Date	Interpolated X-ray flux	X-ray Date	Observed X-ray flux
1852.222	1.10 ±0.13	1851.631	1.37 ±0.13
		1853.551	0.51 ±0.11
1865.185	1.84 ±0.14	1865.178	1.84 ±0.14
1879.148	1.61 ±0.11	1879.632	1.83 ±0.13
1893.131	1.23 ±0.10	1893.637	1.41 ±0.13
1909.066	1.14 ±0.15	1909.184	1.14 ±0.19
1929.926	0.35 ±0.17	1929.794	0.35 ±0.17

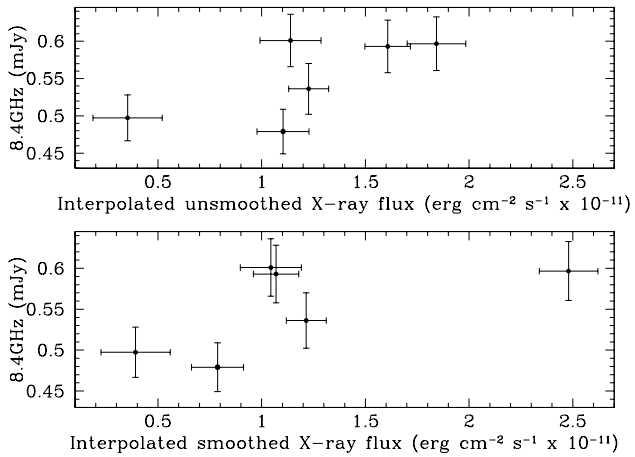

Figure 2.4: In both panels the 8.4 GHz A configuration peak flux densities derived from maps made with a **fixed** restoring beam plotted against the X-ray flux. In the top panel the observed X-ray fluxes are plotted from the bottom panel of Figure 2.2, interpolated to the time of the radio observations, but not smoothed. The exact time of the radio and nearest X-ray observations are given in Table 2.3. All radio observations have an X-ray observation within 0.6 days and, in 3 cases, within 3 hours. For the case of the unsmoothed X-ray and fixed 8.4 GHz values (top panel) the pearson rank coefficient r is 0.69, suggesting a moderate positive correlation exists. In the bottom panel I plot the X-ray fluxes interpolated from the slightly smoothed X-ray fluxes (third panel of Figure 2.2) against the peak 8.4 GHz radio fluxes.

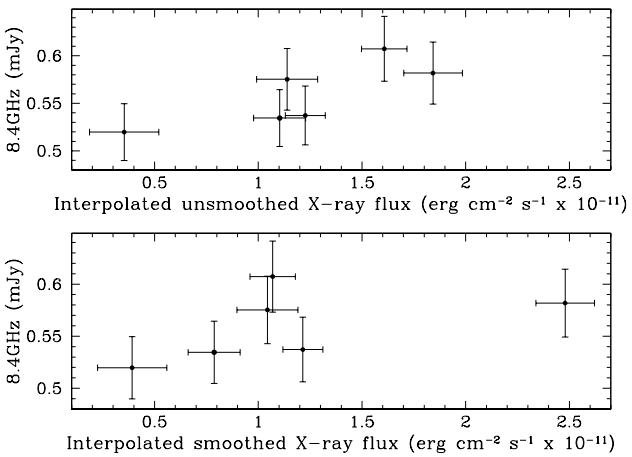

Figure 2.5: Peak 8.4 GHz core flux densities derived from maps made with the **default** restoring beam in A configuration plotted against the X-ray flux. In the top panel the observed unsmoothed X-ray fluxes are plotted. For the case of the unsmoothed X-ray and default 8.4 GHz values (top panel) the Pearson rank coefficient r is 0.79, suggesting a moderate correlation exists. In the bottom panel the X-ray fluxes has been slightly smoothed and are again plotted against the default peak 8.4 GHz radio fluxes, as in the top panel.

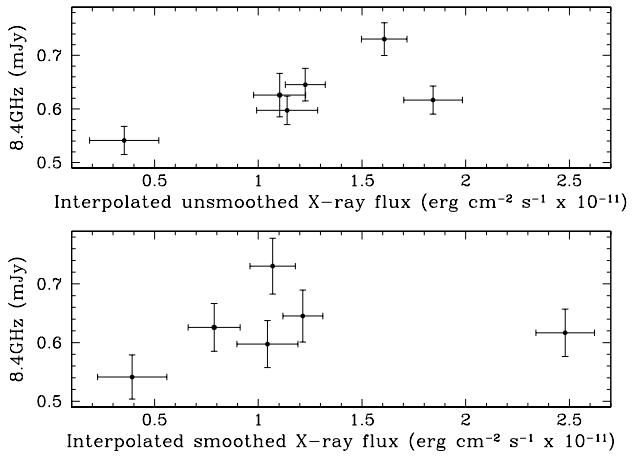

Figure 2.6: Integral Intensity radio flux densities at 8.4 GHz are plotted against the X-ray flux. In the top panel the core integral flux derived from maps made with the **default** restoring beam in A configuration, plotted against the observed (unsmoothed) X-ray fluxes. For the case of the unsmoothed X-ray and default 8.4 GHz values (top panel) the pearson rank coefficient, r is 0.69, suggesting a weak correlation exists.In the bottom panel the integral intensity radio flux densities at 8.4 GHz are plotted against the slightly smoothed X-ray fluxes.

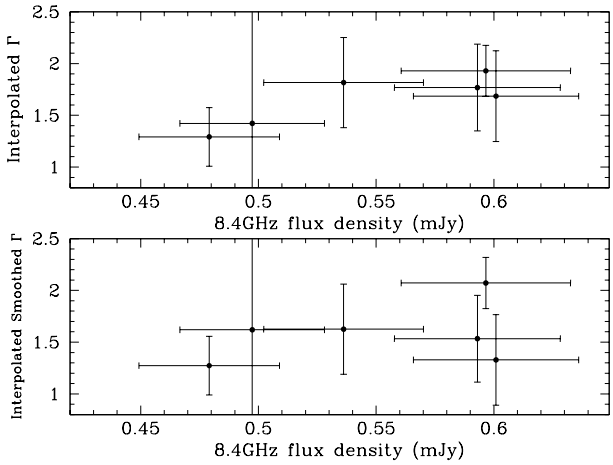

Figure 2.7: Peak 8.4 GHz flux densities from A configuration maps with a **fixed beam** plotted against RXTE 2-10 keV photon number spectral index, Γ. In the top panel I interpolate from a slightly smoothed lightcurve of Γ and in the bottom panel I simply interpolate Γ between the nearest observed values. A weak positive correlation is shown here with a Pearson rank coefficient, r of 0.83.

measured from maps made with the default beamshape and those with a fixed beam. As with the A configuration observations, the values derived from maps made with the same/fixed restoring beam (0.76 " $\times$ 0.64 " and PA -25.13°) are quite similar to those made with the default beam. The X-ray observations are as described for the A configuration observations. Again, at most, only marginal radio variability with the 8.4 GHz flux density is seen, consistent with being constant.

2.3.2.2 Radio/X-ray correlation

The relationship between the radio and X-ray fluxes in the B configuration is shown in Figure 2.9, again displaying both the smoothed and unsmoothed X-ray fluxes. The hint of a positive X-ray/radio correlation seen in the A configuration observations is not seen here. For the top panel, where the X-ray fluxes are not smoothed, the pearson rank correlation coefficient value, r is -0.13, suggesting that the weak to moderate correlation which exists for A configuration does not exist in B configuration. With the possible exception of the highest X-ray flux point, there is no sign of any variation of the radio flux despite considerable variation in the X-ray flux. Unfortunately the highest X-ray flux point is derived from the largest extrapolation of fluxes as the RXTE observation closest to that time had zero useful exposure. This meant extrapolating between two observations which were 4 days apart.

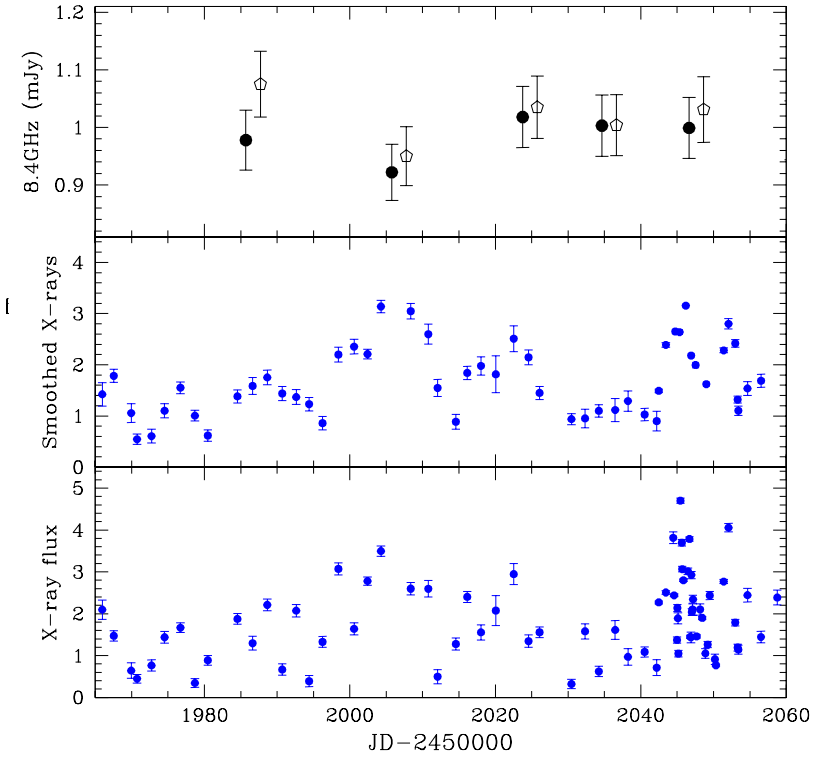

Figure 2.8: B configuration maps at 8.4 GHz made with the default/unfixed restoring beam and fixed beam. Plotted in the top panel are the peak core flux densities at 8.4 GHz derived from B configuration maps made with the default/unfixed restoring beam (open pentagons) and fixed beam (filled circles). Note, the unfixed beam points have been increased by 2 days, to stop overlap and make them easier to see. These are plotted against the unsmoothed and smoothed X-ray flux values for the period of the B configuration observations in the second and third panel respectively.

2.3.3 All configurations

Although the errors increase, it is possible to measure peak and integrated flux densities for the C and D array configurations. Figure 2.10 plots the resultant 8.4 GHz flux densities for all configurations together with the observed, and slightly smoothed, X-ray fluxes. Within the individual array configurations there is no evidence of strong variability although, over months timescales, it appears visually as if there is a strong correlation between the radio and X-ray fluxes.

Unfortunately, by chance, the period of the lowest X-ray flux occurs during the high resolution A configuration observations (which have the lowest signal to noise ratio (SNR) for the core region) and the period of largest X-ray flux occurs during the period of the lowest resolution D configuration observations (which have the

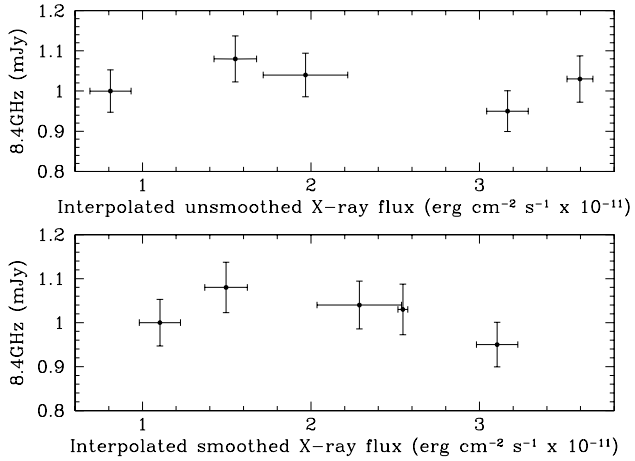

Figure 2.9: As in Figure 2.5 the peak radio flux densities of the core at 8.4 GHz derived from maps made with the **default beam** are plotted against the observed X-ray fluxes, however; in this case I plot B configuration points, as opposed to A configuration. The top panel shows the peak radio flux in B configuration at 8.4 GHz derived from maps made with the default restoring beam plotted against the observed X-ray fluxes. For the top panel the Pearson rank correlation coefficient value, r is -0.13, suggesting that the weak to moderate correlation which exists for A configuration does not exist in B. In the bottom panel the X-ray fluxes has been slightly smoothed.

highest SNR in the core region). Note however, that in Figure 2.10 the observed radio flux densities are plotted without any removal of the contributions to the core flux density from extended emission. The nuclear radio flux will be most contaminated by extended emission during the D configuration observations, it is probable that at least part of the apparent correlation between the radio and X-ray fluxes is actually a consequence of the changing array configuration. In order to properly compare the radio and X-ray variability one must therefore remove contribution from the extended radio flux from the measurement of the core flux, as is described in Section 2.4.

2.4 Comparing radio fluxes between arrays

The procedure for removing the contribution to the core flux density from extended emission is carried out in stages, offsetting by one array configuration change at a time. For example, in offsetting from B configuration to A configuration I first determine, from real observations with B configuration, what the typical beam shape and size is in B configuration. I then take the A configuration observations and taper the *uv* datasets, using UVRANGE within IMAGR, so that the beam sizes are the

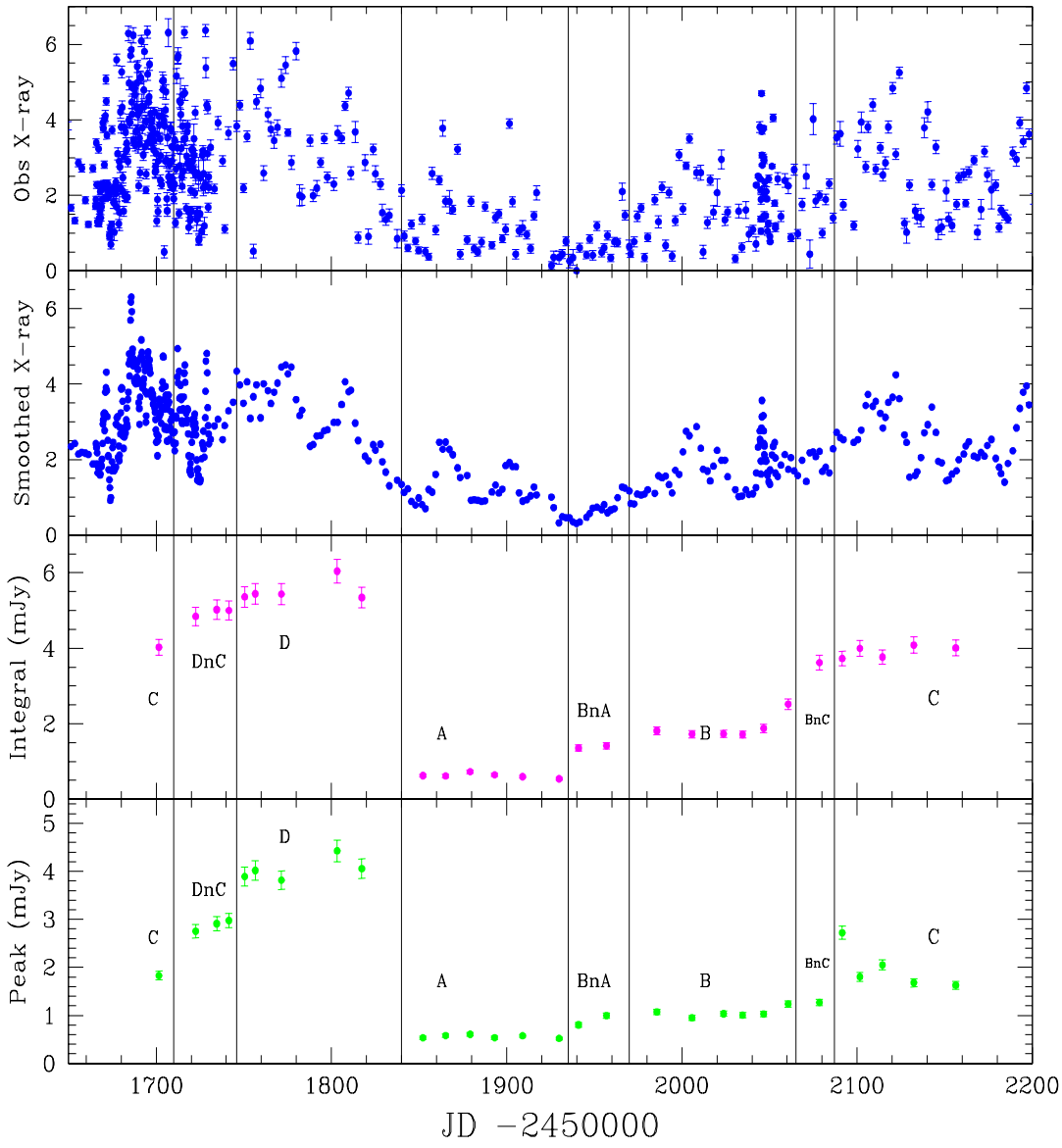

Figure 2.10: RXTE lightcurves and integral and peak flux density lightcurves at 8.4 GHz. Top panel: Directly observed X-ray fluxes $\times 10^{-11}$erg cm^{-2}s^{-1}. Second panel: X-ray flux $\times 10^{-11}$erg cm^{-2}s^{-1} smoothed with a 4 point boxcar. Third panel: Integral flux densities at 8.4 GHz labelled with VLA array configuration. Fourth (Bottom) panel - peak flux densities at 8.4 GHz labelled with VLA array configuration. The apparent variability in the radio flux densities is largely due to the changing array configuration of the VLA every $\sim$ 100 days.

same as they would be in B configuration. I refer to the resulting map as a pseudo B configuration map. I then measure both the peak and integral flux densities in the pseudo B configuration map and determine the differences, or offsets, between values measured from the original, untapered, A configuration map. I repeat the process for all of the A configuration datasets and determine the average offsets to the B configuration, and an rms error thereon, for the peak and integral flux densities.

To offset the real observed B configuration observations to an A configuration observation I remove the average offset derived above for each of the observed B configuration flux densities and combine the rms error on the offset with the observational errors (from Gaussian fitting in JMFIT and from the standard 5% error on flux) on the B configuration flux densities in quadrature.

I performed this offset method on the other configurations to get average offset values for D to C, and C to B. Combining these offsets with the offset from B to A allows one to offset all data to A array configuration flux values. For example, the average peak flux density offset in going from A to B configuration is 0.32 ± 0.07 mJy and in going from C to D configuration it is 2.31 ± 0.21 mJy. In offsetting over more than one array configuration change I combine the offsets linearly and the errors in quadrature. Thus these average offset values were used to offset all flux density values to those of an equivalent A configuration observation. The resultant offset peak and integral flux density lightcurves for both data sets are shown in Figure 2.11. In the intermediate configurations such as BnC there are few epochs of observation, and the configuration is slightly different in all of them. It is therefore very difficult to estimate the offset here. These observations give rise to the more deviant peak flux densities. However, even including these points with the single configuration gives peak flux densities consistent with being constant, as long as one assumes the more realistic larger error. For the integral flux densities, although the variations are now considerably reduced, there is still some residual variability, which follows the X-ray variability. I note, however, that the changes still mainly follow the changing array configurations. Within all configurations apart from the A configuration, there is no evidence for variability so one must be wary of an error in the offsetting procedure for integral flux densities. In Section 2.5 I simulate the offset method for integral flux densities to determine the accuracy of the offsetting method.

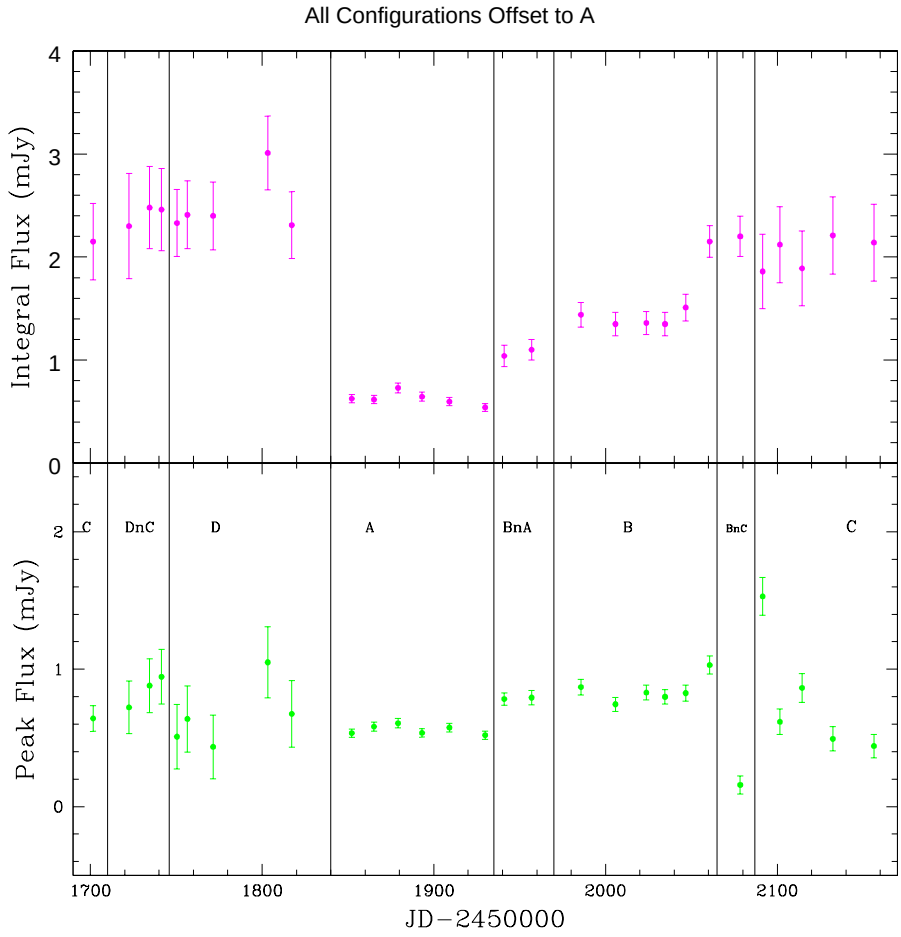

Figure 2.11: Peak and integral flux densities offset to A configuration. Core integral flux density (top panel) and peak flux density (bottom panel) at 8.4 GHz. Flux densities for all observations are offset from their original configuration (see labelling in bottom panel) to A array configuration. The peak flux density is consistent with being constant.

2.5 Simulating the Offset Method

The first step in simulating the offset method was to make a model of the source. Although it is preferable that the model resembles the real source, it is not essential that it is identical to the real source as the aim of the simulations is only to test the offsetting method and could, in principle, be carried out on any extended source.

To make the model all the *uv* data sets from the A, B, C & D configurations were combined into one *uv* data set which was imaged (Figure 2.12). The 28 clean components from this combined image which best represented the structure of the AGN were then selected. Using the task UVSUB I added the model contribution from these components to the residual *uv* data sets produced by IMAGR during the

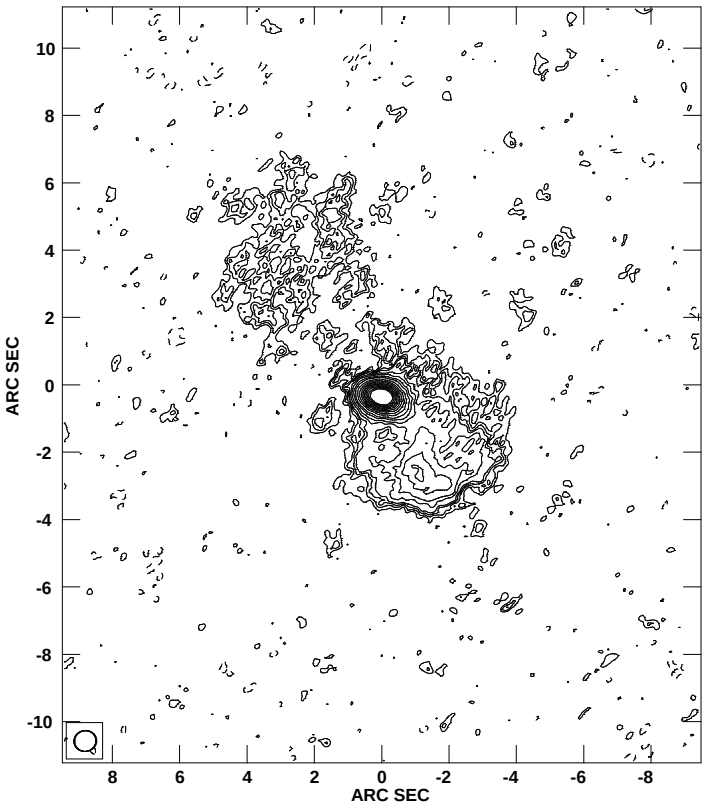

Figure 2.12: 8.4 GHz image from combining *uv* data from the 4 main VLA arrays. *uv* data from all single arrays were combined at 8.4 GHz and restored with a typical B configuration beam (0.65" × 0.60"). The rms noise level is 0.11 Jy/beam and contours are at the following multiples of the rms noise level -2, 2, 3, 4, 5, 6, 7, 8, 9, 12, 15, 20, 25, 30, 35, 40, 45, 50, 55, 60.

original imaging of the 22 observations in each of the 4 singular array configurations (A, B, C & D). The resultant data sets represent how the actual observational setups would have seen this model of NGC 4051. I then repeated the offsetting procedure, which was described in Section 2.4, for the real data, on the simulated data, to produce a simulated integrated flux density offset to the A configuration. This procedure should result in a constant flux density level equal to the model A configuration values. The actual simulated offset lightcurve is shown in Figure 2.13. The dotted horizontal line in Figure 2.13 represents the expected A array integral flux density value. From this figure one can see that the B configuration data are at the same level as the A configuration data but the C and D configuration data are too high by about 0.5-0.6 mJy, which represents an approximate systematic error in the process of offsetting the integral C and D configuration flux densities. If this systematic error is subtracted from the original offset integral flux densities (Figure 2.11), then most of the apparent long term variation is removed from the integral flux den-

sities. It is unfortunate that the array configuration changes follow the approximate changes in long term X-ray flux, and hence that the very small residual variation in the integral flux densities appears to follow the X-ray flux. Given the particular difficulties of measuring the integral flux densities it cannot be proven that these flux measurements represent the intrinsic core flux, as the integral intensity values closely follow the array configurations changes and the long term variability is not seen in the peak flux densities values.

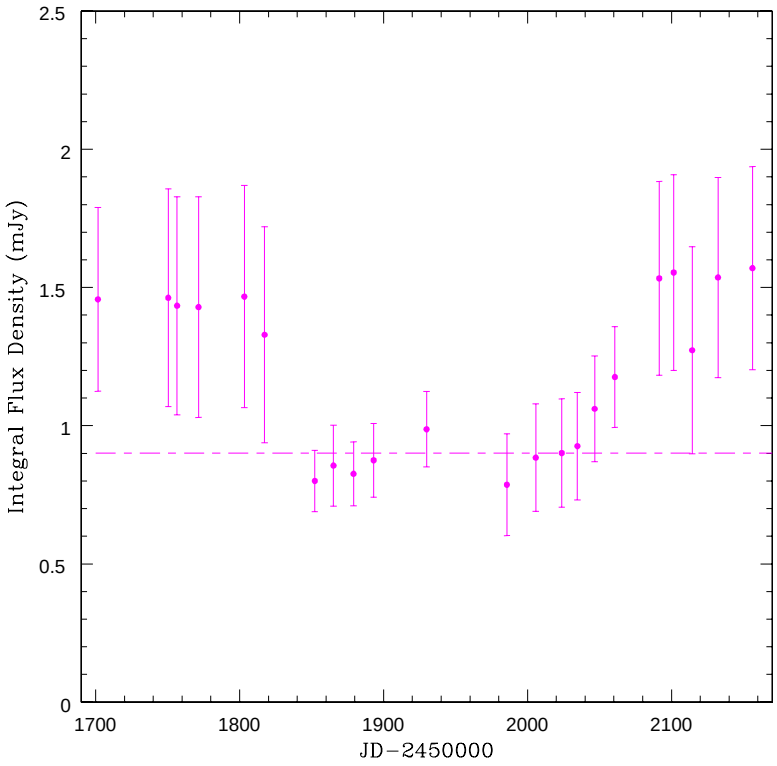

Figure 2.13: Integral flux densities for the simulated model NGC 4051 data, offset to A array. Here the mean A configuration model value is 0.9 mJy (shown by the dotted line). In offsetting from array to array, offsetting errors are added in quadrature to the JMFIT error and the 5% error on the flux. It is noted that the B configuration model data, when offset to A are at the expected A array flux values, but the mean C and D configuration data differ, on average, from the expected offset value by ~ 0.5 mJy.

2.6 Discussion

2.6.1 Radio variability

The radio and X-ray variability of the probable soft state Seyfert galaxy NGC 4051 was monitored over a period of 16 months with observations approximately every 2 weeks. I have carefully subtracted the contributions to the core flux density from the differing amounts of extended flux density which will be detected in the different restoring beams in the different VLA configurations. A lightcurve was produced equivalent to those which would have been produced by observations within A configuration. The core peak flux density, which in this context is the best measurement of true core radio luminosity, is consistent with being constant.

Within the A configuration, which is the only configuration within which the core is resolved from close neighbouring components to the east and west, there is a hint of correlated X-ray and radio variability, with radio (and X-ray) spectral variations approximately following the flux variations. Although the X-ray flux varies by factors of a few, the maximum radio variations are, at most, 25% between observations separated by ~ 2 weeks. The amplitude of variability is, at most, 0.12 mJy. Whilst the percentage changes, timescales of change, and spectral hardening during a rise are entirely consistent with the observations of radio variability of another similar Seyfert galaxy, NGC 5548 (Wrobel, 2000). NGC 5548 has a SNR approximately ten times greater than NGC 4051 and so there is no doubt about the credibility of its radio variability. Unfortunately for NGC 4051, the credibility of the variability depends strongly on the error associated with each measurement. Taking the larger of the errors which could be associated with the radio measurements (discussed in Section 2.3.1.1) the radio lightcurve would be consistent with being constant. Thus, overall I conclude that there is no strong evidence for any large amplitude variability in the core radio flux of NGC 4051 at 8.4 GHz over the course of a year but one cannot absolutely rule out very low amplitude (~ 0.1 mJy) variability correlated with the X-ray variability.

2.6.2 Implications for emission models

In Figure 2.14 I plot values of the averaged radio luminosity and the average X-ray luminosity on the so-called 'fundamental plane' of black hole accretion activity (Merloni *et al.*, 2003; Falcke *et al.*, 2004). This plane relates the X-ray and radio luminosities to the mass of the black hole, in order to plot NGC 4051 onto the plane I have a assumed black hole mass of $1.91 \times 10^6 M_{\odot}$ (Peterson *et al.*, 2004). The

version plotted of the plane uses only 'hard state' black holes from the sample of Körding *et al.* (2006a). I note that NGC 4051, which is almost certainly a 'soft state' object, lies a factor of 3 below (in the sense of being more radio quiet) the best-fit relationship defined by the hard state objects, although it is just about within the scatter of the relationship. 'Hard state' objects, however, typically show much more radio variability than NGC 4051 and are typically described by $L_R \propto L_X^{\beta}$ where $\beta \sim 0.7$ for variations in individual objects (Corbel *et al.*, 2003; Gallo *et al.*, 2003, 2006).

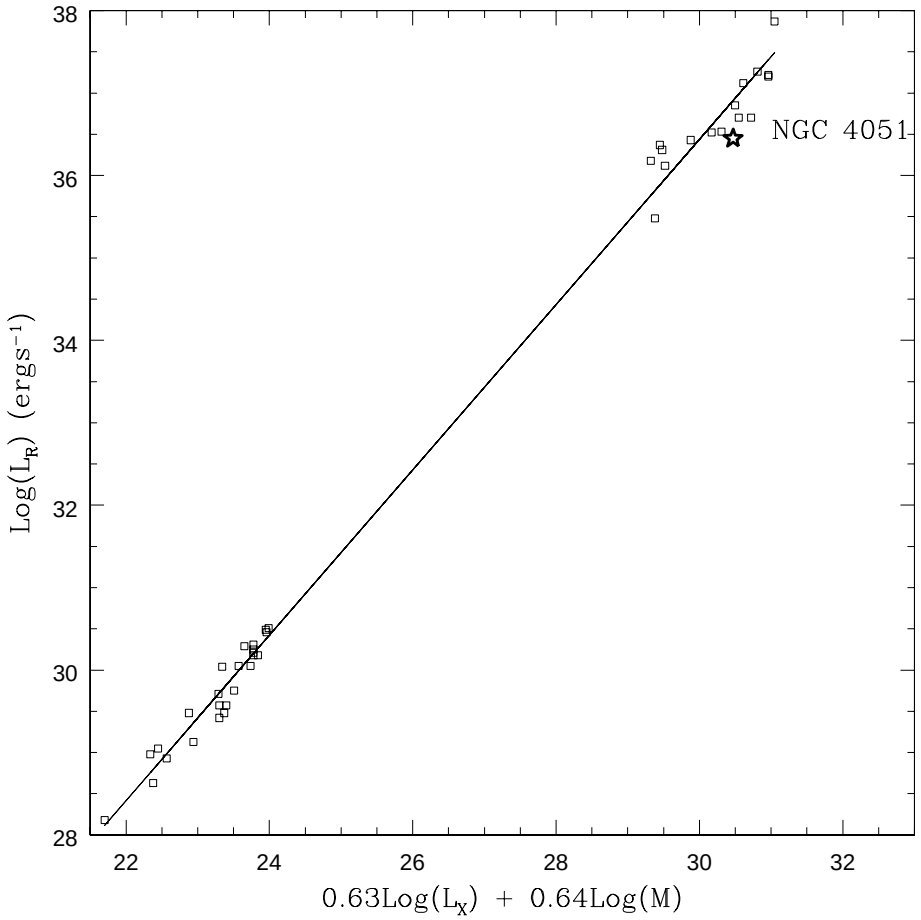

Figure 2.14: The radio/X-ray/black hole mass 'fundamental plane' for hard state accreting black holes (i.e. hard state X-ray binary systems and LINERS) using the data from the Körding *et al.* (2006a) sample. NGC 4051 is the large black star, and is labelled.

For the LINER NGC 7213 Bell *et al.* (2011) find a significant correlation between X-ray and radio emission with factors of ~ 3 or more variability in both bands. Given its very low accretion rate, NGC 7213 is thought to be a 'hard state'

system so correlated radio/X-ray variability is expected. However although Wrobel (2000) has demonstrated radio variability in the Seyfert galaxy NGC 5548, which has an accretion rate not far below that of NGC 4051 and so is probably also a 'soft state' system, there have been no previous studies of correlated X-ray/radio variability in similar Seyfert galaxies. The X-ray/radio relationship has, however, been investigated for samples of objects. Panessa *et al.* (2007) find $\beta = 0.97$ at 4.8 GHz and $\beta = 0.98 - 1.25$ at 15GHz for a sample of Seyfert galaxies. For a sample of ROSAT-selected AGN, and using 1.4 GHz radio observations, Brinkmann *et al.* (2000) find $\beta = 0.48 \pm 0.049$ for radio quiet objects, similar to Seyferts, and $\beta = 1.012 \pm 0.083$ for radio loud objects; however, no mass correction was carried out on these objects .

Although there is a wide range in the reported values of β, there is evidence for radio/X-ray correlation within samples of Seyferts and radio quiet AGN. Considering the radio/X-ray data for the only well studied 'soft state' Seyfert so far (NGC 4051) , there is no evidence for a value of β much above 0.1 (see Section 3.4 for further work on this).

One possibility is that even in the VLA A configuration 8.4 GHz maps, the core still contains substantial contribution from emission which is extended but on scales below that detectable with the VLA. I note that with a beam of ~ 8 mas, Giroletti and Panessa (2009) find an unresolved source with 5 GHz flux density of 0.20 ± 0.02 mJy, which is substantially less than the average 4.8 GHz measurement of ~ 0.6 mJy presented in this work. The tentative observations of ~ 0.1 mJy variability would then provide a value of β consistent with the values derived from observations of samples of similar sources, although NGC 4051 would then be even more radio quiet compared to the hard state objects which define the fundamental plane.

The VLBI observations show structure which is strongly indicative of a collimated jet (Giroletti and Panessa, 2009; M^{c}Hardy, 2005). In Section 4 I present high resolution global VLBI observations which confirm this structure. At first sight the lack of radio variability is surprising. However if the jet is in the plane of the sky, rather than pointing at the observer as in blazars, radio variability would be slower. Falcke *et al.* (2001b) speculate similarly regarding the lack of strong radio variability in radio-loud quasars although they do not reach any firm conclusions.

Another alternative idea is that the radio emission in Seyfert galaxies does not come from a jet, as in hard state sources, but arises in the outer parts of the X-ray emitting corona (Laor and Behar, 2008). In Figure 2.15 I plot current data onto Figure 2 from Laor and Behar (2008) and see that NGC 4051 agrees reasonably with

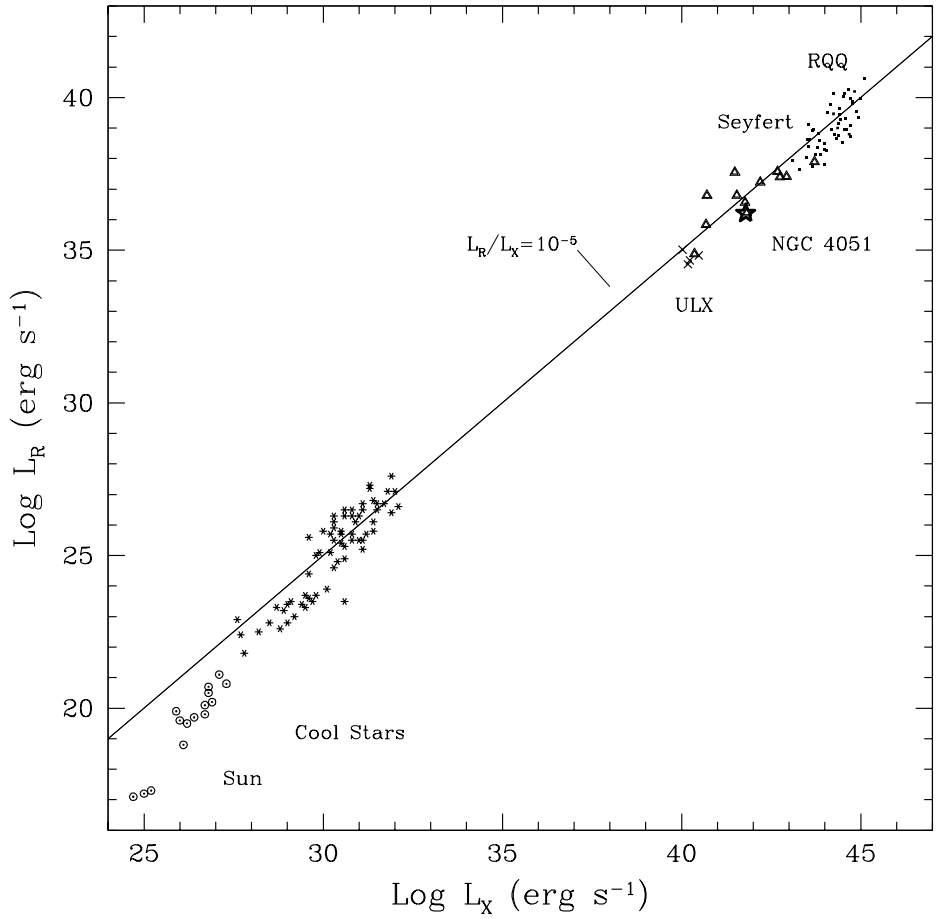

Figure 2.15: Mean values of X-ray and peak radio luminosity with NGC 4051 (large 5-pointed star) superposed. The solid line is the G*ü*del-Benz relation, i.e. $L_R/L_X = 10^{-5}$, for coronally active stars (Gudel and Benz, 1993). *Figure from Laor and Behar (2008).*

the Güdel-Benz 1993 relationship for coronally active stars, $L_R/L_X = 10^{-5}$. The fact that this model for coronally active stars fits the data from Radio Quiet Quasars (RQQs), Seyfert AGN and ULXs may imply that the AGN corona are also magnetically heated. The radio emission is then a result of this coronal activity. In the coronal model, rapid large amplitude radio variability is not expected at frequencies where the source is optically thick. This situation is approximately the case during our A configuration observations which indicate a spectral index of $\alpha \sim -0.3$. Such variability is, indeed, not seen. Similar considerations would, of course, also apply to some extent to a side-on jet and the highly collimated co-linear structure of the compact VLBI components is a significant problem for the coronal model. As jets are generally agreed to arise from the corona, the truth may lie part way between

the pure coronal and pure jet models. In this galaxy where an outflow of large solid angle is seen in [OIII] observations (Christopoulou *et al.*, 1997), the compact radio components separated from the nucleus may arise from a central, higher velocity region within the overall outflow. The core radio emission may arise from a combination of a jet and a corona. If there is any long term correlated variation between the radio and X-ray bands, they may simply reflect long term changes in accretion rate, upon which both bands depend, rather than a direct link between the emission processes. In order to further investigate the physics of the emission processes in this AGN I discuss the radio and X-ray variability of more recent data in Chapter 3.

2.7 Conclusions

Despite X-ray variability of factors of 10, no clear evidence for variability of the core is detected in NGC 4051 at 8.4 GHz over the whole 2000-2001 lightcurve with the possible exception of very low amplitude (~ 0.12 mJy) variations during the A configuration observations, where the core is best resolved from surrounding structures. The VLA A configuration observations reveal a spectral index $\alpha \sim -0.3$ for the core of NGC 4051. This relatively flat spectrum suggests that the core represents a self absorbed jet.

The tentative radio variations correlate weakly with the much larger amplitude X-ray variations and the radio (and X-ray) spectral variations approximately follow the observed flux variations. However, there is no evidence for a β value (from the $L_R \propto L_X^{\beta}$ relation) much greater than ~ 0.1. The resultant radio and mean X-ray luminosity make NGC 4051 a factor of ~ 3 radio quieter than the hard state objects which define the 'fundamental plane' for hard state accreting black holes, although the scatter about the plane is of the same order. Given the collimated VLBI structure which hints at the presence of an unseen jet, the lack of radio variability is, at first sight, surprising, although a side-on jet, particularly if it is observed at a frequency where it is optically thick, would not vary as rapidly as a face-on blazar jet.

A coronal model agrees well with the radio/X-ray flux ratio, and the lack of radio variability, but the collimated radio structure is then hard to explain. A mixture of jet and coronal emission may explain the observations but further, more sensitive, radio observations, with high angular resolution and a fixed beam shape, are required to confirm whether the radio emission from NGC 4051 does indeed vary. The possibility of a jet in NGC 4051 is discussed further in the following chapters.

Not even the darkness surrounding the vast cosmic web can
extinguish the light from a single candle.

MAM

3

A distinct disc jet coupling in NGC 4051?

A paper on the work in this chapter is in preparation.

In this chapter I discuss the possible disc-jet coupling in the AGN NGC 4051. A few days after the work described in Chapter 2 was accepted to Monthly Notices of the Royal Astronomical Society, work on the same subject was accepted by the Astronomical Journal. The work by King *et al.* (2011) is titled 'A distinctive disc-jet coupling in the Seyfert-1 Active Galactic Nucleus NGC 4051' and claims that there is an anti correlation between the X-ray and radio core flux variations of NGC 4051. In this chapter I discuss my own reduction of archival VLA 8.4 GHz data which they used/analysed, along with quasi-simultaneous *Chandra* data. I also compare this re analysed radio data to RXTE X-ray data, which is available as part of the long term monitoring of this Seyfert AGN. The radio/X-ray correlation presented in Chapter 2 (for the 2000-2001 VLA data) is also re-investigated here in order to present a strong counter argument to the distinctive disc-jet coupling result claimed by King *et al.* (2011).

3.1 Introduction

3.1.1 Results presented by King *et al.* (2011)

The X-ray and radio lightcurves from data presented in King *et al.* (2011) (hereafter referred to as K11) are shown in Figure 3.1. Their lightcurves consist of eight *Chandra* X-ray observations and six VLA/EVLA radio observations of Seyfert 1 AGN NGC 4051 taken over a seven month period. Measurements in the X-ray and radio bands were carried out every two to four weeks. See Table 3.1 for observational details. The radio flux density lightcurve presented by K11, shown in Figure 3.1, varies by more than a factor of three. Note that both the integral flux and peak flux density values are presented in work by K11, but only the integral flux is used in comparison with the X-ray light curve to determine the disc to jet coupling. I propose, from the analysis described in Chapter 2, that the peak flux density is a better estimate of the flux density of radio core emission from NGC 4051 than the integral flux density.

For the X-ray light curve the second and fourth data points shown in Figure 3.1 were not used in their analysis because no 'simultaneous' radio data existed for these X-ray points. The X-ray light curve shows variability by a factor of 3. The anti-correlation between the two regimes presented in the work by K11 is shown in Figure 3.2. Here the dashed line shows a fit to their data with $\beta = -0.72 \pm 0.04$ where β is the gradient in the relationship $Log(L_{Radio}) = \beta Log(L_{X-ray}) + c$ (also referred to as the $L_R \propto L_X^{\beta}$ relationship). Another fit to the graph in Figure 3.2 is shown by the dotted line which excludes the A configuration data point. This is described by a weaker negative correlation with $\beta = -0.12 \pm 0.05$. The reason given by King *et al.* (2011) for producing a fit which excludes the A configuration data point is that this extended configuration has resolved out a substantial amount of flux in this high resolution image, which makes the flux value for this point inaccurately low. However, from the analysis described in Chapter 2, I show that the opposite view is correct; that the measurement of the extended emission is prone to far greater uncertainty than measurement of the core flux. I confirm this view with regard to the 1991 and 2008-2009 data sets later in Section 3.3.

In order to investigate if there is a time delay between the radio and X-ray emission, K11 calculate the discrete cross correlation function (DCCF) for the radio and X-ray data, shown in Figure 3.3. After linearly interpolating the data every 17 days (which corresponded to the shortest time between two of the *Chandra* X-ray observations) they calculate a DCCF with a minimum of -0.48 ± 0.1 at a time lag

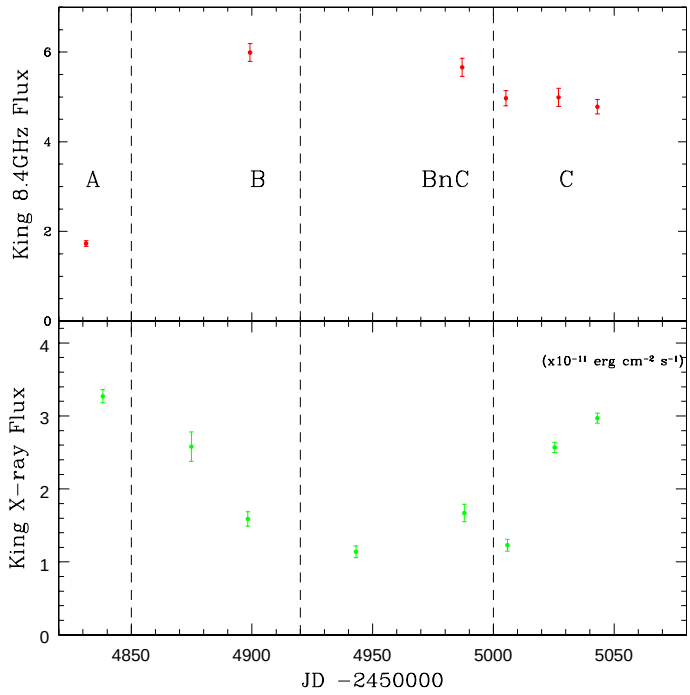

Figure 3.1: Radio and X-ray lightcurves from King *et al.* (2011). Top panel: The six integral flux density at 8.4 GHz values from K11. Bottom Panel: The eight *Chandra* X-ray points from K11. The array configurations for each epoch is labelled. The X-ray data was integrated over 2-10 keV with units of 10^{-11} $erg\ cm^{-2}\ s^{-1}$ and radio flux density measurements are in units of mJy. These radio and X-ray lightcurves are used by K11 to determine the inverse correlation shown in Figure 3.2.

of -2.5 ± 5.3 days, which they suggest indicates that X-ray dips are leading radio flares. Based on this time lag value at -2.5days $\approx 0.5\sigma$ which is much less than the bin size used (17 days) I argue that the DCCF actually shows that X-ray and radio emission are constant in time.

3.1.2 Distinct disc-jet coupling?

For 'soft state' AGN (like NGC 4051) the radio/X-ray luminosity relationship is unknown. Nevertheless, one would expect that different investigations of the same source should give similar results for the $L_R \propto L_X^{\beta}$ relationship. From my own analysis in Chapter 2, I calculate a very weak positive correlation with a slope of $\beta \sim 0.1$; however, as summarised in Section 3.1.1, K11 calculate an anti-correlation where $\beta = -0.72 \pm 0.04$ (or $\beta = -0.12 \pm 0.05$ if the A configuration point is excluded). In an effort to determine a reason for the opposing results of the two studies, I

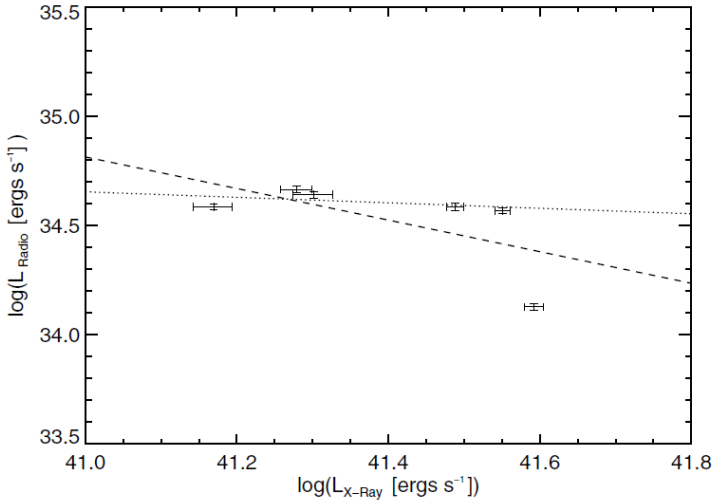

Figure 3.2: Figure from King *et al.* (2011) showing the inverse correlation between the X-ray and radio regimes. The dashed line is a fit to the relationship $L_{Radio} \propto L_{X-ray}^{\beta}$ with $\beta = -0.72 \pm 0.04$. The dotted line excludes the A configuration data point (point with the lowest L_{Radio} measurement), and is described by $\beta = -0.12 \pm 0.05$.

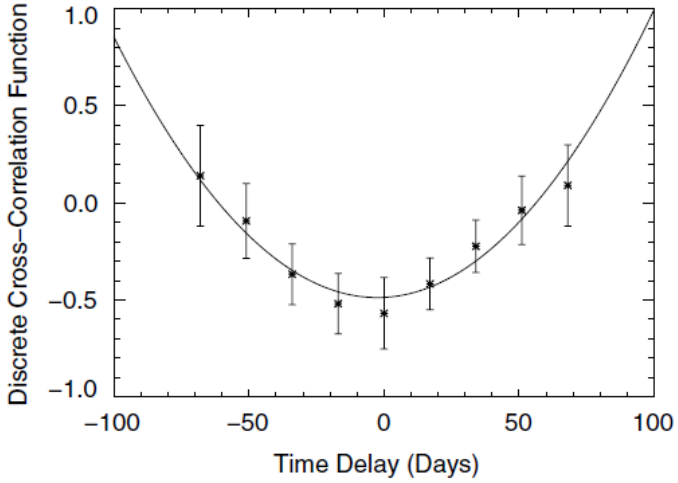

Figure 3.3: Figure from King *et al.* (2011) showing their DCCF of interpolated X-ray and radio luminosities. DCCF has a minimum of -0.48 ± 0.1 at -2.5 ± 5.3 days, which suggests that X-ray dips are leading radio flares.

have reduced the VLA/EVLA radio data from the VLA archive, which was initially observed and reduced by K11, and examined RXTE data from this epoch. I then compare findings from my own method of reduction, imaging and data analysis (discussed in Chapter 2) to the method of K11 in order to determine if radio/X-ray emission is correlated.

It is important to note here that for both studies the accuracy of the results is greatly affected by both extended emission, which contaminates the core flux, and by small number statistics; there are only 6 radio flux values for the epoch of the K11 data (the radio data, is referred to hereafter as the 2008-2009 dataset). As discussed in Chapter 2, determining an accurate radio luminosity measurement of a source that is contaminated by extended emission is complex. To determine the core flux density for a compact component which is almost resolved in the highest configuration (VLA A configuration), a box is drawn to encompass the core emission only (taking care to exclude as much of the extended emission as possible). Therefore, the radio variability can be assessed within A configuration by repeating this method for each dataset. For the 2008-2009 data, however, only one A configuration data point exists, so assessing the variability during the most accurate of the configurations is not possible. The alternative method is to offset the contributions from the extended emission using the 'offset method' as presented in Section 2.4. The caveat of the 'offset method' is that the core of NGC 4051 is not fully resolved, even during A configuration, which means the measured flux density value is increased by the diffuse extended flux. The use of the A configuration flux values as the best representation of the core flux are contrary to the work of K11 who suggest instead that during A configuration the VLA/EVLA is resolving out core flux, making the A configuration flux value measured inaccurately low. K11 make no attempt to subtract the flux contribution from the extended emission from the value of the core, and for all configurations observed they measure the integrated flux within an area restricted to approximately $8'' \times 6''$. This large area encloses all the diffuse extended emission in each of the maps. It is also worth nothing here that the measured radio flux density values are affected by the size of the beam used to CLEAN the images. This means that the error values presented in this re-investigation are likely to be a slight underestimate of the true total error.

3.1.3 Motivation

There are two motivating reasons for investigating the radio data, which span from 1991-2009, and X-ray data which span 2000-2009, for NGC 4051:

The first is to access the long time scale change in the nuclear core radio emission over more than 17 years of radio observations (1991-2009) at 8.4 GHz.

The second is to compare the radio/X-ray correlation findings, which are presented previously in Chapter 2 (for 2000-2001 data), to those findings of King *et al.* (2011) on the 2008-2009 data. From this comparison I aim to understand the physical coupling, if any, which exists between the radio and X-ray regimes. In this analysis I thoroughly investigate the method used by K11 and attempt to determine why they achieve a 'distinctive' anticorrelation while my own results for a similar investigation produce a weak positive correlation.

In the later part of this chapter I carry out cross correlation analysis of radio data and quasi simultaneous X-ray data (observed between the year 2000 and 2009). This analysis is used to determine the possible time delay between the different emission regions. These measured delays reveal information about the physical scales that exist for individual objects detailing how the signals propagate, for example, from the accretion flow to the jet. Variability studies between X-ray and optical report small lags between the regimes which are consistent with optical variations due to X-ray heating of the accretion disc (Breedt *et al.*, 2009, 2010). In the recent study by Bell *et al.* (2011) of LLAGN NGC 7213 cross-correlation functions revealed time lags between events in the radio and X-ray bands to be 24 ± 12 days (with the 8.4 GHz emission lagging X-ray emission). Cross correlation analysis of the Seyfert AGN NGC 4051 is carried out in Section 3.5 to determine the possible time lag between X-ray and radio emissions, if any, which exist. Measurement of an accurate lag value can give a handle on the scale of accretion onto the SMBH at the centre of NGC 4051 and reveal information on the scalability of accretion onto the SMBH, for example, as signals propagate from accretion flow to the jet.

This chapter represents the first study where quasi-simultaneous radio and X-ray observations exist over a timespan of ~ 2 years (455 days for 2000-2001 and 212 days for 2008-2009) for a study of a 'soft state' narrow line Seyfert 1 galaxy.

This Chapter is summarised out as follows:
In Section 3.2 the observations and data reduction are presented. In Section 3.3 the long term radio variability of the nucleus of NGC 4051 is investigated from 1991 through to 2009. In Section 3.3.2 the X-ray variability is investigated for both RXTE and *Chandra* data during 2008-2009. In Section 3.4 the radio/X-ray correlation is discussed for 2001-2002 and 2008-2009 and in Section 3.5 the cross correlation functions are analysed. The final Sections 3.6 and 3.7 I discuss the implications of these findings on the proposed 'distinct disc-jet coupling in NGC 4051' and the conclusions of this chapter respectively.

3.2 Observations and Data Reduction

3.2.1 Radio data

Three VLA data sets at 8.4 GHz are presented in this chapter. The first set of data is VLA archival data from 1991, and is referred to as the 1991 data set. The second set of data is presented in Chapter 2, and is referred to as the 2000-2001 data set. The third dataset is VLA/EVLA archival data which was presented in K11; this is referred to as the 2008-2009 data set. All datasets were reduced by the author. Note that for the 2000-2001 data set some 4.8 GHz data are also analysed in this chapter.

The 1991 data are used to investigate the long time scale variations of the nuclear flux in comparison with other A configuration data which exists during 2000-2001 and 2008-2009. The 1991 data were taken on 24th June and 1st September 1991. For each observation the total time on source was $\sim$ 14 minutes. The flux calibrator used was 1331+305 and the phase calibrator was 1146+399. The phase calibrator was observed in between each observation of NGC 4051, for $\sim$ 2 minutes on 3 occasions.

The 2000-2001 radio data is presented in Table 2.1 and was discussed previously in Section 2.2.

For the 2008-2009 dataset NGC 4051 was observed a total of 6 times between 31st December 2008 (JD 245 4831.3) and 31st July 2009 (JD 245 5043.1) with a typical interval between observations of 10 weeks (compared with every 2 weeks for 2000-2001 data presented previously). On each occasion the source was observed at 8.4 GHz only, with a total time on source, of $\sim$ 1 hour. One observation was in A configuration, one in B, one in BnC and three in C. Observations were carried out in 2IF mode with 50 MHz bandwidth at both frequencies. During the observations the antennae switch from the source to the phase calibrator (12214+44114) every 3.33 minutes. The flux calibrator used was 3C286 (1331+305) which was observed for 3.33 minutes of integration time at the end of each observation. For more information on 2008-2009 observations see Table 3.1.

3.2.2 Radio data reduction

Both the 1991 and 2008-2009 VLA archive radio data were re-reduced in AIPS by the author. The same method was used in the reduction and imaging of the these two datasets as is described for the 2000-2001 dataset in Section 2.2.2 which ensured consistency with my own work. None of the results presented in this Chapter are taken from the literature, all data has been re-reduced.

Table 3.1: Observational details of VLA 2008-2009 data at 8.4 GHz.

Date JD-2450000	Configuration	Time on Source (s)
4831.814	A	1820
4899.672	B	1783
4987.576	BnC	1873
5005.693	C	1890
5027.500	C	1230
5043.589	C	1883

The more recent 2008-2009 data contains a number of upgraded Expanded Very Large Array (EVLA) antennae. The task VLANT was used (in AIPS) to correct the antennae positions of those antennae which have been upgraded to EVLA. The task BLCAL was also used to compute the closure offset corrections for the new EVLA antennae.

3.2.2.1 RXTE Data

NGC 4051 is part of a long term AGN X-ray monitoring program using RXTE which started in 1996. The data used here were reduced and fit by Phil Uttley and a brief explanation of the X-ray reduction techniques is given in 2.2.1, further description is presented in McHardy *et al.* (2004). The RXTE data, observed to coincide with the 2000-2001 radio data were discussed previously in Section 2.2.1. The RXTE data from 2008-2009 (from 31st December 2008 (JD 245 4831.3) to 31st July 2009 (JD 245 5043.1)) were also chosen to coincide with the 8.4 GHz (2008-2009 data) VLA archive data from this epoch. The unsmoothed, observed RXTE data are presented here, where observations occur every 2 days with a typical duration of 1 ks, along with a smoothed version of the data which uses a running Gaussian with a half width of 2 days, to remove high frequency variability. In order to directly compare the X-ray and radio lightcurves, the X-ray lightcurve was linearly interpolated to the radio dates to achieve a set of quasi- simultaneous data. For further details of the X-ray data and the interpolation see Table 3.2.

3.2.2.2 Chandra Data

Eight *Chandra* X-ray points are presented, all taken directly from the quoted values in the work by K11. The observations were taken between 1st January 2009 (JD 245 4848.2) and 31st July 2009 (JD 245 5043.1) with $\sim$ 10 ks exposure time for

each observation. Continuous clocking mode was used to avoid photon pile up and the total flux associated with each observation was deduced from the power-law component fit within the energy range of 2-10 keV (as with the RXTE data). Further information on the X-ray reduction techniques are given in K11.

3.3 Variability of the Nucleus

3.3.1 Radio variability between 1991 and 2008

3.3.1.1 During A configuration

For the purpose of investigating the variability of the core of NGC 4051 the A configuration data provides the best measure of core flux because at the highest VLA resolution the core region is almost resolved from the extended features i.e. it suffers the least from contamination by extended emission compared to B, C and D configurations. The 2008 A configuration map from JD 2454831.3 (31st December 2008) has a peak flux density (calculated from fitting a Gaussian in the task JMFIT) of (6.07$\pm$0.32) $\times 10^{-4}$ Jy/beam. The map made from observations on 24th June 1991 has a nuclear peak flux density value of (4.98$\pm$0.22) $\times 10^{-4}$ Jy/beam. Both 1991 maps were made with the same size restoring beam, $0.24'' \times 0.19''$ with PA 137 degrees, using COWINDOW box size 7×7 pixels. This beam size is consistent with the fixed beam size used to make the 2000-2001 maps on which the analysis in Chapter 2 is based (the flux density values for 2000-2001 are shown in Table 2.2).

Figure 3.4 shows the variability of the nuclear core during the A configuration for the 1991, 2000-2001 and 2008 data from images made with both fixed beam size and default beam size respectively. With this graph I aim to determine if variation in core flux at 8.4 GHz is observed over the $\sim$ 17.8 year time period. In Figure 3.4 the red points represent fluxes from maps made with a default beam size, and the blue points represent imaging with a fixed beam size $0.24'' \times 0.19''$ with PA 137 degrees. In both maps the flux was deduced from the same box size chosen to enclose all core flux.

In order to establish the 8.4 GHz core flux variability on long timescales (over the $\sim$ 17.8 year time period) I assumed a simple straight line trend by fitting a least square fit. For a least squares fit to the fixed beam core peak flux over the 1991-2008 epoch the gradient is $(2.18 \pm 0.67) \times 10^{-8}$ Jy/day with a reduced $\chi^2 = 2.15$, a fit to a model with a zero gradient at the mean value gives a reduced $\chi^2 = 3.09$. The fit to the default beam data over time is $(2.12 \pm 0.72) \times^{-8}$ Jy/day with a reduced

$\chi^2 = 3.42$, a fit to a model with a zero gradient at the mean value gives a reduced $\chi^2 = 4.49$. These results reveal that there is no statistically significant variation in core flux between 1991 and 2008 between the nine A configuration points; however, a flux increase in time is more statistically likely than a constant model. For images made with a fixed beam the variation in peak flux is equivalent to 0.26 ± 0.16 mJy in 1991-2008, with the caveat that the actual variation in core flux over this time period is unlikely to be a simple straight line trend. Overall the difference between the flux values for the fixed and default beams is not significant, and the strongest variations detected generally occur at the same in both lightcurves (see Figure 3.4). It is worth mentioning here that the errors presented are likely underestimated due to the fact that contamination from extended features can effect the measurement of the core radio flux.

In an effort to investigate the shorter timescale variations, specifically during the period of the 2008-2009 K11 data, one can attempt to remove the extended diffuse radio emission, shown in Figure 3.5 in the same way as is described in Section 2.4 (for the configurations with a lower resolution than the A configuration) using the 'offset method'. The 'offset method' provides a more accurate measure of the core flux because it is designed to 'resolve out' larger scale emission, giving the best measure of the core flux only. The extra flux contributions from diffuse extended emission increase the value of the core flux at lower resolutions, with the extent of contamination being greater the lower the resolution of the VLA array. The main focus of the following sections is to offset the six 2008-2009 radio flux values to an A configuration flux value. The resulting A configuration radio lightcurve is then compared to the quasi-simultaneous RXTE 2-10 keV data which exists for the 2008-2009 data set. Work by K11 uses the sparsely sampled *Chandra* lightcurve. In this analysis I present the well sampled RXTE lightcurve in addition to the *Chandra* X-ray data values from K11. The radio and X-ray variability of the 2000-2001 data which were discussed in Chapter 2 is also re-investigated here in comparison with the radio and X-ray variability results from the 2008-2009 data set to assess the long term radio/X-ray variability.

3.3.1.2 Radio variability during 2008-2009

Figure 3.5 shows maps reduced by the author of radio emission from NGC 4051 during B and C configurations. Both maps are centred on the nucleus with North up and East to the left. The extended flux is clearly visible in both maps: In the B configuration map, on the left (beam size $0.66''$) the extended flux is seen to the

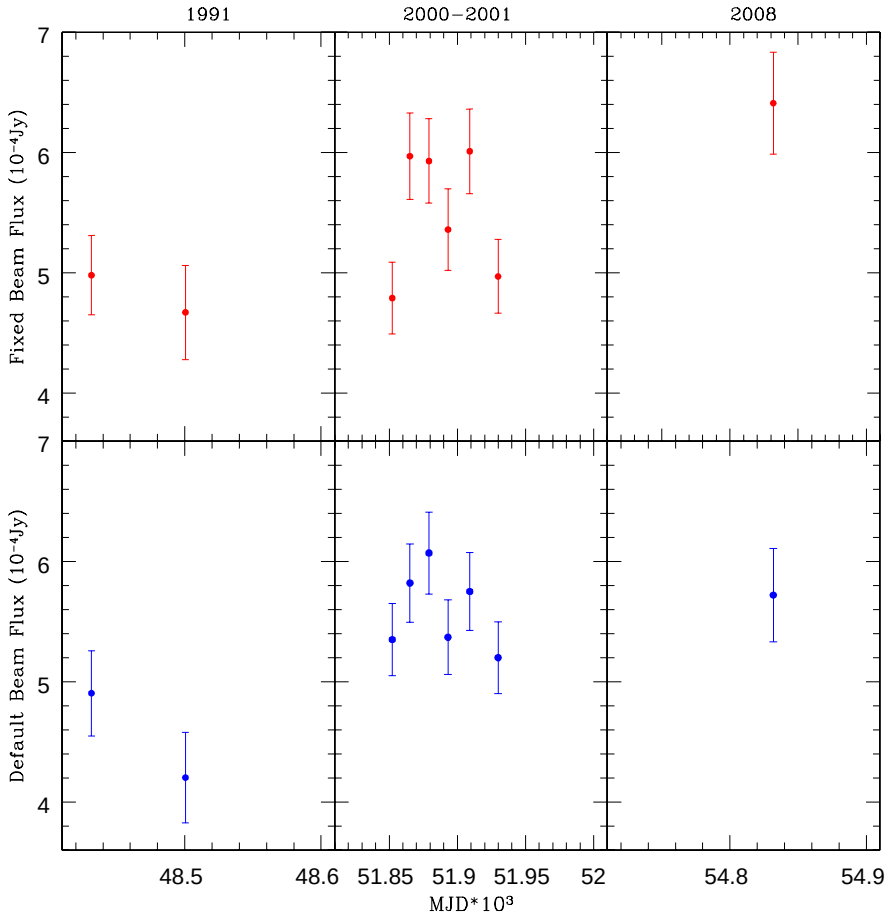

Figure 3.4: A configuration radio peak flux values for 1991, 2000-2001 & 2008 data (panels from left to right). The top panels with red points represent flux values with images made from the **default beam** size within IMAGR. The bottom panels with blue points represent flux density values with a **fixed beam** size ($0.24'' \times 0.19''$ with PA 137 degrees). The time axis is to scale within each panel, but date gaps exist between each of datasets/panels. For a least squares fit to the fixed beam core peak flux over the 1991-2008 epoch the gradient is $(2.18 \pm 0.67) \times 10^{-8}$ Jy/day with a reduced $\chi^2 = 2.2$ and the fit to the default beam data over time is $(2.12 \pm 0.72) \times 10^{-8}$ Jy/day with a reduced $\chi^2 = 3.4$. The increase in flux over time is more statistically significant than a constant core flux. Assuming that the trend between points is a simple straight line (least squares fit not shown) the core flux for fixed beam images increases very slightly over time by 0.26 ± 0.16 mJy (1.6σ) between 1991 and 2008.

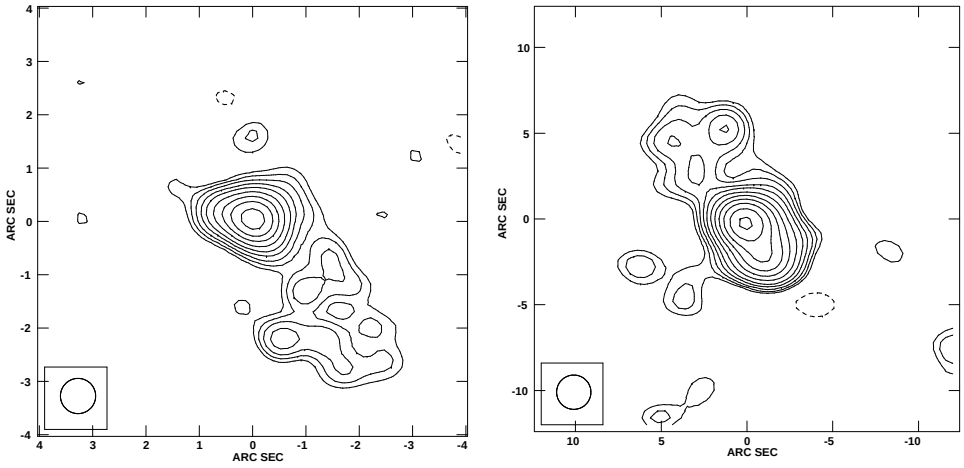

Figure 3.5: Images from B & C Configuration for the 2008-2009 dataset. Both maps are centred on the nucleus with North up and East to the left. Left image shows the B configuration map and right image shows the C configuration map. Both are made with the default restoring beam. The peak flux density from JMFIT is 10.1 $\pm$0.21 $\times 10^{-4}$ $Jy/beam$ and 18.5 $\pm$0.21 $\times 10^{-4}$ $Jy/beam$ respectively. The rms noise level in both maps is 2×10^{-05} Jy and contour levels are placed at rms noise $\times$ $-2.8, 2.8, 4, 5.6, 8, 11, 16, 23, 32, 45, 64, 90, 127, 180, 250$.

south-west. In C configuration map, on the right (beam size $2''$) there is extended structure in both the north-east and south-west. The extended flux at these lower resolutions prohibits an accurate measurement of the core flux density. In order to isolate the core and calculate the flux density I devised a method, referred to throughout this work as the 'offset method' (more detail on this method is given in Section 2.4). In brief, this method involves measuring the flux confined to a box which encompasses the core region only. The 'offset method' is carried out on the 2008-2009 data set to achieve a more accurate estimate of the intrinsic radio flux measurements than those estimated by K11. The method used by K11 for measuring the core flux is inclusive of all extended emission flux. They do not take into account the fact that the changing of the VLA configuration effects the measured nuclear flux.

For the 'offset method' the box drawn around the core is kept the same size within each array configuration. The box size is chosen to encompass all of the core flux, and very little contribution from diffuse extended flux emission. Box sizes are $\approx 0.4 \times 0.4$, 2×2 and 6×6 arcsec^2 for A, B and C configurations respectively. Experiments with fixing the beam size over which JMFIT integrates the flux revealed minimal difference in flux between those made with default beams and fixed beams. Therefore, all flux density values which I present are from maps made with a default beam size, unless otherwise stated. On the left of Figure 3.6 the

integral flux density and peak flux density values are plotted from my own reduction of the archival 2008-2009 data. This dataset was also separately reduced and presented in the paper by K11. On the right I plot the integral flux density and peak flux density values taken from work by K11. The peak flux lightcurves from both methods are consistent with each other and show a rise in flux density by ~ 1.6 mJy over the 212 days of observation, however, as proposed in Section 2.1, this rise in flux density is not intrinsic to the core of NGC 4051 but results from the changing of the array configuration. The contrasting methods used by myself and K11 reveal dramatic differences between measurements of integral flux density. The integral intensity values from my own lightcurve rise steadily, as a result of the changing array configuration, as is detected for the peak lightcurve, but show a larger increase in flux (3.22 mJy over 212 days), however; for the integral flux density lightcurve presented by K11 the flux is greater during the second observation (in B configuration they measure a flux value of 5.99 mJy) than during the next flux measurement during the lower resolution of C configuration (4.78 mJy). K11 suggest that because their measured flux value during B configuration is higher than during C configuration this is evidence for the rise in flux being a result of a variation which is intrinsic to the core. They assume the changing resolution of the VLA array does not effect the total integral flux density values measured. K11 perform no 'offsetting' to the integral flux density lightcurve presented in top right of Figure 3.6 and use this lightcurve in all of the variability analysis in their work.

I propose that the differences in the flux densities presented in Figure 3.6, between my own method and that of K11 is due to fact that we use different box sizes to integrate flux. The method used by K11 involves integrating over the whole image, however; my method integrates flux over a smaller box size to isolate the core only. I use a different box size for each array, with a maximum box size of 6×6 arcsec^2 during C configuration, however; K11 restrict their Gaussian fits to a box size of $\approx 8 \times 6$ arcsec^2 for all configurations to include all of the structures present in the whole image. This means that their integral flux value includes both the core flux and that of the extended structure, making their values of integral flux much higher than by my own method. As proposed in Section 2.1, the most likely reason for the flux increase in the VLA lightcurves is the changing of the VLA configuration to a lower resolution array. K11 argue that the variation seen in their integral flux density lightcurve where the second (B configuration point) is higher than the following 3 points at a lower resolution (all C configuration points) is evidence that the radio variation is intrinsic to the source, and not an instrumental effect due to the changing of the array. In my own reduction no such flaring during B configu-

ration is detected and all flux measurements increase with time as the resolution of the array is lowered, as expected. I argue that the increase in flux which is detected over time by both methods is not intrinsic to NGC 4051. I propose that the detection of variability within single array configurations (particularly A configuration) is a more accurate estimate of the core variation. Considering the three points measured within C configuration using my own method (left panels in Figure 3.6) the peak flux varies by a maximum of 0.5 mJy, compared to the integral flux density which varies by as much as 1.3 mJy. This difference between the peak and integral flux variations indicates the difficulty of obtaining reliable integral flux measurements and for this reason peak flux density measurements are given more credibility in investigations of radio variability in this thesis.

Following the 'offset method' described in Section 2.4 a light curve was produced for the 2008-2009 data set. All 6 data points were offset to A configuration, shown in Figure 3.7. The 'offset method' removes some average flux value from the lower resolution array measurements to give an estimate of the core flux as seen from the highest resolution A configuration. The initial flux density values are calculated by drawing a box around the core, but it is unavoidable that there will be additional flux from extended emission included in the measurement, this has the effect of making the core flux density value greater than the 'true' intrinsic flux value of the core. It is worth noting here that K11 consider that the A configuration flux they measure is actually an underestimate of the true intrinsic flux due to flux being resolved out at the relatively high resolution (with comparison to B and C) of the A array configuration.

In Figure 3.7 I show the 8.4 GHz lightcurves offset to A configuration. The panels on the left of this figure show the light curve for the 1991 data (just 2 data points). Note that the 1991 data shown here represents real A configuration data and is not 'offset'. The middle panel shows the 2000-2001 offset to A configuration data (from VLA data presented in Chapter 2), and the right panels show the 2008-2009 data offset to A configuration (from my own reduction of the VLA/EVLA archive data presented previously in K11). All flux values were measured from maps made with a default restoring beam. All variations in flux detected in the 2008-2009 data are within the same factor of the variations seen in the 2000-2001 data (left panels in Figure 3.7) for both the integral flux density and peak flux density, this suggests that the conclusions made in Section 4.6 are still valid, i.e. there is no strong evidence for any large amplitude variability in the core radio flux of NGC 4051 at 8.4 GHz. These results suggest that the same physical process occur in both datasets (2000-2001 and 2008-2008). Assuming a simple straight line trend

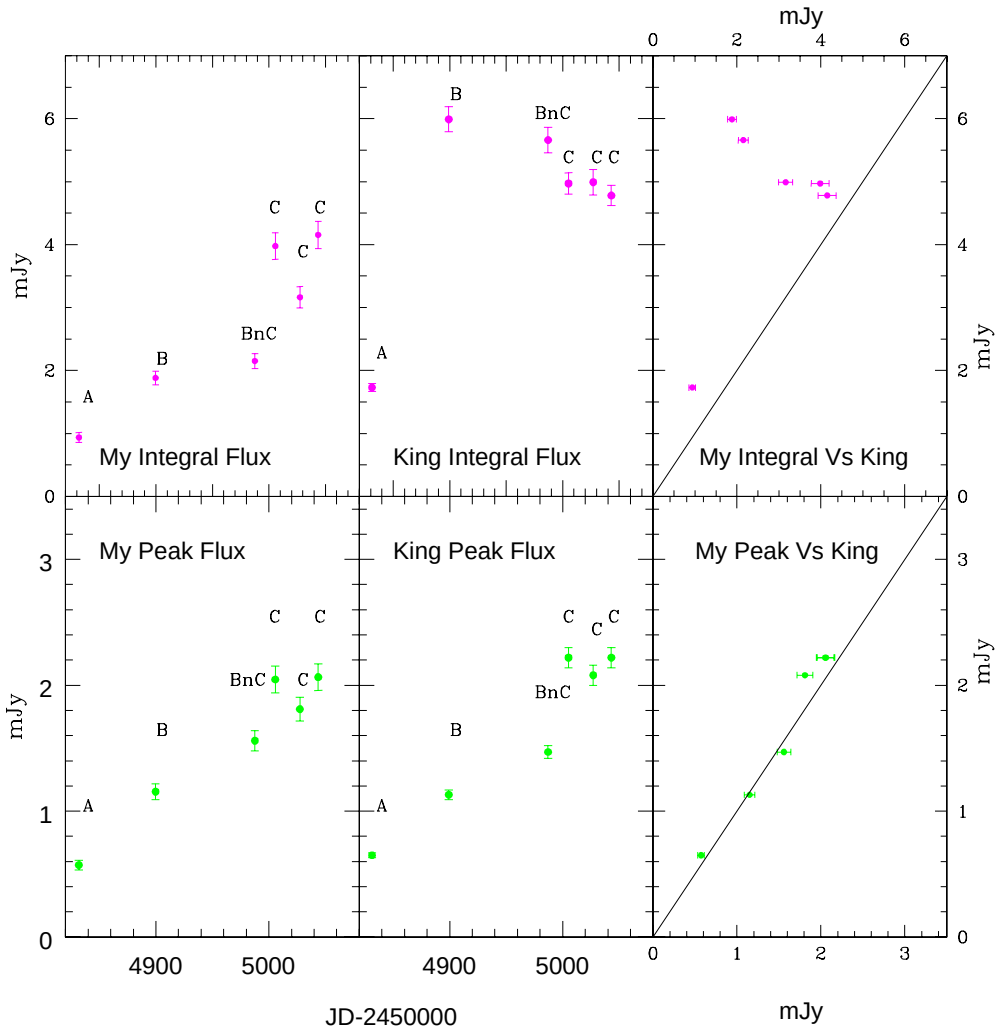

Figure 3.6: Integral and peak flux density values for both my reduction and the King reduction of 2008-2009 data. While the lightcurves derived from peak density (bottom panels) are similar, the integral flux lightcurves are dramatically different due to the contamination of extended flux. This can be clearly seen from the plots on the far right which show my flux values versus the King flux values. Top left panel: Integral flux density values at 8.4 GHz from my reduction. Bottom left panel: Peak flux density values at 8.4 GHz from my reduction. Top right panel: Integral flux densities at 8.4 GHz from King *et al.* (2011). Bottom right panel: Peak flux densities at 8.4 GHz from King *et al.* (2011).

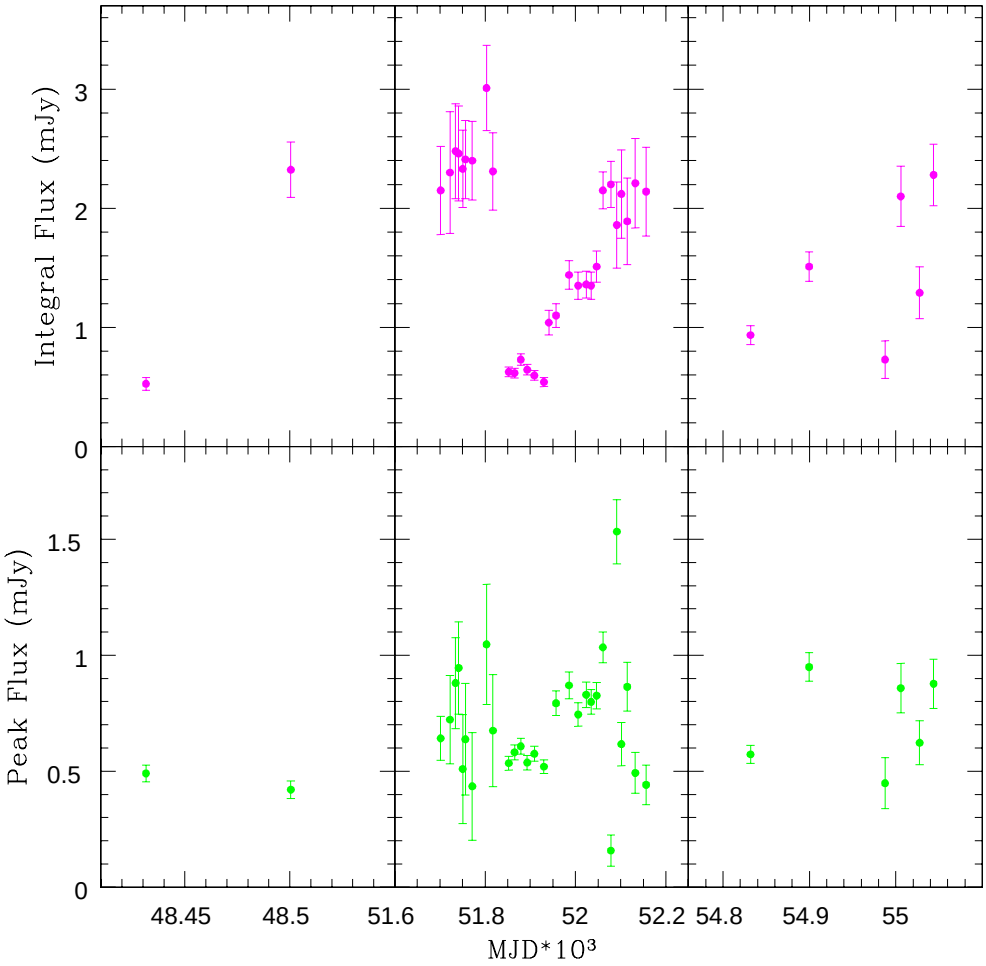

Figure 3.7: Radio flux density values from 1991, 2000-2001 and 2008-2009 'offset' to A configuration. Core Integral flux density (top panels) and peak flux density (bottom panels) at 8.4 GHz for 1991 on left, 2000-2001 data in the middle and the 2008-2009 data on the right. Flux densities for all observations are offset to the A array configuration using the 'offset method' discussed in Section 2 and all images are made with the default beam size. The peak flux density is consistent with being constant i.e the majority of peak flux density values represent a factor of 0.5 variability (which represents ~ 0.5 mJy change in flux.)

between points I suggest that the peak flux density is consistent with being constant. The majority of peak flux density values plotted (excluding 2 outlying points within 2000-2001 data) represent an increase by a factor of 0.5 equivalent to ~ 0.5 mJy change in flux.

3.3.2 X-ray Variability during 2008-2009

X-ray lightcurves from both the RXTE and *Chandra* observatories are available for the epoch of 1st January 2009 (JD 245 4848.2) to 31st July 2009 (JD 245 5043.1). Both the smoothed and unsmoothed RXTE data and *Chandra* data presented by K11 are shown in Figure 3.8. Comparison between the observed RXTE X-ray light curve (fifth panel) and the *Chandra* X-ray lightcurve (sixth panel) presented by K11, for the same period reveals that the ~ 2 day sampling of the RXTE light curve conveys the variability of the core region in a much more comprehensive manner than the poorly sampled *Chandra* data (sampled every ~ 24 days). In both light curves the X-ray flux drops at $\sim$ JD 245 4900 before beginning to rise again at $\sim$ JD 245 5000. However, for the duration of the lightcurve shown in Figure 3.8 the RXTE flux changes by a factor of 19.6 compared to a change by a factor of only 2.9 during the *Chandra* observations. Given the thorough ~ 2 day sampling of the X-ray flux from RXTE I give more weight to conclusions made using this data. It is impossible to detect the short time scale variations from the *Chandra* data taken from K11 because only six X-ray data points exist and these are separated by a range of $17-45$ days. Therefore, only long timescale variations are detected from this lightcurve.

Visual inspection of the lightcurves presented in Figure 3.8 reveal no obvious correlation between the X-ray and radio, this possible relationship is quantified later in the investigations in Section 3.4. To produce a quasi-simultaneous dataset of X-ray and radio data (as in Chapter 2 for 2000-2001 data) I linearly interpolated the observed (unsmoothed) RXTE X-ray light curve to the exact dates of the 6 VLA 2008-2009 observations at 8.4 GHz (see Table 3.2). Due to the ~ 2 day sampling of the RXTE light curve interpolating between points results is a fairly accurate representation of the 'true' flux at the time of interpolation, and there is very little difference between the nearest observed flux values and real flux values. The interpolated RXTE measurements are within the errors of the nearest observed flux values. However, I do not attempt to interpolate the *Chandra* values reduced by K11 to the nearest radio dates because of the sparsity of *Chandra* data. There are only 8 flux values for this data set, and because the sampling is much greater than the

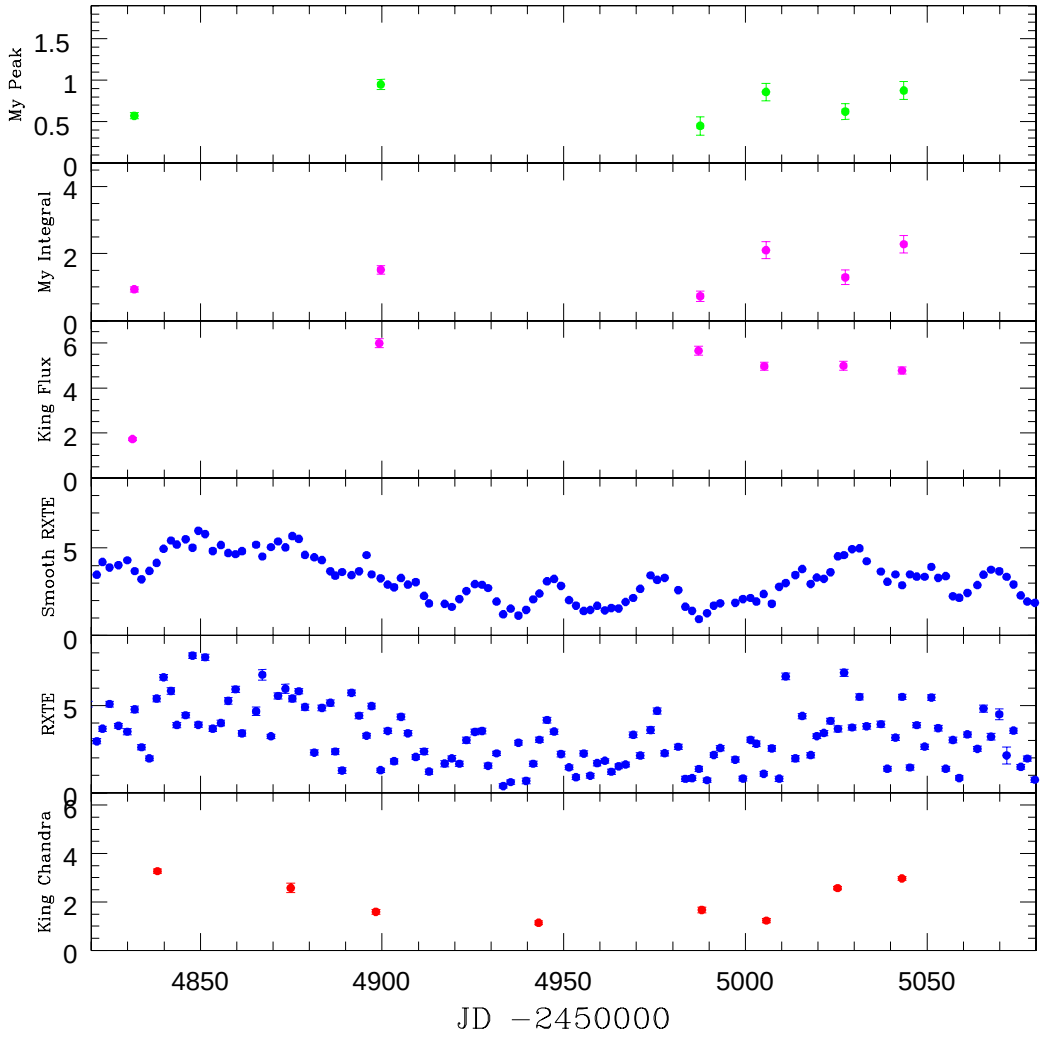

Figure 3.8: Three radio lightcurves and three X-ray lightcurves from the period 2008-2009. Top panel: Peak flux density at 8.4 GHz, from my reduction of the 2008-2009 data, offset to A configuration. Second panel: Integral Intensity at 8.4 GHz from my reduction of the 2008-2009 data offset to A configuration. Third panel: The six integral flux density data points at 8.4 GHz presented in King *et al.* (2011). Fourth panel: The smoothed RXTE lightcurve. Fifth panel: The unsmoothed 'observed' RXTE lightcurve. Sixth panel: The eight *Chandra* X-ray points presented in King *et al.* (2011). All X-ray data was integrated over 2-10 keV with units of 10^{-11}

RXTE-radio spacing (see Table 3.2) linear interpolation would be inaccurate. The long term variability of the observed RXTE is consistent with the observed Chandra fluxes (see last two columns in Table 3.2) and the Spearman rank coefficient for the two X-ray lightcurves is 0.78, suggesting a high correlation between the two X-ray lightcurves on long timescales.

The separation in time between the 8.4 GHz radio and X-ray *Chandra* dates varies from 0.11-6.39 days (see Table 3.2), so by linearly interpolation this data I would have to assume that the flux does not vary on short timescales and that it follows a simple straight line trend. This of course is not the case given the flux variations observed in the RXTE lightcurve for the same epoch (5th panel in Figure 3.8). As a result i do not interpolate the Chandra data to the radio dates in this analysis.

Table 3.2: 8.4 GHz observation dates presented with the nearest observed RXTE & *Chandra* X-ray observation dates.

Radio Date [a]	Nearest RXTE Date[a]	Δ(Radio -RXTE)[b]	Nearest *Chandra* Date[a]	Δ(Radio- -*Chandra*)[b]	Interpolated RXTE flux [c]	Observed RXTE flux [c]	Observed *Chandra* flux [d]
4831.81	4831.91	0.10	4838.20	6.39	4.71 ±0.13	4.77±0.18	3.27 ±0.09
4899.67	4899.59	0.08	4898.30	1.37	1.39 ± 0.12	1.30 ±0.11	1.59 ±0.10
4987.58	4987.20	0.38	4988.00	0.42	1.26 ±0.14	1.37 ±0.14	1.67±0.12
5005.69	5005.06	0.63	5005.80	0.11	1.51 ±0.13	1.10 ±0.13	1.23±0.08
5027.50	5027.15	0.35	5025.40	2.10	6.38 ±0.19	6.87 ±0.19	2.57±0.07
5043.59	5043.17	0.42	5043.10	0.49	4.69 ±0.16	5.49 ±0.16	2.97±0.07

[a] Dates are JD-2450000

[b] Δ values are in units of days.

[c] X-ray fluxes are in units of 10^{-11} erg cm^{-2} s^{-1} and are shown as observed and interpolated to the time of the radio observation.

[d] Chandra observed values were taken directly from work by King *et al.* (2011).

3.4 Radio/X-ray Correlation

The RXTE X-ray data used in this study has a ~ 2 day sampling which is ideal for assessing the variability of the X-ray flux density in the nuclear region of NGC 4051. However, measuring the variability at radio wavelengths accurately from the 2000-2001 and 2008-2009 VLA data is much more challenging due to contamination from extended emission, as discussed previously in Section 2.4. It is important to mention here that the small number of radio data points (in comparison to the X-ray data points) and the poor time sampling of the radio lightcurve both greatly effect the conclusions made from the following analysis of the radio/X-ray correlation. Note that I have reduced and imaged all radio peak and integral flux density measurements which follow myself unless otherwise stated.

3.4.1 During A configuration

As a first step in investigating a radio/X-ray correlation for emission from the core of NGC 4051, specifically the 'distinctive' coupling between the radio and X-ray emission which is found by K11 for the 2008-2009 data, I first reduced and imaged the A configuration data from the 2008-2009 data set. For the 2000-2001 data several flux measurements exist within the highest resolution A configuration so it is possible to determine the variability during the period of the actual observed A configuration data. However, of the 6 data points at 8.4 GHz from 2008-2009 just one A configuration point exists. In order to investigate the long term correlation between the X-ray and radio emission observed during A configuration I plot the peak flux at 8.4 GHz data for both 2000-2001 and 2008 data sets against the interpolated unsmoothed RXTE flux. Note that no RXTE X-ray data exists for the epoch of the 1991 data so the X-ray/radio correlation could not be investigated for this epoch.

In Figure 3.9, the radio/X-ray relationship for the period of the 2000-2008 data is shown. In this figure the red points represent the 2000-2001 data and the green point represents the single A configuration 2008 data point. Visual inspection of this graph suggests a very weak radio/X-ray correlation between the observed flux values during A configuration for the core of NGC 4051. This weak positive correlation is shown in Figure 3.9, the correlation has a Spearman rank coefficient ρ=0.68 which for 7 data points is equivalent to a 1.7σ detection. The correlation observed here is the first evidence (from this work) that contradicts the anti-correlated relationship for the 2008-2009 radio and X-ray data proposed by K11.

To investigate the weak correlation observed during the A configuration for radio

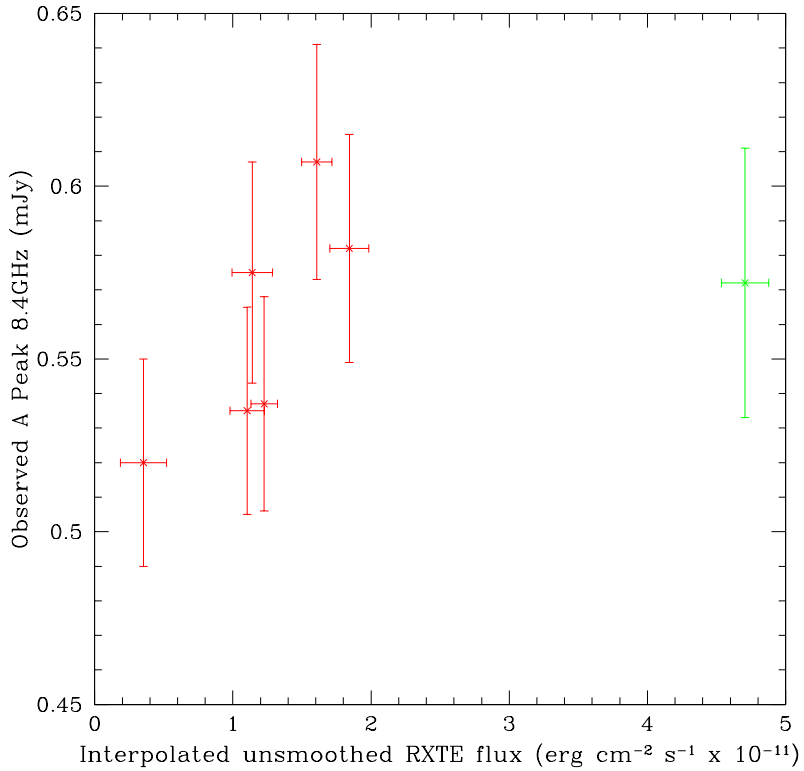

Figure 3.9: Peak 8.4 GHz core flux densities from the 'real' observed A configuration points (six from 2000-2001 data and one from 2008). The 2000-2001 data is shown in red and the 2008-2009 data set shown in green. The flux from the core during A configuration is the most accurate representation of the core flux as it suffers least from extended emission flux contributions. A weak positive correlation is detected between the X-ray and radio regimes here with a Spearman rank coefficient of 0.68 and a least squares fit gradient of $\approx$ 0.01 with a reduced $\chi^2 = 0.9$ calculated from 5 degrees of freedom (dof). This correlation is investigated in Logarithmic space in the next figure.

and X-ray emission I plot the logarithm of both to compare with the logarithmic relationship presented in K11 and other studies into the radio/X-ray correlation in hard state objects (Corbel *et al.*, 2003; Gallo *et al.*, 2003, 2006). In studies of 'hard state' objects (typically BHBs) the radio variability is generally described by $L_R \propto L_X^{\beta}$ where $\beta \sim 0.7$. In Figure 3.10 the logarithmic relationship between peak radio luminosity of the core observed at 8.4 GHz and the interpolated unsmoothed X-ray luminosity at 2-10 keV of the observed A configuration points is shown for NGC 4051. Data from both 2000-2001 and 2008-2009 is fit with a least squares relationship to determine a value for the gradient, β and a reduced χ^2 value. The six points from 2000-2001 are fit with a red line giving $\beta = 0.08 \pm 0.05$, with a reduced $\chi^2 = 0.65$, the single A configuration point from 2008-2009 is shown in

green. The black line fits all 7 A configuration points and gives least squares fit of $\beta = 0.05 \pm 0.03$ again with a low reduced $\chi^2 = 0.71$ calculated from 5 degrees of freedom (dof). Both plots result in a very weak positive correlation with a maximum $\beta = 0.086$, a factor of 8 shallower in logarithmic space than the correlation which exists for hard state objects. A weak positive correlation is in contrast to the anti-correlation results determined by K11, who calculate $\beta = -0.72 \pm 0.04$ or $\beta = -0.12 \pm 0.05$ if the A configuration point is removed. To investigate the significance of the weak positive correlation fit to data presented in this work I also performed a least squares fit to the data with a gradient, $\beta = 0$, and determined a reduced $\chi^2 = 1$ for this fit. Performing an F-test on the χ^2 values from fits with one free parameter ($\beta = 0$ from 6 dof's) and two free parameters ($\beta = 0.081$ from 5 dof's) gives an F value $= 3.635$, equivalent to a probability of exceeding F with the $\beta = 0.081$ fit versus the $\beta = 0$ fit at $\sim 20\%$. The positive correlation is thus marginally significant.

To further investigate the radio/X-ray anti-correlation found by K11 the logarithmic relationship of peak and integral flux density at 8.4 GHz versus the X-ray *Chandra* data is analysed. All data plotted in Figure 3.11 is as presented in K11 and no offsetting between array configurations is carried out at this stage. Including the low radio flux A configuration point (lowest point in both graphs in Figure 3.11) the best fit is an anti-correlation similar to that found by K11. An anti-correlation is found for the integral flux density $\beta = -0.95 \pm 0.05$ with reduced $\chi^2 = 150$ and $\beta = -0.85 \pm 0.04$ with reduced $\chi^2 = 180$ for the peak flux density, both value are calculated from 4 dof. The large values of reduced $\chi^2 > 100$ (given only 4 degrees of freedom) show that the anti correlation result, which was produced by K11 using a least square fit, as is represented here, is an extremely poor fit to the data. The very weak positive correlation found in this work, from reducing and refitting the data (Figure 3.10) is fit with a much higher accuracy (from comparing χ^2 values) and is therefore more statistically likely than an anti-correlation.

Excluding the A configuration points in both graphs shown in Figure 3.11, gives $\beta = 0.32 \pm 0.05$ with reduced $\chi^2 = 70$ for the peak flux density and $\beta = -0.13 \pm 0.06$ with reduced $\chi^2 = 8.2$ for the integral flux density. I do not consider the exclusion of the A configuration point to be an accurate method of determining the flux variability, as my work in Section 2.3.1 has revealed the A configuration is actually the most reliable value for the core flux. However, to investigate the anti-correlation proposed by K11 I repeat their method of excluding the A configuration point in this logarithmic fit. They present the integral flux density alone and fit a value of $\beta = -0.12 \pm 0.05$, which is in agreement with the $\beta - 0.13 \pm 0.06$ value measured in this investigation (see Figure 3.11). In this work I also present

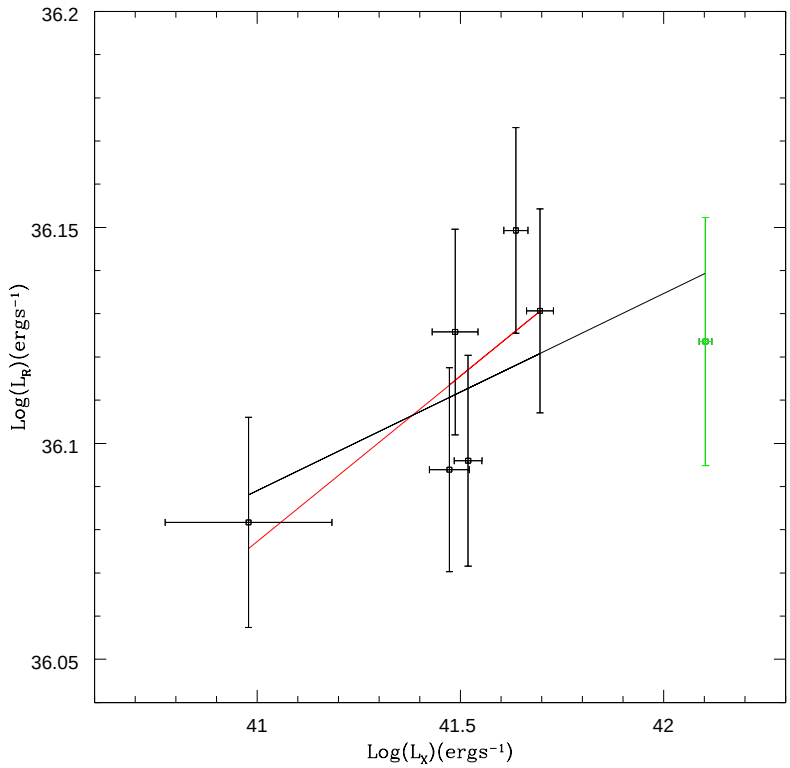

Figure 3.10: Logarithmic relationship between the peak radio luminosity at 8.4 GHz versus interpolated unsmoothed X-ray luminosity of the 'real' observed A configuration points. The six A points from 2000-2001 are fit with the red line giving $\beta = 0.08 \pm 0.05$ with a reduced $\chi^2 = 0.65$. The black line fits all seven points, including the one A configuration point from 2008-2009 (shown in green). This least squares fit has a gradient of $\beta = 0.05 \pm 0.03$ with a reduced $\chi^2 = 0.71$ calculated from five degrees of freedom (dof). The Spearman rank correlation (for seven points) is 0.68 representing a 1.7σ detection, suggesting a weakly significant, but positive correlation exists overall between X-ray and radio regimes.

their peak flux density value and, interestingly, a positive correlation is found with $\beta = 0.32 \pm 0.05$. This positive correlation detected between the peak flux values is another piece of evidence against the claimed anti-correlation of K11 because as I have reiterated throughout this work, the combination of A configuration observations and peak flux density measurements give the most accurate measure of the core flux value.

3.4.2 After offsetting all data to A configuration

To further investigate the positive weak correlation between X-ray and radio regimes all the 2000-2001 and 2008-2009 data were offset to A configuration to

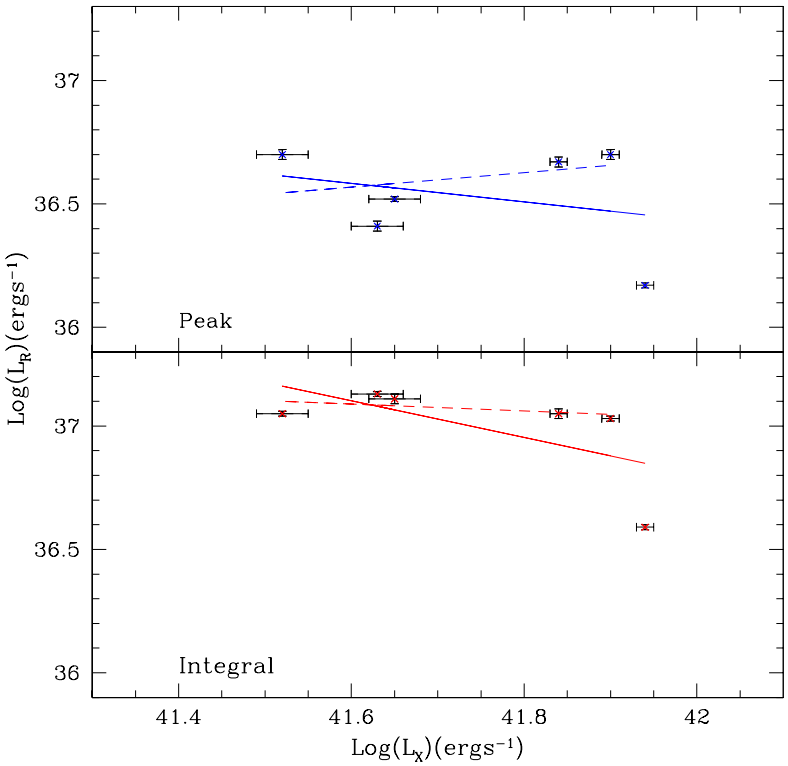

Figure 3.11: Logarithmic relationship between the peak (top graph in blue) and integral (bottom graph in red) luminosities at 8.4 GHz versus the *Chandra* luminosity. All values presented in this graph are as presented in work by King *et al.* (2011). From my own least square fit to the data an anti-correlated result is found where $\beta = -0.95 \pm 0.05$ with reduced $\chi^2 = 150$ for the integral flux density and $\beta = -0.85 \pm 0.04$ with reduced $\chi^2 = 180$ for the peak flux density (see solid lines). Note the lowest radio luminosity point in both the peak and integral graphs is from A configuration. Excluding the A configuration points in both graphs (following the method of K11) gives $\beta = 0.32 \pm 0.05$ with reduced $\chi^2 = 70$ for the peak flux density and $\beta = -0.13 \pm 0.06$ with reduced $\chi^2 = 8.2$ for the integral flux density (see dotted lines).

create lightcurves which span a longer timerange. Both data sets include data from the lower resolution configurations,B ,C and D therefore the 'offset method' was used to offset all 6 radio flux values to A configuration. For further details on the 'offset method' I point the reader to Section 2.4. Assuming that the peak flux density is the best representation of the core flux (over integral flux density) all flux densities presented in the following discussion are peak flux density values measured from my own reduction, unless otherwise stated.

Figure 3.12 shows the peak 8.4 GHz core flux densities offset to A configuration plotted against the unsmoothed interpolated 2-10 keV RXTE flux derived from both

datasets. There is no obvious variation in radio flux or correlation between the radio and X-ray flux seen by visual inspection. The 2008-2009 data points (shown in green) are within the scatter of the more numerous 2000-2001 data (shown as red points) suggesting that a similar relationship between radio and X-ray emission exists at both epochs. I note that one of the green points (from the 2008-2009 data set) has an interpolated flux value $> 6 \times 10^{-11}$ erg cm^{-2} s^{-1}, a factor of ~ 1.2 higher than any of the RXTE flux measurements observed during 2000-2001. Similarly for the radio fluxes from 2000-2001 one red point is at ~ 1.5 mJy, a factor of 2 higher than the mean radio flux value at ~ 0.7 mJy. These out lying points suggest 'flare' events may have occurred at these times. The least square fit to all the data in Figure 3.12 has a gradient=0.018 ± 0.008, a Spearman rank test reveals a correlation co-efficient=0.22 which represents a 1.3σ detection. The low correlation (ρ) value (< 1) suggests that while the null hypothesis is rejected, the positive correlation is very weak and at a low significance for all the data (from 2000-2001 and 2008-2009).

A fit to the 2008-2009 radio and X-ray data only is shown in Figure 3.13. It shows the peak flux density offset to A configuration with both the interpolated RXTE fluxes and observed *Chandra* X-ray fluxes (top and bottom panels respectively). The result is a weak anti-correlation for both relationships, with $\beta = -0.27 \pm 0.06$ with reduced $\chi^2 = 5$ (from 4 degrees of freedom) for RXTE and $\beta = -0.47 \pm 0.1$ with reduced $\chi^2 = 4.7$ for *Chandra*(from 4 degrees of freedom). The lack of 'real' data greatly effects the accuracy of conclusions which can be made based on the 2008-2009 radio data along. For the conclusions made by K11 I propose that there are two major factors which effect their work.

Firstly, despite the fact that the radio and X-ray data is stated as being 'simultaneous' by K11, the X-ray observation dates actually differ from the radio dates within a range of $\sim 0-7$ days; see Table 3.2. The X-ray flux from the core of NGC 4051 is shown to vary on short timescales, less than a day, as seen in previous work on the X-ray variability of NGC 4051 by McHardy *et al.* (2004); Breedt *et al.* (2010); Jones *et al.* (2011); Vaughan *et al.* (2011). I suggest that the non-simultaneity of the radio and X-ray data used by K11 introduces inaccuracies into the resulting correlation.

The second factor affecting the accuracy of the K11 findings is their assumption that the radio variability detected is intrinsic to Seyfert NGC 4051 because the (integral) flux density value they observe during B configuration is higher than that in the lower resolution C configuration. From my own method (where effort is made to isolate core flux only) a steady rise from B to C configuration is in fact detected,

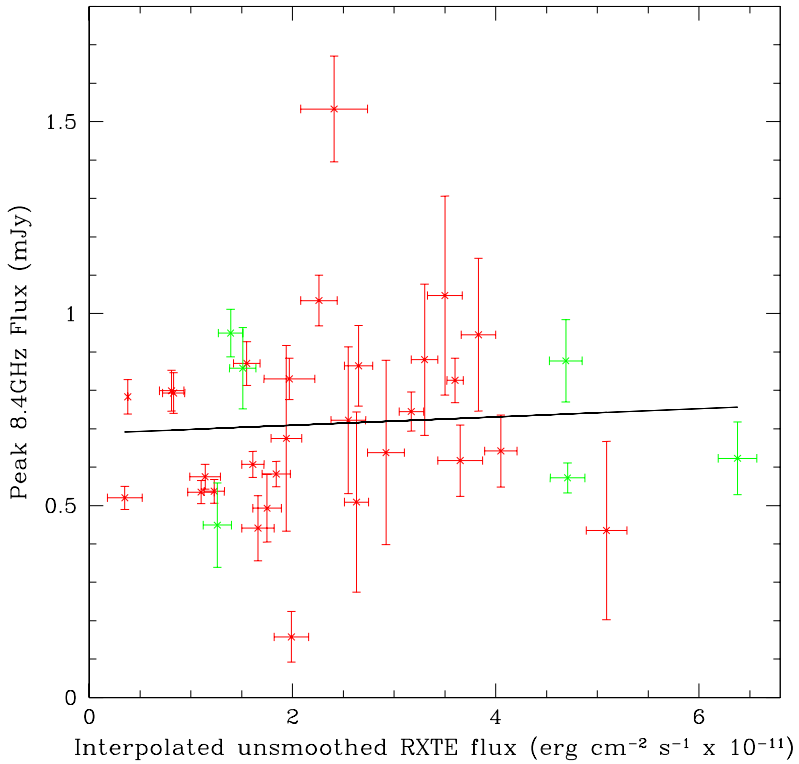

Figure 3.12: Peak 8.4 GHz core flux densities offset to A configuration plotted against the unsmoothed interpolated 2-10 keV RXTE flux derived from both datasets. The 2000-2001 data is shown red and the 2008-2009 data set shown in green. The least square fit to the data has a gradient=0.018 ± 0.008 with a reduced $\chi^2 = 8.8$. A Spearman rank test reveals a correlation co-efficient=0.22 which represents a 1.3σ detection. All radio maps are made with the default restoring beam and the interpolated observed X-ray flux data is from RXTE.

which is in agreement with the proposition that the flux rise is actually due to the changing array.

The logarithmic relationship between the well sampled RXTE lightcurve and the 8.4 GHz radio lightcurves determined by my own reduction method is presented in Figure 3.14. This graph was produced in order to compare the radio/X-ray logarithmic relationship for both the 2000-2001 and 2008-2009 datasets to the well established $L_R \propto L_X^{\beta}$ relationship which exists for 'hard state' BHXRBs where $\beta \sim 0.7$ and the value for β found by K11. All flux values shown are from maps made with a default restoring beam and were offset to A configuration fluxes. Values are plotted against the unsmoothed interpolated 2-10 keV RXTE flux derived from both the 2000-2001 and 2008-2009 datasets. The 2000-2001 data presented in Chapter 2 is shown in red with $\beta = 0.12 \pm 0.02$ with reduced $\chi^2 = 5.8$. The 2008-2009 data

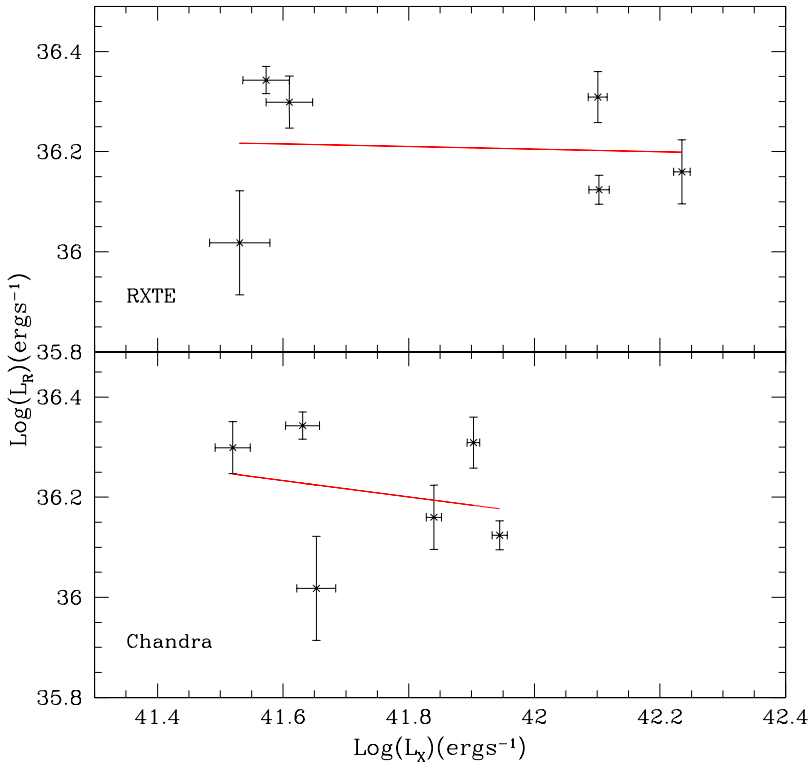

Figure 3.13: Logarithmic peak 8.4 GHz core luminosities from 2008-2009 offset to A configuration, derived from maps made with the default restoring beam plotted against interpolated RXTE values (top panel) and observed X-ray *Chandra* values (bottom panel). The least squares fit to the RXTE data gives $\beta = -0.27 \pm 0.06$ with reduced $\chi^2 = 5$ and the fit to the *Chandra* gives $\beta = -0.47 \pm 0.10$ with reduced $\chi^2 = 4.7$ (Both fits using 4 dof's).

set shown in green with $\beta = -0.27 \pm 0.06$ with reduced $\chi^2 = 5$ and the black line which is a fit to all the data has a value of $\beta = 0.077 \pm 0.02$ with reduced $\chi^2 = 9.7$. The large reduced χ^2 for all data which has been 'offset' to A configuration reveals that all fits are of poor quality. I suggest one reason for the poor quality of the fits it that the original errors, prior to offsetting, were likely an underestimation due to the fact that even at A configuration the core flux values are effected by extended features which are not resolved from the core. The extended emission itself is not varying however; the variation to the core flux can vary between individual maps. Assuming larger errors the quality of the fit (reduced χ^2) might improve, however, overall the β value suggests a weak positive correlation. Under the assumption that NGC 4051 has a jet this measurement of β for NGC 4051 ($\beta = 0.08$) which is much lower than the value for for BHBs ($\beta = 0.7$) might suggest that parts of the radio emission from NGC 4051 are constant (not strongly varying) and are diluting the

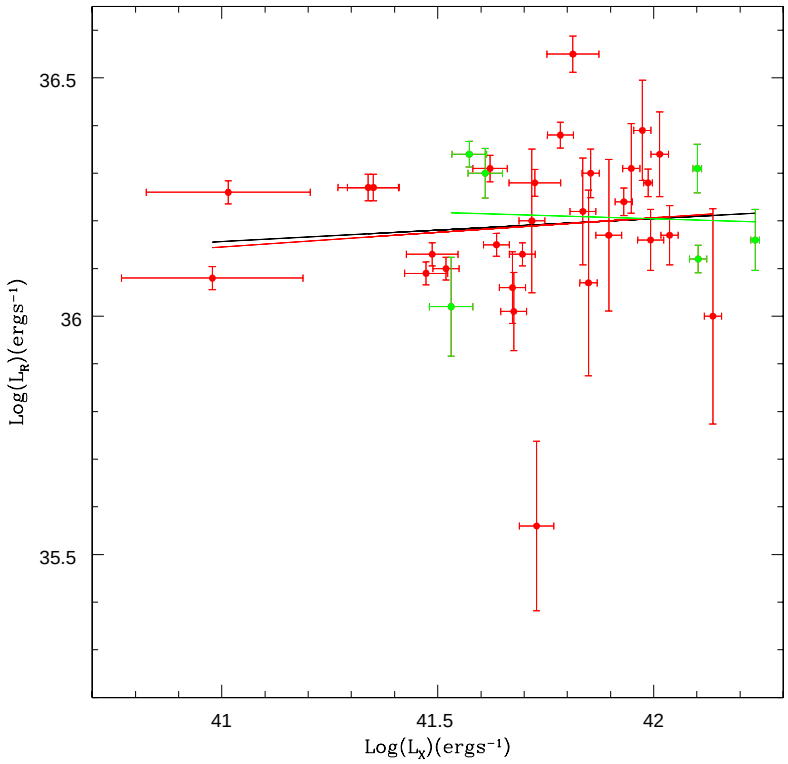

Figure 3.14: Logarithmic relationship between peak 8.4 GHz core flux **offset to A configuration** and the unsmoothed interpolated 2-10 keV RXTE flux for 2000-2001 and 2008-2009 data sets. The 2000-2001 data is shown in red with $\beta = 0.13 \pm 0.02$ with reduced $\chi^2 = 9.6$ (from 28 dof's) . The 2008-2009 data set shown in green with $\beta = -0.27 \pm 0.06$ with reduced $\chi^2 = 5$ (from 4 dof's). The black line shows the fit to ALL the data and has a value of $\beta = 0.08 \pm 0.02$ with reduced $\chi^2 = 9.7$. A Spearman rank test reveals a correlation co-efficient=0.22 which represents a 1.3σ detection. All radio maps are made with the default restoring beam and X-ray fluxes are the interpolated observed X-ray fluxes observed by RXTE.

overall relationship.

3.5 Cross Correlation Analysis

3.5.1 Cross correlation method and simulations

The cross correlation method is used in this section to quantify the degree of linear correspondence between two time series as they are shifted in time with respect to one another. These cross correlation functions can be used to investigate if the X-ray and radio emission from the core of NGC 4051 is related through a physical process, where a delay between emission peaks in the two lightcurves corresponds

to the light travel time between the X-ray and radio emission sources. There are two separate cross correlation methodologies used to quantify the lags between the flux variations in AGN, these are the interpolated method of Gaskell and Sparke (1986) and White and Peterson (1994) and the discrete correlation function (DCF) method of Edelson and Krolik (1988). The two methods are generally in good agreement; however, for sparsely sampled data the interpolation method is most accurate as the interpolated method can yield results for a limited number of data points provided that interpolating between measurements is a reasonable approximation to the real data White and Peterson (1994).

To quantify the time delay between the radio and X-ray lightcurves for NGC 4051 during both epochs (2000-2001 and 2008-2009) I use the interpolated cross correlation function (CCF) method. I used the interpolated method rather than the because the data investigated here (specifically the radio data) is poorly sampled; therefore, the interpolation method is more likely to yield a meaningful lag value. I examined the range between -60$<$ lag $>$ 60 days with a binning timestep of 6 days.

The significance of the lags which result from the CCF analysis is determined by carrying out 1000 Monte Carlo simulations. The simulations are used to generate 1000 random red noise light curves. Each simulated lightcurve has the same statistical noise properties as the observed X-ray light curve and is deduced by the method of Timmer and Koenig (1995) and the X-ray power spectrum parameters for NGC 4051 from Summons (2008). Each of the randomised lightcurves is sampled in the same way as the observed X-ray lightcurve and then cross correlated with the real radio light curve. The CCF which results is recorded and compared with the CCF of the observed light curves. These simulations assess the probability of finding spurious correlations, by which I mean a chance correlation due to the red noise character of the light curves which might result in peaks in the real observed light curve. All figures show the 'local' 99% , 95% and mean confidence levels on top of the CCF calculated as a dotted, dashed and solid line. Both the cross correlation function and Monte Carlo simulation scripts were written by Elme Breedt and were used previously to investigate the optical and X-ray CCFs for NGC 4051 in Breedt *et al.* (2010). In the work by Breedt *et al.* (2010) on NGC 4051, the lag value for optical and X-ray data is predicted as a zero day lag value. This prior knowledge of the lag allows one to estimate the 'local' significance of one peak only, at a certain lag. The significance is determined from the fraction of the simulated CCFs which have a CCF value (at zero lag) that exceeds the measured peak value. In the work in this Chapter on the radio to X-ray lag, I have no prior knowledge of the lag value expected so to be statistically rigorous the confidence levels need

to take account of multiple trials; this significance level is known as the 'global' significance. The 'global' significance will show what fraction of the simulated random light curves have CCFs at better than the observed confidence level for any lag value. The 'global' significance will therefore modify the 'significance' based on the number of 'peaks' expected within the time period investigated (120 days or 200 days in this study) . The 'global' significance values are determined by using the auto-correlation of each light-curve (radio with radio and X-ray with X-ray). The autocorrelated lightcurves will peak at zero with a correlation co-efficient of 1. The Full Width at Half Maximum (FWHM) of the auto-correlation will reveal the number of peaks which are expected within the calculated CCF. The 'global' significance, for example, at a 'local' value of 99% confidence is then calculated using by $(0.99)^n$, where n is the number of peaks expected in that lightcurve. Therefore, if 2 peaks of a certain width are expected within the time period then the 'global' significance of the CCF is actually 98%.

Under the assumption that radio emission lags X-ray emission, as discussed in Section 3.6, then only peaks with positive lags need consideration when calculating the 'global' significance for this data. In all CCFs presented the 'local' 99% , 95% and mean confidence levels are shown on top of the CCF calculated as a dotted, dashed and solid line. The figure caption shows the 'global' significance values which apply to the CCF shown.

To measure the time lag between the radio and X-ray emission regions I investigate only peaks above the 'local' 95% confidence level. The lag value I present in this work is the centroid lag, τ_{cent}, as opposed to the peak ,τ_{peak}, since the τ_{cent} value has been shown to better represent the physical lag (Koratkar and Gaskell, 1991) and τ_{peak} is often an underestimation of the true lag. The centroid width is calculated using Equation 3.1 for all peaks which have a CCF value above 95% confidence. Note that only CCF coefficients above the mean confidence level were used in the calculation of τ_{cent}.

$$\tau_{cent} = \frac{1}{N}\Sigma_i \frac{c_i \tau_i}{c_i} \tag{3.1}$$

In Equation 3.1 c_i and τ_i are the CCF coefficients and lags respectively and τ_{cent} is the centroid lag. The error in the τ_{cent} is deduced from the binning timestep; for all CCFs shown in the following section the binning timestep is 6 days, therefore the error value for all τ_{cent} presented is ± 6 days. For all CCFs shown in this chapter a positive centroid lag suggests the radio emission is lagging the X-ray emission. In discussing the significance of the time lag values I assume only positive lag values

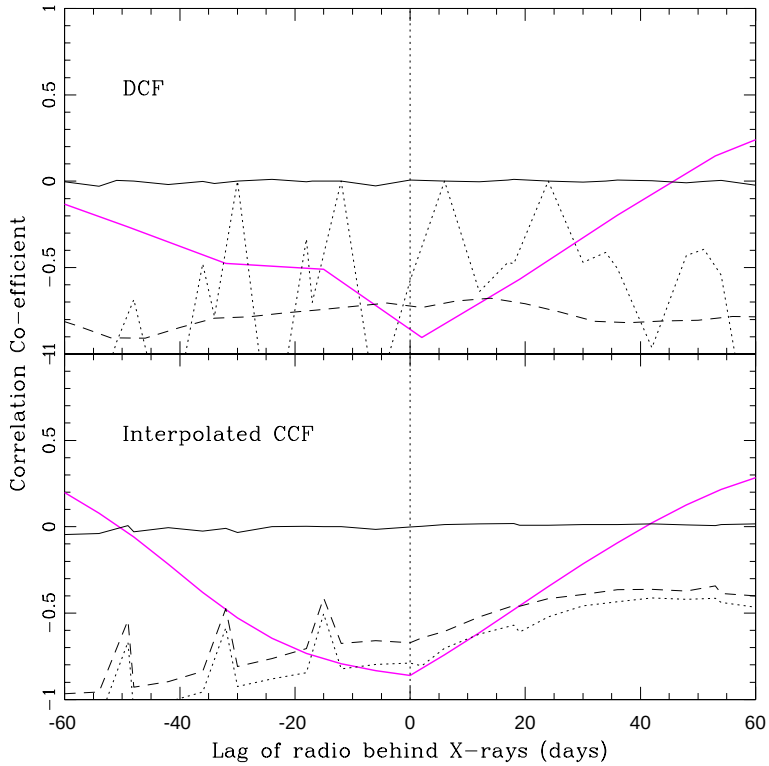

Figure 3.15: DCF and interpolated CCF of 8.4 GHz integral radio flux and *Chandra* X-ray lightcurves using K11 data. Top panel: DCF of 8.4 GHz radio and *Chandra* X-ray lightcurves (shown in magenta) following method detailed in K11. See Section 3.5.1 for further details on their method. Bottom panel: The interpolated CCF for the data presented in K11 (shown in magenta). The CCF interpolates to a 6 day time step in both lightcurves. In both graphs the horizontal solid black line, dashed and dotted line show the 'local' mean, 95% and 99% confidence levels respectively. The 'local' significance can be used here as I am only looking at the significance of a single peak at $\approx$ zero lag. The vertical dotted line shows the zero lag position. Both the DCF and interpolated CCF show an anti-correlation between the two regimes with a ~ 0 day lag above 99% confidence.

(radio lagging X-ray) are real, as a negative lag value (X-ray leading radio) cannot be easily explained by current models. For discussion of these X-ray/radio jet models see Section 3.6.

3.5.2 Discussion of 2008 -2009 CCFs

3.5.2.1 King *et al.* (2011) method

To test the chosen method of K11 I began this cross correlation analysis by following the method of King *et al.* (2011) exactly. I used their flux measurements,

as presented in K11. The first step in reproducing their method is to assess how the discrete correlation function (DCF) method was implemented. To recreate the DCF shown in their work I linearly interpolate to a 17 day time step between points in both lightcurves and then perform a DCF. The DCF I calculated by reproducing their method is shown in Figure 3.15. As in Figure 9 of K11 (shown in Figure 3.3 of this work) an anti-correlation is detected with a peak in the function close to zero lag. K11 place the minimum of the DCCF at -0.48 ± 0.1 with a lag of the radio behind X-ray of -2.5 ± 5.3 days. The negative lag value here actually suggests that radio emission is leading X-ray emission by ~ 2.5 days. Visual inspection of the lightcurves in Figure 3.8 reveals why an anti-correlation relationship is the result of both cross correlation investigations. By linearly interpolating the *Chandra* X-ray data K11 assume that the X-ray flux does not vary over short timescales, i.e. that the transition between the flux is smooth between the six measurements. However, the variation in the X-ray flux from NGC 4051 is not smooth and does vary on short timescales, as can be clearly seen in the unsmoothed RXTE lightcurve shown in Figure 3.8. The anticorrelation found between the X-ray and radio emission in NGC 4051 is an artifact of this incorrect interpretation procedure. Conclusions based on this DCF alone are bound to be inaccurate, as both light curves are poorly sampled and linear interpolation is an over simplification of the source behaviour. One of the advantages of using the DCF to calculate a correlation is that it only uses the real, observed data points. When using this method there is no need to interpolate the date to an evenly spaced set of points as was done by K11. However, the DCF is limited in its ability to measure lag between the lightcurves, so for my own analysis, I used the interpolation cross correlation instead. To measure a precise lag from a DCF the sampling needs to be roughly half of the expected lag, or better, and for this work the 'expected' lag is not yet known. The interpolated CCF is more likely to yield a meaningful lag value (White and Peterson, 1994), as stated previously in Section 3.5.1. For all interpolated cross correlation results which follow I interpolated using a 6 day time step corresponding to approximately half the shortest time between the radio observations. I only investigate lags on timescales up to a maximum of 100 days, as this of the order of the size of the radio lightcurve, which is the shorter of the two lightcurves.

After reproducing a DCF following the method of K11 I also carried out an interpolated CCF on their data. I then assessed the significance of both correlations found using simulations of the *Chandra* lightcurve. Details of both the cross correlation methods are given in Section 3.5.1. As expected, on reproducing the DCF method of K11 I too find an anticorrelation with a ~ 0 day lag. A similar anti-

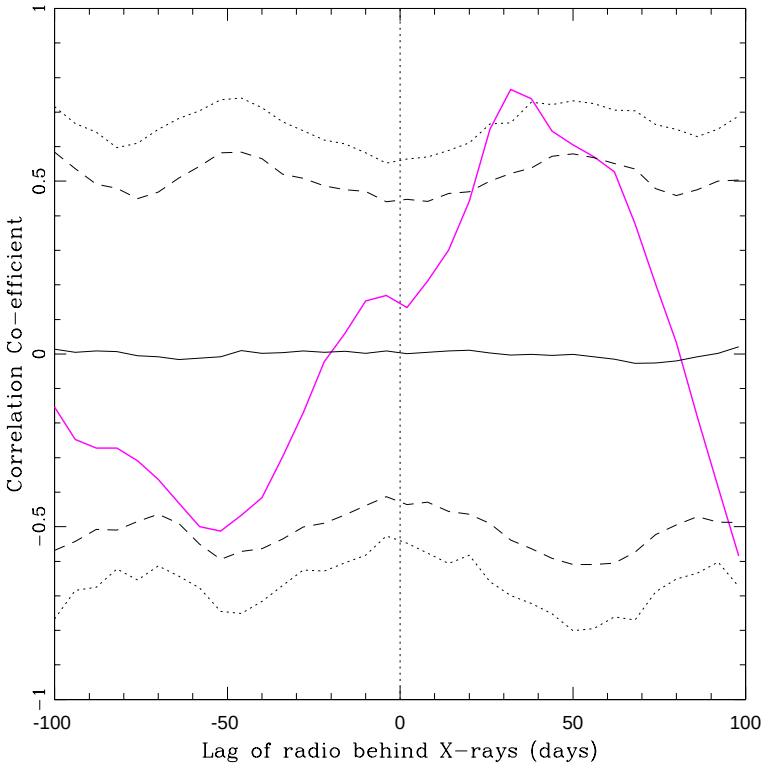

Figure 3.16: Interpolated CCF for the 2008-2009 radio data which has been re-reduced by the author and **'offset' to A configuration** lightcurve compared with the unsmoothed RXTE X-ray light curve from 2008-2009 shown in Figure 3.8. The horizontal solid line, black dotted line and dashed line show the 'local' mean confidence level and the 99% and 95% levels respectively (calculated from 1000 Monte Carlo simulations). The vertical dotted line shows the zero lag position. For this CCF the width of the expected peak is 78 days, so I expect one peak in the range of lags which are positive (> 0 days) which means the 'local' significance and 'global' significance values are the same for this CCF. The magenta line shows the interpolated CCF has a single peak above the 'local' 99% confidence level at $\tau_{cent} = 32 \pm 6$ days.

correlation is found using an interpolated CCF. However, as the sparsely sampled lightcurves are not a true representation of the flux variability, the CCFs derived from them should be interpreted with caution. For this reason all CCFs presented in the reminder of this section use the well sampled unsmoothed RXTE lightcurves which exist for both the 2000-2001 and 2008-2009 epochs.

3.5.2.2 My method

For the 2008-2009 radio lightcurve which I have produced from re-reducing the VLA archive data and following my own method there is only one observed A con-

figuration point. Therefore, the lightcurve used to produce the interpolated CCF in Figure 3.16 is the 'offset' lightcurve which consists of 6 peak flux data points at 8.4 GHz which have been offset to A configuration. I cross correlated the 'offset' radio lightcurve with the unsmoothed RXTE 2-10 keV light curve. Both lightcurves used are shown in Figure 3.8. The resulting interpolated CCF is shown in Figure 3.16. For this interpolated CCF one peak is found with a positive correlation. The horizontal solid line, black dotted line and dashed line show the 'local' mean confidence level and the 99% and 95% levels respectively (calculated from 1000 Monte Carlo simulations). The vertical dotted line shows the zero lag position. After carrying out an auto-correlation on both the radio and X-ray light curve the width of the expected peak is calculated at 78 days. I note that even after accounting for 'multiple lags' which depends on the width of the auto-correlation peaks, it is likely that the 'global' significance is still overestimated in this work. This over-estimation is especially prevalent here in Figure 3.16 where the FWHM of the peak suggests there is only one peak expected for range of lags which are positive (> 0 days); this means the 'local' significance and 'global' significance values are the same values for this CCF. The peak of the positively correlated CCF shown in Figure 3.16 suggests that radio emission lags the X-ray emission by ≈ 32 days.

3.5.3 Discusion of 2000-2001 CCFs

For the complete 2000-2001 data set (not 'real' A configuration only) the lightcurve extends over $\sim$400 days (compared to the 2008-2009 data which extends over $\sim$200 days). NGC 4051 was observed simultaneously at 8.4 GHz and 4.8 GHz using the VLA during 2000-2001 so an investigation of the delay between 'flares' seen at 8.4 GHz and 4.8 GHz is also presented in this section.

As with the 2008-2009 CCFs discussion presented previously, the 2000-2001 data is investigated firstly using the radio lightcurve observed during A configuration only. Visual inspection of the A configuration radio and X-ray lightcurves presented in Figure 3.17 reveals two peaks or 'flares' within the period of 1850 MJD-50000 and 1950 MJD-50000; however, these 'flares' only represent a $\approx 2\sigma$ variation in the radio and are not significant and a possible time lag between either 4.8 GHz and 8.4 GHz emission, or X-ray emission is not obvious from this Figure. All 'flares' appear more or less simultaneous on visual inspection.

Figure 3.18 shows the 2000-2001 interpolated CCF between the 'real' 8.4 GHz radio data during A configuration (imaged with the default beam lightcurve) and the unsmoothed RXTE X-ray lightcurve. As discussed in Section 2.3.1 the 'real'

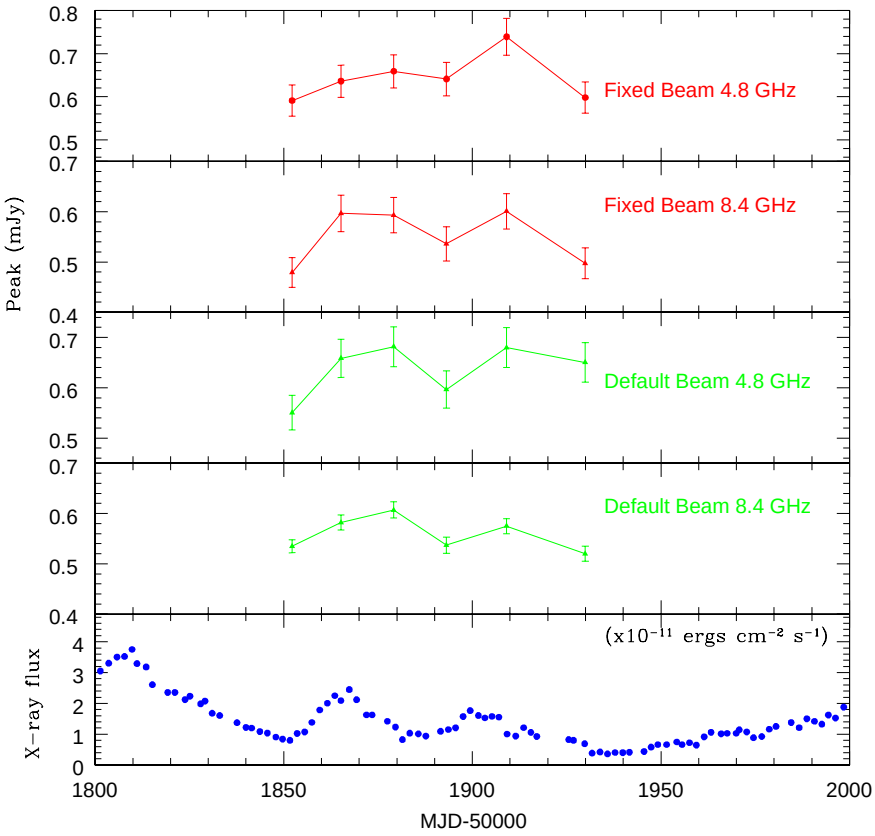

Figure 3.17: Lightcurves from 2000-2001 during A configuration for both 4.8 GHz and 8.4 GHz including smoothed RXTE lightcurve for comparison.

observed peak A configuration flux data is the best representation of the core flux. For the 2000-2001 data set 6 data points exist during A configuration and these are cross correlated with the unsmoothed RXTE lightcurve from 2000-2001 here. Both the 'real' observed A configuration and RXTE lightcurves used in this CCF are as in Figure 2.2. The radio lightcurves were interpolated every 6 days, corresponding to half of the shortest time between the radio observations. Despite having only 6 data points for the 8.4 GHz light curve, this CCF is given the most weight in this analysis of NGC 4051, due to fact that no 'offsetting' was carried out to calculate the radio fluxes. Figure 3.18 reveals one peak above the 'global' 98% confidence line at 12 ± 6 days.

Figure 3.19 shows the interpolated CCF between the 'real' 8.4 GHz lightcurve from data imaged with a fixed beam during A configuration and the unsmoothed RXTE X-ray lightcurve for the 2000-2001 data set. Both the 'real' observed A configuration and RXTE lightcurves used for this CCF are as in Figure 2.2. The

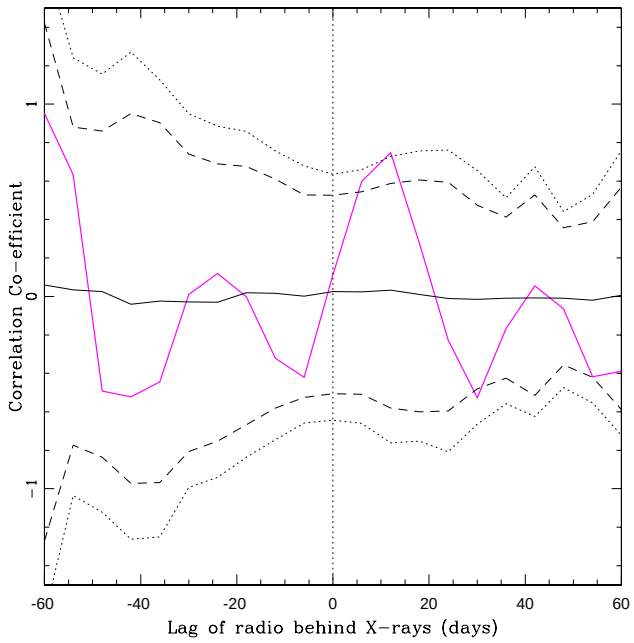

Figure 3.18: Interpolated CCF for six **'real' A configuration peak flux values** at 8.4 GHz with **default beam** and the RXTE X-ray light curve from 2000-2001, both lightcurves shown in Figure 3.17. The horizontal black line, dotted line and dashed line show the 'local' mean, 99% and 95% confidence levels respectively and the vertical dotted line shows the zero lag position. For this CCF the width of the expected peak is 37 days, so I expect ≈1.6 peaks in the range of lags which are positive (>0 days). Therefore, the 'global' significance is 98% (at 99% local significance) and 92% (at 95% local significance). The magenta line shows one positively correlated peak above the 'global' 98% confidence line at $\tau_{cent} = 12 \pm 6$ days.

CCF reveals four peaks above the 'global' 92% confidence level (95% 'local') at $\tau_{cent} = -15 \pm 6$ days, 12 ± 6 days, 30 ± 6 days and 48 ± 6 days. In line with the emission models I am only concerned with positive lags (¿0 days). A peak is seen at 12 ± 6 days for both the default and fixed beam lightcurves above the 98% 'global' confidence level.

Figure 3.20 shows the interpolated CCF between the 'real' 4.8 GHz A configuration lightcurve with a fixed beam and the unsmoothed RXTE X-ray lightcurve for the 2000-2001 data set. For this CCF the width of the expected peak is 39 days, so I expect ≈1.5 peaks in the range of lags which are positive (¿0 days). The magenta line shows one peaks above the 'global' significance at 98% confidence line at 39 ± 6 days. There is a peak above the 'local' 95% confidence level with a negative lag value at -10.8 ± 6 days, however; when considering all possible peaks in the 120 day period the 'local' 95% confidence level is equivalent to a 'global'

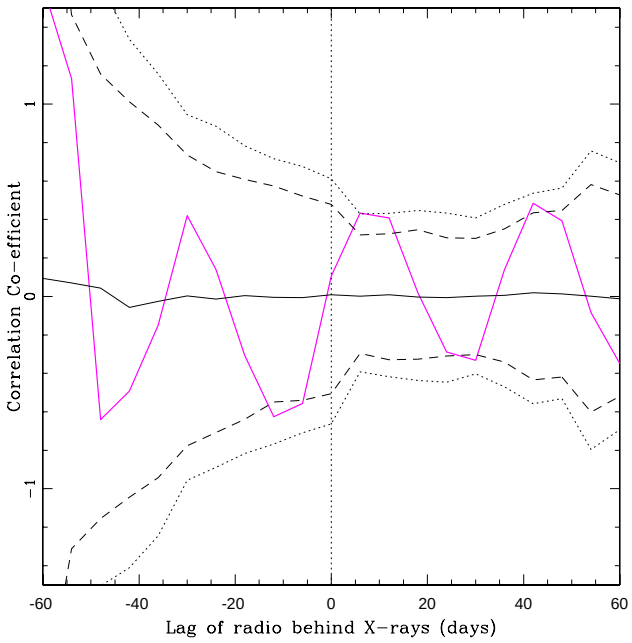

Figure 3.19: Interpolated CCF for 6 'real' A configuration peak flux values at 8.4 GHz with **fixed beam** and the RXTE X-ray light curve from 2000-2001 (both lightcurves shown in Figure 3.17). The horizontal solid black line, dotted line and dashed line show the 'local' mean, 95% and 99% confidence levels respectively and the vertical dotted line shows the zero lag position. For this CCF the width of the expected peak is 36 days, so I expect ≈1.6 peaks in the range of lags which are positive (>0 days). Therefore, the 'global' significance is 98% (at 99% local significance) and 92% (at 95% local significance). The magenta line shows one peaks above the 98% 'global' confidence level at 12 ± 6 days and another three peaks above the 'global' 92% confidence level at $\tau_{cent} = -15 \pm 6$ days, 30 ± 6 days and 48 ± 6 days.

significance of only 85% confidence.

Figure 3.21 shows the interpolated CCF between the 'real' 4.8 GHz A configuration lightcurve imaged with a **default beam** and the unsmoothed RXTE X-ray lightcurve for the 2000-2001 data set. For this CCF the width of the expected peak is 37 days, so I expect ≈1.6 peaks in the range of lags which are positive (>0 days). The magenta line shows two peaks at a 'global' confidence of 98% (equivalent to the 99% 'local' confidence level) at $\tau_{cent} = 30 \pm 6$days and 48 ± 6 days, which represent a negative correlation and a positive correlation respectively. There is another peak with a positive lag above a 'global' confidence level of 92% ('local' 95%) at 15 ± 6 days.

To assess the long time scale correlation I performed an interpolated CCF on the peak radio 'offset' to A configuration at 8.4 GHz, imaged with a default beam. This

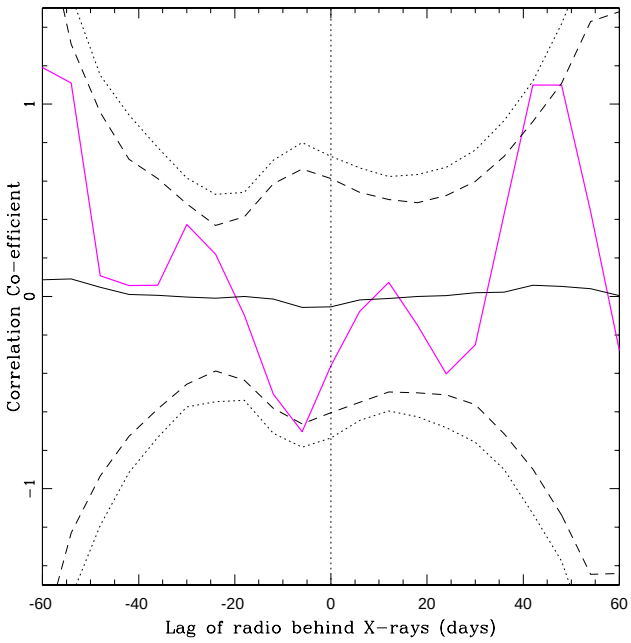

Figure 3.20: Interpolated CCF for six 'real' A configuration peak flux values at 4.8 GHz with **fixed beam** and the RXTE X-ray light curve from 2000-2001, both lightcurves shown in Figure 3.17. The horizontal black line, dashed line and dotted line show the 'local' mean, 99% and 95% confidence levels respectively and the vertical dotted line shows the zero lag position. For this CCF the width of the expected peak is 39 days, so I expect ≈1.5 peaks in the range of lags which are positive (> 0 days). The magenta line shows one peaks above the 'global' 98% ('local' 99%) confidence level at 39 ± 6 days.

radio lightcurve (and RXTE lightcurve from same epoch) is approximately 500 days in length compared with the observed 'real' A configuration lightcurves from 2000-2001 and 2008-2009 which are $\sim$ 100 days. Figure 3.22 shows the 8.4 GHz peak flux density lightcurve offset to A configuration and smoothed RXTE lightcurve for the 2000-2001 dataset. Visual inspection of the lightcurves reveals 2 possible 'flaring' events during the 8.4 GHz radio observations at 1803.3 and 2091.5 JD-2450000. I used the interpolated CCF to assess the linear correspondence between the radio 'flares' and X-ray 'flares' as the lightcurves are shifted with respect to one another. The interpolated CCF is shown in Figure 3.23, the width of the expected peak is 38 days, so I expect ≈2.6 peaks in the range of lags which are positive (> 0 days). Considering only positive lags (in agreement with emission models) there are no significant peaks seen above the 'global' 97% confidence level ('local' 99% confidence level). The peak with a negative lag which is seen above the 'local' 95% confidence level at ≈ -65 days is represented by a 'global' confidence level of

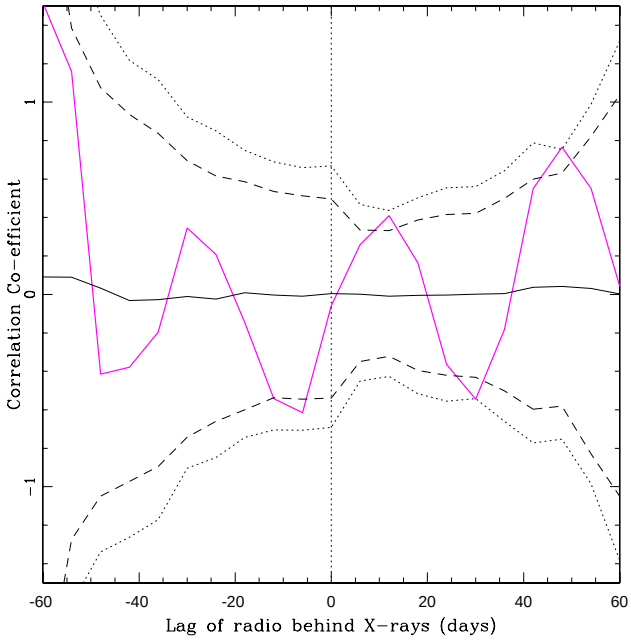

Figure 3.21: Interpolated CCF for six 'real' A configuration peak flux values at 4.8 GHz with the **default beam** and the RXTE X-ray light curve from 2000-2001, both lightcurves shown in Figure 3.17. The horizontal solid black line, dotted line and dashed line show the 'local' mean, 99% and 95% confidence levels respectively and the vertical dotted line shows the zero lag position. For this CCF the width of the expected peak is 37 days, so I expect ≈1.6 peaks in the range of lags which are positive (> 0 days). The magenta line shows two peaks at a 'global' confidence of 98% (equivalent to the 99% 'local' confidence level) at $\tau_{cent} = 30 \pm 6$days and 48 ± 6 days, which represent a negative correlation and a positive correlation respectively.

76% and is not statistically significant.

3.5.3.1 CCFs discussion

For all CCFs discussed I have assumed that radio emission lags X-ray emission in line with the models discussed in Section 3.6. In all the interpolated CCFs from the 'real' (not offset) A configuration points, which represent the most accurate value of core flux in this investigation, all the most statistically significant peaks are positively correlated.

A statistically significant lag is found for both data sets observed at 8.4 GHz at $\tau = 12 \pm 6$ days (above the 98% 'global' confidence level) for the 2000-2001 data and at $\tau = 32 \pm 6$ days (above the 99% 'global' confidence level) for the 2008-2009 data. For the 4.8 GHz data imaged with a default beam during 2000-2001 two

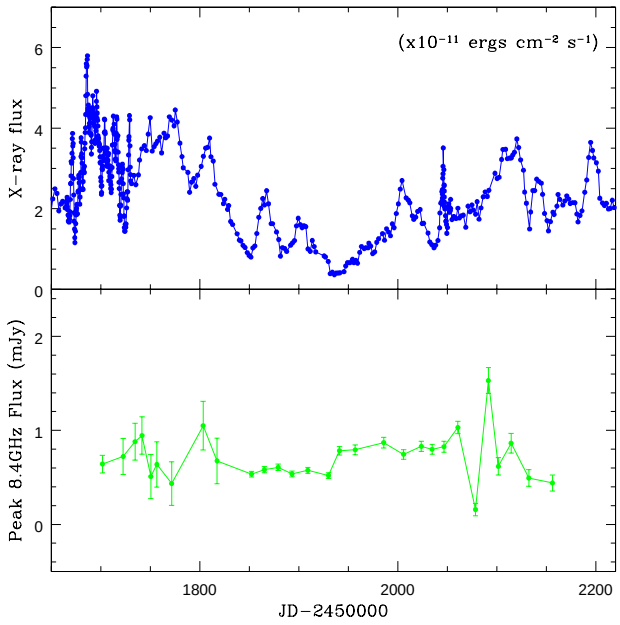

Figure 3.22: 8.4 GHz peak flux density lightcurve offset to A configuration and smoothed RXTE lightcurve for 2000-2001 dataset. Top panel: RXTE lightcurve smoothed with a 6 point boxcar. Bottom panel: Peak flux density offset to A configuration.

peaks are present above the 'local' 99% confidence ('global' 98% confidence) level at $\tau_{cent} = 30 \pm 6$ days and 48 ± 6 days, which represent an anti correlation and a positive correlation respectively. For the fixed beam 4.8 GHz data the τ_{cent} values are not in such good agreement as was seen for the 8.4 GHz CCFs with the fixed and default beam (see Figures 3.20 and 3.21). This suggests that slight changes in the beam size are having a greater effect on the measured τ value for the 4.8 GHz data, therefore, caution should be used when interpreting the CCFs presented in this work (especially the 4.8 GHz CCFs).

I interpret the most statistically significant peaks in all CCFs investigated (at or above the 'local' 99% confidence level) as strong evidence for a positive correlation existing between the X-ray and radio regimes. Given both the 'limited data' available and the effects of the beam size on the measured τ value, caution should be taken in a quantitative interpretation of the noted time lags. A physical interpretation of the time lags imply that the radio emission lags the X-ray emission within a range of $\tau = 12 \pm 6$ to 32 ± 6 at 8.4 GHz and $\tau = 15 \pm 6$ to 48 ± 6 at 4.8 GHz. The delay detected between the 4.8 GHz and 8.4 GHz is as expected, under the assumption that the higher frequency emission becomes optically thin first. Assuming that

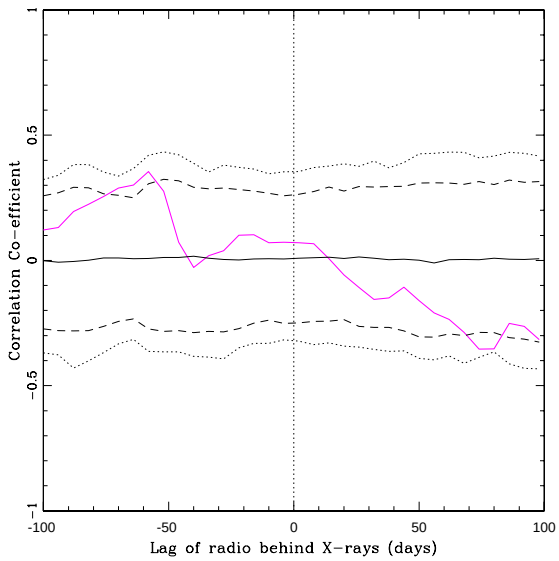

Figure 3.23: Interpolated CCF between the peak radio 'offset' to A configuration, imaged with a **default beam** at 8.4 GHz and the unsmoothed RXTE X-ray light curve from 2000-2001. The horizontal black line, dashed line and dotted line show the 'local' mean, 99% and 95% confidence levels respectively and the vertical dotted line shows the zero lag position. Both lightcurves were shown previously shown in Figures 2.11 and 2.10. For this CCF the width of the expected peak is 38 days, so I expect ≈2.6 peaks in the range of lags which are positive (> 0 days). Considering only positive lags (in agreement with emission models) there are no significant peaks seen above the 'global' 97% confidence level ('local' 99% confidence level). The peak with a negative lag which is seen above the 'local' 95% confidence level represents a 'global' confidence level of 76% and is not statistically significant.

the lag between emission in the X-ray and radio is approximately 30 days (≈ a light month), this is equivalent to a light travel distance of $\approx 10^{15}$m which is equivalent to $\approx$ 0.03 pc. A high resolution VLBI image of the centre of NGC 4051, presented later in this thesis (Figure 4.7) shows that the radio core itself represents an area approximately 4 pc in diameter. It is therefore difficult to determine what this calculated lag value means physically with reference to the core. Nevertheless, the fact that the highest peaks have positive lag values in the range of 6 days $< \tau >$ 54 days strongly suggests that there is a real physical relationship between the two regimes in this AGN. The current physical models which yield a positive correlation, with a positive lag value, indicating radio emission lagging X-ray emission are presented in the next section.

3.6 X-ray/radio jet connection

There are a number of models that might explain the X-ray and radio lags found from cross correlation studies in both AGN and BHXRBs (e.g. Marscher and Gear (1985)). The most notable of the current physical models are the 'internal shock model' (Blandford and Konigl, 1979; Rees, 1978) and the 'plasmon model' (van der Laan, 1966). First I consider the 'plasmon model'. Assuming that disc accretion mechanism(s) push matter into the jet, then this matter or plasmon, which is initially optically thick (synchrotron self absorbed) will travel at relativistic speeds down the path of the jet. As the plasmon expands it will become optically thin and will be detectable at a given frequency (in this case 4.8 GHz and 8.4 GHz). Note that the higher frequency emission will become optically thin first, so a delay between 8.4 GHz and 4.8 GHz emission is expected, with 8.4 GHz leading the 4.8 GHz emission. The time delay for material to become optically thin will only be constant if the jet is being fed at a constant mass rate, density and velocity. As a result of the variable parameters the X-ray and radio delay will also be variable assuming that the disc and jet are coupled (Falcke *et al.*, 2009; van der Laan, 1966).

The second model is the 'internal shock model' which explains the synchrotron emission observed from jets (Blandford and Konigl, 1979; Rees, 1978). The emitting regions in the model are referred to as 'knots' and are usually displaced from the core emission. The timescales of variability which are detected in these 'knots' are explained by localised shocks within these regions (Rees, 1978). The flat spectrum jet which is commonly observed in both AGN and BHXRB jets is explained using jet shock scenarios in several models e.g. Marscher and Gear (1985); Spada *et al.* (2001); Jamil *et al.* (2010).

It is difficult to completely disentangle these models and both adequately explain the time lags measured in this study. Based on the lack of radio variability for NGC 4051 and the lack of radio data I do not over interpret the measured time lags. Despite seeing evidence for jet structure one cannot identify discrete events or 'knots' in the jet of NGC 4051. However, given the evolution of the spectral index for the 2000-2001 dataset, which is shown in Figure 2.3, I attempt to analyse the nature of the time lags detected for this Seyfert. The first flare in the X-ray and radio which starts at 1850 JD-2450000 corresponds to an increase in α from -0.5 to -0.1. Shortly afterwards as the flux in both regimes decreases the spectral index steepens and decreases to a value of $\alpha \sim -0.3$. I interpret this behaviour as shocked plasma in the jet, which on becoming energised, due to an increase in accretion power, is pushed into the optically thick regime. The plasmon subsequently

becomes optically thin. The variable time lag which is detected in the CCF analysis can be interpreted as the time taken for the newly injected material to 'catch up' with older matter, which on expansion produces a flare in the jet. The observed lag depends on the Lorentz factor of the injected plasma, which is related to accretion rate (Falcke *et al.*, 2009).

Assessing the time lags which may exist between radio and X-ray emission in the core is difficult with such sparsely sampled radio lightcurves. However, analysis of the cross correlation functions for 2000-2001 and 2008-2009 data revealed that a positive correlation is most likely. Considering the current disc/jet coupling models (discussed here) I expect radio emission to lag X-ray emission. For NGC 4051 the lag of radio behind X-ray is 12 ± 6 days and 15 ± 6 days for 8.4 GHz and 4.8 GHz emission respectively. I compared these results to a similar X-ray/radio variability investigation of the LLAGN NGC 7213 by Bell *et al.* (2011). In their work the lag of radio behind X-ray is of 24 ± 12 days and 40 ± 13 days for 8.4 GHz and 4.8 GHz emission respectively. A quantitative comparison between these two AGN may be of little value, but for a very simplistic case I can calculate the mass scaling and Eddington ratio scaling for comparison from knowing that the black hole in NGC 7213 is ~ 64 times more massive and has an Eddington ratio of $7 \times 10^{-4}\ L_{Edd}$. This Eddington value is ~ 140 times smaller than the accretion rate of NGC 4051. If I assume the simple relationship that time lag scales with mass as $\tau_{lag} = \tau_{NGC\ 7213} \times \frac{M_{NGC\ 4051}}{M_{NGC\ 7213}}$ the τ_{lag} for NGC 4051 is estimated at ~ 0.5 days at 8.4 GHz, which is smaller than the observed relationship. Scaling this τ_{lag} by the Eddington ratio to give a second time lag value,τ_{lag2}, gives a value of ~ 70 days for NGC 4051. It is difficult to carry out a quantitative analysis and compare time lags between two sources which are so different, for example, NGC 7213, unlike NGC 4051, has no signatures which would suggest the presence of an inner thin accretion disc. Until the jet structure and the relationship between jet and accretion rate for both systems is better understood only a qualitative comparison is valuable.

3.7 Conclusions

This chapter has revealed that a 'distinctive' anticorrelation does not exist between the radio and X-ray emission from the core of NGC 4051, and that a positive correlation is more likely. I have shown in this work that the method used by K11, which results in an anti-correlated result has several inaccuracies. I have revealed these inaccuracies by comparing their method with my own method and by following

their method to reproduce the anticorrelation result. The 'distinctive' anticorrelation claimed by K11 is prooven to be as a result of the sparse sampling of the *Chandra* X-ray light curve and their measurement of the radio flux.

Re-investigation of the 2000-2001 (presented previously in Chapter 2) and the 2008-2009 data (presented initially by K11) reveals that the coupling which exists between the radio/X-ray regimes, if any, is very weak and there is little evidence for a strong positive correlation between the radio and X-ray emission. During the most accurate A configuration observations the $L_R \propto L_X^{\beta}$ relationship gives $\beta = 0.08 \pm 0.05$ for the 2000-2001 data only and $\beta = 0.05 \pm 0.03$ for the combined 2000-2001 and 2008-2009 dataset, and is therefore quite consistent with a constant radio luminosity. This weak (or zero) positive correlation, although not strongly significant is determined more accurately in this work by using a well sampled X-ray lightcurve and more accurate measurement of radio flux. This work also shows that had King *et al.* (2011) presented the peak flux density (rather than integral flux) they too would have found a positive correlation between radio and X-ray regimes with $\beta = 0.32 \pm 0.05$. When all data (from 2000-2001 and 2008-2009) are offset to A configuration using the 'offset method' the relationship between radio and X-ray is statistically insignificant, nevertheless it is positive with $\beta = 0.08 \pm 0.02$. King *et al.* (2011) measure $\beta = -0.72 \pm 0.04$, and because the relationship is negative and differs from the 'fundamental plane of black hole activity' of Gültekin *et al.* (2009) by 11σ they suggest that 'a separate mode of accretion and ejection operates in this AGN'. If their anticorrelation was accurate then this conclusion that the disc to jet coupling is different for NGC 4051 is valid assuming that all black holes follow a relationship $\beta \sim 0.7$ relationship of Gallo *et al.* (2003); Corbel *et al.* (2003); Gültekin *et al.* (2009). My own analysis has shown that the radio/X-ray coupling is most likely weakly positive. However, for all data from 2000-2009 observed during A configuration $\beta = 0.05 \pm 0.03$, this very weak correlation, differs from the plane by a factor of 6σ. This result also suggests that the disk to jet coupling may be different for NGC 4051. However, this difference is not as 'distinctive' as inferred from results of K11. A reason for a significantly lower β value for Seyfert NGC 4051 might be that it has more quiescent radio emission features than hard state jets, these features are constant and dilute the variability seen in the overall relationship. Another possibility is that NGC 4051 does not have a jet, and its lack of radio variability is explained by radio emission originating in the corona rather than in the jet, see Section 2.6.2. However, this possibility cannot explain the collimated jet structure which is investigated further in Chapter 4.

Very weak radio variability is detected in all the radio datasets investigated in

this chapter (2008-2009, 2000-2000 and 1991). To assess the long term variation in the core flux (over ~ 17 years I made the simple assumption that the radio variation is a linear trend over long time scales (between 1991 and 2008). The core flux is found to increases very slightly by 0.26 ± 0.16 mJy during the 'real' A configuration observations. This change in flux is equivalent to an increase in flux between 1991 and 2008 by a factor of ~ 1.3. Under the assumption that X-ray flares lead radio flares for NGC 4051, the radio emission is found to lag X-ray emission by 12 ± 6 days and 15 ± 6 days for 8.4 GHz and 4.8 GHz emission respectively.

Considering the mounting evidence for jet emission from NGC 4051 the lack of radio variability detected is at first sight somewhat puzzling given that powerful jet-dominated quasars vary by far greater amounts (e.g. factor of 5 variability seen in 4C 29.45 (Hovatta *et al.*, 2008)). It is possible that both the low resolution of VLA (with respect to VLBI for example) and the changing of the array configuration during both data sets has meant that the varying part of the jet cannot be distinguished from surrounding quiescent emission with the VLA imagery of the core. The lack of variability may also be an orientation effect from viewing the NGC 4051 jet side on, however; this assumes that NGC 4051 has a jet behaviour similar to that in jet-dominated blazars which when viewed along the jet making are highly variable in the radio.

Go forth and slay the dragon, she of the astrobiological sword.

MY MAM

4

Radio structure and spectral investigation of NGC 4051

In this chapter I present radio observations from both the VLA and VLBI to determine the structural and spectral properties of the Seyfert galaxy NGC 4051 as diagnostics of both present and past radio activity. The 2000-2001 VLA radio data presented previously in Chapter 2, are used here to probe much deeper than previous VLA observations to focus on the structure and morphology of NGC 4051. The flux measurements of the source are used in combination with spectral index measurements of the core and extended emission to determine the physical properties and energetics of the core and jet/lobe features. High resolution VLBI radio imaging is also presented here to examine the possibility of jet emission. Optical [OIII]$\lambda\lambda$5007 Å emission line data is used to investigate the inner regions of the galaxy i.e. the vicinity of the black hole. Using a combination of radio data at different resolutions and frequencies, optical [OIII]$\lambda\lambda$5007 Å data and X-ray data I attempt to determine whether a faint jet is produced in this 'soft state' AGN and if such a jet has been active in the past. I address this question with reference to 'soft state' BHXRBs and the 'fundamental plane of black hole activity' which exists for 'hard state' BHs.

4.1 Introduction

The Seyfert galaxy NGC 4051 has been known for some time to host a weak nuclear radio source of unknown origin and has been investigated by a number of studies at radio wavelengths, at various scales (e.g. **?**Baum *et al.*, 1993; Kukula *et al.*, 1995; Christopoulou *et al.*, 1997; Ho and Ulvestad, 2001; M^{c}Hardy, 2005; Gallimore *et al.*, 2006; Giroletti and Panessa, 2009; Jones *et al.*, 2011). These radio investigations, which are summarised below, have revealed evidence for nuclear, extra-nuclear and disc radio emission.

? found two components separated by $0.4''$($\sim$29pc) at 6 cm with PA $78^\circ \pm 6^\circ$ and at 20 cm towards the south west they detect diffuse extended emission. They note the elongation along the diffuse emission is roughly perpendicular to the major axis of the optical galaxy. Haniff *et al.* (1988) compare the radio structure presented by **?** to an [OIII]$\lambda\lambda$5007-Å image where a compact emission line region with an overall extent of $3''$ is detected at PA $81^\circ \pm 5^\circ$.

Baum *et al.* (1993) present 3 radio images at different resolutions see Figure 4.1. At $3.5'' \times 5.7''$ resolution (top left in Figure 4.1) Baum *et al.* (1993) detect a 'banana shaped' source at 4874 MHz with its major axis orientated along PA 32° and a total extent of $15''$ ($\sim$1100 pc). At lower resolution (Very Large Array (VLA) D-configuration (top right in Figure 4.1) at $21'' \times 14''$ resolution they detect the diffuse radio emission associated with the spiral arms of the galaxy (later work by Gallimore *et al.* (2006) at this resolution revealed the same structure). At $72'' \times 46''$ resolution (bottom right in Figure 4.1) they detect radio emission with PA 80° which is representative of the large scale radiation associated with the entire galaxy. Baum *et al.* (1993) suggest that the radio morphology of NGC 4051 and that of 11 other Seyferts may be a manifestation of a circumnuclear starburst. They suggest that the starburst generates cosmic-ray electrons which sweep the radio emitting plasma out in a starburst driven wind, along the minor axis of the galaxy disk.

The optical image from the digitised sky survey (bottom left in Figure 4.1) shows that the 'bar' in this barred spiral galaxy is aligned along the major axis of the galaxy ($\approx$ *PA* 45°), therefore the high resolution images of radio emission from the core (discussed later in this chapter) aligned perpendicular to the host galaxy, is unlikely to be a result of star formation in the 'bar' of the galaxy. At 8.4 GHz Kukula *et al.* (1995) who also investigate NGC 4051 find a bright source extended along the north east and south west with a total extent of $15''$ in a VLA C configuration map. [OIII]$\lambda\lambda 5007 - $Å data presented by Schmitt and Kinney (1996) shows an unresolved nucleus with extended emission along PA 100°.

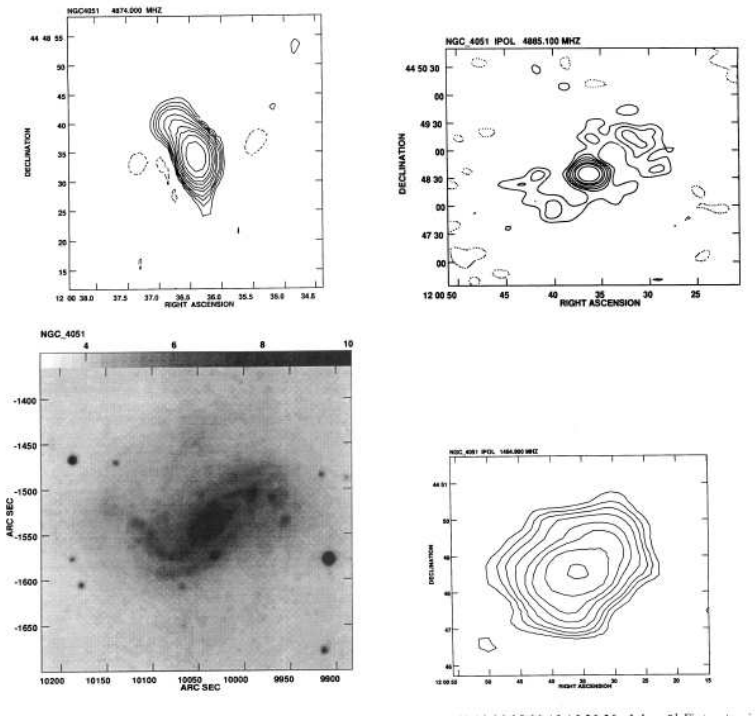

Figure 4.1: Three radio images and one optical image of NGC 4051. *Figure 8 from Baum* et al. *(1993)*. Top Left: WSRT 6cm image. Top Right: VLA D-configuration 6cm image. Bottom Left: Grey scale display of NGC 4051 from the digitised sky survey from the STScI Guide Star Support System. Bottom Right: VLA D configuration 21cm image.

Christopoulou *et al.* (1997) used MERLIN data at 1658 MHz, and found a triple source extended by about $0.8''$ along PA 73° and weak emission extending over $8''$ in PA $\sim$30 , which is consistent with the previous results given by Baum *et al.* (1993) and Kukula *et al.* (1995). Christopoulou *et al.* (1997) investigated Hubble Space Telescope (HST)[OIII]F502N archive data and Manchester Echelle Spectrograph (MES)[OIII]$\lambda\lambda$5007 – Å emission lines in combination with VLA radio data. They also find an edge-brightened emission-line region exhibiting [OIII]$\lambda\lambda$5007 – Å line splitting of up to $\sim$ 120kms^{-1} at $1.5''$ from the core. They suggest this is due to a conical outflow from a flow with a velocity of 250 kms^{-1}. They plot HST[OIII] F502N line emission onto the MERLIN radio maps at the same scale and all the radio emission is engulfed. They also plot the MES [OIII]$\lambda\lambda$5007 – Å data on the scale of a C configuration VLA map, as shown in the top image in Figure 4.10 where the linear extent of the [OIII]λ5007 – Å is aligned along the same position angle as the radio emission. Christopoulou *et al.* (1997) state the high resolution observations used were consistent with a compact origin (collimated jet outflow from the core of the NGC 4051) rather than a starburst at similar scale. This work showed

that the [OIII]$\lambda\lambda$5007 – Å emission region is co-located with the extended radio emission detected by Kukula *et al.* (1995) in VLA C configuration. Christopoulou *et al.* (1997) stated that while both [OIII]5007 – Å emission and radio emission are extended in the NE, no extention is seen in the [OIII]5007 – Å emission to SW. These findings suggested that the [OIII]$\lambda\lambda$5007 – Å emission and radio emission regions were both collimated by the same coplanar disc/torus (Christopoulou *et al.*, 1997). Nagao *et al.* (2000) use [FeX]$\lambda\lambda$6374 emission line observations to report a high ionisation region extending 3.0″ south-east of the nucleus.

Ho and Ulvestad (2001) use 6 cm VLA data and find the same overall radio structure as in previous work. They estimate the total extent of the 'jet' to be 1.2 kpc lying along PA 41°, perpendicular to the host galaxy major axis (at $PA = 135°$).

Giroletti and Panessa (2009) use VLBI data at 1654 MHz which reveals 3 sub-millijanksy radio components. They state that two of the components which are separated by 20 pc are associated with the small-scale double structure seen in VLA images by **?** and the third component, which is almost symmetric to the easternmost one with respect to the central one is associated with the emission at 8.4 GHz shown in Kukula *et al.* (1995). The VLBI image (presented in Figure 4.8) shows that the central component is slightly extended to the south. The core, which Giroletti and Panessa (2009) also detect at 5 GHz, is found to have a moderately steep spectral index value α=-0.7. They give an upper limit for the source radius of 0.31 pc ($\sim 2.5 \times 10^6 R_S$), which is a factor of ∼50 larger than the measured broad-line region size (∼0.006 pc; Kaspi *et al.* (2000)).

In Figure 2.1 VLA maps are shown in A, B, C and D configurations. The highest resolution ($\approx 0.2''$ in A configuration) VLA imaging of the source revealed a triple structure consisting of a compact core with marginally resolved components on each side of the core, separated by $\sim 0.5''$, almost in a straight line. This structure is similar to the core and hot spots of an FRII radio source and strongly suggests an underlying jet, with the hot spots being the places where the jet interacts with the interstellar medium (ISM). The three co-linear structures observed in these A configuration maps are aligned along PA $\sim 73°$ in agreement with the structure found in previous papers on NGC 4051 (e.g. Giroletti and Panessa, 2009; Gallimore *et al.*, 2006; M^{c}Hardy, 2005; Christopoulou *et al.*, 1997).

In the lowest resolution VLA maps ($\sim 7''$ in D configuration) shown in Figure 2.1 the radio structure is not resolved. However, diffuse radio emission associated with the spiral arms is detected in previous work extending out to 100″ from the core (7.4 kpc at 15.2 Mpc distance (Russell, 2003)) aligned along PA $\sim$ 135° (e.g. Baum *et al.*, 1993; Gallimore *et al.*, 2006). Baum *et al.* (1993) who also imaged

NGC 4051 using VLA in D configuration (at $\sim 7''$ resolution) and using the using the Westerbork Synthesis Radio Telescope (WSRT) at $\sim 5''$ resolution attribute the diffuse 'bubble like' emission to a radio-emitting superwind that is swept out along the galaxy's minor axis by circumnuclear starburst. The ratio of Far InfraRed (FIR) 60μm emission to 4.8 GHz radio flux measured in Condon *et al.* (1995) also suggests NGC 4051 is a starburst galaxy. However, the compact structures detected at higher resolutions (e.g. Jones *et al.*, 2011; Giroletti and Panessa, 2009; Gallimore *et al.*, 2006; M^{c}Hardy, 2005; Christopoulou *et al.*, 1997) provide strong evidence for a collimated ejection along PA 73°, rather than radio emission coming purely from starburst activity.

The radio structure is also investigated at high resolution ($\sim 0.02''$) using VLBI observations at 1654 MHz from the European VLBI Network (EVN) in 2003 and the Global VLBI network in 2004 (M^{c}Hardy, 2005). These results are discussed further in this work, in Section 4.3.3.

The reminder of this Chapter is laid out as follows: In Section 4.2 the radio observations and data reduction is discussed. In Section 4.3 I discuss the structure, spectra and proper motions which were revealed by the 4.8 and 8.4 GHz VLA data and the high resolution VLBI data at 1652 MHz. In Section 4.4 the anisotropic radio and optical emission is shown, with focus on the [OIII]$\lambda\lambda 5007 - $Å emission region and the deep radio structure revealed by 4.8 GHz combined VLA data. In Section 4.5 the power in the lobes and jet is calculated from equipartition arguments and finally, in Section 4.6 I present the conclusions of this chapter.

Note that throughout this Chapter I assume a distance to NGC 4051 of 15.2 Mpc, calculated from the Tully-Fisher relationship by Russell (2003) where 1 arcsec is equivalent to 74 pc. I also assume a black hole mass of $M_{BH} = 1.91 \times 10^6\ M_{\odot}$ calculated by Peterson *et al.* (2004) using broad emission-line reverberation-mapping data.

4.2 Radio Observations and Data Reduction

4.2.1 4.8 GHz & 8.4GHz VLA data

NGC 4051 was observed by the VLA 29 times between 16 June 2000 and 3 September 2001 with a typical interval between observations of 2 weeks. On each occasion the source was observed at both 8.4 GHz and 4.8 GHz with a total time on source, in each band, of approximately 12 minutes. The observations were made with the VLA in various configurations. For more information on these observations see

Table 2.1 and the discussions in Section 2.2.2.

The data were flagged and calibrated, using AIPS, in the standard manner described fully in Section 2.2.2. Maps were made using IMAGR with clean fields set around two fainter neighbouring sources, one approximately 5.5 arcminutes to the NE and another approximately 3.5 arcminutes to the south. After experimenting with different iterations of cleaning I standardised on 10,000 iterations. Self calibration was not used on the final images.

4.2.1.1 Imaging structure maps

The aim here is to produce maps with the best signal to noise ratio (SNR) possible. To achieve this I combined together the *uv* data sets from the same array configuration e.g. I combined the 6 A configuration *uv* data sets at 8.4 GHz into one larger *uv* data set. Note that the data which contains baselines from more than one array configuration (BnA, BnC and DnC) were not used to create combined data sets due to the lack of data and the added complexities of working with data from several arrays over singular arrays. After combining the single array *uv* data sets using the task DBCON within AIPS I then checked the amplitude and phase of the data using the tasks UVPLT and TVFLG to remove all erroneous data such as RFI, correlator errors, or instrumental errors that might effect the SNR in the final image. I repeat this method to create combined maps for all the single arrays (A, B, C & D) at both 8.4 GHz and 4.8 GHz (referred to hereafter as the combined A, combined B maps etc). The combined data sets have greater integration times on source as a result of the combination of several *uv* datasets. For example, each A configuration *uv* data set for NGC 4051 is observed for $\sim$ 18 minutes giving a total integration time for the combined A image of 112.6 minutes (1.87 hours).

All *uv* data from the 4 single array configurations (A, B, C and D) were then combined into one *uv* data set at both 8.4 GHz and 4.8 GHz, referred to hereafter as the combined ABCD maps. All maps presented in this work have weighting value ROBUST$=0$, unless otherwise stated, to ensure a balance between resolution and sensitivity.

4.2.1.2 Imaging spectral index maps

To make spectral index maps of NGC 4051 I took the combined *uv* data at 8.4 GHz and 4.8 GHz (used in Section 4.3.1) and inspected the range of the *uv* data at each frequency. The 8.4 GHz data had a UVRANGE from 0-1 Mλ while the 4.5 GHz extended from 10-590 kλ, I therefore re-imaged both data sets to a matched UVRANGE

of 0-590 kλ within IMAGR with the same cell size (0.07" by 0.07"). The resulting images were then convolved to a beam size of 0.4" × 0.4" using the task CONVL. Spectral index maps were made from these matched resolution images in the task COMB. To ensure that I calculated the spectral index for real emission only I restrict the spectral index calculations to all pixels with a flux density $\geqslant 3$ times the rms noise level in the image.

4.2.2 VLBI data

The VLBI data of NGC 4051 presented in this thesis consist of three data sets. The first (EM51) from 22 May 2003 consists of EVN data only. The second (GM053) from 4 June 2004 contains both EVN and VLBA data. Both data sets were observed at a frequency of 1653 MHz, with the phase referencing calibrator J1221+4411, $\sim 3.3^{\circ}$ away from NGC 4051. The two data sets were combined and reduced by Valeriu Tudose. In comparison to the EM51 set, the combined data had an rms noise factor ~ 2 lower and the beam was a factor ~ 4 smaller. Within this chapter this combined data set is referred to as Tudose VLBI. The third set of EVN data from 6 June 2007 is as presented (and reduced) by Giroletti and Panessa (2009). NGC 4051 was observed by Giroletti and Panessa (2009) at both 1653 MHz and 5000 MHz and is hereafter referred to as Giroletti EVN. Image analysis of the VLBI data sets was carried out by the author.

4.2.3 OIII Data

NGC 4051 was observed on 11 June 1993 using the Manchester Echelle Spectrograph (MES) on the 4.2m William Herschel Telescope (WHT) in imaging mode. The resulting narrow band imagery of the $[OIII]\lambda\lambda 5007 - $ Å emission line was reduced by Christopoulou *et al.* (1997), and their imaging is presented in this work and shown with the deep radio image of the combined ABCD configuration VLA data at 4.8 GHz (see Figure 4.10) to investigate the structure of NGC 4051. Details of the reduction of the optical $[OIII]\lambda\lambda 5007 - $ Å data are presented in Christopoulou *et al.* (1997).

4.3 Radio Structure, Spectra and Proper Motions

4.3.1 4.8 GHz and 8.4 GHz VLA data

In order to investigate the growing evidence for an outflow of emission from the core of NGC 4051 I first examine the radio structure at 8.4 GHz and 4.8 GHz using the VLA data from 2000-2001 (presented previously in Chapter 2). To examine the overall radio structure with the best signal to noise possible I imaged the combined ABCD data set, which contains all observations from single array configurations from 2000-2001. For investigation of the structure at the highest resolution only ($\sim$ 0.2") I imaged the combined A configuration data. To achieve a low resolution ($\sim$ 7") but high sensitivity image of the galaxy I imaged the *uv* data from the combined D configuration dataset. Images were produced at both 8.4 GHz and 4.8 GHz.

Figure 4.2 shows the radio maps made from combined ABCD *uv* data at 4.8 GHz and 8.4 GHz. Both maps are centred on the nucleus of NGC 4051 with an rms noise level of 11.65μ Jy/beam and 10.14μ Jy/beam respectively. At both frequencies the extended emission is aligned along PA$\sim$ 55°. The linear extent of the emission in the north-east is more easily observed in the 4.8 GHz image than at 8.4 GHz the north-east component appears disconnected from the core. Measuring from the north-east, in a south-westerly direction, the structure extends approximately 15$''$ on the sky ($\sim$ 1.1 kpc). This gives a 'jet' length, measuring from core at $\sim$ 0.7kpc. This measured value is in agreement with work on other Seyferts (including NGC 4051) by Gallimore *et al.* (2006) who state that virtually all of the jet power of a Seyfert nucleus is lost to the nuclear ISM within the inner kiloparsec.

Figure 4.3 shows the structure of NGC 4051 using combined A configuration data only. In the 8.4 GHz map three co-linear structures are imaged, as in previous work (e.g. Giroletti and Panessa, 2009; Gallimore *et al.*, 2006; M^{c}Hardy, 2005; Christopoulou *et al.*, 1997). Measuring from the core out to the component in north-east an extent of $\sim 0.4''$($\sim$ 30 pc) is calculated. This value is in agreement with the work of **?** who also state that the two main components are separated by $0.4''$ in an east-west direction.

Figure 4.4 shows the structure of NGC 4051 using combined D configuration data only, where the morphology of the host galaxy is shown. The diffuse radio emission observed (most visible in the 4.8 GHz map) is likely the result of star formation in the spiral arms of the galaxy. The emission from the spiral arms is extended along PA 113°, perpendicular to the extended structure seen in Figure 4.2 associated with possible jet activity. The major and minor axis of the host galaxy

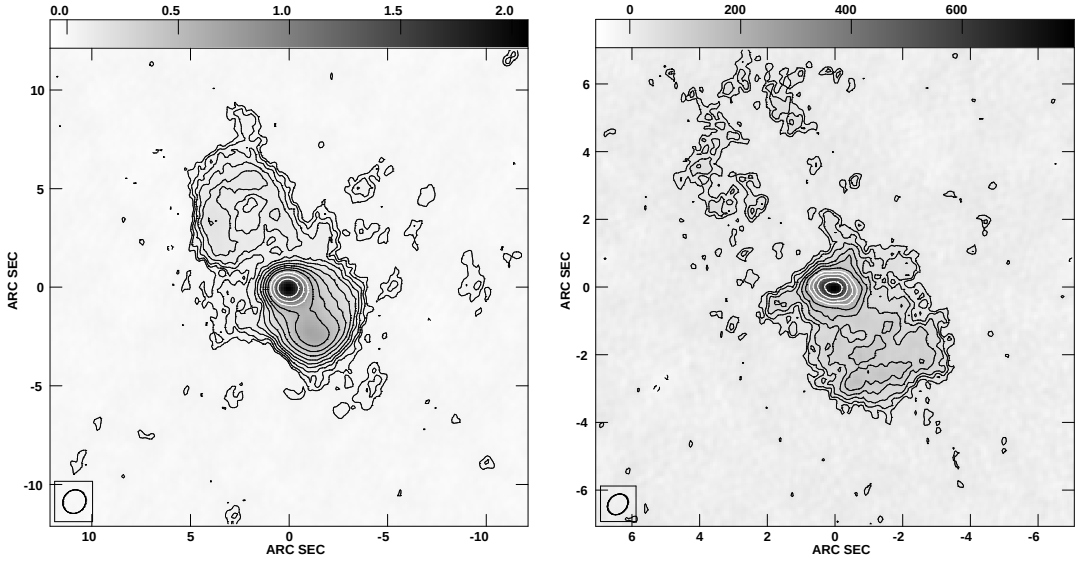

Figure 4.2: Maps made from combining A, B, C and D configuration *uv* data from all arrays at 4.8 GHz (left) and 8.4 GHz (right). The extention in the north-east is most visible at 4.8 GHz. Both maps are centred on the nucleus of NGC 4051 and made with ROBUST=0 to get a balance between the sensitivity and resolution weighting. Left map: At 4.8 GHz the rms noise level = 11.65μ Jy/beam and the beam size is $1.24'' \times 1.12''$. Right map: At 8.4 GHz, rms noise level = 10.14μ Jy/beam and the beam size is $0.67'' \times 0.54''$. The contours in both maps are at rms noise level $\times -$ $2.8, 2.8, 4, 5.6, 8, 11, 16, 23, 32, 45, 64, 90, 127, 180, 254$.

are $\sim$14 kpc and $\sim$7 kpc respectively.

4.3.2 Spectral indicies of VLA Data

The spectral index (α) value for a radio component can be determined from the flux value at two separate frequencies using $S = \nu^{\alpha}$. The spectral index values calculated in this section give an indication of the physical properties of the individual radio components. For example, in typical particle acceleration methods optically thin synchrotron emission is associated with a value of $\alpha = -0.7$. The method for producing the combined images which are used to make the spectral index maps shown in this section, is given in Section 4.2.1.2.

The resulting spectral index map for the combined ABCD data at 4.8 GHz and 8.4 GHz is shown in Figure 4.5. The spectral index is shown in grey scale (left map) and in colour (right map). The colour index of the right map reveals that the majority of the emission is optically thin i.e. assuming a spectral index of the form, α, the combined ABCD map has values of in the range of $0.9 < \alpha < -1.6$ with the majority of the values having steep spectral index values $-1.0 < \alpha < -1.6$.

In Figure 4.6 the contours which show the core region of the AGN (left map)

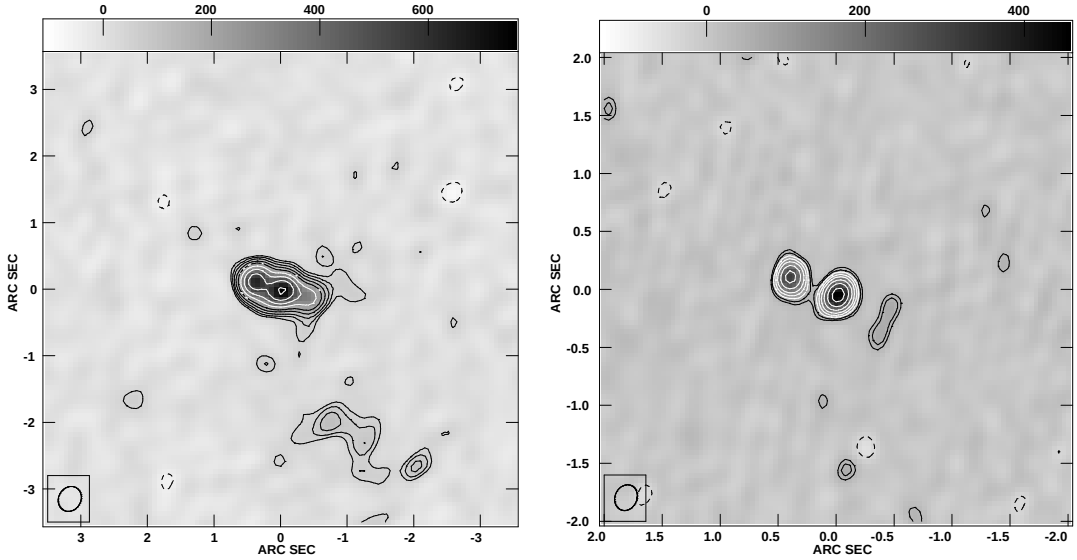

Figure 4.3: Maps made from combined the A configuration data at 4.8 GHz (left map) and 8.4 GHz (right map), in both maps I used ROBUST= 0 to give a balance between sensitivity and angular resolution. In the first map (left) at 4.8 GHz the rms noise level = 15.61μJy/beam and beam size is $0.38741'' \times 0.33345''$. For second (right) map at 8.4 GHz the rms noise level = 12.05μ Jy/beam and the beam size is $0.22742'' \times 0.18835''$. The contours in both maps are at rms noise level $\times -$ 2.8, 2.8, 4, 5.6, 8, 11, 16, 23, 32, 45, 64, 90, 127, 180, 254.

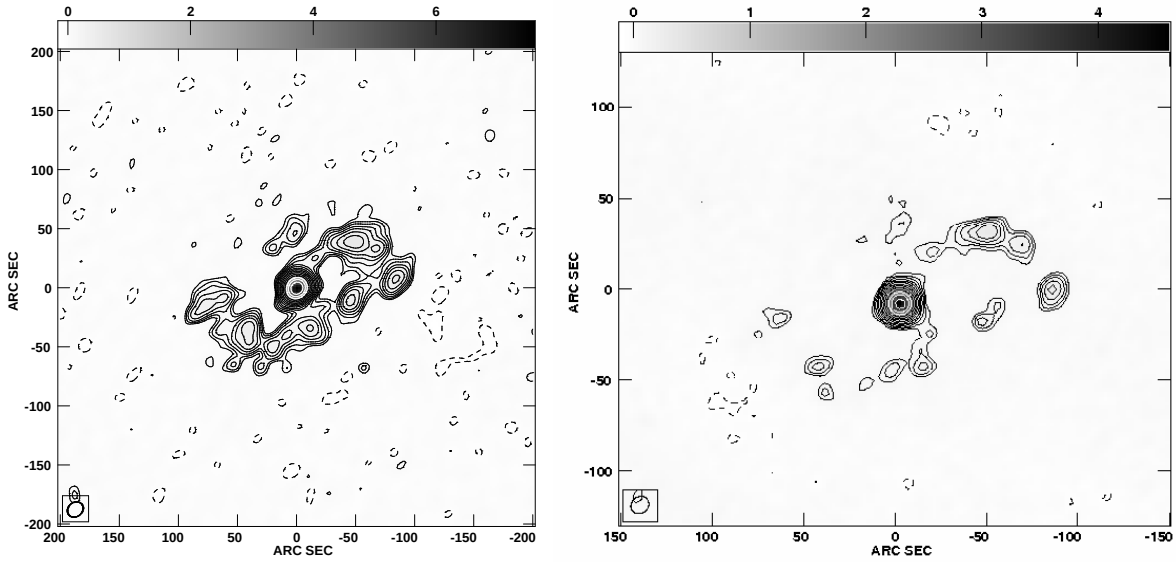

Figure 4.4: Maps made from combined D configuration data at 4.8 GHz (left map) and 8.4 GHz (right map), in both maps natural weighting (ROBUST =5 is used to give the highest sensitivity to the diffuse emission of the spiral arms. In the first map (left), at 4.8 GHz the rms noise level = $20.73\mu Jy/beam$ and the beam size is $14.19'' \times 11.96''$. For second map (right) at 8.4 GHz the rms noise level = $16.81\mu Jy/beam$ and the beam size is $8.02'' \times 6.82''$. The contours in both maps are at rms noise level $\times -$ 2.8, 2.8, 4, 5.6, 8, 11, 16, 23, 32, 45, 64, 90, 127, 180, 254.

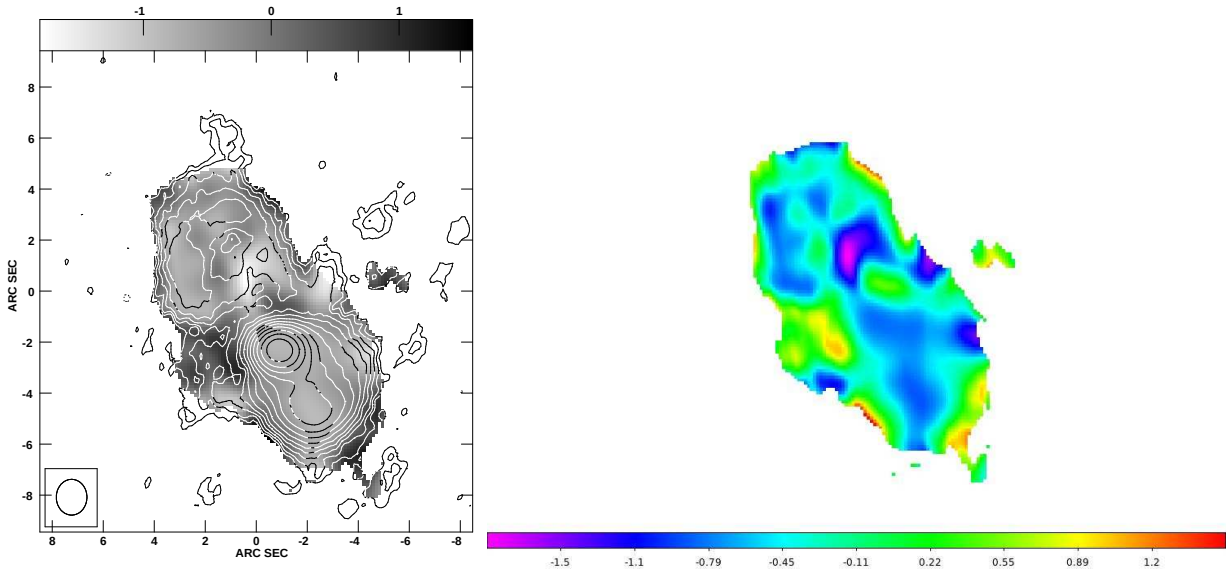

Figure 4.5: Maps of combined ABCD spectral index data. Left map: Flux contours from the 4.8 GHz map shown in Figure 4.2 overlaid on greyscale of spectral index. Contours are placed at 11.86 μ×-2.8,2.8,4,5.6,8,11,16,23,32,45,64,90,127,180,254 Jy/beam. Right map: Spectral index map as in left map with colour scale. Note that throughout this work I use $S = \nu^{\alpha}$.

give a spectral index value for the core $\alpha \sim -0.3$ (seen in green in right map in Figure 4.6). The relatively flat spectral index value is consistent with a self absorbed jet. The surrounding emission has steeper values, with most in the range of $-0.3 < \alpha < -1.6$ suggesting that the surrounding emission is optically thin and shows some signs of electron ageing. The spectral index value for the core , $\alpha \sim -0.3$, is consistent with the average value of the core spectral index presented earlier in Section 2.3.1.2 (see Figure 2.3 specifically), but inconsistent with the value obtained by Giroletti and Panessa (2009) who detect a moderately steep spectral index value of $\alpha = -0.7$ for the core. I suggest that the difference in resolution in the Giroletti and Panessa (2009) maps (one at 1.6 GHz and the other at 5 GHz) might explain this difference in measured α value. The extended structure was not detected in their 5 GHz maps.

4.3.3 1.6 GHz VLBI data

The structure of the inner regions of NGC 4051 is investigated using high resolution VLBI imaging. The image shown in Figure 4.7 is made from *uv* data reduced by Valeriu Tudose and image analysis was carried out by the author. The VLBI map shown in Figure 4.7 of NGC 4051 has a resolution of $\sim 0.02''$ and contains

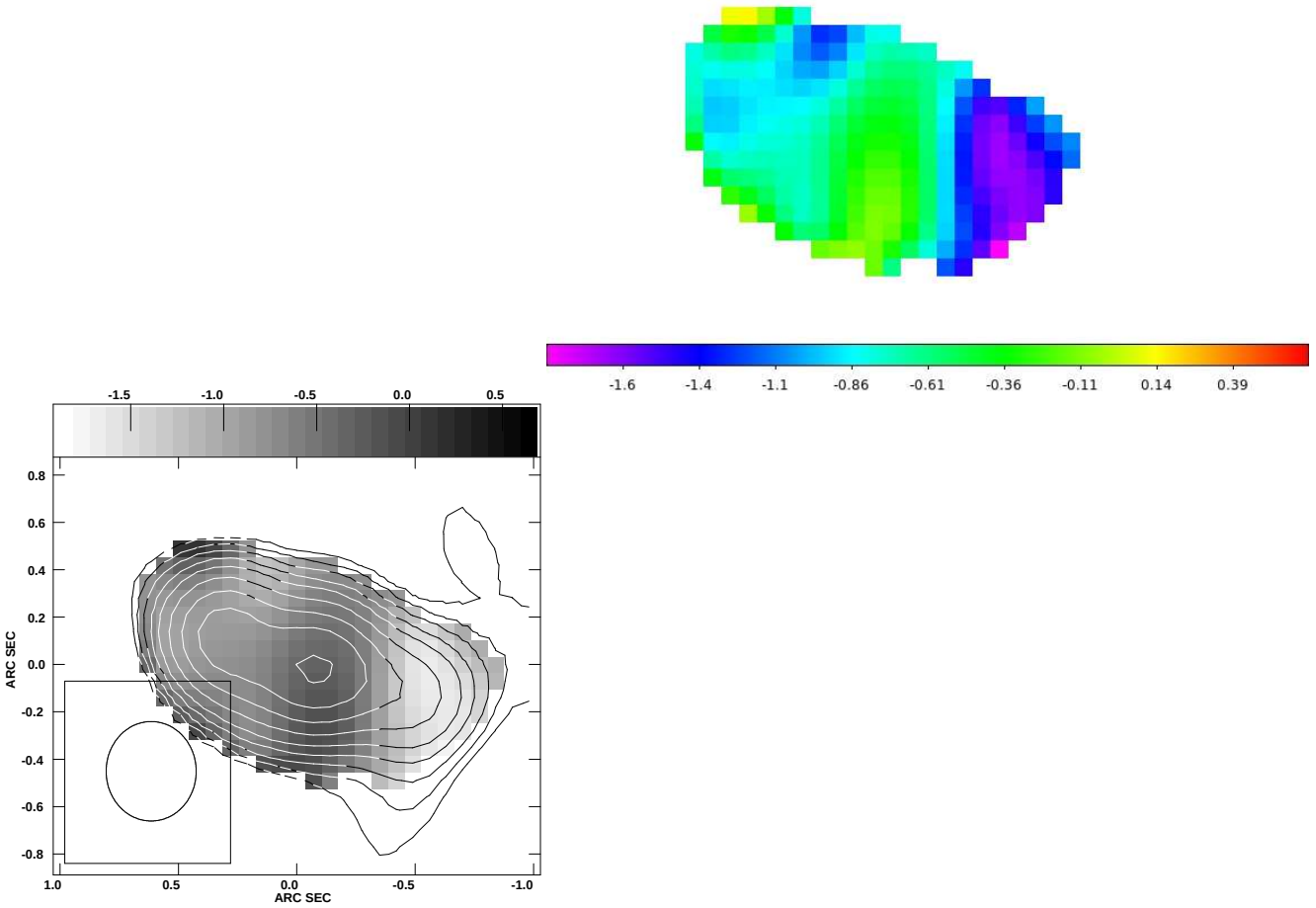

Figure 4.6: Maps showing A configuration spectral index data. Left map: Flux contours from the 4.8 GHz map shown in Figure 4.3 overlaid on greyscale of spectral index. Right map: Spectral index map as in left map with colour scale. Comparison between the two maps and the radio nuclei shown in the left map reveal that the core spectral index value is $\sim$ 0.3, which is consistent with the findings in Section 2.3.1.2.

combined data from both the VLBA, taken on 4th June 2004 (GM053) and EVN data observed on 22nd May 2003 (EM051); this map is referred to hereafter as the GM053+EM051 map. The GM053+EM051 map reveals a nuclear core and 2 components, a North-East (NE) component and a South-West (SW) component. The upper limit for the radius of the central source is $0.035''$ (equivalent to 2.6 pc). The two outer components are almost symmetrical about the core, with the NE component at PA 60 $^\circ$ with respect to the core. The NE and SW components are at a separation of $0.9''$ (equivalent to $\sim$ 66 pc). Each component is $\sim 0.45''$ from the core (see Table 4.2). The same 2 components are seen on both sides of the core in the A configuration maps in Figure 4.3. The structure of the NE component resembles a hotspot structure, much like that seen from an FRII jet. The 'hotspot' observed could represent the end point of an active jet which is slowly moving out into the intergalactic medium. Alternatively, the 'hotspot' might represent an area where the jet hits some surrounding gas/torus and is deflected. Within 40 mas from the compact core, extended radio emission toward the east is observed at ~ 3 σ level. This feature is likely an artifact, although its reality cannot be ruled out given the present data.

Figure 4.8 shows another image of the inner region of NGC 4051 reduced by Giroletti and Panessa (2009) (EVN data only) from 6th June 2007. This high resolution map is also observed at 1.6 GHz, and is referred to hereafter as the GP09 map. There are no obvious differences in the structure seen by visual inspection of the GM053+EM051 and GP09 maps. My analysis of the peak flux for all 3 components over the 3 year time period reveals no flux variations in the core or SW component. The core peak flux remained constant, 0.24 ± 0.03 mJy/beam in 2004, and 0.21 ± 0.03 mJy/beam in the 2007. However, a decrease in the measured peak flux of the NE component is detected which is not within the estimated error values, measured as 0.32 ± 0.04 mJy/beam in GM053+EM051, and 0.23 ± 0.03 mJy/beam in GP09. The core and the SW component are marginally resolved while the NW component is resolved. Given the higher spatial resolution of the GM053+EM051 data compared to the Giroletti and Panessa (2009) data, it is possible that some of the radio emission was resolved out in GP09.

As an aside I investigate if the core flux is being resolved out at VLBI resolutions $\sim 0.02''$ using the core flux value from VLA images at 4.8 GHz. I extrapolate an expected flux density value at VLBI frequency (1.65 GHz) from the actual core peak flux density at 4.8 GHz ($F_{4.8\ GHz} = 0.7$ mJy). I assume the spectral index value for the core is $\alpha = -0.3$, measured from VLA A configuration maps and the spectral index map in this chapter, see Figure 2.3 and Figure 4.6. The calcula-

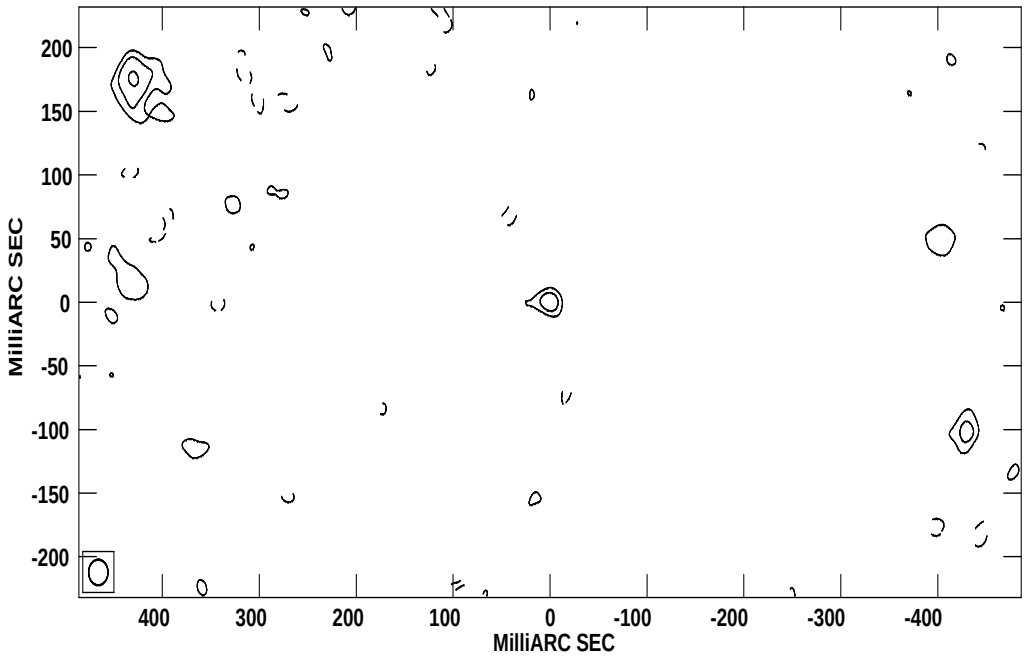

Figure 4.7: VLBI map of the GM053+EM051 data at 1652 MHz. Map is imaged with a beam size $0.02'' \times 0.02''$ and contours are at levels of 34 $\mu \times -3, 3, 5, 10$ Jy/beam. The 2 components to the NE and SW of the core are at a separation of $\sim 0.9''$ (equivalent to ~ 67 pc) and are assumed to be hotspots from a jet. Each component is $\sim 0.45''$ from the core (see Table 4.2). The same 2 components are seen on both sides of the core in the A configuration maps in Figure 4.3.

tion reveals a predicted value for the peak flux density of the core at 1.65 GHz is $F_{1.65\ GHz} = 1$ mJy. I measure a value of 0.24 ± 0.03 mJy for the core from VLBI maps this suggests that ~ 0.76 mJy of flux is being resolved out in the higher resolution images.

Figure 4.9 shows the 2007 GP09 map (in colour) overlaid with the 2004 GM053+EM051 map (contours). Both maps are imaged with the same beam size, cell size and contoured at the same levels so they can be easily compared. The radio emission from the 3 components appears coincident in the image plane, and no obvious relative motion is seen by visual inspection between 2004 and 2007. The proper motions of the outer (SW and NE) components (hotspots) are analysed further in the next Section 4.3.4.

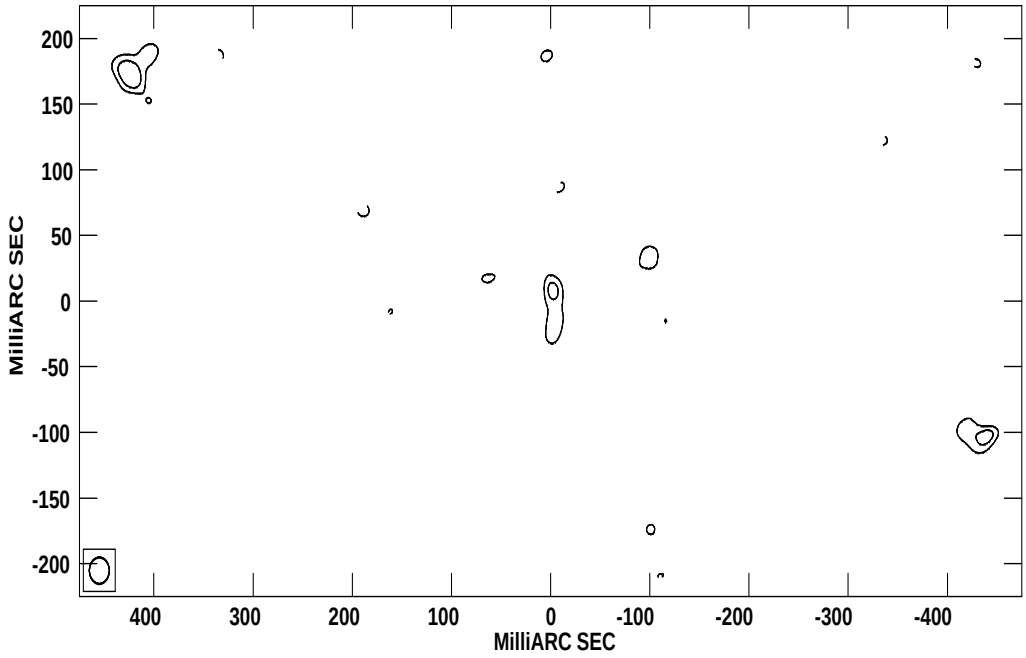

Figure 4.8: EVN Image of NGC 4051 observed in 2007 at 1652 MHz. Contour levels are at $34\mu \times -3, 3, 5, 10$ Jy per beam. Image made from work by Giroletti and Panessa (2009), convolved to a beam size $0.02'' \times 0.02''$ consistent with VLBI map in Figure 4.7.

4.3.4 Relative motion of hotspots

To investigate if the hotspots shown in VLBI maps are moving outwards with respect to the core I estimated the positions of each component in the 2004 and 2007 maps (the GP09 map and the GM053+EM051 map). Proper motion observed over a ~ 3 year period may indicate that the jet is 'active' and help confirm that the outer components represent the hotspots of a jet.

In Table 4.1 the absolute coordinates of radio positions from both VLBI maps from 2004 and 2007 are listed, see Figures 4.7 and 4.8 respectively. Coordinate positions were measured in the image plane using the AIPS task JMFIT. The task fits a Gaussian to a box drawn around the source and outputs the position of that source (peak of the Gaussian) and an error on the position in units of seconds and arcseconds. The overall error in the position depends on the accuracy of the Gaussian fit to the source, and the error in the position of the phase calibrator (J1221+4411 for both data sets). The error in the position of the phase calibrator in units of arcseconds was taken from the NRAO calibrator list. To calculate the total error for the three sources (the core, NE and SW components) I added both error sources in quadrature. The absolute coordinate positions of the core and NE component are

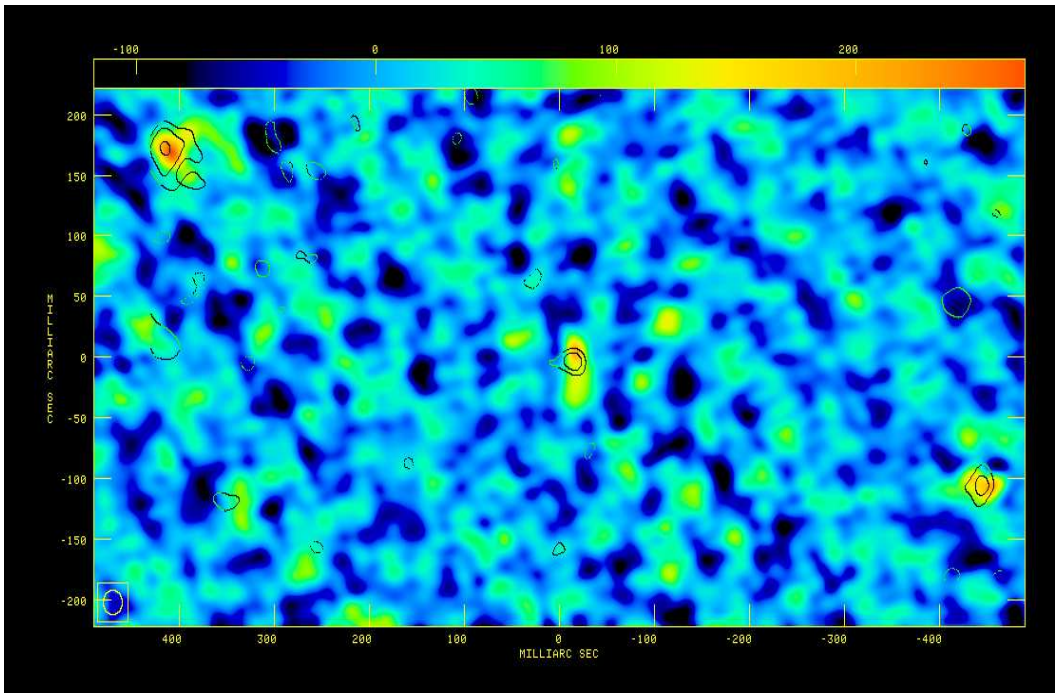

Figure 4.9: 2007 EVN Image shown in colour overlaid with 2004 VLBI contours. Both maps are imaged with a beam size $0.02'' \times 0.02''$ and a cellsize 0.001. The possible shift in the peak of the SW component can be clearly seen (orange coloured peak in 2007 EVN map) displaced slightly to the right with respect to the peak contour of the 2004 VLBI map.

compatible over the 3 year period i.e. within the estimated errors. However, the absolute positions of the SW components from VLBI imaging measured with a $\sim$ 3 year time gap, reveal a possible shift in the declination (DEC) which is not within the estimated errors. On visual inspection of Figure 4.9 the motion of SW component is plausible. However, the inclination angle of jet is not known for this AGN so calculating the absolute space motion cannot be achieved here. To further investigate the possible motion of the components with respect to one another, and to the core, I measured the relative positions in both maps. The relative distances between the NE-SW, Core-NE, and Core-SW components are shown in Table 4.2. Distances were measured in the image plane assuming that 1 arcsec = 74 pc. There is a very small increase in relative distance detected between the core and SW component (which can be seen in Figure 4.9 where the orange coloured peak in the EVN map is displaced slightly to the right with respect to the peak contour of the VLBI map). This small increase in relative distance over 3 years is equivalent to $<$ 0.5 mas (0.037 pc). The estimated upper limit on the speed of the SW component relative to the AGN core is 0.012 pc yr^{-1}, equivalent to a speed of $\sim 11,700$ km s^{-1} ($\sim$ 0.04c). This estimated speed is low compared with superluminal motion de-

Table 4.1: Absolute co-ordinate positions of NGC 4051 in the image plane from VLBI maps taken between 2004 & 2007.

		4 Jun 2004	6 Jun 2007
Component	Position[a]	Tudose VLBI	Giroletti EVN
Core	RA 12 03	09.61033 ±0.00018	09.61018 ±0.00020
	DEC 44 31	52.6769±0.0013	52.6789 ±0.0021
NE	RA 12 03	09.65054 ±0.00007	09.65011 ±0.00022
	DEC 44 31	52.8462±0.0010	52.8470 ± 0.0015
SW	RA 12 03	09.57053 ±0.00011	09.57029 ± 0.00024
	DEC 44 31	52.5677±0.0014	52.5715 ± 0.0014

[a] RA and DEC coordinates measured using the position of the peak flux density output from the task JMFIT.

tected in powerful AGN sources, and in Blundell *et al.* (2003) where superluminal motion is detected in a radio-quiet quasar. However, this apparent speed of ~ 0.04c is comparable with work by Ulvestad *et al.* (2005) on Seyfert galaxy NGC 4151 who measure speeds less than 0.050c and 0.028c at respective nuclear distances of 0.16 pc and 6.8 pc. These 'low' speed limits found in both this investigation and that of Ulvestad *et al.* (2005) indicate nonrelativistic jet motion dominated by a thermal plasma. The motion of the 'hotspot' components is investigated further in Section 4.5.

4.4 Anisotropic radio and optical emission

4.4.1 [OIII] Morphology

In this section I investigate the relationship between the radio structure (using the 4.8 GHz combined ABCD map, see Figure 4.2), and the optical [OIII]$\lambda\lambda 5007$ $-$ Å emission, typically associated with the forbidden line region (FLR). The nucleus

Table 4.2: Relative positions of NGC 4051 in the image plane from VLBI maps taken between 2004 & 2007.

Components	Relative Distance (arcsecs)	Relative Distance [a] (parsecs)
Tudose VLBI	4 Jun 2004	
NE-SW	0.90702±0.00333	67.127±0.247
Core-NE	0.46572±0.00320	34.464±0.237
Core-SW	0.44311±0.00337	32.790±0.249
Giroletti EVN	6 Jun 2007	
NE-SW	0.90425±0.00447	66.914±0.330
Core-NE	0.46248±0.00412	34.223±0.305
Core-SW	0.44361±0.00451	32.827±0.334

[a] Converted to parsec assuming that $1'' = 74\ pc$.

of NGC 4051 was observed using narrow band imaging of [OIII]λλ5007 -Å emission by Christopoulou *et al.* (1997) in 1993 using the Manchester Echelle Spectrograph (MES). The top image in Figure 4.10 shows the [OIII]λλ5007 $-$ Å emission overlaid with contours of the 8.4 GHz C array VLA map from work by Kukula *et al.* (1995). Christopoulou *et al.* (1997) explain that the linear extent of the [OIII]λλ5007 $-$ Å points along the minor axis of the galaxy and matches with the radio emission seen in this direction. From the top map in Figure 4.10 it is difficult to determine if the radio and [OIII]λλ5007 $-$ Å emission is one sided or two sided. To investigate this relationship with a deeper radio map, showing more detailed extended radio structure I use the combined ABCD map at 4.8 GHz (shown previously in Figure 4.2) in place of the contour map by Kukula *et al.* (1995). The deep combined ABCD map shows that the radio emission is clearly two sided, indicative of an outflow from the radio nucleus along PA 60 °in both directions. Further visual inspection reveals that the [OIII]λλ5007 $-$ Å emission region (shown in purple) is totally engulfed by the extended radio emission in the south-west and north-east. The fact that the [OIII]λλ5007 $-$ Å emission is brightest at the position of the radio nucleus and extends outwards on both sides (coincident with the radio extention) suggests that there are ionising cones of radiation centred on the radio nucleus. Both the ionising cone and radio emission point along the minor axis of the galaxy, at PA60 °. The observed alignment (seen in the bottom image in Figure 4.10) is strong evidence that the ionising area is double sided, and not single sided as suggested by Christopoulou *et al.* (1997) (they detected no extended

emission to the south west of the nucleus in their study (top map)). The ionisation cone and radio emission region are likely collimated by the same structure, such as the nuclear disk or torus. Assuming that the ionising cone is centred on the radio nucleus, then the extent of the [OIII] emission along the major axis of the galaxy at $PA \sim 135°$is $\sim 6'' = 444$ pc (measured from bottom map in Figure 4.10).

4.4.2 Radio morphology

Visual inspection of Figure 4.2 reveal radio morphology on scales of a few arcsecs with extended radio lobes detected at ~ 600 pc from the nucleus. While NGC 4051 is not bright enough in the radio to be classed as a 'radio galaxy' (it has a $L_R < 10^{39}$) I thought it would be interesting to access its radio morphology in the context of what is expected for a 'radio galaxy'. NGC 4051 has small scale 'weak' jet-like radio emission which exists on sub-kpc scales is indicative of an Fanaroff-Riley (FR) class I source. Regarding luminosity, I assume that all sources below a typical luminosity of $L_{FRI_{(178\ \mathrm{MHz})}} = 2 \times 10^{32}$ erg s^{-1}Hz^{-1}sr^{-1} are FRIs, from work by Fanaroff and Riley (1974). The total luminosity of NGC 4051 at 4.8 GHz from Figure 4.2 is $L_{4.8\ \mathrm{GHz}} = 2.42 \times 10^{27}$ ergs^{-1}Hz^{-1}sr^{-1}. Assuming the spectral index value $\alpha = -0.8$ (where $S = \nu^{\alpha}$) I estimate the typical FRI luminosity limit at 4.8 GHz, $L_{FRI_{(4.8\ \mathrm{GHz})}} = 1.38 \times 10^{31}$ ergs^{-1}Hz^{-1}sr^{-1}. Therefore, the observed luminosity value for NGC 4051 is a factor of 10^4 below the luminosity limit deduced by Fanaroff-Riley and suggests that NGC 4051 is an FRI source on luminosity grounds, as well as morphological grounds.

As an aside I investigated the radio properties using the radio loudness parameter, $\Re$ (Kellermann *et al.*, 1989). This is defined as the ratio of the galaxy flux density at at 5 GHz ($F_{5\ \mathrm{GHz}}$) to the 4400Å flux density (F_{4400}). For NGC 4051 at 4400Å the flux density is measured as $F_{4400} = 11.5$ mJy (measurement from Breedt (2009)) and from averaging the core A configuration flux at 5 GHz from the 2000-2001 data I measure a flux density at 5 GHz at $F_{5\ \mathrm{GHz}} = 1.8$ mJy. Given that the ratio is $\Re = 0.16$ and Radio Quiet (RQ) galaxies are defined as those with $\Re < 10$, NGC 4051 is therefore a RQ AGN. The fact that NGC 4051 is RQ, in combination with the findings of this section suggest that NGC 4051 is indeed an FRI type radio galaxy.

Note that from inspection of the small scale structure in Figure 4.7 NGC 4051 appears more like an FRII source and the measured core luminosity is lower than the hotspot luminosity value for the NE component (see Table 4.3). However, the FR galaxy type is usually determined from the images on scales $\approx 1-900$kpc (Fanaroff and Riley, 1974), which for NGC 4051 is more consistent with the scale observed in

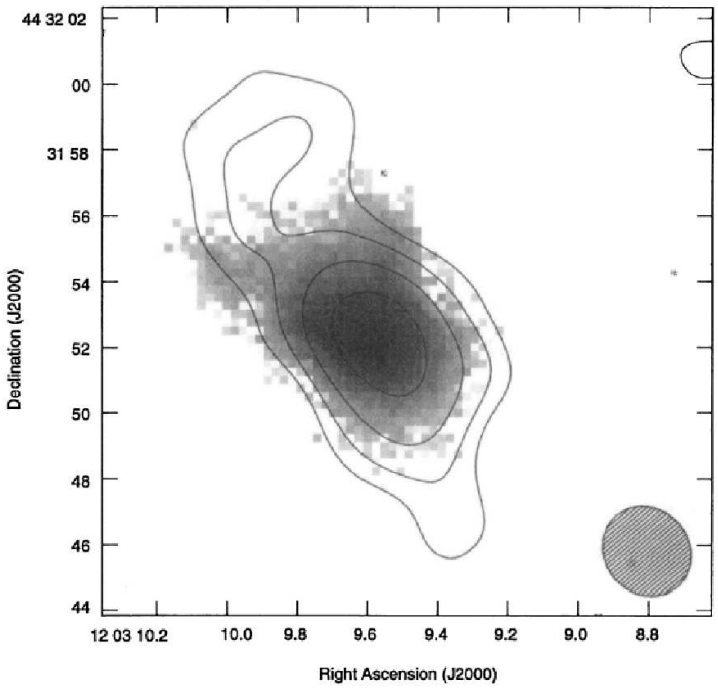

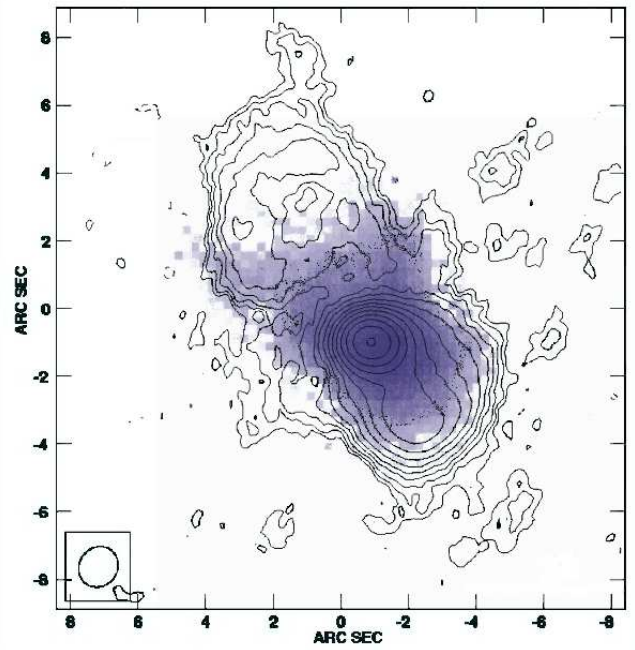

Figure 4.10: Top map: The MES [OIII] $\lambda\lambda 5007 -$ Å data is shown after continuum subtraction of NGC 4051 from V-band image in greyscale using a negative logarithmic scale. A contour map at 8 GHz from a C configuration VLA map from Kukula *et al.* (1995) is overlaid on the optical OIII greyscale map, as presented in Christopoulou *et al.* (1997). Bottom map: Combined ABCD contour map at 4.8 GHz from 2001-2002 VLA data overlaid on [OIII]$\lambda\lambda 5007 -$ Å data from Christopoulou *et al.* (1997) shown in purple. The optical emission region is engulfed by the extended radio emission in the south-west and north-east.

the combined ABCD map in Figure 4.2, where NGC 4051 has FRI-like morphology. I note here that from both the VLA and VLBI radio maps it is difficult to determine if the observed 'jet' is active i.e. currently being powered by the black hole. By calculating the jet energetics and timescales in the next sections I attempt to resolve this issue.

4.5 Energetics of Core and Lobes

Several studies have put forward the idea that the different spectral states observed in BHXRBs are analogous to different *classes* of AGN (Pounds *et al.*, 1995; Maccarone *et al.*, 2003; Fender *et al.*, 2009). Recent work on the 'fundamental plane of black holes' (Falcke *et al.*, 2004; Gültekin *et al.*, 2009; Broderick and Fender, 2011) has provided observational evidence that a correlation exists between radio and X-ray emission from black holes across a large range of masses. Assuming that the radio emission is from jet activity and that X-ray emission results from accretion this relationship indicates common disc/jet link for all BHs observed. The NLS1 AGN discussed in this work, NGC 4051, has an PSD comparable to the BHXRB, Cygnus X-1 during its 'soft state' (see Figure 1.8). Other constraints on the 'state' of NGC 4051 involve comparison of the radio luminosity $L_{8.4\ GHz}$ (where $L_{8.4\ GHz}$ is the luminosity over the observing frequency band i.e. $\nu \times L_{\nu}$) and the Eddington luminosity L_{Edd}. For NGC 4051 $L_{8.4\ GHz} = 2.5 \times 10^{36}\text{ergs}^{-1}$ and $L_{Edd} = 2.3 \times 10^{44}\text{ergs}^{-1}$ therefore, $L_{Edd} >> L_{8.4\ GHz}$, which suggest NGC 4051 is definitely not in a 'hard state'. When a BHXRB is in a 'soft state' it is assumed that the jet is suppressed (Gallo *et al.*, 2003; Fender *et al.*, 2009; Fender, 2001b). The 'fundamental plane of black holes' is defined best by 'hard state' BHs (where it is assumed the jet is active). Radio quiet sources such as Seyferts are a source of scatter in the 'fundamental plane' relation, the reason for the observed scattering of Seyfert galaxies about the plane is as yet unknown (Gültekin *et al.*, 2009), however, several possible reasons for the scatter are discussed later in Section 5.2.

This thesis has shown much evidence for jet emission from the core of the AGN NGC 4051. If one naively assigns the accretion states used for BHBs, then NGC 4051 is in a 'soft state' where jet activity is not expected. To investigate this 'jet' behaviour further I investigated the position of the AGN with regard to the 'fundamental plane of black hole activity' which is well defined by black hole sources. As yet no relationship exists for 'soft state' BHs as they are not associated with jet activity. I find that NGC 4051 is $\sim$ 3 times radio fainter than 'fundamental

plane of black hole activity' (when the plane is defined by only hard state BHBs and LINERS) using the relationship from Körding *et al.* (2006a) (shown previously in Figure 2.14).

At present there are no other studies of AGN synonymous with 'soft state' BHXRBs for comparison to this AGN; however, in recent work on the soft state BHXRB 4U 1957+11 by Russell *et al.* (2011) they attempt to determine where this 'soft state' BHB system lies with regard to the 'fundamental plane'. This work reveals that the soft state BHXB 4U 1957+11 is at least 330-810 times fainter than the established hard state radio-X-ray correlation of (Corbel *et al.*, 2000; Gallo *et al.*, 2003) where $L_{Rad} \propto L_X^{0.7}$. There is no evidence for a jet in this BHXRB and measurements of radio emission for the source allow Russell *et al.* (2011) to estimate a stringent upper limit on the radio flux density for 4U 1957+11 at 5-7 GHz at $F_{4U} < 11.4\mu$Jy. This flux density measurement is equivalent to a logarithmic radio luminosity value of

In this section the magnetic field strength (B), pressure (P) and minimum energy density (U_{min}) are estimated for both the extended emission (lobes) in the NE and SW and for the core of NGC 4051. These physical parameters are calculated by assuming equipartition of the energy density between the relativistic particles (U_e) and the magnetic field (U_B). An introduction to equipartition theory is given in Section 1.6.2. To calculate the physical parameters I assume the distance to NGC 4051 is 15.2 Mpc so $1''$ is equivalent to 74 pc using the distance estimate from Russell (2003). I also assume a black hole mass $M_{BH} = 1.91 \times 10^6\ M_\odot$ from (Peterson *et al.*, 2004).

For all the maps presented here I have calculated the flux density for the North-East component (NE), the Core and the South-West (SW) component, and measurements are shown in Table 4.3. The flux density values are used in combination with the spectral index to determine the minimum energy in each component using equipartition theory.

The flux density values for the first 6 measurements in Table 4.3 are calculated from the maps made at 4.8 GHz. The last three measurements are from VLBI Maps at a frequency of 1.6 GHz. The flux density values were taken from the combined maps (labelled COM in Table 4.3, see Figure 4.2), the A configuration maps (Figure 4.3) and the VLBI maps (Figure 4.7) presented in this chapter. To calculate the core flux density for the central compact component in each map a rectangular box was drawn. The size of the rectangular box used to integrate the flux is shown in Table 4.3 under the heading 'Component size'. The complex nature of the ex-

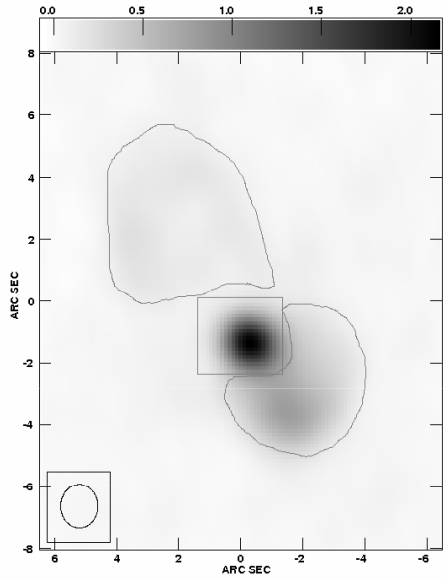

Figure 4.11: 4.8 GHz map showing the approximate area used to calculate the flux density values for the COM-NE, COM-Core and COM-SW components presented in Table 4.3.

tended emission in the combined maps (in both the NE and SW) required drawing out an area by hand around the extended emission, this area was approximated to an ellipse for calculating the energetics of the lobes. The flux density from the area drawn by hand was then used to calculate the values of COM-NE and COM-SW in Table 4.3. The peak flux density stated are those calculated by the task JMFIT within AIPS. This task fits a Gaussian to the pixels within a box, and can be used on the A configuration and VLBI data since the components in these high resolution maps are resolved or almost resolved. The error in the flux density values is calculated from summing in quadrature the JMFIT error and the standard 5% error on the flux density. The flux density values quoted for the core components in the 'Flux Density' column of Table 4.3 are peak flux values; however, the core is marginally resolved therefore the peak flux density and the 'total' (or integral) flux density are comparable (within the measured errors). For the combined 4.8 GHz map (see Figure 4.2) the NE and SW components are extended, which means the components are not well modelled as Gaussians. I therefore, did not use the task JMFIT here, but instead took the flux density integrated over an area drawn out by hand around the extended features (see Figure 4.11 for the approximate size of areas integrated over). The error in the flux density for the combined maps is calculated differently also because errors cannot be estimated from a Gaussian fit, as with JMFIT. As a result the error for the COM-NE and COM-SW components is calculated by summing in quadrature the rms noise (which is of the same order as the error output by

JMFIT) with the standard 5% error on the flux density value.

At VLBI resolution I have only one frequency of data (1.6 GHz) so the spectral index values measured from A configuration maps at 8.4 GHz and 4.8 GHz were used to calculate the energetics of the 3 VLBI components. Use of the spectral index values in both A and VLBI maps is a reasonable assumption since the 3 almost linear components seen in the A configuration maps (Figure 4.3) have the same co-ordinate positions in the VLBI maps (Figure 4.7).

Table 4.3: Physical Properties and Energetics of the NE, SW and Core Components.

Component	Flux Density [a] ($\times 10^{-4}$Jy)	Spectral Index [b] $\alpha_{8.4}^{4.8}$	Component size (arcsec^2)	B_{min} (10^{-9} Tesla)	Pressure (P) (10^{-10}Nm^{-2})	$U_{\rm min}$ (10^{-9} Jm^{-3})	$E_{\rm min}$ ($10^{50} erg$)
COM-NE	15.03 ± 0.81	-0.30	6.0×4.5	1.5	0.004	0.0012	90.3
COM-Core	20.20 ± 1.02	-0.80	2.4×2.4	5.1	0.034	0.010	86.6
COM-SW	27.47 ± 1.41	-0.69	5.0×3.0	3.0	0.061	0.0069	169.0
A-NE	7.26 ± 0.36	-0.73	0.8×0.8	9.0	0.110	0.031	10.0
A-Core	7.81 ± 0.38	-0.30	0.4×0.4	22.0	0.63	0.19	7.56
A-SW	6.06 ± 0.24	-0.68	0.6×0.6	10.3	0.14	0.043	5.6
VLBI-NE	3.22 ± 0.35	-0.73	0.03×0.03	94.6	11.9	3.6	0.059
VLBI-Core	2.41 ± 0.34	-0.30	0.02×0.02	100.0	13.2	4.0	0.019
VLBI-SW	1.80 ± 0.32	-0.68	0.04×0.04	60.6	4.9	1.5	0.057

[a] For the first 6 components in this table the 4.8 GHz maps are used to measure flux density values. The VLBI data (bottom 3 values in table) were at a frequency of 1653 MHz.

[b] Using $S = \nu^{\alpha}$, consistent with the scale used in the spectral index maps (see Figure 4.6) and other spectral index results in this thesis.

4.5.0.1 Core jet power from radio luminosity

Throughout this work I have assumed that NGC 4051 is analogous to a 'soft state' BHB system. I can therefore also assume that it is radiatively efficient and the Eddington ratio, can be estimated from the bolometric luminosity L_{bol}. Assuming equipartition, the upper limit on the jet power $P_{jet_{core}}$ can be compared to the accretion power (equivalent to L_{bol}) to investigate if $P_{jet_{core}} < L_{bol}$ which is the expected relationship for 'soft state' BHs with a high accretion rate (optically thin accretion disc) and a 'quenched' jet. Note that for 'hard state' BHs the opposite applies and $P_{jet} > L_{bol}$ since this state is associated with a powerful jet and inefficient accretion. L_{bol} is calculated using Equation 21 from Marconi *et al.* (2004) using the average X-ray luminosity at 2-10 kev during the period of the 2000-2001 observations is $L_{2-10\text{ kev}} = 6.27 \times 10^{41}$ ergs^{-1}, which gives a bolometric luminosity value $L_{bol} = 2.3 \times 10^{43}$ ergs^{-1}.

To calculate jet power one must assume the NGC 4051 jet behaves like the standard 'hard state' jet since no 'soft state' AGN or BHXBs with a 'jet' currently exist. Körding *et al.* (2006b) have devised a novel way to determine the jet power independent of X-ray luminosity. Their method assumes that radio emission from the jet can be used as a tracer of the accretion rate. The resulting P_{jet} value is normalised using sources with known accretion rates. To normalise the jet power in this work they use radio luminosity of several 'hard state', efficiently radiating BHs close to state transition at 8.6 GHz $L_{8.6\text{ GHz}}$, giving a normalising luminosity of $L_0 = 10^{30}$erg s^{-1}. At this measured radio luminosity the accretion disc around a 10 $M_\odot$ BH changes its spectral state. From Equation 4.1 (Equation 5 in Körding *et al.* (2006b)) the calculated value of the kinetic jet power for NGC 4051, $P_{4051\,jet}$ is calculated:

$$P_{jet_{core}} = 3.6 \times 10^{37} (\frac{f}{0.75})(\frac{\eta}{0.1})(\frac{L_{8.4\ GHz}}{L_0})^{\frac{12}{17}} \text{ergs}^{-1} \text{ergs}^{-1}{}_{\text{ergs}^{-1}{}_{\text{ergs}^{-1}}} \qquad (4.1)$$

In Equation 4.1 f reflects the part of the total accretion rate external to the radiating region which is actually accreted and not ejected into the jet or winds and η is the disc efficiency. The factor f can depend on the accretion rate, but for this work it is assumed that $f = 0.75$, as is this case for all objects studied in Körding *et al.* (2006b). The disc efficiency for NGC 4051 is assumed as $\eta = 0.1$, which is the standard assumption for the efficiency of accretion onto a compact object, such as a black hole. The average radio luminosity for the core at 8.6 GHz used in

Equation 4.1 was taken from measurements of the 8.4 GHz radio emission in the 2000-2001 A configuration maps (see Figure 4.3). The average radio luminosity of the core of NGC 4051 at 8.4 GHz is approximately the same as the luminosity at 8.6 GHz, therefore, I substituted $L_{8.6\ GHz} = 2.5 \times 10^{36}$erg s^{-1} into Equation 4.1 to determine the jet power for NGC 4051, $P_{jet_{core}} = 1.18 \times 10^{42}$erg s^{-1}. Therefore, from previous calculations of L_{bol}, $P_{jet_{core}} < L_{bol}$ as expected for a 'soft state' BH. Assuming a black hole mass for NGC 4051 of $M_{SMBH} = 1.91 \times 10^6 M_{\odot}$ from (Peterson *et al.*, 2004), the Eddington Luminosity for NGC 4051 is $L_{Edd} = 2.29 \times 10^{44}$erg s^{-1} therefore, from the value of L_{bol} calculated I estimate that NGC 4051 is radiating at $\approx 10\%\ L_{Edd}$.
After calculating the core jet power $P_{jet_{core}}$ the next step in this analysis is to investigate if $P_{jet_{core}}$ can provide enough power to inflate the observed lobes.

4.5.0.2 Lobe jet power from equipartition theory

In this section I determine the energy and jet power for the observed lobes from the physical parameters in Table 4.3. The radio lobes are visible in the combined ABCD map at 4.8 GHz shown in Figure 4.5 and from measuring the flux density and approximate area of the lobes the pressure (P) is determined from equipartition theory. In order to estimate the jet power from the pressure I follow the method of Allen *et al.* (2006). Allen *et al.* (2006) estimate the energy required to create the observed lobes in nine X-ray luminous elliptical galaxies from the thermal pressure (P) of the X-ray emitting gas, using Equation 4.2.

$$E = \frac{1}{(\gamma - 1)PV + PdV} = \frac{\gamma}{\gamma - 1} PV = 4PV \tag{4.2}$$

In Equation 4.2 the total energy (E) is equivalent to the sum of the internal energy within the bubble and the PdV work done. The thermal pressure (P) is estimated from the observed X-ray temperatures and densities of the surrounding gas, V is the volume of the cavity and γ is the mean adiabatic index of the fluid within the cavity. For the X-ray luminous galaxies in work by Allen *et al.* (2006) the X-ray temperatures and densities are known for the regions of observed radio lobes. For NGC 4051 X-ray data exists for the vicinity of the core only and therefore one cannot calculate a value for pressure using the known physical properties of the gas surrounding the lobes. However, for NGC 4051 I can use the pressure (P) measurement calculated from equipartition arguments to calculate the energy (E), using Equation 4.2, assuming that the lobe consists of a relativistic plasma where $\gamma = \frac{4}{3}$. The resulting value of the energy of the lobes is $E = 4PV$. From knowing

this energy value (E) another measurement of the jet power P_{jet} can be calculated from an estimate of the lobe age, t_{buoy} from $P_{jet} = \frac{E}{t_{buoy}}$.

Following work by Dunn *et al.* (2005) I assume that the small scale lobes to the NE and SW of the core, shown in Figure 4.2 behave as detached bubbles (like the radio bubbles in clusters of galaxies). In the study by Dunn *et al.* (2005) bubbles of radio emission are assumed to rise upwards (in a direction perpendicular to the major axis of the host galaxy) at their buoyancy velocity. The buoyancy velocity, v_{buoy} is defined as $\nu_{buoy} = \sqrt{(2gV/SC_D)}$, where S is the cross-sectional area of the bubble and V is the volume. The value of g is calculated from $g = GM(< R_{dist})/R_{dist}^2$ for the lobe/bubble centre at R_{dist} from the cluster core. $C_D = 0.75$ is the drag coefficient from work by Churazov *et al.* (2001). The age of the lobe/bubble (t_{buoy}) is estimated from the time required for the bubbles of the observed size to rise buoyantly through a uniform medium from the galaxy centre to their current radii, and is defined by $t_{buoy} = \frac{R_{dist}}{v_{buoy}}$. Other methods for calculating the age of the bubble/lobe are discussed further in Dunn *et al.* (2005). It is worth noting here that for bubbles attached to jets the age defined as $t_{age} = \frac{R_{dist}}{c_s}$ is used by Dunn *et al.* (2005), over the t_{buoy} age. However, for NGC 4051 the adiabatic sound speed c_s cannot be calculated since the temperature of the X-ray emitting gas is not known. Nevertheless, the work by Dunn *et al.* (2005) shows that both t_{age} and t_{buoy} give comparable timescales, thus t_{buoy} is used here as an approximation.

$t_{inflate}$ is calculated assuming that the lobes are inflated with the core jet power calculated in Section **??** ($P_{jet_{core}} = 1.18 \times 10^{42}$erg s^{-1}). This is 5 orders of magnitude greater than the power to inflate the lobes ($P_{jet_{lobe}} \approx 10^{37}$erg s^{-1}), therefore I can conclude that the core jet does have enough power to inflate the observed lobes. The estimated $t_{inflate}$ value is determined for the NE and SW components assuming that $t_{inflate} = \frac{E_{min}}{P_{jetcore}}$. The inflation speed is given by $v_{inflate} = \frac{R_{dist}}{t_{inflate}}$, which gives superluminal speeds for the lobes. From these very large speed estimates $v_{inflate} \geqslant c$ I conclude that it is most likely that Equation 4.1 does not apply to this AGN. Another reason for this over estimate of $v_{inflate}$ could be that the E_{min} value for the lobes calculated from equipartition arguments (see Table 4.3) is overestimated. However, it is unlikely that it would be overestimated by factors > 10 which are required to account for these large speeds.

c = 2.99×10^{-5}kms^{-1}

As an aside I investigate the use of a radio spectral break for estimating the lifetime of the jet. A steepening of the radio spectra towards higher frequencies is

Table 4.4: Energetic properties of the lobes detected in the NE and SW in Figure 4.5.

Component	$E = 4PV$	v_{buoy}	t_{buoy}	$t_{inflate}$	$v_{inflate}$	$P_{jet_{lobe}} = \frac{E}{t_{buoy}}$
Units	10^{52} erg	kms^{-1}	10^7 yrs	yrs	c	10^{37} erg s^{-1}
COM-NE	1.19	6.7	3.2	319.8	4	1.16
COM-SW	6.76	11.2	1.6	1807.5	0.4	13.3

suggestive of electron ageing. A break in the spectrum occurs at a frequency where the electrons are no longer being accelerated. Measuring this break frequency allows an estimation of the break timescale, which indicates the length of time passed where the electrons have not been accelerated. Estimating a short break timescale indicates that the jet is active. To determine the break timescale (T) for NGC 4051 (where $T \propto \nu^{-\frac{1}{2}}$) one must first deduce the frequency (ν) of the spectral break. A break in the radio spectrum is not detected for NGC 4051 from current observations. Assuming that the break occurs at $\nu \sim 4.8$ GHz the break timescale is calculated at $T = 5 \times 10^6$ years. However, the value of ν_{break} is very uncertain here, and probably $\nu_{break} < 4.8$ GHz in the lobes, therefore the actual break timescale is more likely $T > 5 \times 10^6$ years, which is consistent with the estimated buoyancy times (t_{buoy}) shown in Table 4.4. This predicted lower limit on the break timescale provides further evidence for a jet age $T > 10^6$ years, which is in opposition to the calculated $t_{inflate}$ values of $\sim 10^3$ years (for the SW component) shown in Table 4.4. Assuming the speed of $11,700$ kms^{-1} ($\sim 0.04c$) estimated from the relative motion of the SW hotspot the age of the jet is again estimated at a younger age of $\sim 10^3$ years. It is difficult to determine which is the best estimate for the jet age, given the many assumptions which have been made in this section, both estimates are plausible. The hotspot and lobe emission which is detected within < 1 kpc from the nucleus could be a result of a young jet aged $\sim 10^3$ years, however, the jet scales detected may be a result of frustrated jets which are impeded by dense interstellar medium where jet age is $T > 10^6$ years.

4.6 Conclusions

In this chapter I have presented the deepest radio observations of NGC 4051. This data included a combination of VLA and VLBI data which was used to determine both the structural and spectral properties of this Seyfert galaxy. This investigation of high resolution VLBI radio imaging in combination with the lower resolution VLA data (presented in previous chapters) provides strong evidence for jet emission from the nuclei of NGC 4051.

The spectral index maps of the core (during A configuration) indicate a central self absorbed jet (where $\alpha \sim$ -0.3). The surrounding structure has a steeper spectral index value, indicating optically thin synchrotron emission. The VLBI images show that the core emission is confined to a radius of $\sim$ 3pc and hotspots are detected at $\sim$ 35pc aligned along PA$\sim 60^{\circ}$(comparable to the alignment of the extended emission in the combined maps). Extended lobes of radio emission (associated with the jet) are detected up to $\sim$ 600pc from the nucleus in the combined ABCD configuration VLA maps.

Both the absolute and relative positions of the NE and Core components appear unchanged over the 3 years between VLBI observations. An upper limit on the small increase in the relative distance between the core and SW component is measured at 0.5 mas (0.037 pc) over $\sim$ 3 years. This is equivalent to an apparent velocity for the SW component relative to the core of 0.012 pc yr^{-1}, which corresponds to a speed of $11,700$ kms^{-1} ($\sim$ 0.04c). This value is comparable to work by Ulvestad *et al.* (2005) on Seyfert galaxy NGC 4151 who measure speeds less than 0.050c and 0.028c at respective nuclear distances of 0.16 pc and 6.8 pc this calculated speed gives an estimated jet age of $\sim 10^3$ years.

Estimates of the buoyancy speed of the lobes, and the break timescales from the radio spectral index provide evidence for radio activity in NGC 4051 occurring on timescales greater than $> 10^6$ years. Given the radio structure observed and the calculated timescales it is difficult to determine if the jet is 'active' (particles being pumped into the radio lobes) since at VLBI scales radio emission is not detected connecting core to lobe emission, higher resolution imaging is required to detect such emission.

The nucleus of the optical [OIII]$\lambda\lambda 5007 -$ Å emission is coincident with core radio emission and extends away from the core on both sides. These findings suggest that a double sided ionisation cone exists. The alignment of the radio emission and [OIII]$\lambda\lambda 5007 -$ Å emission along $PA \sim 60^{\circ}$suggests they are collimated by the same disc or tori.

The jet detected in NGC 4051 is of non-negligible power. It is more powerful than ‘soft state’ binaries and not far different from the ‘hard state’ systems which define the fundamental plane of black hole activity. Therefore, I conclude that the analogy between AGN and BHBs may not be exact despite Seyferts having PSDs which resemble those of ‘soft state’ BHBs.

Sometimes answers lead to more questions.

AGENT OLIVIA DUNHAM

5 Conclusions and Future Work

In this concluding chapter, I give a summary of all findings of this work and discuss the implications of these results. Finally, I comment on the potential for future work.

5.1 Summary of Findings

I have presented in this thesis one of the first studies of the short and long timescale radio/X-ray variability of an individual Seyfert AGN. This work offered the first in depth look not only at the complex radio variability but also the deep radio structure and the possible radio/X-ray correlation of the Seyfert NGC 4051 whose PSD is analogous with a 'soft state' BHB.
The radio data used in this thesis are a combination of VLA and VLBI data. The X-ray data are part of an ongoing X-ray monitoring program using RXTE to measure the broadband X-ray power spectral densities of AGN.

The main conclusions of this work are summarised as follows:

- Despite factors of 10 X-ray variability, there is no clear evidence for radio variability in the core emission of NGC 4051 at 8.4 GHz with the possible exception of very low amplitude (~ 0.12 mJy) variations during the A

configuration observations where the core is best resolved from surrounding structures.

- The deep VLA observations reveal a mean spectral index value $\alpha \sim -0.3$ (where $S = \nu^{\alpha}$) for the core of NGC 4051. This relatively flat spectrum suggests that the core represents a self absorbed jet. The surrounding emission has steeper spectral index values in the range of $-0.5 < \alpha < -1.6$ which suggests this emission is optically thin synchrotron emission.

- During the A configuration observations both VLA radio data sets (2000-2001 and 2008-2009) reveal a very weak positive correlation between the radio and much larger amplitude X-ray variations. There is no evidence for a β value much greater than ~ 0.1 for the $L_R \propto L_X^{\beta}$ relationship, which is consistent with constant radio luminosity. This weak correlation which is as much as $\sim 6\sigma$ different to the $\beta = 0.7$ relationship (Gallo *et al.*, 2003; Merloni *et al.*, 2003; **?**; Gültekin *et al.*, 2009) suggests that the disc to jet coupling may be different for NGC 4051. A reason for the difference of β value between NGC 4051, and the 'hard state' objects which define this relationship is that NGC 4051 has more quiescent radio emission than is typical for 'hard state' jets. Features which are constant will therefore dilute the variability of the core. Another possibility is that NGC 4051 does not have a jet, and its lack of radio variability is explained by radio emission originating in the corona. A coronal model agrees well with the radio/X-ray flux ratio, and the lack of radio variability, but the collimated radio structure is then hard to explain. A mixture of jet and coronal emission may explain the observations.

- The resultant mean radio and X-ray luminosity make NGC 4051 a factor of ~ 3 radio quieter than the hard state objects which define the 'fundamental plane of black hole activity', although the scatter about the plane is of the same order.

- On re-examination of the 2008-2009 radio observations of King *et al.* (2011) flaws were found in their analysis. From my own analysis of the 2008-2009 VLA data and quasi-simultaneous RXTE data a weak positive relationship between the two regimes is found, which is in agreement with the results found for 2000-2001 VLA data. A positive correlation is therefore more likely than the anti-correlated disc/jet coupling which King *et al.* (2011) proposed for AGN NGC 4051.

- The radio and X-ray lightcurve data used in CCF analysis have very limited sampling and the lack of priori knowledge regarding the lags has the effect of lowering the significance of the CCF peaks. However, there is suggestive evidence that that radio emission lags X-ray emission by 12 ± 6 days and 15 ± 6 days for 8.4 GHz and 4.8 GHz emission respectively.

- The core radio flux is found to increase very slightly by 0.26 ± 0.16 mJy between 1991 and 2008 during A configuration observations, this is equivalent to a flux increase of a factor of ~ 1.3.

- VLBI images show that the core emission is confined to a radius of $\sim$ 3pc. Hotspots are detected at $\sim$ 35pc from the core aligned along PA$\sim 60^{\circ}$. Extended lobes of radio emission (associated with the jet) are detected up to $\sim$ 600pc from the nucleus in the combined ABCD configuration VLA maps.

- The absolute positions of the NE and SW components from VLBI imagery measured with a $\sim$ 3 years time gap reveal a possible shift in the SW. An upper limit on the small increase in the relative distance between the core and SW component is measured at 0.5 mas (0.037 pc). This change in relative distance gives an apparent velocity for the SW component relative to the core of 0.012 pc yr^{-1}, equivalent to a speed of $11,700$ kms^{-1} (~ 0.04 c). This value is comparable to work on Seyfert galaxy NGC 4151 by Ulvestad *et al.* (2005) who measure speeds less than 0.050c and 0.028c at respective nuclear distances of 0.16 pc and 6.8 pc.

- Deep VLA radio imaging reveals double lobed radio emission, which lies along the same PA as the [OIII]$\lambda\lambda 5007 -$ Å emission. The nucleus of optical [OIII]$\lambda\lambda 5007 -$ Å emission is also coincident with the core radio emission from NGC 4051 (PA$\sim 60^{\circ}$). This structure reveals a double sided ionisation cone, where both radio and optical emission are collimated by the same disc or tori.

Overall, low level radio variability is detected in the core of NGC 4051 at 8.4 GHz. These low level radio variations are weak in comparison to the X-ray variability. The exact relationship between the radio/X-ray emission in the core is unclear, with a weak positive correlation being most likely. NGC 4051 lies just below the well defined 'hard state' fundamental plane of black hole activity, but within the scatter of the plane. It is more radio bright than than the extrapolated value for a single 'soft state' BHB system. These findings suggests that disc to jet coupling may

be different for this AGN, and that the analogy between AGN and BHBs may not be exact despite this and other Seyferts having PSDs which resemble those of 'soft state' BHBs. Both VLBI and deep VLA radio observations provide strong evidence for jet structure and there is evidence for radio activity for timescales $> 10^6$ years.

5.2 The Implications of this Work

Nuclear radio emission is detected in many Seyferts, on subkiloparsec scales (e.g. de Bruyn and Wilson, 1978; Ulvestad and Wilson, 1984a,b, 1989). The current favoured explanation for this nuclear radio emission is based on the model of accretion onto a central supermassive black hole. The presence of a directed outflow/jet from the nucleus of Seyferts provides strong support for a central black hole and accretion disc model (Kukula *et al.*, 1999; Mundell *et al.*, 2003). Also, recent work by Foschini *et al.* (2011) has revealed the first gamma-ray outburst from a NLS1 galaxy, PMN J0948+0022. This work combined with previous evidence for Seyfert outflows shows that NLS1's can host powerful jets, despite having a gas rich environment due to a high Eddington accretion rate. Much evidence is presented in this work which indicates that despite being Radio Quiet, the Seyfert galaxy NGC 4051 does have a weak jet which provides further proof that Seyferts exhibit jet emission on subkiloparsec scales. Comparisons between the PSDs of NGC 4051 and the Cygnus X-1 suggest that NGC 4051 is analogous with a 'soft state' BHB, therefore, the jet radio emission which is detected in this work may imply that jet emission is a feature of 'soft state' BHBs, and they are not fully quenched in the 'soft state'. However, high sensitivity radio observations of BHBs are needed to prove this. From this work it is difficult to be sure if the observed jet in NGC 4051 is 'active' (jet currently fuelling the detected radio lobes), the relative motion of the SW component relative to the core hints at this possibility. High resolution imagery which shows that the core emission is connected to hotspot emission is required to be certain of such activity.

Several recent surveys of Seyfert galaxies have detected nuclear radio variability (e.g. Mundell *et al.*, 2009; Wrobel, 2000) and many studies have also investigated the X-ray variability of both the continuum and line emission from Seyferts (e.g. Turner *et al.*, 1999; McHardy *et al.*, 2005; Breedt *et al.*, 2009). Work in this thesis provided one of the first attempts to investigate the quasi-simultaneous radio and X-ray variability of a Seyfert galaxy. Very weak radio variability is detected in NGC 4051, and this is at a much lower level than that detected in previous Seyfert

radio variability studies (e.g. Neff and de Bruyn, 1983; Mundell *et al.*, 2009; Falcke *et al.*, 2004). It is difficult to determine why NGC 4051 has such a small amount of radio variability detected in its core, one possibility is that a variable nucleus does exist, but it is mixed in with unresolved constant flux density radio-jet emission. Another possibility for the lack of variability may be orientation effects. Further radio/X-ray monitoring of NGC 4051 and other Seyferts at higher resolution e.g. VLBI, is required to accurately measure the nuclear radio variability of NGC 4051 and other similar Seyferts.

The weak positive radio/X-ray correlation which is detected in this work hints at a possible disc/jet connection. The disc/jet connection for black holes has been studied extensively for 'hard state' BHs using the 'fundamental plane of black hole activity' where the radio/X-ray emission scales with mass over many orders of magnitude. For Seyferts, where radio and X-ray luminosities have been measured, averages of these values, usually archival data, have been presented in studies of the 'fundamental plane'. In Radio Quiet Quasars (RQQs) the majority of the X-ray emission is thought to be a result of accretion flow as opposed to synchrotron emission (as in BL Lacs where most of the X-ray emission is from synchrotron). This makes RQQs more comparable to the 'soft state' BHBs than 'hard state' BHs. However, Seyferts sources lie relatively close to the 'hard state' plane, and do not appear to totally drop off the correlation like the 'soft state' BHBs (Körding *et al.*, 2006a). RQQs (usually Seyferts) generally provide much scatter in the relationship and the inclusion of a Seyfert sample, as opposed to using only 'hard state' samples changes the correlation value and increases the observed scatter (Körding *et al.*, 2006a; Gültekin *et al.*, 2009). The Seyfert discussed in this thesis lies only a factor of ~ 3 below the fundamental plane, and is within the scatter of the 'hard state' low luminosity AGN sample, therefore, the work presented in this thesis is in good agreement with previous findings for Seyferts, and shows that the quenching of radio jets in 'soft state' AGN is not as extreme as that observed in BHBs. However, this finding is grounded in the analogy between 'soft state' BHBs and AGNs with similar spectral states. Overall, the reason for the scatter in the fundamental plane is uncertain, some suggestions are measurement errors, beaming effects (Heinz and Merloni, 2004), effects of black hole spin and the spectral state of the accretion disc (Maccarone *et al.*, 2003). Gültekin *et al.* (2009) propose the scatter of Seyferts may be an indication that they are diverging away from the fundamental plane relation. There is also a "fundamental plane conspiracy" based on the fact that different X-ray emission processes exist in the BHs which are presented in fundamental plane investigations. In jet dominated sources, such as 'hard state' BHBs and BL Lacs, the

X-ray emission and radio emission is attributed to a jet, in RQQs, 'soft state' BHBs and LLAGN, the X-ray emission is more likely to be the result of accretion flow. However, all sources appear to follow the fundamental plane relationship despite having different X-ray emission processes (Körding *et al.*, 2006a). More accurate measurements of the radio and X-ray luminosities and BH masses are required for a large sample of black holes (specifically Seyferts and other sources of scatter) in order to better understand the disc/jet coupling in BHs.

5.3 Future work

The obvious first step in assessing the radio variability of NGC 4051 involves more sensitive, systematic, multi-frequency radio monitoring. Such radio monitoring should also be carried out on similar Seyfert galaxies, specifically those synonymous with 'soft state' BHBs. Observations of a large sample of Seyferts will allow characteristic timescales and the amplitudes of variations for the sample of Seyferts to be determined. Future variability studies should not use telescopes like the VLA which change configuration during the observation of the source. The changing of the array configuration adds unwanted complexity to studies of core radio variations. Telescopes such as the VLA should only be used to investigate radio variability when variability time scales are short (i.e. several 'flare events' within timescales of $\sim$ 100 days). The VLA is also better designed to measure variability in 'point like' cores, where surrounding complex extended emission is not a feature. Future radio variability investigations should be made with high angular resolution (e.g. VLBI) and Seyferts galaxies should be observed on a daily basis, giving well sampled, long period ($\approx$ year long) light curves. Such (VLBI) observations, where core emission is not contaminated would confirm whether the core radio emission from NGC 4051 (and similar Seyferts) is variable, giving a measurement of the variability scale for Seyferts. With the next generation of radio telescopes such as EVLA, eMERLIN and MeerKAT such long term radio monitoring observations will become routine.

Given the short time scale variability detected at X-ray wavelengths, future observations of X-ray and radio should be taken simultaneously (ideally VLBI with X-ray). Simultaneous, well sampled observations are needed, as large time gaps between badly sampled X-ray and radio luminosity measurements (which are averaged) are likely to introduce inaccuracies in radio/X-ray correlation experiments. Measurement errors, and other problems such as insufficient sampling and non-

simultaneity of data are proposed reasons for the observed scatter in the fundamental plane. Ideally future investigations of the fundamental plane should use the same method of measuring BH mass for the entire sample; however,it is not as easy to use M-σ relationships for bright AGN, or reverberation mapping for faint AGN. An increased number of accurately measured data points on the plane would reveal if the scatter at the high-mass end of the plane is the result of intrinsic source differences or the result of a few outlying galaxies. To better understand the reason why Seyfert galaxies introduce much scatter into the fundamental plane the simultaneous radio and X-ray emission of many other Seyfert sources (with accurate mass estimates) will need to be investigated. Also, analysis of Seyferts which have similar spectral states is required to determine if the spectral state of the accretion disc is a cause of observed scatter in the fundamental plane (Maccarone *et al.*, 2003). Further investigation is also required to determine if the direct comparison between 'soft state' AGN (like NGC 4051) and their lower mass counterparts is accurate. Specifically more 'soft state' AGN should be investigated at radio and X-ray wavelengths to see if they scale by mass in line with 'soft state' BHBs (and vice versa) i.e. is there a 'soft state' branch/plane below the well defined 'hard state' plane (e.g. Calvelo *et al.* (2010); Russell *et al.* (2010)).

The scatter in the fundamental plane is also likely to result from radio observations where the nuclear flux is over-estimated due to unresolved extended emission or under-estimated due to observations with long baselines resolving out nuclear flux (Bell *et al.*, 2011). Future studies need to find a balance between high resolution and sensitivity so that the measured nuclear radio flux is an accurate measure of intrinsic core flux only. Future studies of the plane should also analyse the CCFs of the observed X-ray and radio lightcurves. Such analysis will determine if a statistically significant time lag exists between the X-ray and radio emission for the BH studied. A lag will indicate that lightcurves should be shifted with respect to one another first so that corresponding luminosities are used to determine the $L_R \propto L_X^{\beta}$ relationship for the BH. This method makes it more likely that radio/X-ray luminosity values plotted onto the relationship correspond to the same physical event. Work by (Bell *et al.*, 2011) has shown that shifting the X-ray and radio data by the measured time lag increased the gradient found for the $L_R \propto L_X^{\beta}$ relationship for LLAGN NGC 7213 from $\beta = 0.2 \pm 0.056$ to $\beta = 0.58 \pm 0.14$, where the latter value is more in line with the fundamental plane relationship of Merloni *et al.* (2003) who measure $\beta = 0.6 \pm 0.11$. Other possible causes of scatter should also be investigated, such as beaming effects (Heinz and Merloni, 2004) and the effects of black hole spin.

Future structure studies of NGC 4051 and Seyferts should use a combination of high sensitivity and high resolution imaging at several radio frequencies to give imaging on both parsec and sub-parsec scales. Such imaging will provide a valuable insight into the presence of the (jet) outflows, which have already been detected in a few Seyferts (e.g. Kukula *et al.* (1999); Mundell *et al.* (2003)), and their relationship with the accretion disc. For NGC 4051, such imaging will not only help to determine if the proposed jet is 'active', but also provide spectral index values and astrometry measurements for both the core and SW and NE components. For the case of NGC 4051 further VLBI observations taken at a time > 3 years since the last observation (in 2007) will help reveal if the tentative relative motion detected for the SW hotspot is real. Further deep imaging of both the optical [OIII] and radio emission from NGC 4051 and other Seyferts will be important in understanding the interaction between radio lobes and the surrounding line-emitting gas. Also, detailed X-ray imaging of NGC 4051 and other Seyferts which have radio lobes will provide temperature and density estimates for the observed lobes, which can be used to estimate the thermal pressure, leading to more accurate measurements of lobes energies and jet power.

Banish the wonky data, oh she of the troublesome pipeline!

MAM

A

The 610 MHz survey of the 13^H Field

The radio reduction of deep survey data of the 13^H field was carried out by the author at 610 MHz. The aim of this reduction was to combine the 610 MHz observations with 1.4 GHz observations from Seymour *et al.* (2004) to obtain spectra of faint sources. The spectral index of each of the sources would then be used to discriminate between AGN and starburst emission. The discrimination of sources requires very deep radio imaging so there must be very little structure to the noise so that all sources detected at $> 3.5\sigma$ are real sources. Despite radio reduction and imaging that achieved rms noise values close to the theoretical noise the extended noise features around bright sources in these images prevented completion of this work within the time frame of this thesis. In this section the radio reduction techniques for reducing the deep field Giant Meterwave Radio Telescope (GMRT) data are discussed. I explain the challenges that arose during the reduction of this data set and the potential for future work using this data set.

A.1 Introduction

The 13^H field was previously observed and analysed in Moss (2007) using 4.5 hours of data from August 2004, and 20 hours of data from 2006. Attempts at imaging the 2004 data revealed a dominant source of noise in the images due to side lobes from a bright source, which it was assumed, was caused by imperfect deconvolution of its extended structure and/or small residual phase errors. Moss (2007) attempted to remove the side lobes using a model of the source from the *uv* database which was free from imaging artifacts. However, despite reducing the flux density of the brightest source in the map the noise surrounding the source was not significantly reduced. This revealed that the reason for the high noise levels were due to phase calibration errors rather than deconvolution problems. As a result, future observations of the 13^H field were taken in 2006, these observations however had large amplitude ripples in the uncalibrated visibilities which made the data unusable. The make-up observations taken in 2007 are presented in this Appendix. These were carried out with shorter interval between scans of the phases calibrator with the intention of improving the phase calibration and hence the effects of the bright source on the extended map.

The motivation for studying deep surveys, specifically those of faint radio sources stems from research which showed that radio luminosity was directly linked to star formation rate (SFR) for galaxies with weak or no AGN radio emission (Condon, 1992). Using two radio flux density measurements to estimate the spectral index of a source is just one of the diagnostics used to discriminate between Active Galactic Nuclei (AGN) and Star Forming Galaxies (SFGs). Other diagnostics include the use of radio morphology, radio to mid-IR flux density ratio, radio to near-IR flux density ratio and radio spectral index. The GMRT 13^H field survey presented in this Appendix is currently one of the deepest radio surveys and is ideal for observing faint sources.

The long term goal of this work is to provide a view of the sub-mJy population. Present results show an upturn in radio source counts below 1 mJy. Discrimination of sources in the 13^H field survey will reveal which type of source is more prevalent, AGN or SFGs, giving astronomers a better understanding of how galaxies form at this early stage of universe formation.

The 13^H field was originally the target of one of the deepest ROSAT X-ray surveys (McHardy *et al.*, 1998), chosen to provide low absorption in the X-ray. It was not selected to avoid bright radio sources, so the effects of the bright source near the centre of the field was not considered.

A.2 Non-thermal Radio Sources

There are several processes other than AGN (which were discussed extensively in the main body of this thesis), that emit radiation via non-thermal processes. Two examples are the hyperfine transition of the 21cm Hydrogen line which emits at radio wavelengths, and star formation.

A.2.1 Star forming galaxies

For a star to form, a triggering mechanism and a reservoir of gas are required. The massive, most short lived stars explode and die leaving supernovae remnants (SNRs). Inside the massive SNRs synchrotron radio emission is given off by cosmic ray electrons being accelerated in the magnetic fields of the remnant. There is also free-free emission from HII regions ionised by main sequence stars ($M > 15M_{\odot}$). These massive stars and the cosmic ray electrons both have life times far less than the age of our galaxy, which has an estimated age $> 10^{10}$ years. The radio emission from the cosmic rays accelerated in the supernova can be used as an extinction free tracer of star formation (Seymour *et al.*, 2008). The massive stars within star formation regions often exist in binary systems, such as high mass X-ray binaries where matter is accreted onto a compact object producing X-ray emission. X-ray emission is also produced by soft X-rays from diffuse gas. As a result of the radio and X-ray emission, star formation galaxies (SFGs) are often brighter than normal galaxies at radio and X-ray wavelengths. Figure A.2.1 shows the rounded morphologies of SFGs, they exhibit little to no extended features. The differences between the morphologies of SFGs and AGN is one of the diagnostics for discriminating between sources.

A.3 Radio spectral index

After imaging as deeply as possible, a source catalogue can be produced, where sources are selected from pixel values greater than 3.5σ (using the task SAD in AIPS). The spectral index of each source can be determined by matching the resolutions of the GMRT data at 610 MHz with VLA (A & B array data) at 1.4 GHz which has been reduced and imaged by Seymour *et al.* (2004).

The spectral index is calculated using $\alpha = 2.77\log((S_{1.4})/(S_{610}))$. AGN have a wide spread of expected spectral index values, inverted ($\alpha > 0$) to the very steep $\alpha < -1.3$ and starbursts lie within the limits of $-1 < \alpha < -0.4$. The radio spectra,

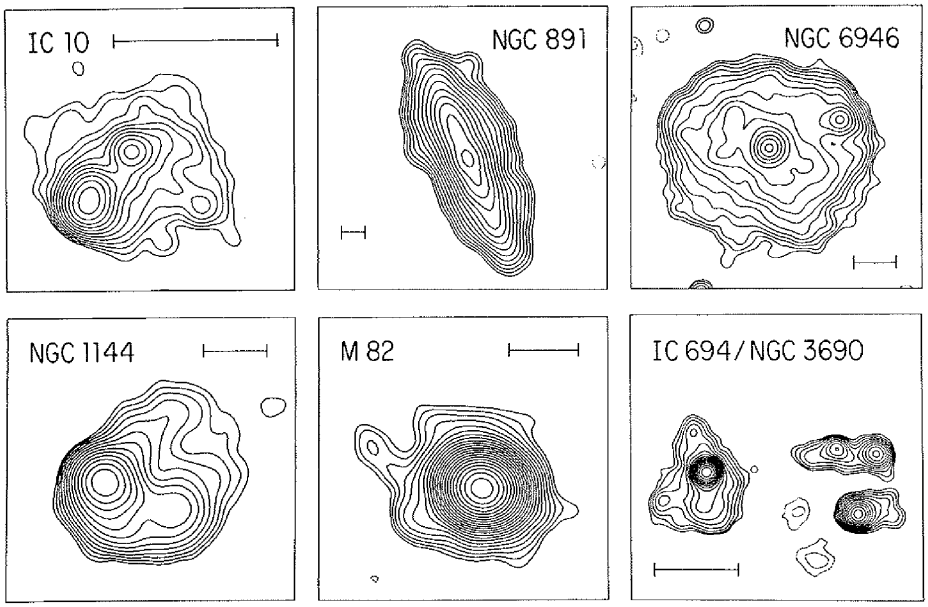

Figure A.1: Contour plots of the 1.49 GHz continuum emission from a range of nearby galaxies (Condon, 1992). Generally all the star forming galaxies have rounded morphologies. The differences between the morphologies of SFGs and AGN is an important diagnostic for discriminating sources. In all plots the horizontal bars are 3 kpc long and contours are spaced by factors of 212 in brightness.

although very useful, are not the only diagnostic available to discriminate between galaxy types. Another useful discriminator which is used is that of radio morphology. Figure A.3 and Figure 1.7 both show a bright FRI source, which is seen in the bottom right of the 13^H field. The symmetry of the two radio structures observed suggest the presence of a jet, which is strong evidence that this particular radio source is an AGN. For other sources radio morphology must be used in combination with the spectral index to determine the source type. Other AGN/SFG diagnostics also exist such as radio/IR ratios, radio luminosities, SED fitting and radio/optical ratios.

A.4 Radio Observations

In July 2007 the 13^H field (RA 13h 34m 37s and DEC 37°54'43") was observed with the Giant Metrewave Radio Telescope (GMRT). Observations from 24th -31st July contained 7 days of observations, each containing 2 sidebands of data with an integration time of $\sim$ 220minutes per sideband. The total integration time on source was therefore $\sim$ 50 hours, the actual amount of usable data was found to be $\sim$ 36 hours. Unlike the VLA data which was discussed in the main body of this

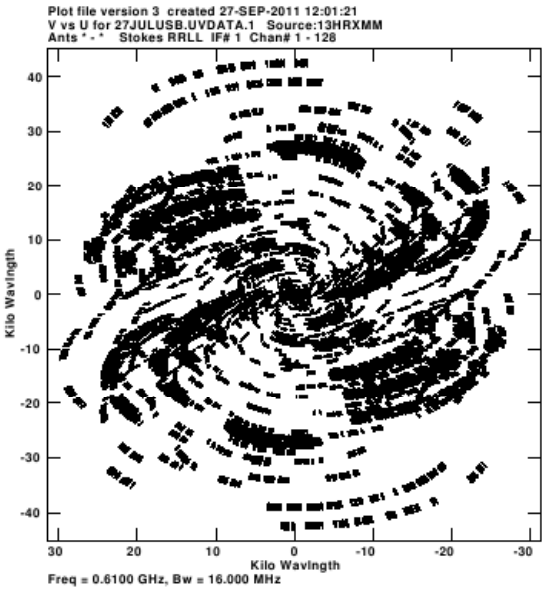

Figure A.2: The *uv* plane coverage for the USB dataset taken on 27 July 2007 with an integration time on source of $\sim$ 220 minutes.

thesis, the GMRT correlator operates in spectral line mode. It splits the observed bandwidth into many spectral channels and visibilities are recorded as a function of frequency. Observations were carried out in dual band mode to maximise bandwidth, spectral line mode to minimise chromatic aberration, and the splitting of the bandwidths into channels will minimise bandwidth smearing. Each side band (Upper Side Band (USB) & Lower Side Band (LSB)) contains 128 spectral channels with width 125 kHz centred at 602 and 618 MHz, giving a total bandwidth of 32 MHz with two independent circular polarisations are recorded.

The phase and flux calibration source, 3C286, was observed between each scan of the 13^H field typically for $5-20$minutes each time (giving a total time of calibrator observation at $\sim$ 120minutes per sideband). Note that the 13^H field was observed for $\sim$ 20 minutes in between each scan of the calibrator. The observations of 3C286 provided both the bandpass and absolute flux calibration. The *uv* plane coverage for the GMRT from a single sideband observation taken on on 27 July 2007 with an integration time on source of $\sim$ 220 minutes is shown in Figure A.2.

A.5 Radio Reduction

I reduced each GMRT *uv* data set using the NRAO AIPS software and all 'tasks' which are mentioned in this Appendix are AIPS tasks. The reduction method dis-

cussed in the following sections involves calibration, preliminary imaging and self calibration of each sideband independently. The aim of this project was to reduce and image all 14 sidebands of *uv* data and then combine these into a single deep image where faint sources are easily distinguishable from the thermal noise. After initial investigations of the amplitude and phase variations with time, for each sideband *uv* data I decided to remove 4 sidebands of data from the sample. Problems such as power outages and high levels of RFI made these sidebands un-usable.

A.5.1 Bandpass Calibration

The bandpass calibration is the first step in the calibration of the sideband data. It corrects for complex gain variations as a function of frequency. In order to calibrate the bandpass over the entire spectrum an amplitude correction is applied. The relative frequency response of the 128 channels can be determined by observing the calibrator source, 3C286; the spectrum over this source must be flat over the frequency band (Perley, 2003). The first step in the standard reduction involves using the task POSSM to examine the amplitude and phase variations across the 128 channels in each sideband to determine the best channels to determine the amplitude correction for the bandpass. In order to do this I chose 6 consecutive channels where the amplitude was steady, to average over for amplitude correction of each baseline. By looking at plots of amplitude and phase variations versus channel number features from interference, cross talk between antennas and instrumental glitches are easy to find by visual inspection. The channels 80-85 were chosen because the spectrum was relatively flat at these frequencies for all sidebands inspected, these channels contained no large amplitude difference and phase differences that would result in an inaccurate bandpass calibration. A bandpass calibration is carried out before making the channel zero file and then again after making the channel zero file, before spectral flagging. The bandpass table produced is checked each time using the task BPLOT to ensure that the spectrum is flat for all baselines.

A.5.2 Calibration & Flagging

After producing a bandpass table the amplitude and phase of both the flux and phase calibrator is checked using TVFLG by averaging the 128 channels into one channel. Note that for this data set 3C286 is used to calibrate both phase and amplitude. Only obvious instances of Radio Frequency Interference (RFI) or glitches are flagged out at this stage . For the calibrator, such ‘glitches’ were instances where the amplitude

is dramatically below or above it's expected flux value of ≈ 21.2 Jy or where the phase difference for a specific baseline is greater than 3°.

After visually inspecting the source and calibrator a channel zero (hereafter CH0) file is produced to perform the calibration. A CH0 file made from averaging 6 channels which have no RFI or correlator errors, is created in order to get an accurate calibration which can be applied to all 128 channels. The method which I used to calibrate the CH0 file is the same as the method used to calibrate the VLA continuum data which is presented in depth in Chapter 2. A brief discussion of the GMRT calibration is given below:

The first step in calibration is to use the task SETJY which enters the flux of the flux calibrator source into the solution table so it can be used in the calibration. The flux and phase calibrator for the 13^H field is 3C286(1331+305) which has a flux at 610MHz of ≈ 21.2 Jy. The tasks CALIB and CLCAL are then used to calibrate data using 3C286. The calibration was checked using the tasks UVPLT and VPLOT to plot *uv* coverage, graphs of amplitude against *uv* distance and phase against *uv* distance for each baseline, the phase difference and amplitude difference for each baseline were also investigated. The task TVFLG was used to flag out bad data by displaying amplitude, amplitude difference, phase and phase difference versus baseline plots in both IF's, finally after removing all erroneous data the calibration was then re-run before imaging.

An image of the CH0 file is produced at this stage to check the accuracy of the calibration; if the image has a low noise level and no obvious phase errors around bright sources this suggests this single channel file is well calibrated. The calibration and flag tables from the CH0 file can then be copied onto the 128 channels of spectral line data for that day and sideband. Before performing any flagging on the calibrated data set the bandpass calibration is carried out and then applied to the data to take into account the relative frequency response of each of the 128 channels. Further flagging on all 30 antennas across all 128 channels, for both the calibrator source, 3C286 and the 13^H field is done using the task SPFLG.

A.5.3 Imaging Strategy

After flagging and calibrating the 13^H field, I checked the *uv* data by graphing the amplitude difference and phase difference values versus baseline. I then create an image of a single sideband of data. Deconvolution of the dirty beam was performed using the Clean algorithm in the task IMAGR using a 5×5 grid of facets, to account for 3D smearing. This smearing effect needs to be considered when using several

hours of data. After several hours of observing has passed an appreciable fraction of Earth rotation has occurred which will means the array of baselines occupies the surface of a sphere; not a plane. For a setup with a wide primary beam like the GMRT the sources at the edge of the primary beam are far from the phase tracking centre. The net result is a smearing of the flux whose magnitude increases with radius from the phase centre; to get around this effect I have made images from a series of flat image facets where the *uv* data is re-phased at the centre of each facet. There are 51 facets in total, 25 facets for the 13^H primary beam area and 26 facets outside the primary beam around bright sources. Using a field of 25 facets ensures that each point in the facet is no more than 10 arcmin from the pointing centre (Moss, 2007). After imaging the 51 facets were combined into a single image using the task FLATN.

I chose to image from channel number 5 to 120 inclusive because the first and last channels of data are susceptible to errors. Images were made with a $1.2''$ cellsize to well sample the synthesized beam which was $6.12'' \times 5.40''$ in the final image shown in Figure A.3. After experimenting with different iteration of clean I deduced that 300,000 iterations with a FACTOR value -0.8 produced the best images. Note that the factor value was chosen to perform a deep clean of extended structure. After imaging both the LSB and USB from a single day, the spectral line data is then combined into one *uv* plane. The noise in the final images was estimated using the IMEAN which fits a histogram to all the pixels in the image and estimates the rms noise value.

A.5.4 Self Calibration

Self calibration is the final step in the imaging process. It fits a model of the actual science source to the image to improve the complex gain of the individual antenna. This is used because the ionosphere and the troposphere introduce variable phase effects; these can be calibrated out by using an image created in the external calibration. This image is an accurate model of the sky flux distribution, and can therefore be used as a model for what we expect the science source to look like.

To produce the final self calibrated image shown in Figure A.3 one run of phase calibration was performed, followed by a second run of amplitude and phase self calibration. Both runs of self calibration were performed on all 51 clean fields and the number of clean components used in each run of self calibration was determined by using all clean components in each field up to the first negative component i.e. up to the first component with a negative flux value.

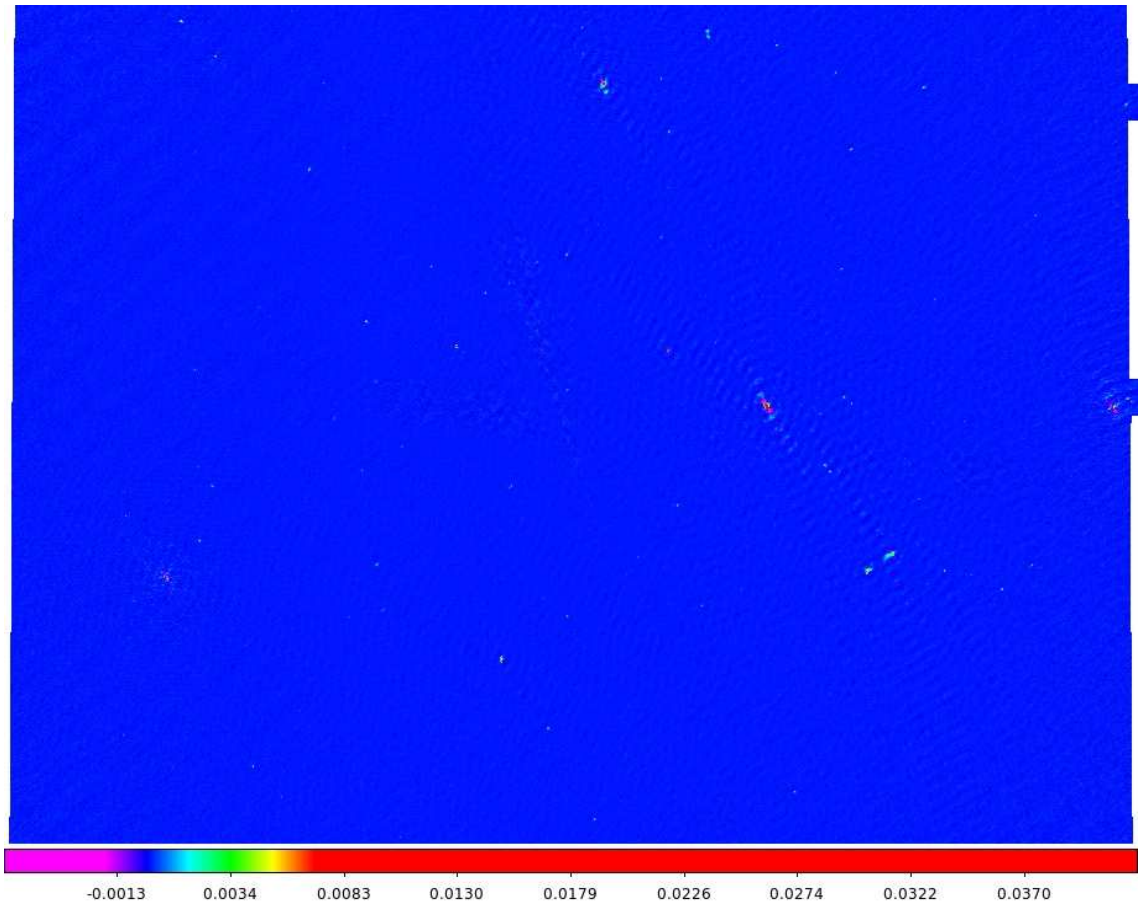

Figure A.3: Image of the 13^H field using robust 0 weighting from the USB *uv* data from 27 July 2007. Consists of 3.6 hours of integration time on source with self calibration performed on phase and amplitude. The angular resolution of the image is $6.12'' \times 5.40''$, and it has not been corrected for degradation in sensitivity of the primary beam. The rms noise level in the image is calculated using IMEAN and is estimated at 51μ Jy. The structure which remains in the noise due to a bright source with a flux density $\sim$ 160 mJy.

It was suggested in work by Moss (2007) that the new radio observations (from 2007, presented in this work) which observe the phase calibrator every 15 to 20 minutes, would be able to keep track of phase instabilities in the instrument and atmosphere. The new data would provide a more accurate phase calibration of the dominant bright source which was problematic in previous observations of the 13^H in 2004. This combined with the best possible self calibration model should remove the noise due to the brightest source. However, despite personally experimenting with various self calibration models the structure in the noise due to the brightest source could not be removed in this new dataset (see Figure A.4).

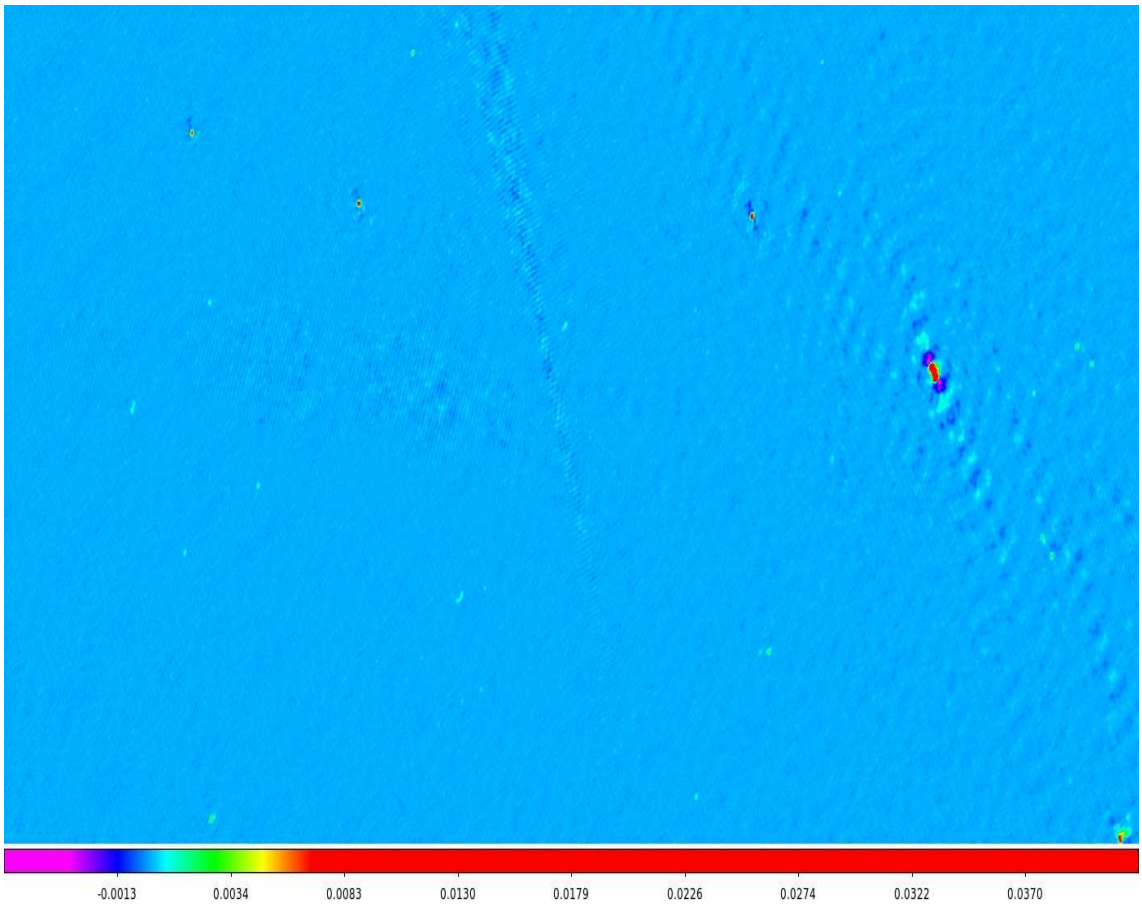

Figure A.4: Zoomed in image of the bright dominant source in the 13^H field after self calibration, from Figure A.3. The dominant bright source with a flux density $\sim 160\ mJy$ is the cause of much structure in the noise which is at a level that it can be confused with faint sources in the field.

A.6 Image Analysis

The rms noise level in the image shown in Figure A.3 which represents a ~ 3.6 hour integration time is calculated using IMEAN and is estimated at 51µJy. This noise level is an improvement on the best rms noise value at 55µJy for an image with a ~ 4.5 hour integration time for the 13^H field presented in Moss (2007). The theoretical rms noise level in units of mJy for the GMRT is calculated from the following equation:

$$\sigma_m = \frac{K}{\sqrt{N(N-1)(N_{IF}\tau\Delta V_m)}} \quad \text{(A.1)}$$

In Equation A.1 σ_m is the rms noise in units of mJy, K is a parameter based on the system temperature and the efficiency of the antenna, τ is integration time in hours, ΔV_m is the spectral line channel width in MHz, N_{IF} is the number of spectral line channels used and N is the number of antenna used. For the GMRT image shown in Figure A.3 at an observing frequency of 610 MHz during 2007 ΔV_m=125 kHz, τ=3.6 hours, and N_{IF}= 116. Therefore, the theoretical noise for this sideband is estimated at 30μJy which is a factor of 1.7 below the rms noise in the single side band image shown in Figure A.3. The dynamic range calculated from the ratio of the maximum flux and the rms noise in the image (Figure A.3) is 853:1. Given that the theoretical and actual rms noise are in good agreement, the theoretical dynamic range (based on the theoretical rms) value of 1393:1 suggests that weak sources should be detectable, in the presence of strong sources. Despite this 'impressive' rms noise value for the image I am still unable to detect faint sources near to the bright sources. The rms noise near to the brightest source is 1130μJy, a factor of 20 above the rms noise value in the whole image. This localised noise, around bright sources meant I was not able to detect any faint sources in this region. Future experiments to improve the localised noise, near bright sources should include experimenting with ROBUST 5 (natural weighting) and self calibration.

A.7 Combining Data

After each sideband has been successfully self calibrated, the sidebands are combined together to make a deeper image. The two sidebands (USB and LSB) from 26 July 2007 were combined using the tasks DBCON, FLOPM and BLOAT. This involved averaging 110 channels into 11 channels, giving a final dataset of 23 channels. The 51 clean fields were combined into a final image using the task FLATN. The final combined image which consisted of 250,000 clean iterations using FACTOR -0.8, is shown in Figure A.5. This image was made with a UVRANGE from 0.5 to 0 to remove the shortest baseline lengths below 0.5 kλ giving a beam size of $7.15'' \times 4.40''$. The sidelobes from the dominant bright source are not present in this combined image, however, the reduction of this imaged involved both the removal of the short baseline data (below 0.5 kλ) and the removal of 18 channels from each sideband i.e. removal of the side lobes has also resulted in many of the faint sources which were visible in Figure A.3 no longer being detected. This lack of faint sources is not useful for a study of the faint source population and future work on this data require investigation of the shorter baselines. From this study it

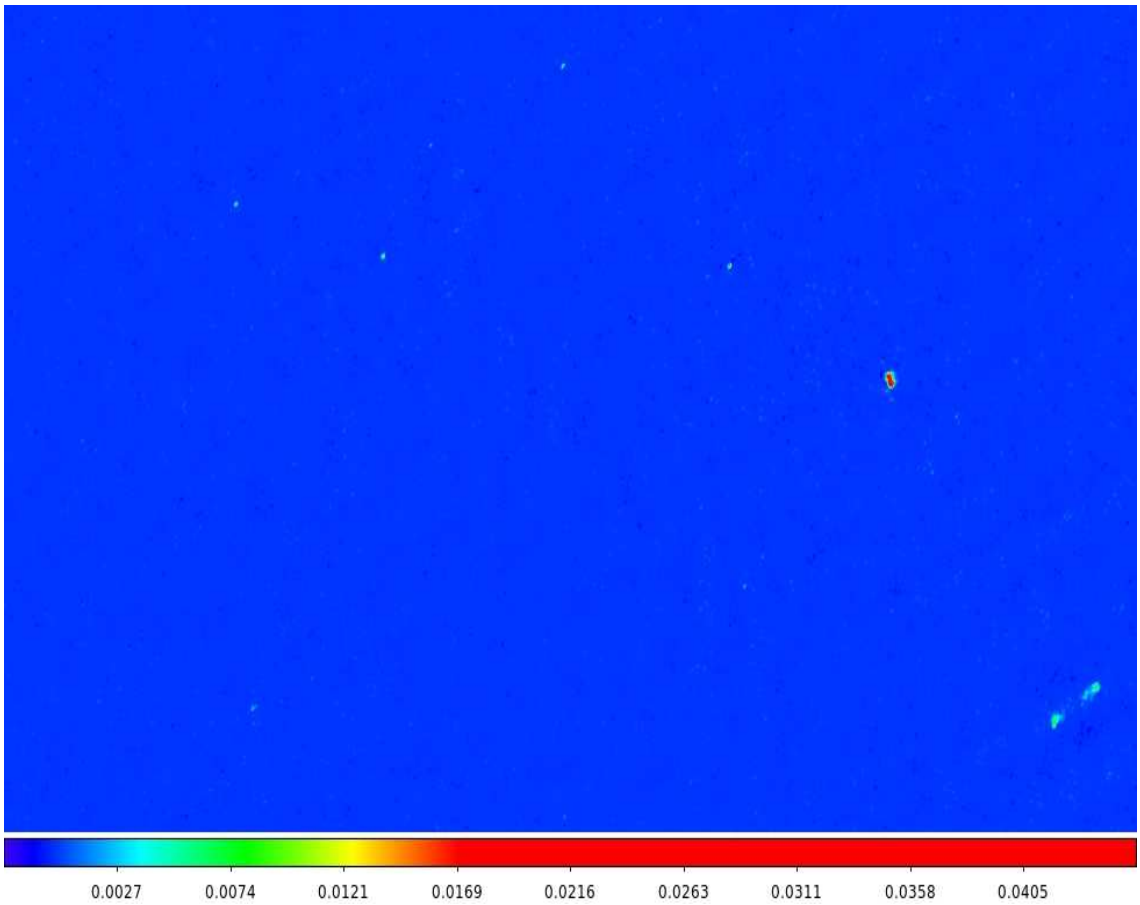

Figure A.5: Image of the 13^H field from combining data from two sidebands (USB and LSB) observed on the 26 July 2007. The sidelobes from the dominant bright are not present in this combined image; however, the reduction of this imaged involved both the removal of the short baseline data (below 0.5 kλ) and the removal of 18 channels from each sideband. The removal of data which led to the side lobes from the bright source disappearing has also resulted in many of the faint sources which were visible in Figure A.3 no longer detected, this is not useful for a study of the faint source population.

appears that the short baselines (which give the best sensitivity) may be responsible for the bad phase calibration which causes the noise structure around the bright source.

At the time of writing the structure in the noise due to a dominant bright source is a 'feature' of many of the sidebands of *uv* data which have been reduced by the author. Therefore, the production of deep field images from which a source catalogue can be formed is beyond the time framework of this thesis. In the following section I discuss the short range future for this deep field imaging of the 13^H field and the long range future of deep surveys.

A.8 Future work on deep surveys

A.8.1 Short range

The obvious future for the 2007 data set is to experiment further with both the phase calibration and imaging. The first step should involve construction of a model of the bright source using clean components from the 1.4 GHz VLA A configuration map from Seymour *et al.* (2004), following the method in Moss (2007). This model should then be subtracted from the *uv* database in an effort to remove the bright sidelobes.

Experiments should also be carried out on the weighting of the image. In the 'natural' weighting scheme (using ROBUST= 5 in AIPS) each visibility is given a weight based on its system temperature, this achieves the highest possible sensitivity which is required in this deep survey. This weighting should be used as opposed to 'uniform' weighting (ROBUST= -5 in AIPS) which gives the best resolution, or ROBUST= 0, which was used in this work gives a balance between resolution and sensitivity. The majority of sources in the 13^H are point-like and well separated spatially, therefore, resolution is not important. Using the natural weighting scheme should result in a lower noise value which will improve the detection limit which can be achieved; however, experimenting with weighting alone will not removed the sidelobes from the brightest sources.

Further investigation should be carried out on the CHO file, since errors in the calibration of this file will effect all 128 spectral line channels which are used to make the final image. Also the self calibration procedure should be investigated, as careful self calibration may rectify some of the phase errors which cause the artifacts in the image around the brightest sources.
On completion the final image (with $\sim$ 36 hours of integration on source) of the 13^H field will rival the deep imaging of the field using the VLA at 1.4 GHz, allowing new sources to be discovered in the extended area of the images. The new image may also reveal some steep spectrum sources which are not present in the VLA data.

A.8.2 Long range

The long term future for deep radio surveys lies in upgrades to the current telescopes, such as eMERLIN and the EVLA, and in projects to construct new arrays, such as - the LOw Frequency ARray (LOFAR) and the Square Kilometer Array (SKA). LOFAR, which operate at low frequencies (10-240 MHz) will consist of an

array of small omni-directional antennas spread around the North West of Europe. The final interferometer is estimated to have 15,000 elements, achieving a maximum baseline of $\sim$ 100 km. The improved sensitivity of this instrument, compared to the GMRT, will provide deeper radio imagery providing a better view of the sub mJy population and allowing the detection of many more sources out to far higher red shifts. The SKA should reach sub-μJy noise levels with sub-arcsec resolution at centimetre wavebands, like LOFAR this will achieve very deep imaging providing better star formation estimates. Together the upgraded and new radio telescopesthe will provide greater understanding of the star formation history of the Universe.

BIBLIOGRAPHY

Allen S. W., Dunn R. J. H., Fabian A. C., Taylor G. B., Reynolds C. S., 2006, Mon. Not. R. Astron. Soc., 372, 21

Antonucci R., 1993, Ann. Rev. Astron. Astrophys., 31, 473

Antonucci R. R. J., Miller J. S., 1985, Astrophys. J., 297, 621

Arévalo P., Papadakis I. E., Uttley P., McHardy I. M., Brinkmann W., 2006, Mon. Not. R. Astron. Soc., 372, 401

Baum S. A., O'Dea C. P., Dallacassa D., de Bruyn A. G., Pedlar A., 1993, Astrophys. J., 419, 553

Bell M. E., Tzioumis T., Uttley P., Fender R. P., Arévalo P., Breedt E., McHardy I., Calvelo D. E., Jamil O., Körding E., 2011, Mon. Not. R. Astron. Soc., 411, 402

Belloni T. M., 2010, in T. Belloni (ed.), *Lecture Notes in Physics, Berlin Springer Verlag*, vol. 794 of *Lecture Notes in Physics, Berlin Springer Verlag*, pp. 53–+

Blandford R. D., Konigl A., 1979, Astrophys. J., 232, 34

Blundell K. M., Beasley A. J., Bicknell G. V., 2003, Astrophys. J. Lett., 591, L103

Booler R. V., Pedlar A., Davies R. D., 1982, Mon. Not. R. Astron. Soc., 199, 229

Breedt E., 2009, *The relationship between the X-ray and Optical Variability in Seyfert Galaxies*, Ph.D. thesis, University of Southampton, UK

Breedt E., Arévalo P., McHardy I. M., Uttley P., Sergeev S. G., Minezaki T., Yoshii Y., Gaskell C. M., Cackett E. M., Horne K., Koshida S., 2009, Mon. Not. R. Astron. Soc., 394, 427

Breedt E., McHardy I. M., Arévalo P., Uttley P., Sergeev S. G., Minezaki T., Yoshii Y., Sakata Y., Lira P., Chesnok N. G., 2010, Mon. Not. R. Astron. Soc., 403, 605

Brinkmann W., Laurent-Muehleisen S. A., Voges W., Siebert J., Becker R. H., Brotherton M. S., White R. L., Gregg M. D., 2000, Astron. Astrophys., 356, 445

Brocksopp C., Fender R. P., McCollough M., Pooley G. G., Rupen M. P., Hjellming R. M., de la Force C. J., Spencer R. E., Muxlow T. W. B., Garrington S. T., Trushkin S., 2002, Mon. Not. R. Astron. Soc., 331, 765

Broderick J. W., Fender R. P., 2011

Browne I. W. A., Marcha M. J. M., 1993, Mon. Not. R. Astron. Soc., 261, 795

Burbidge G. R., 1959, Astrophys. J., 129, 849

Calvelo D. E., Fender R. P., Russell D. M., Gallo E., Corbel S., Tzioumis A. K., Bell M. E., Lewis F., Maccarone T. J., 2010, Mon. Not. R. Astron. Soc., 409, 839

Christopoulou P. E., Holloway A. J., Steffen W., Mundell C. G., Thean A. H. C., Goudis C. D., Meaburn J., Pedlar A., 1997, Mon. Not. R. Astron. Soc., 284, 385

Churazov E., Gilfanov M., Revnivtsev M., 2001, Mon. Not. R. Astron. Soc., 321, 759

Cohen M. H., Pearson T. J., Readhead A. C. S., Seielstad G. A., Simon R. S., Walker R. C., 1979, Astrophys. J., 231, 293

Condon J. J., 1992, Ann. Rev. Astron. Astrophys., 30, 575

Condon J. J., Anderson E., Broderick J. J., 1995, Astron. J., 109, 2318

Condon J. J., Condon M. A., Gisler G., Puschell J. J., 1982, Astrophys. J., 252, 102

Corbel S., Fender R. P., Tomsick J. A., Tzioumis A. K., Tingay S., 2004, Astrophys. J., 617, 1272

Corbel S., Fender R. P., Tzioumis A. K., Nowak M., McIntyre V., Durouchoux P., Sood R., 2000, Astron. Astrophys., 359, 251

Corbel S., Nowak M. A., Fender R. P., Tzioumis A. K., Markoff S., 2003, Astron. Astrophys., 400, 1007

de Bruyn A. G., Wilson A. S., 1978, Astron. Astrophys., 64, 433

Di Matteo T., 1998, Mon. Not. R. Astron. Soc., 299, L15+

Di Matteo T., Fabian A. C., Rees M. J., Carilli C. L., Ivison R. J., 1999, Mon. Not. R. Astron. Soc., 305, 492

Dunn R. J. H., Fabian A. C., Taylor G. B., 2005, Mon. Not. R. Astron. Soc., 364, 1343

Edelson R. A., Krolik J. H., 1988, Astrophys. J., 333, 646

Fabian A. C., Sanders J. S., Ettori S., Taylor G. B., Allen S. W., Crawford C. S., Iwasawa K., Johnstone R. M., Ogle P. M., 2000, Mon. Not. R. Astron. Soc., 318, L65

Falcke H., Körding E., Markoff S., 2004, Astron. Astrophys., 414, 895

Falcke H., Lehár J., Barvainis R., Nagar N. M., Wilson A. S., 2001a, in B. M. Peterson, R. W. Pogge, & R. S. Polidan (ed.), *Probing the Physics of Active Galactic Nuclei*, vol. 224 of *Astronomical Society of the Pacific Conference Series*, pp. 265–+

Falcke H., Markoff S., Bower G. C., 2009, Astron. Astrophys., 496, 77

Falcke H., Markoff S., Fender R., 2001b, in *Astronomische Gesellschaft Meeting Abstracts*, pp. 107–+

Fanaroff B. L., Riley J. M., 1974, Mon. Not. R. Astron. Soc., 167, 31P

Fender R., 2010, in T. Belloni (ed.), *Lecture Notes in Physics, Berlin Springer Verlag*, vol. 794 of *Lecture Notes in Physics, Berlin Springer Verlag*, pp. 115–+

Fender R., Corbel S., Tzioumis T., McIntyre V., Campbell-Wilson D., Nowak M., Sood R., Hunstead R., Harmon A., Durouchoux P., Heindl W., 1999, Astrophys. J. Lett., 519, L165

Fender R. P., 2001a, in *Black Holes in Binaries and Galactic Nuclei*, pp. 193–+

Fender R. P., 2001b, Mon. Not. R. Astron. Soc., 322, 31

Fender R. P., Belloni T. M., Gallo E., 2004, Mon. Not. R. Astron. Soc., 355, 1105

Fender R. P., Gallo E., Russell D., 2010, Mon. Not. R. Astron. Soc., 406, 1425

Fender R. P., Homan J., Belloni T. M., 2009, Mon. Not. R. Astron. Soc., 396, 1370

Foschini L., Angelakis E., Bonnoli G., Calderone G., Colpi M., D'Ammando F., Donato D., Falcone A., Fuhrmann L., Ghisellini G., Ghirlanda G., Hauser M., Kovalev Y. Y., Maraschi L., Nieppola E., Richards J., Stamerra A., Tagliaferri G., Tavecchio F., Thompson D. J., Tibolla O., Tramacere A., Wagner S., 2011, in G. E. Romero, R. A. Sunyaev, & T. Belloni (ed.), *IAU Symposium*, vol. 275 of *IAU Symposium*, pp. 176–177

Gallimore J. F., Axon D. J., O'Dea C. P., Baum S. A., Pedlar A., 2006, Astron. J., 132, 546

Gallo E., Fender R. P., Miller-Jones J. C. A., Merloni A., Jonker P. G., Heinz S., Maccarone T. J., van der Klis M., 2006, Mon. Not. R. Astron. Soc., 370, 1351

Gallo E., Fender R. P., Pooley G. G., 2003, Mon. Not. R. Astron. Soc., 344, 60

Gaskell C. M., Sparke L. S., 1986, Astrophys. J., 305, 175

Giroletti M., Panessa F., 2009, Astrophys. J. Lett., 706, L260

Gudel M., Benz A. O., 1993, Astrophys. J. Lett., 405, L63

Gültekin K., Cackett E. M., Miller J. M., Di Matteo T., Markoff S., Richstone D. O., 2009, Astrophys. J., 706, 404

Haniff C. A., Wilson A. S., Ward M. J., 1988, Astrophys. J., 334, 104

Heinz S., Merloni A., 2004, Mon. Not. R. Astron. Soc., 355, L1

Ho L. C., Filippenko A. V., Sargent W. L. W., 1994, in T. Courvoisier & A. Blecha (ed.), *Multi-Wavelength Continuum Emission of AGN*, vol. 159 of *IAU Symposium*, pp. 275–278

Ho L. C., Filippenko A. V., Sargent W. L. W., 1997, Astrophys. J. Suppl. Ser., 112, 315

Ho L. C., Ulvestad J. S., 2001, Astrophys. J. Suppl. Ser., 133, 77

Hornschemeier A. E., Heckman T. M., Ptak A. F., 2003, in *American Astronomical Society Meeting Abstracts*, vol. 35 of *Bulletin of the American Astronomical Society*, pp. 1352–+

Hovatta T., Nieppola E., Tornikoski M., Valtaoja E., Aller M. F., Aller H. D., 2008, Astron. Astrophys., 485, 51

Jamil O., Fender R. P., Kaiser C. R., 2010, Mon. Not. R. Astron. Soc., 401, 394

Jansky K. G., 1933, Nature, 132, 66

Jones S., McHardy I., Moss D., Seymour N., Breedt E., Uttley P., Körding E.,

Tudose V., 2011, Mon. Not. R. Astron. Soc., pp. 120–+

Kaspi S., Smith P. S., Netzer H., Maoz D., Jannuzi B. T., Giveon U., 2000, Astrophys. J., 533, 631

Kellermann K. I., Sramek R., Schmidt M., Shaffer D. B., Green R., 1989, Astron. J., 98, 1195

Khachikian E. Y., Weedman D. W., 1974, Astrophys. J., 192, 581

King A. L., Miller J. M., Cackett E. M., Fabian A. C., Markoff S., Nowak M. A., Rupen M., Gültekin K., Reynolds M. T., 2011, Astrophys. J., 729, 19

Koratkar A. P., Gaskell C. M., 1991, Astrophys. J. Suppl. Ser., 75, 719

Körding E., Falcke H., Corbel S., 2006a, Astron. Astrophys., 456, 439

Körding E. G., Fender R. P., Migliari S., 2006b, Mon. Not. R. Astron. Soc., 369, 1451

Krolik J. H., 1998, *Active Galactic Nuclei: From the Central Black Hole to the Galactic Environment*

Kukula M. J., Ghosh T., Pedlar A., Schilizzi R. T., 1999, Astrophys. J., 518, 117

Kukula M. J., Pedlar A., Baum S. A., O'Dea C. P., 1995, Mon. Not. R. Astron. Soc., 276, 1262

Lamer G., McHardy I. M., Uttley P., Jahoda K., 2003, Mon. Not. R. Astron. Soc., 338, 323

Laor A., Behar E., 2008, Mon. Not. R. Astron. Soc., 390, 847

Lister M. L., 2001, Astrophys. J., 561, 676

Longair M. S., 2010, *High Energy Astrophysics*

Maccarone T. J., Gallo E., Fender R., 2003, Mon. Not. R. Astron. Soc., 345, L19

Marconi A., Risaliti G., Gilli R., Hunt L. K., Maiolino R., Salvati M., 2004, Mon. Not. R. Astron. Soc., 351, 169

Margon B., 1982, Science, 215, 247

Marscher A. P., Gear W. K., 1985, Astrophys. J., 298, 114

McClintock J. E., Remillard R. A., 2006, *Black hole binaries*, pp. 157–213

McHardy I., 2007, in *From Planets to Dark Energy: the Modern Radio Universe*

McHardy I. M., Gunn K. F., Newsam A. M., Mason K. O., Page M. J., Takata T., Sekiguchi K., Sasseen T., Cordova F., Jones L. R., Loaring N., 2003, Mon. Not. R. Astron. Soc., 342, 802

McHardy I. M., Gunn K. F., Uttley P., Goad M. R., 2005, Mon. Not. R. Astron. Soc., 359, 1469

McHardy I. M., Jones L. R., Merrifield M. R., Mason K. O., Newsam A. M., Abraham R. G., Dalton G. B., Carrera F., Smith P. J., Rowan-Robinson M., Wegner G. A., Ponman T. J., Lehto H. J., Branduardi-Raymont G., Luppino G. A., Ef-

stathiou G., Allan D. J., Quenby J. J., 1998, Mon. Not. R. Astron. Soc., 295, 641

McHardy I. M., Papadakis I. E., Uttley P., Mason K. O., Page M. J., 2004, Nuclear Physics B Proceedings Supplements, 132, 122

Meier D. L., 2001, Astrophys. J. Lett., 548, L9

Merloni A., 2003, in Durouchoux P., Fuchs Y., Rodriguez J. (eds.), *New Views on Microquasars*, pp. 113–+

Merloni A., Heinz S., di Matteo T., 2003, Mon. Not. R. Astron. Soc., 345, 1057

Miller C. J., Nichol R. C., Gómez P. L., Hopkins A. M., Bernardi M., 2003, Astrophys. J., 597, 142

Moran E. C., Kay L. E., Davis M., Filippenko A. V., Barth A. J., 2001, Astrophys. J. Lett., 556, L75

Moss D., 2007, *Radio Spectral Properties of Faint Source Populations*, Ph.D. thesis, University of Southampton, UK

M^{c}Hardy I., Lawson A., Newsam A., Marscher A. P., Sokolov A. S., Urry C. M., Wehrle A. E., 2007, Mon. Not. R. Astron. Soc., 375, 1521

M^{c}Hardy I. M., 2005, in Gierlinski M., Done C. (eds.), *http://star-www.dur.ac.uk/∼gier/bennevis/frameset.html*

M^{c}Hardy I. M., Gunn K. F., Uttley P., Goad M. R., 2005, Mon. Not. R. Astron. Soc., 359, 1469

M^{c}Hardy I. M., Papadakis I. E., Uttley P., Page M. J., Mason K. O., 2004, Mon. Not. R. Astron. Soc., 348, 783

Mullin L. M., Riley J. M., Hardcastle M. J., 2008, Mon. Not. R. Astron. Soc., 390, 595

Mundell C. G., Ferruit P., Nagar N., Wilson A. S., 2009, Astrophys. J., 703, 802

Mundell C. G., Wrobel J. M., Pedlar A., Gallimore J. F., 2003, Astrophys. J., 583, 192

Mundt R., 1985, in D. C. Black & M. S. Matthews (ed.), *Protostars and Planets II*, pp. 414–433

Nagao T., Taniguchi Y., Murayama T., 2000, Astron. J., 119, 2605

Nagar N. M., Wilson A. S., Mulchaey J. S., Gallimore J. F., 1999, Astrophys. J. Suppl. Ser., 120, 209

Neff S. G., de Bruyn A. G., 1983, Astron. Astrophys., 128, 318

Osterbrock D. E., 1984, , 25, 1

Panessa F., Barcons X., Bassani L., Cappi M., Carrera F. J., Ho L. C., Pellegrini S., 2007, Astron. Astrophys., 467, 519

Perley R., 2003, *Synthesis Imaging in Radio Astronomy II*

Peterson B. M., 1997, *An Introduction to Active Galactic Nucleui*

Peterson B. M., Ferrarese L., Gilbert K. M., Kaspi S., Malkan M. A., Maoz D., Merritt D., Netzer H., Onken C. A., Pogge R. W., Vestergaard M., Wandel A., 2004, Astrophys. J., 613, 682

Peterson B. M., McHardy I. M., Wilkes B. J., Berlind P., Bertram R., Calkins M., Collier S. J., Huchra J. P., Mathur S., Papadakis I., Peters J., Pogge R. W., Romano P., Tokarz S., Uttley P., Vestergaard M., Wagner R. M., 2000, Astrophys. J., 542, 161

Ponti G., Miniutti G., Cappi M., Maraschi L., Fabian A. C., Iwasawa K., 2006, in A. Wilson (ed.), *The X-ray Universe 2005*, vol. 604 of *ESA Special Publication*, pp. 479–+

Pounds K. A., Done C., Osborne J. P., 1995, Mon. Not. R. Astron. Soc., 277, L5

Pounds K. A., Vaughan S., 2011, Mon. Not. R. Astron. Soc., pp. 219–+

Rafter S. E., Crenshaw D. M., Wiita P. J., 2011, Astron. J., 141, 85

Rees M. J., 1978, Mon. Not. R. Astron. Soc., 184, 61P

Rosario D. J., Whittle M., Nelson C. H., Wilson A. S., 2008, , 79, 1217

Russell D. G., 2002, Astrophys. J., 565, 681

Russell D. G., 2003, ArXiv Astrophysics e-prints

Russell D. M., Lewis F., Roche P., Clark J. S., Breedt E., Fender R. P., 2010, Mon. Not. R. Astron. Soc., 402, 2671

Russell D. M., Miller-Jones J. C. A., Maccarone T. J., Yang Y. J., Fender R. P., Lewis F., 2011, Astrophys. J. Lett., 739, L19+

Ryle M., Hewish A., 1960, Mon. Not. R. Astron. Soc., 120, 220

Ryle M., Vonberg D. D., 1948, Royal Society of London Proceedings Series A, 193, 98

Schmidt M., 1963, Nature, 197, 1040

Schmidt M., 1969, Ann. Rev. Astron. Astrophys., 7, 527

Schmitt H. R., Kinney A. L., 1996, Astrophys. J., 463, 498

Seyfert C. K., 1943, Astrophys. J., 97, 28

Seymour N., Dwelly T., Moss D., McHardy I., Zoghbi A., Rieke G., Page M., Hopkins A., Loaring N., 2008, Mon. Not. R. Astron. Soc., 386, 1695

Seymour N., Huynh M., Dwelly T., Symeonidis M., Hopkins A., McHardy I. M., Page M. J., Rieke G., 2009, Mon. Not. R. Astron. Soc., 398, 1573

Seymour N., M^{c}Hardy I. M., Gunn K. F., 2004, Mon. Not. R. Astron. Soc., 352, 131

Shapiro S. L., Lightman A. P., Eardley D. M., 1976, Astrophys. J., 204, 187

Smith F. G., 1974, *Radio astronomy*

Spada M., Ghisellini G., Lazzati D., Celotti A., 2001, Mon. Not. R. Astron. Soc., 325, 1559

Stirling A. M., Spencer R. E., de la Force C. J., Garrett M. A., Fender R. P., Ogley R. N., 2001, Mon. Not. R. Astron. Soc., 327, 1273

Summons D., 2008, Ph.D. thesis, University of Southampton, UK

Sunyaev R. A., Titarchuk L. G., 1980, Astron. Astrophys., 86, 121

Tanaka Y., Nandra K., Fabian A. C., Inoue H., Otani C., Dotani T., Hayashida K., Iwasawa K., Kii T., Kunieda H., Makino F., Matsuoka M., 1995, Nature, 375, 659

Terashima Y., Gallo L. C., Inoue H., Markowitz A. G., Reeves J. N., Anabuki N., Fabian A. C., Griffiths R. E., Hayashida K., Itoh T., Kokubun N., Kubota A., Miniutti G., Takahashi T., Yamauchi M., Yonetoku D., 2009, Publ. Astron. Soc. Jpn., 61, 299

Timmer J., Koenig M., 1995, Astron. Astrophys., 300, 707

Turner T. J., George I. M., Nandra K., Turcan D., 1999, Astrophys. J., 524, 667

Ulvestad J. S., Wilson A. S., 1984a, Astrophys. J., 278, 544

Ulvestad J. S., Wilson A. S., 1984b, Astrophys. J., 285, 439

Ulvestad J. S., Wilson A. S., 1989, Astrophys. J., 343, 659

Ulvestad J. S., Wilson A. S., Sramek R. A., 1981, Astrophys. J., 247, 419

Ulvestad J. S., Wong D. S., Taylor G. B., Gallimore J. F., Mundell C. G., 2005, Astron. J., 130, 936

Urry C. M., Padovani P., 1995, Publ. Astron. Soc. Pac., 107, 803

Uttley P., M^{c}Hardy I. M., Vaughan S., 2005, Mon. Not. R. Astron. Soc., 359, 345

van der Laan H., 1966, Nature, 211, 1131

Vaughan S., Uttley P., Pounds K. A., Nandra K., Strohmayer T. E., 2011, Mon. Not. R. Astron. Soc., 413, 2489

White R. J., Peterson B. M., 1994, Publ. Astron. Soc. Pac., 106, 879

Wiita P. J., 2006, ArXiv Astrophysics e-prints

Wilson A. S., Colbert E. J. M., 1995, in *American Astronomical Society Meeting Abstracts #186*, vol. 27 of *Bulletin of the American Astronomical Society*, pp. 830–+

Wilson A. S., Heckman T. M., 1985, in J. S. Miller (ed.), *Astrophysics of Active Galaxies and Quasi-Stellar Objects*, pp. 39–109

Wilson A. S., Tsvetanov Z. I., 1994, Astron. J., 107, 1227

Wilson A. S., Ulvestad J. S., 1982, Astrophys. J., 263, 576

Wrobel J. M., 2000, Astrophys. J., 531, 716